A study of layered contact problems with particular application to tyre-wheel interfaces

by

Saverio Reina

A thesis submitted to Imperial College London
for the degree of Doctor of Philosophy
and Diploma of Imperial College (D.I.C.)

June 2010

Tribology Section
Department of Mechanical Engineering
Imperial College London

Abstract

This thesis is concerned with the characterization of layered contact problems. The research project has been prompted by an investigation into creep, and ultimately, gross sliding, of rubber tyres fitted around steel wheels in earth moving equipment. In general, slippage between tyre and rim is experienced in common engineering applications employing tyred systems. A general and systematic approach for investigating the interfacial behaviour of tyred systems has consequently been proposed. Classical techniques together with novel numerical approaches based on advanced mathematical programming have been implemented to support the investigation. Creep between mating surfaces, frictional shakedown and measuring friction in partial slip condition are the main objects of investigation. The analytical and numerical models developed by the author have been complemented by experimental work, whose detailed description is also included in this thesis. Finally, further studies have been performed to shed light on some of the design issues offered by the three-dimensional full-scale engineering application. The numerical approach based on finite element modelling used to tackle these aspects of the project and the experimental work carried out by the author to corroborate the numerical findings are also presented.

Dedication

To my parents, Sandra and Augusto. None of this would have been possible without their unconditional love and constant support throughout my life.

Acknowledgements

I would like to express my sincerest gratitude to my supervisor Dr. Daniele Dini for his superb guidance, his precious advice and for the patience shown in our many long and fruitful discussions. I am also profoundly indebted to Dr. Daniele Dini for giving me the unvaluable and unique opportunity to be part of the Tribology Group at Imperial College London. Finally, I am extremely grateful to him not only for his moral and technical support but also for having given me the privilige to meet and work with Prof. D.A. Hills from the University of Oxford. I wish to convey here my deepest gratitude to Prof D.A. Hills, not just for his precious time spent discussing solid mechanics problems, but also for his invaluable advice and his fantastic lessons in British humour.

I wish to convey my gratitude to Prof. J.R. Barber from Michigan University with whom I have had the privilege to work.

I acknowledge the support of all the academics of the Tribology Group: Prof. H. Spikes, Dr. A. Olver, Dr. R. Sayles, Dr. J. Wong, Dr. P. Cann and Dr. D. Dini. I wish to thank the always very supportive post-docs of the Tribology Lab: Dr. R. Underwood, Dr. T. Fan, Dr. T. Reddyhoff, Dr. S. Medina, Dr. A. Kadiric, Dr. M. Chennaoui, Dr. A. Manzoor, Dr. M. Ingram and Dr. M. Fowell, to whom a special thanks goes for the time he spent correcting my thesis. Finally, I wish to express my gratitude to Ms. Chrissy Stevens for her great support throughout my PhD.

I acknowledge the financial support of GKN, JCB, Corus, Michelin and the UK Technology Strategy Board (TSB) for this thesis (grant TP/5/MAT/6/I/H0324L). I am also grateful for the technical support received from Mr. Steve Cragg (GKN), Mr. GianPietro Brame (GKN), Mr. Vaughan Ashton (GKN), Mr. Vincenzo Zuccarotto (GKN), Mr. Marc Aichele (Michelin FR), Mr. Dominique Dessevre (Michelin FR), Mr. John Redford (Michelin UK), Mr. Alex McCristal (JCB) and Mr. T.B. Jones (Corus), whose expertise has been invaluable.

I acknowledge Rema Tip Top for providing the tyre lubricants free of charge.

I wish to take a moment to express my gratitude to all my collagues of the Tribology Group and, especially, to Tom Reddyhoff and Marc Ingram, for their special friendship, moral support and constant dose of great humor when I needed it most. I wish to thank Angelos for the time we spent together on our research project and for his precious advice. Also, a special thanks goes to my friends of the Mechanical Engineering Department, in particular Panos and Tino, and of the MIM (Mechatronics in Medicine) lab, Luca, Yaroslav, Tassanai, Matthew, Seong-Young and Abby.

I wish to express my gratitude to Dr. Ferdinando Rodriguez Y Baena for giving me the privilige to work with Luca on his project.

I wish to thank Dr. Yusuke Iida, Mr. Robert Paynter and Mr. Paul Jobson for their invaluable support in carrying out the experimental part of my work. Not to be forgotten all the final year students who worked with me on the project, James, Mauro, Zhaohan, Byron, Shufan and Yu.

Not to forget all my friends at OLOV (Our Lady of Victories, Catholic Church, Kensington, London) where I fostered friendships for which I will be eternally grateful: Fr. Perry, my two special and always supportive housemates Ian and Luca(& Livia), two very special friends Andrea(& family) and Silvia, and also Cristian, Elisa, Marina, Andrew, John, Matthew, Paulina, Ryan, Joan, Tiziano, Miguel, Anita, Amy and many others who have been part of the Young Adults Group at OLOV.

A special thanks goes to the Daughters of St Paul and, particularly, to Sister Gregoria, for the unconditional support that I have received from her since my arrival in London.

Another very special thanks goes to the Indian crew and, particularly, to Sandeep for his true and unforgettable friendship. Thank you for your constant support through the difficult moments of our time at Imperial College.

Finally, a special thanks goes to my parents, Sandra and Augusto, and to my sisters, Clara and Paola, for standing by me at all times.

Preface

This thesis is a collection of research work carried out by the author in the Department of Mechanical Engineering, Imperial College London, under the supervision of Doctor Daniele Dini and in collaboration with Professor David A. Hills, who is based at the University of Oxford. The research project was funded by the UK Technology Strategy Board (TSB) (grant TP/5/MAT/6/I/H0324L) in collaboration with the following industrial partners: GKN, JCB, Corus and Michelin. The research is original, and no part of it has previously been submitted for a degree at this university or elsewhere. The work of other authors has been given due acknowledgement in the text. Some of the work described in this thesis has been published in the following papers:

Journal articles

1. Reina S., Hills D.A. and Dini D., (2010), "Determining the coefficient of friction without sliding", Wear (2010), Wear (2010), doi:10.1016/j.wear.2010.04.017.

2. Reina S., Dini D. and Hills D.A., (2010), "Interfacial Slip and Creep in rolling contact incorporating a Cylinder with an Elastic Layer", European Journal of Mechanics A/Solids (2010), doi:10.1016/j.euromechsol.2010.02.009.

3. Reina S., Hills D.A. and Dini D., (2010), "Contact of a rigid cylinder indenting an elastic layer sliding over a rigid substrate", European Journal of Mechanics A/Solids (2010),

doi:10.1016/j.euromechsol.2010.02.006.

4. Reina S., Hills D.A. and Dini D., (2010), "Incipient slip conditions in rolling contact of tyred wheels", Proceedings of the Institution of Mechanical Engineers, Part C: Journal of Mechanical Engineering Science, doi:10.1243/09544062JMES2075.

5. Reina S., Dini D., Hills D.A., Iida Y., (2010) ,"A Quadratic Programming Formulation for the Solution of Layered Elastic Contact Problems: Example Applications and Experimental Validation",

in preparation.

Conference contributions

1. Reina S., and Dini D. (2008), “Incipient slip and frictional creep of tyred systems”, ASME/STLE International Joint Tribology Conference, 20-22 October 2008, Miami, USA.

2. Reina S., Dini D. and Hills D.A. (2009), “On the accurate prediction of interfacial micro-slip in frictional joints using distributed dislocations and quadratic programming techniques”, Mesomechanics 2009, 24-26 June 2009, Oxford, UK.

3. Reina S. and Dini D. (2009), “A theoretical and experimental investigation of interface local slip and creepage in layered systems”, World Tribology Congress 2009, 6-11 September 2009, Kyoto, Japan.

4. Reina S., Dini D. And Hills D.A. (2009), “Measuring friction in partial slip fretting tests: theoretical and experimental investigations of “walking” contact pairs”, presented at ESMC 2009, 7th Euromech solid mechanics conference, 7-11 September 2009, Lisbon, Portugal.

5. Reina S., Dini, D. Nowell, D. and Hills D.A. (2009), “On the evolution of frictional hysteresis loops in fretting experiments” – ASME International, Mechanical Engineering Congress and Exposition, 13-19 November 2009, Lake Buena Vista, Florida, USA

6. Reina S., Dini D. and Hills D.A. (2009), “Measuring friction without sliding”– ASME International, Mechanical Engineering Congress and Exposition, 13-19 November 2009, Lake Buena Vista, Florida, USA

7. Reina S., Dini D. (2009), “Frictional shakedown in contact problems of layered systems”, ASME/STLE International Joint Tribology Conference, 19-21 October 2009, Memphis, USA.

8. Hills D.A., Dini D., Paynter R.J. and Reina S. (2010), “Fretting of complete contacts: an analytical solution for partial slip”, ECCM2010 IV European Conference on Computational Mechanics, 16-21 May 2010, Paris, France.

9. Reina S., Dini D., Hills D.A. (2010), “Interfacial frictional behaviour of layered systems under cyclic loading”, ECCM2010 IV European Conference on Computational Mechanics, 16-21 May 2010, Paris, France.

10. Hills D.A., Dini D., Paynter R.J. and Reina S. (2010), “On the calibration of fretting fatigue tests for complete contacts using asymptotic techniques”, USNCTAM2010 16th US National Congress of Theoretical and Applied Mechanics, June 27 – July 2, 2010, Pennsylvania, USA.

11. Reina S., Dini D., Hills D.A. (2010), “An Investigation of the Frictional Shakedown Behaviour of Elastic Layered Systems”, *submitted to* ASME/STLE International Joint Tribology Conference, 17-20 October 2010, San Francisco, USA.

Contents

Abstract 2

Dedication 3

Acknowledgements 4

Preface 6

Contents 9

List of Figures 14

Nomenclature 21

CHAPTER 1 Tyre-wheel interfaces in off-highway vehicles 26

1.1 Introduction 26

1.2 Literature review 27

1.2.1 Modelling technique 29

1.2.2 Layered systems - Onset of slip and interfacial slip modelling 35

1.2.3 Layered system - Modelling of gross sliding layers 39

1.2.4 Layered system - On the application of optimisation technique to elastic contact problems modelled using the distributed dislocation technique 42

1.2.5 Frictional shakedown in frictional elastic contact problems 43

1.2.6 Frictional joints - on the possibility to measure the friction coefficient in partial slip condition 45

1.3 Thesis outline 47

CHAPTER 2 Interfacial Slip and Creep in Tyred systems 49

2.1 Introduction 49

2.2 Formulation - bilateral solution 49

2.3 Formulation - unilateral solution 51

2.4 Results 55

2.4.1 Limits implied by the validity of the bilateral solution: first point of slip and separation 55

2.4.2 The use of the unilateral solution to study interfacial slip: Stationary loading 58

2.4.3 The use of the unilateral solution to study interfacial slip: Moving loading 61

2.5 Further Properties 66

2.5.1 Development of residual shear stresses and time history dependence 66

2.6 Summary 68

CHAPTER 3 Incipient slip conditions in rolling contact of tyred wheels 69

3.1 Introduction 69

3.2 Formulation 70

3.3 Results 72

3.4 Summary 77

CHAPTER 4 The case of an elastic layer sliding over a rigid substrate 78

4.1 Introduction 78

4.2 Formulation for unit tractions 78

4.2.1 Imposition of the boundary conditions 81

4.2.2 Influence Function for a Triangle of Surface Traction 83

4.2.3 Results 83

4.3 Example Application 91

4.4 Results 95

4.5 Summary 99

CHAPTER 5 Analysis of interfacial slip using quadratic programming 101

5.1 Introduction 101

5.2 Stationary loads 101

5.3 Moving loads 109

5.4 Numerical model validation 110

5.4.1 Cyclic loading - Tangential load - similar materials 113

5.4.2 Moving load 116

5.5 Experimental validation 118

5.6 Summary 122

CHAPTER 6 Frictional shakedown of layered systems 123

6.1 Introduction 123

6.2 Description of the problem 123

6.3 Results 127

6.3.1 Simplified loading cases - Flamant's problem 127

6.3.2 Rolling problem 133

6.4 Summary 140

CHAPTER 7 Measuring friction in partial slip 141

7.1 Introduction 141

7.2 Optimisation techniques applied to contact problems 143

7.3 Experiment 151

7.4 Summary 154

CHAPTER 8 Investigation on 3D tyre/wheel assembly 155

8.1 Introduction 155

8.2 Onset of slip-Preliminary considerations 156

8.3 FE models and numerical results 159

8.3.1 Loading conditions 160

8.3.2 Mesh optimisation, convergence issues and model set-up 160

8.3.3 Interfacial pressure: model vs experiment 163

8.3.4 Determination of the onset of slip 164

8.3.5 Effect of speed on the onset of slip 165

8.4 Effect of wheel deformability on pressure 171

8.5 Alternative rim profile 172

8.6 Tyre-Rim friction coefficient 174

8.7 Effect of knurling on tyre-rim interface slip 182

8.8 Tyre misfit and effect of improper lubrication 185

8.9 WFT and Rim stress field 187

8.10 Summary 193

CHAPTER 9 Conclusions and future work 194

9.1 Theoretical and experimental investigation 194

9.2 Future work 198

Reference 200

Appendix A 209

Appendix B 210

Appendix C ***215***

List of Figures

1 Figure 1.1. Example of Off-High Vehicle (*image courtesy of JCB - http://www.jcb.com*). 28

2 Figure 1.2. Schematic representation of the problem (*image courtesy of Michelin - http://www.michelin.com*). 29

3 Figure 1.3. Contact patch schematic. 30

4 Figure 1.4. Schematic representation of pressure distribution. 32

5 Figure 1.5. Rolling contact of a tyred roller with a second rigid roller. 33

6 Figure 1.6. (a) Schematic of the system - line contact; (b) Reduced problem and potential interfacial scenarios. 35

7 Figure 1.7. Review of the approaches available in the literature for the case under investigation. 36

8 Figure 1.8. Schematic of the system, the possible interface regimes, and review of the approaches available in the literature for the case under investigation. 40

9 Figure 2.1. Minimum friction coefficient f to guarantee adhesion as a function of the normalised layer thickness B for various friction coefficients μ and ν = 0.3 – full sliding of external contact over layer surface. 56

10 Figure 2.2. Minimum friction coefficient f to guarantee adhesion as a function of the normalised layer thickness B for various friction coefficients μ and ν = 0.5 – full sliding of external contact over layer surface. 57

11 Figure 2.3. (a) Minimum friction coefficient f to guarantee adhesion with and without the application of tangential forces (induced by an applied torque sufficient to cause full sliding of external contact over the layer surface) and (b) separation limit and as a function of the normalised layer thickness B for $\mu = 0.7$ and $\nu = 0.3$. 59

12 Figure 2.4. Normal, tangential tractions and tangential shift for B=1, ν=0.3, μ=0.7, λ=1 and f=0.2 - stationary case - full sliding of external contact over layer surface. 61

13 Figure 2.5. Slip region location and extent for B=1, ν=0.3, μ=0.7, f=0.2 and different values of the dimensionless constant pressure, λ=1 - stationary case (*traslational velocity=0*) - full sliding of external contact over layer surface. 62

14 Figure 2.6. Tangential tractions, normal tractions and dimensionless net tangential shift per cycle for B=1, ν=0.3, μ=0.7, λ=1 and f=0.2 - steady state solution for the moving load case - full sliding of external contact over layer surface. 63

15 Figure 2.7. Slip region location and extent for B=1, ν=0.3, μ=0.7, λ=1 and f=0.2 and different values of λ - steady state solution for the moving load case - full sliding of external contact over layer surface. The accumulated net displacement per cycle, $Cd/(a_H p_H)$, is also reported for some example cases in full sliding condition. 63

16 Figure 2.8. Snapshot of the transient FE solution: normal tractions at the layer/substrate interface for B=1, ν=0.3, μ=0.7, λ=1 and f=0.2 - moving load

case - full sliding of external contact over layer surface. The comparison with the steady state solution displayed in Fig. 2.6 is also presented. 65

17 Figure 2.9. Normal and tangential tractions for *B*=1, ν=0.3, μ=0.7, λ=1 and *f*=0.15 - stationary case - full sliding of external contact over layer surface. 67

18 Figure 3.1. Schematic of the problem: (a) Layered cylinder indenting a homogeneous cylinder; (b) Equivalent problem – cylinder rolling on a layered substrate; (c) Zoom-in showing the contact area and the salient parameters; (d) Example plot of the von Mises stresses induced by the application of the external loads. Note that for $R_1 \to \infty$ the schematic in (a) represents a typical wheel/rail contact. 71

19 Figure 3.2. Minimum interfacial friction coefficient f to guarantee adhesion for *B* = 1.5, ν = 0.3, λ = 0.05 (dimensionless constant pressure) and various surface friction coefficients, μ. 75

20 Figure 3.3. Minimum interfacial friction coefficient f to guarantee adhesion for $\nu = 0.3$, $\lambda = 0.005$ and various surface friction coefficients, μ, and layer thicknesses, B. 76

21 Figure 3.4. Minimum interfacial friction coefficient f to guarantee adhesion for $\nu = 0.3$, $\lambda = 0.01$ and various surface friction coefficients, μ, and layer thicknesses, B. 76

22 Figure 3.5. Minimum interfacial friction coefficient f to guarantee adhesion for $\nu = 0.3$, $\lambda = 0.05$ and various surface friction coefficients, μ, and layer thicknesses, B. 77

23 Figure 4.1. Reference system and triangular traction elements applied to discretise generic traction distributions at the layer surface; sign conventions are shown (positive directions). 79

24 Figure 4.2. Normal and shear tractions induced along the layer-substrate interface by a triangle of direct and shear traction imposed on the free surface, $-1 < x/b < 1$ ($b/a_{tr} = 1$ and $f = 0.2$). 84

25 Figure 4.3. Bulk stresses associated with the tension imbalance present in the system for a triangle of direct and shear traction imposed on the free surface, $-1 < x/b < 1$ ($b/a_{tr} = 1$ and $f = 0.2$). 85

26 Figure 4.4. (a) free body diagram for a triangle of direct traction - (b) free body diagram for a triangle of shear traction - (c) free body diagram for a generic induced traction distribution at the layer surface. 86

27 Figure 4.5. Comparison between the influence functions for a triangle of direct and shear traction formulated for the case of a layer resting on a substrate in frictionless condition and the influence functions devised for the frictional problem for *f* set to 0. 87

28 Figure 4.6. Normal tractions at the interface between layer and substrate for a triangle of direct traction for different values of the interfacial friction coefficient, *f*, and $\nu_1 = 0.3$. 88

29 Figure 4.7. Normal tractions at the interface between layer and substrate for a triangle of shear traction for different values of the interfacial friction coefficient, *f*, and $\nu_1 = 0.5$. 88

30 Figure 4.8. Comparison between the state of stress induced at the layer/substrate interface by a triangular influence function of direct tractions formulated for the

case of a layer bonded to a substrate and that induced by the same influence function for the sliding frictional problem for f=1. 89

31 Figure 4.9. Comparison between the state of stress induced at the layer/substrate interface by a triangular influence function of shear tractions formulated for the case of a layer bonded to a substrate and that induced by the same influence function for the sliding frictional problem for f=1. 89

32 Figure 4.10. Normal tractions at the interface between layer and substrate for a triangle of direct traction for different values of the ratio b/a_{tr}, B, and $\nu = 0.3$. 90

33 Figure 4.11. Normal tractions at the interface between layer and substrate for a triangle of shear traction for different values of the ratio b/a_{tr}, B, and $\nu = 0.3$. 90

34 Figure 4.12. (a) Schematic of the example application, and (b) equivalent contact model. The inset to figure (b) shows the problem variables and the undeformed and deformed configurations. 92

35 Figure 4.13. Comparison between the pressure distributions for the sliding frictional formulation for f=0 and f=1 and the solution for the frictionless layer problem (Bentall, 1968) and the bonded layer problem (Nowell, 1988b). The solutions are computed for the frictionless contact configuration ($\mu = 0$) and various values of B. It should also be noted that the solution is only plotted along the contact half-width for the three problems which produce symmetric distributions to improve the diagram's legibility. 96

36 Figure 4.14. Normal traction at the interface between layer and indenter for a pure sliding contact ($\mu = 0.5$) for different values of B, $\nu = 0.3$ and $f = 0.2$. 98

37 Figure 4.15. Normal traction at the interface between layer and indenter for a pure sliding contact ($\mu = 0.5$) for different values of B, $\nu = 0.5$ and $f = 0.2$. 98

38 Figure 4.16. "Limit state" sliding condition. The solid line represents the layer/indenter friction coefficient, μ, required to guarantee the equilibrium of the system while spinning for $B = 1$, $R/b = 10$, and for different values of f. The dotted lines represent the values for which separation between the layer and the substrate occurs. The behaviour of the contact problem above and below the limit states is also schematically shown. 99

39 Figure 5.1. Schematic of the layered contact problem and possible interface regimes. 102

40 Figure 5.2. Schematic of the layered system and piecewise linear representation of the dislocation density. 107

41 Figure 5.3. Geometry of the present problem and loading conditions. 111

42 Figure 5.4. Shear tractions and relative displacement between layer and substrate for f=0.25, $\lambda_N = 2$ ($N < 0$) and f=0.4, $\lambda_N = 1.1$ ($N < 0$) - stationary case. 112

43 Figure 5.5. Shear tractions and relative displacement between layer and substrate for f=0.5, $\lambda_Q = 2.36$ - stationary case. 113

44 Figure 5.6. Shear tractions for f=0.5 and $\lambda_Q = \pm 2.36$ (cyclic tangential load) - stationary case. 114

45 Figure 5.7. Shear tractions for f=0.5 and $\lambda_Q = \pm 3.2$ (cyclic tangential load) - stationary case. 115

46 Figure 5.8. Shear tractions and relative displacement between layer and substrate for B=1, f=0.2, $\mu = 0.7$, $\lambda = 1$ and $\nu = 0.3$ - stationary case - full sliding of external contact over layer surface. 116

47 Figure 5.9. Shear tractions and relative net displacement between layer and substrate, *d*, for λ_N=8, for *f*=0.5. 117

48 Figure 5.10. Relative net displacement, *d*, between layer and substrate as a function of the dimensionless constant pressure, λ_N, for *f*=0.5. 117

49 Figure 5.11. Shear tractions and relative net displacement, *d*, between layer and substrate for *B*=1, *f*=0.2, $\mu = 0.7$, $\lambda = 1$ and $\nu = 0.3$ - steady state solution for the moving load case - full sliding of external contact over layer surface. 118

50 Figure 5.12. PCS MPR (*www.pcs-instruments.com/mpr*) experimental apparatus consisting of three tyred rollers and a central roller and schematic of the loading system. 121

51 Figure 5.13. Friction coefficient versus ring displacement measured in the compression test. 121

52 Figure 5.14. Net displacement, *d*, per revolution as a function of the dimensionless constant pressure, λ, and of the interfacial friction coefficient, *f*. In the same graph, comparison with experimental results and, in the inset, with Anscombe's original data classified based on ring thickness (Anscombe et al., 1968 and Chang, 1983). 122

53 Figure 6.1. Schematic of the elastic contact problem and potential frictional shakedown responses. 125

54 Figure 6.2. Schematic of the elastic contact problem and potential loading histories considered here. 129

55 Figure 6.3. Energy dissipated per cycle for *f*=0.5 and $\lambda_Q = 3.1$ - elastic shakedown - and *f=0.5* and $\lambda_Q = 4$ - plastic shakedown. 129

56 Figure 6.4. Energy dissipated per cycle (steady state) as a function of the dimensionless shrink-fit pressure, λ_Q, for an elastic layer resting on an elastically similar substrate and on a rigid substrate as a function of the dimensionless shrink-fit pressure, λ_Q, for *f*=0.25 and *f*=0.5. 130

57 Figure 6.5. Comparison between the elastic shakedown limit as a function of the dimensionless shrink-fit pressure, λ_Q, predicted with Melan's theorem and the unilateral solution for an elastic layer resting on an elastically similar substrate and on a rigid substrate as a function of the dimensionless shrink-fit pressure, λ_Q. 131

58 Figure 6.6. Comparison between the energy dissipated per cycle for a layer resting on an elastically similar substrate when different initial conditions are imposed. 132

59 Figure 6.7. Comparison between the energy dissipated per cycle (steady state) as a function of the dimensionless shrink-fit pressure, λ_Q, when different initial conditions are imposed, for a layer resting on an elastically similar and rigid substrate - *f*=0.25 and $N < 0$. 133

60 Figure 6.8. Comparison between the energy dissipated per cycle (steady state) as a function of the dimensionless shrink-fit pressure, λ_Q, when different initial conditions are imposed, for a layer resting on an elastically similar and rigid substrate - *f*=0.25 and $N > 0$. 134

61 Figure 6.9. Minimum friction coefficient required to ensure shakedown under oscillating normal load and for different values of λ. 135

62 Figure 6.10. Comparison between the shakedown limit obtained by applying Melan's theorem to the bilateral solution and the limit computed using the "marching in time" unilateral solution. 135

63 Figure 6.11. Schematic of the layered system subject to a triangular distribution of normal tractions and potential loading histories. 137

64 Figure 6.12. Comparison between the elastic shakedown limit as a function of the dimensionless layer thickness, B, predicted by Melan's theorem and the unilateral solution, for λ_Q=6 and 8 - elastic layer resting on a rigid substrate. 137

65 Figure 6.13. Friction coefficient required to ensure elastic shakedown as a function of B, for $\lambda_{tr,\min}$=6 and $\lambda_{tr,\max}$=8. 139

66 Figure 6.14. Friction coefficient required to ensure elastic shakedown as a function of $B_{tr,min}/B_{tr,max}$ where $B_{tr,max}$=1 and for $\lambda_{tr,\min}$=6. 139

67 Figure 7.1. Schematic of the test apparatus used to perform the "walking" test. 142

68 Figure 7.2. Loading history and shear traction distributions after loading (point 1) and unloading (point 2) in the steady-state cycle for $Q/\mu N = 0.7$, $\sigma_{xx,\min}/\mu p_H = 0$ and $\sigma_{xx,\max}/\mu p_H = 1.8$. 147

69 Figure 7.3. Loading history and shear traction distributions after loading (point 1) and unloading (point 2) in the steady-state cycle for $Q/\mu P = 0.7$, $\sigma_{xx,\min}/\mu p_0 = 0$ and $\sigma_{xx,\max}/\mu p_0 = 2.2$. 148

70 Figure 7.4. Map showing the transition between "walking" and "no walking" as a function of the loading parameters. 150

71 Figure 7.5. Normalised distance walked per cycle, $E\Delta s/(4\mu a_H p_H(1-\nu^2))$, for $Q/\mu N = 0.7$ and $\sigma_{xx,\max}/\mu p_H = 2.5, 2.75, 3.0$. 150

72 Figure 7.6. Elastic limit vs. friction coefficient for $\sigma_{xx,\max}/\mu p_H = 2.125, 2.2, 2.4$. 151

73 Figure 7.7. Experimental results for a mild steel dogbone specimen ($10mm \times 10mm$ cross-section) in contact with a mild steel cylinder of the same width and radius $100mm$, and pressed by a normal force $N_F = 1.57kN$. The graph shows the accumulated walking distance, $\sum \Delta s/a_H$, and the evolution of the friction coefficient during the test as calculated using the quadratic programming routine. 152

74 Figure 8.1. (a) Michelin XMCL: radial tyre object of our investigation (*image courtesy of Michelin - www.michelin.com*); (b) JCB 4CX: Backhoe loader dedicated to the project (*image courtesy of JCB - www.jcb.com*). 156

75 Figure 8.2. Schematic of the tyre cross-section and of the tyre reinforcements. 157

76 Figure 8.3. FE model of a tyre mounted on a rigid rim; detail of all tyre reinforcements. 161

77 Figure 8.4. Main tyre loading configurations: (i) pure vertical loading; (ii) application of a camber angle; (iii) application of a slip angle. 161

78 Figure 8.5. Detail of the tyre bead mesh. 162

79 Figure 8.6. Schematic of the tyre fitting process. 163

80 Figure 8.7. FE 3D model of a tyre mounted on a rigid rim – Tyre bead interfacial pressure. 166

81 Figure 8.8. Minimum friction coefficient required to avoid slippage between tyre and rim - Normal load only applied. 166

82 Figure 8.9. FE 3D model of a tyre mounted on a rigid rim – Tyre bead interfacial pressure (normal load only applied - position 1, bottom part of the rim) - vertical load of 5 tons. 167

83 Figure 8.10. FE 3D model of a tyre mounted on a rigid rim – Tyre bead interfacial pressure (normal load only applied - position 2,3 and 4) - vertical load of 5 tons. 167

84 Figure 8.11. Tangential tractions for B=1, ν=0.3, μ=0.7, λ=1 and f=0.2 - full sliding condition – absence of slip at the layer-substrate interface. 169

85 Figure 8.12. Minimum friction coefficient f to guarantee adhesion as a function of the normalised layer thickness B for various friction coefficient μ and ν=0.3 – full sliding condition. 170

86 Figure 8.13. Comparison between the minimum friction coefficient needed to prevent the tyre from slipping in presence and absence of rotation. 170

87 Figure 8.14. Tangential tractions for B=1, ν=0.3, μ=0.7, λ=1 and f=0.2 - full sliding condition - presence of slip at the layer-substrate interface. 171

88 Figure 8.15. Contact pressure distribution between tyre and rim for a rigid (blue line) and a deformable rim (red line). 172

89 Figure 8.16. Comparison between the old and the new wheel profile. 173

90 Figure 8.17. Comparison between the numerical and experimental contact pressure distribution between tyre and wheel. 174

91 Figure 8.18. Bowden-Leben test apparatus and detail of the rubber holder (rubber pad 3x3 mm). 175

92 Figure 8.19. Rim specimens: (A) electrically coated, (B) painted and (C) uncoated. 176

93 Figure 8.20. Lubricants (*http://www.rema-tiptop.co.uk*) suggested by Michelin for the tyre-fitting process 177

94 Figure 8.21. Variation of the coefficient of friction between tyre and rim specimens as a function contact pressure for different rim surface specifications and for a sliding speed of 0.03 cm/s. The error bars identify two standard deviations from the mean. 178

95 Figure 8.22. Surface topography for the uncoated rim specimen and the rim specimen coated with white paint (area 10x10 mm). 179

96 Figure 8.23. Measure of the coefficient of friction between tyre and rim specimens as a function of contact pressure for different rim surface specifications in presence of lubrication (lubricant type A); values obtained immediately after lubricant application. 180

97 Figure 8.24. Measure of the coefficient of friction between tyre and rim specimens as a function of contact pressure for different rim surface specifications in presence of lubrication (lubricant type B); values obtained immediately after lubricant application. 180

98 Figure 8.25. Measure of the coefficient of friction between tyre and rim specimens as a function of contact pressure for different rim surface specifications in

presence of lubrication (lubricant type C); values obtained immediately after lubricant application. 181

99 Figure 8.26. Variation of the coefficient of friction between tyre and rim as a function of contact pressure and time passed after the lubricant application for different rim surface specifications - Rim specimen A - Lubricant type A. 182

100 Figure 8.27. Example of knurled wheel (*image courtesy of GKN - http://www.gkn.com*). 183

101 Figure 8.28. Rig concept design to investigate the effect of knurling on the tyre-rim interface (tyre "slice" width=20 mm). 184

102 Figure 8.29. Lateral view of the rig concept design to investigate the effect of knurling on the tyre-rim interface. 184

103 Figure 8.30. Explosion of a sub-assembly of the rig concept design to investigate the effect of knurling on the tyre-rim interface. 185

104 Figure 8.31. Tyre bead rocking effect when the tyre is not correctly seated. 187

105 Figure 8.32. Tyre bead final position when seated as a function of the friction coefficient between tyre and rim (i) friction=0, (ii) friction=0.2 and (iii) friction=0.6 187

106 Figure 8.33. JCB 4CX Backhoe loader equipped with the wheel force transducer (WFT - *http://www.kistler.com*) mounted on the front wheel (*image courtesy of JCB - http://www.jcb.com*). 188

107 Figure 8.34. Breakdown of the vehicle duty cycle. 188

108 Figure 8.35. Example of vehicle load history - static condition (excavating and loading) - front wheel. 191

109 Figure 8.36. Example of vehicle load history - rolling condition (roading) - front wheel. 192

110 Figure 8.37. Example of Von Mises counter plot of the wheel stress field - pure vertical load of 5 tons. 192

Nomenclature

a Contact semi-width

a_H Hertzian contact semi-width

a_{tr} Triangular traction distribution semi-width

$A = a/a_H$ Dimensionless contact ratio

$A_\Gamma, B_\Gamma, C_\Gamma, D_\Gamma$ Constants of Γ

A_p, B_p, C_p, D_p Constants of Γ for a triangle of normal traction

A_q, B_q, C_q, D_q Constants of Γ for a triangle of shear traction

$\tilde{A} = 2\left(1-\nu_1^2\right)/E_1$

$A_{SM} = 2E/\left(\pi\left(\kappa+1\right)\right)$

$A_{DM} = 2E_1\left(1-\alpha\right)/\left(\pi\left(\kappa_1+1\right)\left(1-\beta^2\right)\right) = 2E_2\left(1+\alpha\right)/\left(\pi\left(\kappa_2+1\right)\left(1-\beta^2\right)\right)$

b Layer thickness

b_x Burgers vector

$B = b/a$ Dimensionless thickness parameter – Thickness to contact semi-width ratio

$B_{tr} = b/a_{tr}$ Dimensionless thickness parameter

B_{min}, B_{max} Minimum and maximum thickness to Hertzian contact semi-width ratio during cyclic normal loading

B_x Glide dislocation density

c Speed of the moving load

c_{stick} Stick zone semi-width

C Composite “stiffness”

C_{slip} Slip accumulated from the centre of the contact to the slip region

$D_{ind} = t/a$

d Net relative shift between layer and substrate

d_{sup} Distance between adjacent supports belonging to the layer/substrate interface in the frame of reference shown in Figure 5.2

D_{12}, D_{22} Kernels used to find the influence functions for a glide dislocations on the layer substrate interfacial stress field

e Eccentricity of the contact centre with respect to the direction of indenter centerline

E, E_1, E_2 Young’s modulus

f Interfacial friction coefficient between tyre and wheel (substrate)

f_{Melan} Minimum friction to guarantee frictional shakedown according to the application of Melan’s theorem

$f_{shakedown}$ Minimum friction to guarantee frictional shakedown according to the exact solution obtained employing the unilateral formulation

f_{qp} Linear term of the quadratic programming formulation

F_p, F_q Influence functions describing the contribute to the surface displacements given by a triangular distribution of pressure, F_p, and a triangular distribution of shear tractions, F_q

$\tilde{F}, \tilde{F}_M, \tilde{F}_C$ Functional of the contact problem

F_{xy}, F_{yy} Influence functions describing the contribute of a triangular distribution of glide dislocation density, B_x, to layer/substrate interfacial stress field

G Modulus of rigidity

G_{xy}, G_{yy} Influence functions describing the contribute of a glide dislocation to the layer/substrate interfacial stress field

$h(x)$ Tangential shift due to the distributed dislocations

h_j, h'_j, h''_j Unknown tangential displacement

$\dot{h}(x)$ First derivative in time of the tangential shift due to the distributed dislocations, $h(x)$

$H(x)$ Heaviside step function

H_{qp} Square matrix of the quadratic programming formulation

i Imaginary unit

I_{u_p}, I_{u_q} Influence function describing the lateral displacement given by a triangle of pressure and shear, respectively

I_{v_p}, I_{v_q} Influence function describing the vertical displacement given by a triangle of pressure and shear, respectively

$I\tilde{U}1, I\tilde{U}2$ Integral influence function describing the lateral displacement given by a triangle of pressure and shear, respectively

$I\tilde{V}1, I\tilde{V}2$ Integral influence function describing the vertical displacement given by a triangle of pressure and shear, respectively

i_m, i_n Integers related to the numeration given to the nodes used to approximate the stress distributions

J_2 Second deviatoric invariant of the stress tensor

k Material yield strength in pure shear

m Trailing edge of the interfacial slip region – see (ii) in Figure 1.6(b)

n Leading edge of the interfacial slip region – see (ii) in Figure 1.6(b)

n_p Number of points at which traction and displacement fields are sampled

N Normal load per unit width

N_{12}, N_{22} Kernels used to find the influence functions for a glide dislocations on the layer/substrate

	interfacial stress field
N_F	Normal force
$p(x)$	Contact pressure
p_0	Interfacial uniform constant contact pressure due to the shrink fit
p_i	Unknown surface normal stress
p_H	Hertzian pressure peak
$Pi = pi/\bar{p}$	
$\bar{p} = N/2a$	Average contact pressure
$q(x)$	Contact shear traction
q_i	Unknown surface traction stress
Q	Tangential load per unit width
$Q_i = q_i/\bar{p}$	
Q_F	Tangential force
R_a	Surface roughness
R_1, R_2	Radii of rollers 1 and 2 (see Figure 1.6)
$R^* = R_1R_2/(R_1 + R_2)$	Equivalent contact radius
t	Rigid body normal approach between indenting disc and elastic layer – see Figure 1.6(b)
T, T_1, T_2, T_H, T_P	Applied torques per unit width
$u_{surf}(x)$	Surface tangential displacement at the disc/layer interface
$u_{layer}(x)$	Layer tangential displacement at the layer/substrate interface
$u(x, y)$	Tangential component of the layer displacement
$v(x, y)$	Normal component of the layer displacement
$v_{surf}(x)$	Surface normal displacement at the disc/layer interface
$v_{substrate}(x)$	Substrate tangential displacement at the layer/substrate interface
$\dot{v}(x, t)$	Relative surface slip velocity
$V(x)$	Relative velocity between layer and substrate – slip velocity
$V_1 = v_1(x, y)/a$	
$U_1 = u_1(x, y)/a$	
$V_2 = v_2(x, y)/a$	
$U_2 = u_2(x, y)/a$	
w	Semi-length of the layer in contact with roller 2
x	Horizontal coordinate
x_d	Auxiliary coordinate set used to identify the location of a point belonging to the layer/ substrate interface in the fixed frame of reference during the application of the moving

load

x_i Location of the centre of the triangles of tractions p_i and q_i

$x_k = x_j/2 + x_{j+1}/2$

x_j Auxiliary coordinate set used to identify the location of a point belonging to the layer/ substrate interface in a fixed frame of reference (see Figure 5.2)

$\underline{x}_{qp}$ vector containing the unknown of the quadratic programming formulation

$\tilde{x}=x/b$

$X = x/a$

y Vertical coordinate

$Z = 1/(4SB)$

α, β Dundurs' constants

$\zeta_j = h_j - h_{j+1}$ Difference between the tangential displacement measured at two adjacent supports

ζ'_j, ζ''_j Unknown tangential displacement

$\psi = \phi/(2b)$

ξ Dummy variable

ξ_{creep} Creep ratio

ϕ Wander variable of the Fourier transform

$\delta(\cdot)$ Dirac's delta function

$\lambda = p_0/p_H$ Dimensionless loading parameter

$\lambda_Q = Q/(p_0 b)$

$\lambda_N = N/(p_0 b)$

$\lambda_{tr} = p_n/p_0$

$\kappa = 3 - 4\nu$ Kolosov's constant for plane strain

μ Friction coefficient between disc and tyre (elastic layer) - see Figure 1.6(a)

ν, ν_1, ν_2 Poisson's ratio

ρ_{sub} Sign of the relative between layer and substrate

ρ_{surf} Sign of the relative velocity between layer and rigid indenter

$\sigma_{xy}^{glide}(x, \xi)$ Tangential component of the layer stress field induced by a glide dislocation located at $(\xi, 0)$

$\sigma_{xy}^{bil}(x)$ Tangential component of the layer stress field due to the bilateral solution alone at the layer-substrate interface

$\sigma_{xy}(x, y)$ Tangential component of the overall layer stress field

$\sigma_{xy,\max}^{bil}(x), \sigma_{xy,\min}^{bil}(x)$ Tangential component of the layer stress field at the layer/substrate interface due to the bilateral solution alone and evaluated at the two extremes of the loading cycle

$\sigma_{xy,res}(x)$ Residual shear stresses nucleated at the layer/substrate during application of the normal alternating load

$\sigma^{c}_{xy}(x,y)$ Interfacial shear traction - between layer and substrate (c: contribution from the contact load).

$\sigma^{corr}_{xy}(x)$ Corrective component of the tangential component of the layer stress field at the layer/substrate interface

$\sigma^{glide}_{yy}(x,\xi)$ Normal component of the layer stress field induced by a glide dislocation located at $(\xi,0)$

$\sigma^{bil}_{yy}(x)$ Normal component of the layer stress field due to the bilateral solution alone at the layer/substrate interface

$\sigma_{yy}(x,y)$ Normal component of the overall layer stress field

$\sigma^{bil}_{yy,\max}(x), \sigma^{bil}_{yy,\min}(x)$ Normal component of the layer stress field at the layer/substrate interface due to the bilateral solution alone and evaluated at the two extremes of the loading cycle

$\sigma^{c}_{yy}(x,y)$ Interfacial normal pressure - between layer and substrate (*c*: contribution from the contact load).

$\sigma^{corr}_{yy}(x)$ Corrective component of the normal component of the layer stress field at the layer-substrate interface

$\sigma_{xx}(x,y)$ Bulk component of the overall layer stress field

$\sigma_0 = \sigma_{0,L}(x) - \sigma_{0,R}(x)$ Difference in bulk stress between the strip ends

τ Dummy variable

χ Airy stress function

Γ Fourier transform of the Airy stress function

ω Wander integration variable

ΔS Walking distance

$2S + 1$ Number of nodes used to approximate the stress distributions

$X_1 = D_{ind}/A$

$X_2 = eA^2$

$X_3 = A^2$

$X_4 = \xi_{creep}/A$

$X_5 = C_{slip}/A$

Chapter 1

Tyre-wheel interfaces in off-highway vehicles

1.1 Introduction

The present research project has been prompted by an investigation into creep, and ultimately, gross sliding, of rubber tyres fitted around steel wheel hubs in earth moving equipment, where the assembly is made by having what may be thought of as an interference fit between the tyre and the wheel rim.

The existing literature on the topic is rather limited; therefore, this chapter will not only provide a review of the current understanding of tyre-rim mechanics but also guide the reader through the techniques which may be applied to modelling such a system. The final paragraph of this chapter will include the thesis outline.

Slippage between tyre and rim is experienced in common engineering applications employing tyred (Anscombe and Johnson, 1974), or so called layered systems. Cumulative micro-slip mechanisms are often observed in both pre-stressed and frictionally interlocked components (Chang et al., 1983), consequently such systems may be thought of as belonging to the wider class of problems referred to as frictional joints. Shrink-fitted systems are a classic example of mechanical assemblies for which cumulative micro-slip caused by localised loading conditions may lead to system failures (Truman and Booker, 2007). Engine conrods are another example of mechanical systems subject to severe damage when bushes or conrod bearings slip with respect to their housing (Antoni et al., 2007). In such components, the accumulated relative motion between the mating parts is the result of the

local violation of frictional laws and frequently results in unbounded slip and long-term unwanted rotations or misalignments.

It should be noted that the tyre-rim interface which prompted the current investigation belongs to a complex three-dimensional assembly, which is characterised by a number of parameters (e.g. rim shape, surface interactions and deformation, friction, tyre mechanical properties). Therefore, a simplified model was deemed necessary to enable study of the fundamental mechanisms governing the loss of adhesion between a tyre and the surface on which it is mounted. In this chapter the techniques employed to analyse the underlying mechanisms responsible for interface slippage are discussed in detail. The following chapters outline key results to illustrate a detailed overview of the overall analytical framework. This scheme was developed for generalised problems involving a layer resting or mounted on a substrate or to those frictional joints that can be similarly idealised.

1.2 Literature review

Wheels are the elements that connect vehicles to the ground and usually permit the transfer of angular velocity of the axle to forward velocity of the vehicle. They comprise a radial rubber tyre mounted on a rim which is joined to the axle by a bolted connection.

Several experimental and theoretical studies have been carried out to characterise tyred wheels running on smooth and rough roads. These have led to a number of accurate mathematical models (Pacejka, 2002). Off-Highway vehicle wheels (e.g. Fig.1.1) are, however, very different when compared to car wheels. This is because the absence of an articulated suspension system on such vehicles leads to the use of high aspect ratio tyres. As a consequence, high traction forces are generated at the rim-bead interface and an incremental slip between rim and tyre is sometimes observed. This phenomenon may also be accompanied by leakage of air and internal pressure loss. Incremental slip is the result of the accumulation of regions of micro-slip around the seal interface. A thorough description of this phenomenon requires the definition of loading transfer mechanisms under highly variable loads. Furthermore, the deformability of the soil has to be taken into account.



Figure 1.1. Example of Off-High Vehicle (*image courtesy of JCB - http://www.jcb.com*).

Some experimental and analytical work has been presented in the recent literature to describe the tyre-ground interaction as well as an enhanced tyre model (Gobbi et al., 2005; Wille et al., 2005).

None of the existing analytical and numerical models for car and agricultural wheels found in the literature consider the possibility of slippage occurring between tyre and rim (Pacejka, 2002). However, this is indeed experienced in-service. It was, therefore, decided to focus on this topic in the current work.

The interface interaction to be studied is a complex three-dimensional contact problem involving deformable bodies, the rim and the tyre bead, as well as highly variable loads and variable friction conditions (Lee, 2006; Treloar, 1958; and Persson and Tosatti, 2000). A schematic representation of the problem is given in Figure 1.2.

The complexities that must be faced when attempting to devise a detailed formulation of the problem are now evident. A sensible approach is to investigate the system starting from a simplified model. A first approximation was devised as follows:

1- Identification of a two-dimensional equivalent contact problem.

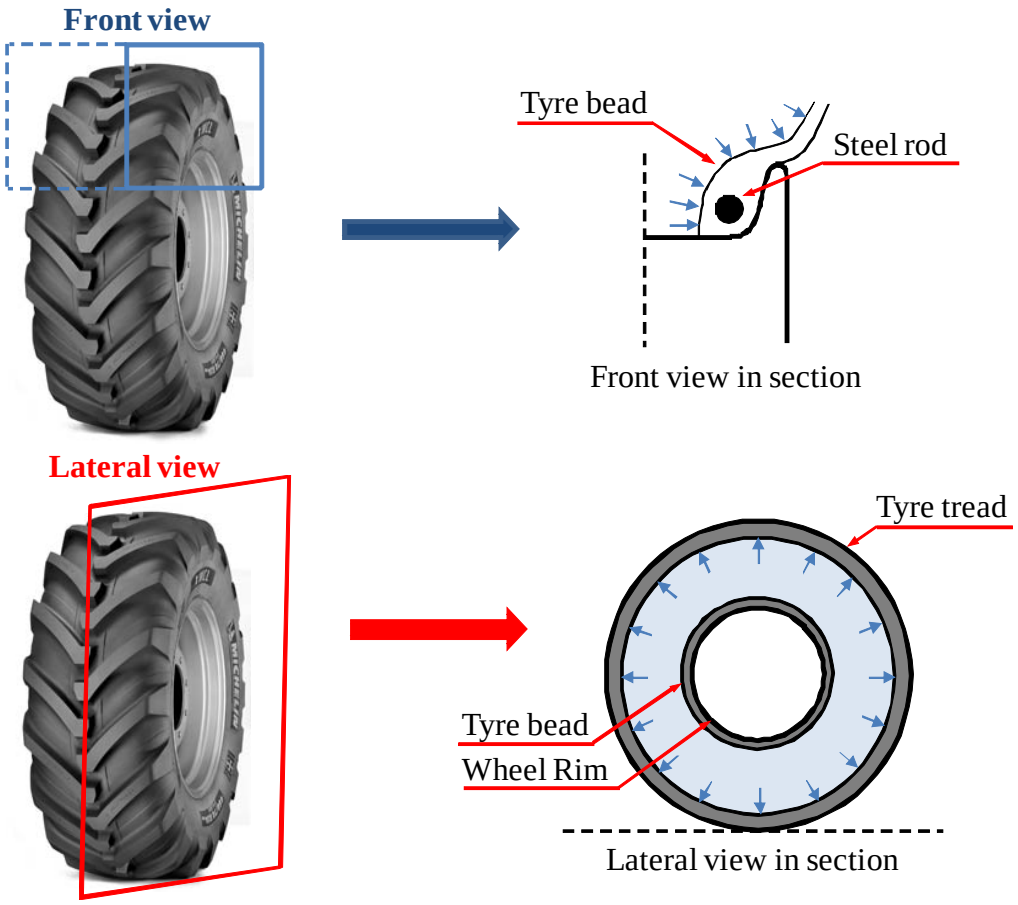


Figure 1.2. Schematic representation of the problem (*image courtesy of Michelin - http://www.michelin.com*).

2- Rim considered, to a first approximation, as a half-plane.

3- Rubber bead modelled as an elastic layer resting on a rigid substrate (representing the rim).

4- Friction coefficient between the mating surfaces taken to be constant and assumed to obey Amonton's (or Coulomb's) law.

The above assumptions allow the effects of each individual parameter influencing the rim-tyre interface to be identified and their individual effects separated. Only when a comprehensive investigation has been carried out using this simplified model, it is sensible to move to a more refined approach.

1.2.1 Modelling technique

Modelling the rim as a half-plane removes the influence of the boundary conditions applied far from

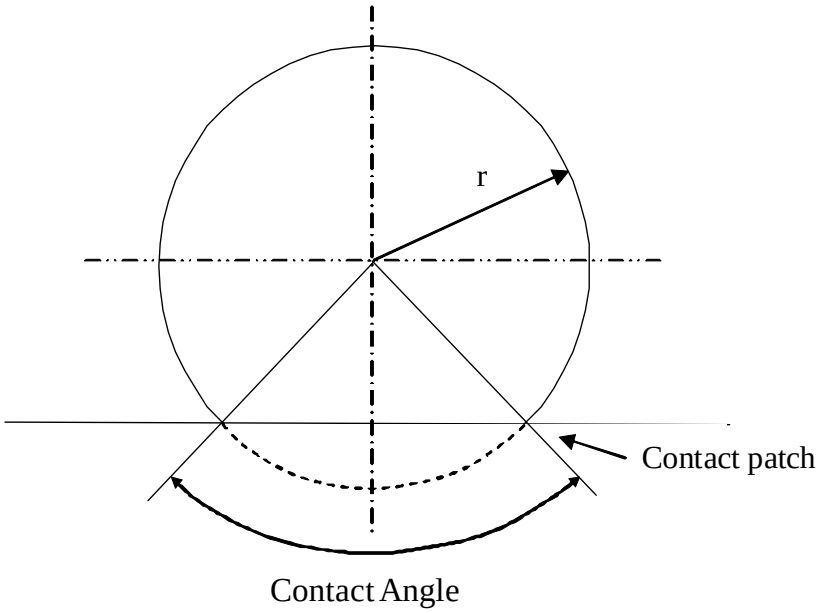


Figure 1.3. Contact patch schematic.

the contact area (Lee, 2006). Including this influence would increase the modelling complexity without adding much insight into the physics of the problem under investigation. In addition, they could only be accounted for by employing a more refined numerical method, such as the Finite Element Method (FEM). A complete three-dimensional model that considers the deformation of the rim can already be found in the literature (Stearns et al., 2004), but no dynamic loads were implemented. Furthermore, air pressure distribution was modelled as an equivalent load on the bead seat flange. Although the problem was presented as three-dimensional, the system was treated as axi-symmetric, and the contact patch was assumed to subtend a constant angle (Fig. 1.3).

Another finite element model was presented by Lee (2006). The problem was taken to be axi-symmetric and a simplified model of the tyre bead including the presence of the metallic rod within the rubber matrix was adopted. Although the results were quantitatively inaccurate, some relevant features can be extracted from this contribution: first, the tyre bead is a complex system which cannot be simply modelled as an elastic rubber strip bonded around a steel rod; second, separation and rotation of the tyre bead with respect to the rim are possible; third, the system can be modelled

using a constant friction coefficient as a first approximation.

While modelling the rubber bead as a complex system using FE has been demonstrated to be inefficient and inaccurate, based on the results of Lee (2006), the following assumptions may still be justified: (1) the bead is an isotropic body since the macro-response of the system rather than the interaction between each component constituting the tyre bead is considered. (2) The tyre rubber compound can be considered as elastic because of the absence of large deformations due to the particular configuration and composition of the bead (Treloar, 1958). Note that this assumption requires experimental corroboration and the effect of temperature, frequency and pre-stress must also be considered (Persson and Volokitin, 2006a).

(3) The coefficient of friction is constant and the interface interaction is described by Coulomb's law. If the surface over which a rubber element slides is rough, as typically the case for road-tyre interactions, the friction is mainly due to fluctuations in space and time of the viscoelastic deformation of the rubber by the substrate asperities (Perrson, 2001; Persson and Volokitin, 2006a; and Persson, 2006b). However, the rim surface can be considered as very smooth compared to a road surface, and the friction mechanism depends on adhesive interaction between rim and tyre (Perrson, 2001; Persson and Volokitin, 2006a; and Vorvolakos and Chaudhury, 2003). In particular, Persson and Volokitin (2006a), presented a model that takes into account the effect of thermal fluctuations on the depinning of small contact patches at the rubber-substrate interface. From these results, it was shown that the influence of small amplitude substrate roughness on rubber sliding makes negligible contribution to the interfacial response. This result was also shown experimentally by Vorvolakos and Chudhury (2003). Therefore, assuming that the contact interfaces are smooth is a reasonable hypothesis (Persson and Volokitin, 2006a) whereas modelling the friction coefficient as constant is an assumption which requires further experimental validation.

On the basis of the above assumptions a simplified model has been developed. Initially, the possibility of studying the contact problem as the actual three-dimensional surface profile was evaluated.

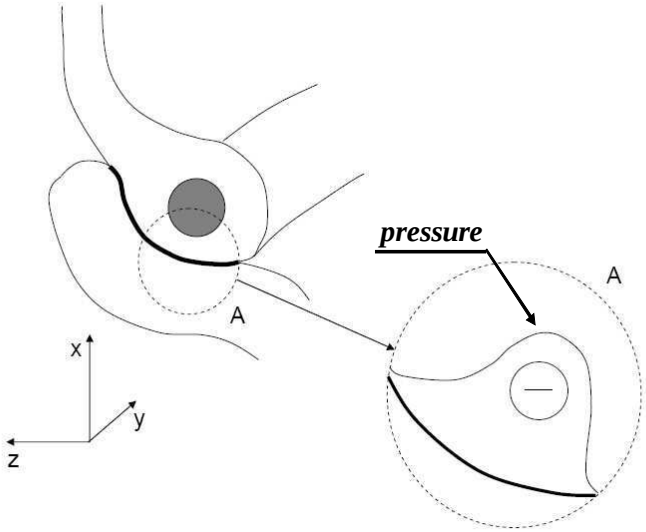


Figure 1.4. Schematic representation of pressure distribution.

However, due to the computational cost of large 3D models and the impossibility of carrying out parametric studies with them, two dimensional approximations were sought. Ciavarella and Demelio (1999) proposed an approach which preserved information about the rim shape in the x-z plane (Fig. 1.4) whilst studying the evolution of the contact patch under the influence of remote loads. This approach allowed the pressure distribution in the x-z plane to be attained, assuming that either the wheel-tyre assembly is axi-symmetric or that the load distribution can be discretised using a piece-wise linear approximation and, therefore, studied in "slices". A typical pressure distribution is shown in the inset to Figure 1.4.

However, since the phenomenon under investigation is concerned with slip occurring locally in the x-y plane, it was decided that a study of two dimensional interfacial behaviour (x-y plane through the rim-tyre interface) was required to investigate the prototypical problem. To achieve this, the simple model first presented by Benthall and Johnson (1968) and then further developed by Nowell and Hills (1988b) was employed. The model consists of two cylinders, one of which carries an elastic tyre, as shown in Figure 1.5.

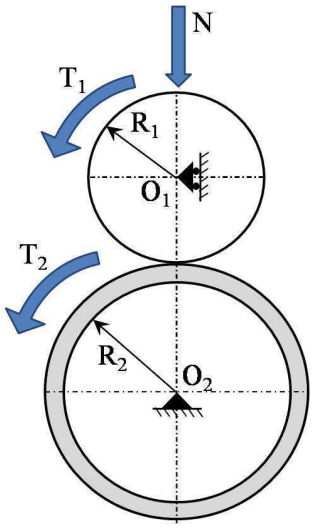


Figure 1.5. Rolling contact of a tyred roller with a second rigid roller.

The top roller allows investigation of different contact interface conditions by varying the rolling regimes between the two cylinders in terms of loading and kinematic conditions. The main characteristics of the system are:

1- The roller axles allow application of static normal load, *N*.

2- Tangential loads are transmitted to the contact interface through a torque.

3- The model is two-dimensional.

4- Information about the out-of-plane profile of the contact problem is neglected and the problem is studied in plane strain.

The effect of a number of parameters on the phenomenon under investigation may potentially be investigated in the form of a comprehensive parametric study. This represents the main advantge of this model together with its simplicity which renders the experimental validation of the analytical model feasible.

Having identified a simplified model, it is possible to focus on the primary aim of the project: investigation of slippage at the interface between the layer and the substrate. This slippage is due to the stress caused by the applied loads and the prescribed boundary conditions at the interface

between the two rollers. In the first instance, the stress field is derived assuming the layer to be perfectly bonded to the substrate (Sneddon, 1951). As only elastic deformations have been allowed within the model, it is possible to apply superposition when computing the effect of various loading conditions on the stress field at the interface between the layer and the substrate (Porter and Hills, 2002a and 2002b).

Two different aspects must be considered: firstly, the conditions for which the layer starts sliding; secondly, how slippage propagates. To investigate this problem the analogy with the movement of an edge dislocation through a crystal has been adopted (Hills et al., 1996; Dundurs and Mura, 1964; and Dundurs and Sendeckyj, 1965). The very first instance of the application of this analogy applied in a simplified manner was proposed by Anscombe and Johnson (1974) to study a test configuration similar to that depicted in Figure 1.5. Although a good agreement with experimental results was found, it was later demonstrated by Chang et al. (1983) that a more rigorous analysis is required to capture the physics of the process. The good agreement was shown to result from a fortuitous choice of friction coefficients.

By admitting the presence of areas of micro-slip, it is implied that tractions must be redistributed along the interfaces. As the problem is assumed to be linear-elastic, interfacial slip may be introduced by a corrective solution (Comninou et al., 1980). This method, based on distributed dislocations, allows both the time-dependent load history (Comninou and Barber, 1983a) and moving loads (Chang et al., 1983; and Comninou et al., 1983b) to be considered. During the first phase of the project transient effects were neglected and various steady state situations were modelled. Hence, an Eulerian reference system was adopted and attention focused on the strip behaviour at various points around the cylinder. Once slip regions had been identified, the possibility of slip propagation around the wheel was analysed using a Lagrangian reference system, letting the loads move. The next section details the use of this technique to model the example problem shown in Figure 1.5.

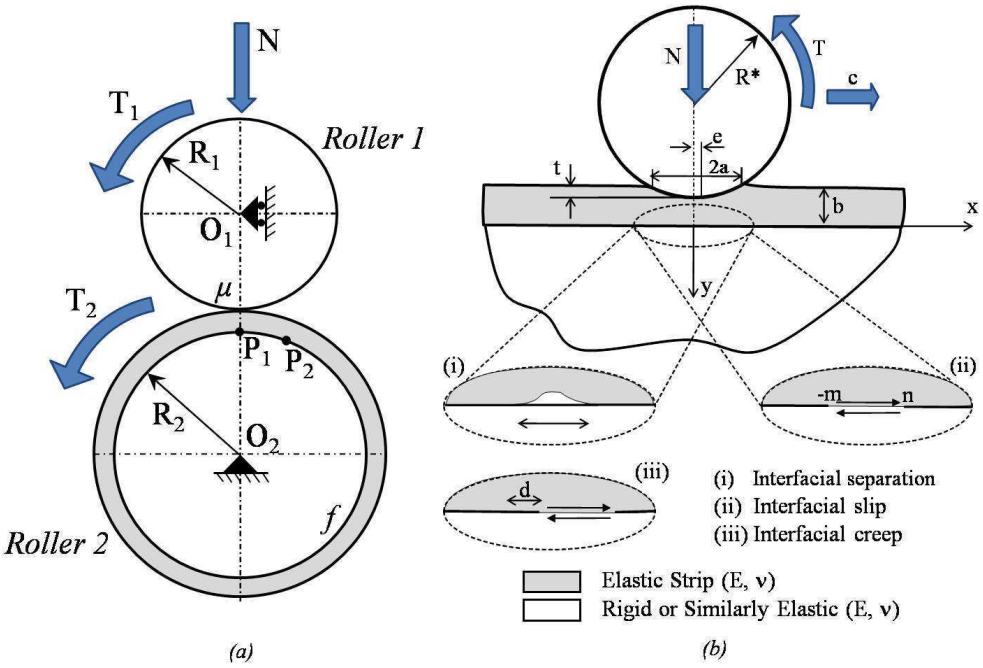


Figure 1.6. (a) Schematic of the system - line contact; (b) Reduced problem and potential interfacial scenarios.

1.2.2 Layered systems - Onset of slip and interfacial slip modelling

This section is concerned with the behaviour of the contact problem introduced in Figure 1.5 and illustrated in more details in Figure 1.6a.

Here roller 1 is used to control both the torque supplied to the contact, and the overall distribution of tractions between the elastic layer, representing the tyre, and roller 2. In its most basic form it mimics the characteristics of test apparatus used by Anscombe and Johnson (1974) to study frictional interfaces in layered contacts, where the assembly is subject to an approximately constant normal force, N, and a monotonically increasing torque, T, under quasi-static conditions. The contacting, homogeneous bodies may, in general, also have a finite surface curvature. It is assumed that the contact half-width, a, is small compared with the radii of both contacting bodies, but not with respect to the tyre thickness, b, so that the problem can sensibly be reduced to one in which the interior of one body, *viz.* the rim carrying the tyre, may be thought of as a half-plane, and the contacting body replaced by a cylinder of radius R^*, which is the harmonic mean of the radii of the actual bodies (Fig. 1.6(b)).

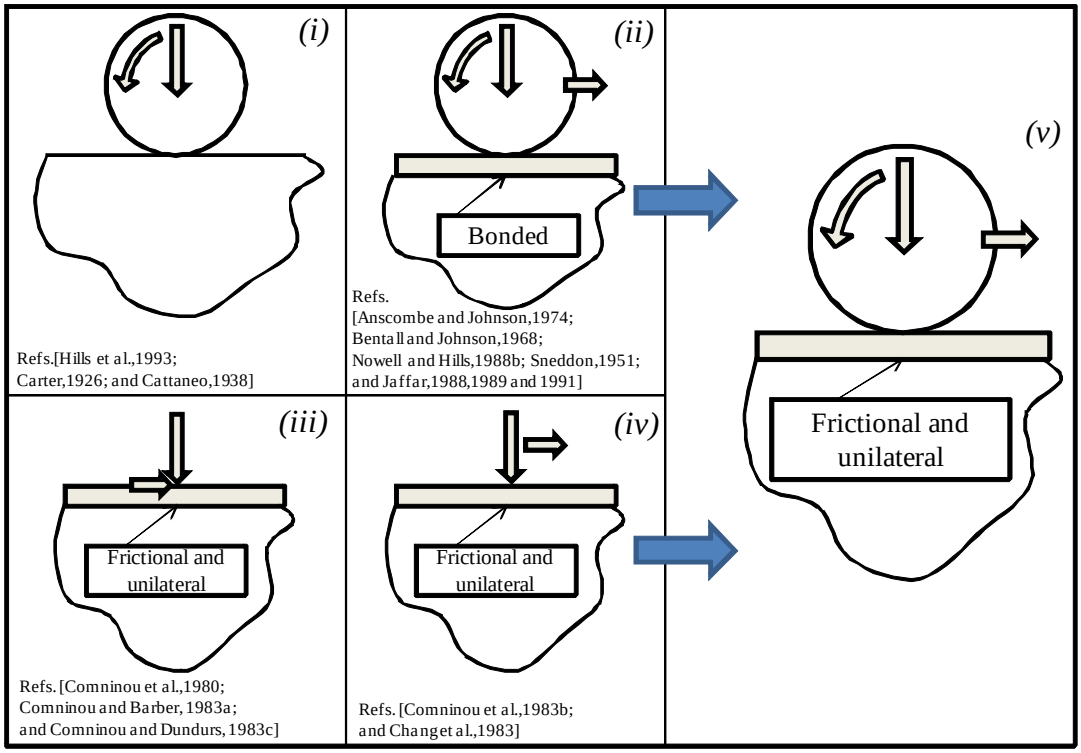


Figure 1.7. Review of the approaches available in the literature for the case under investigation.

Considerable progress has already been made in developing a set of tools to analyse this simplified problem. A review of such developments is reported below with reference to Figure 1.7.

Figure 1.7(i) shows the classical tractive rolling problem for homogeneous bodies, which was first solved by Carter (1926) and later investigated by Nowell and Hills for the case of dissimilar materials (Nowell and Hills, 1988a; and Nowell et al., 1988c). Carter showed that the entry side of the contact was always adhered, whilst the trailing edge suffered partial slip. Bentall and Johnson (1968) analysed a similar problem, however they included the effect of an elastically dissimilar layer perfectly bonded to one of the contacting bodies, Figure 1.7(ii). Their seminal contribution noted that the contact traction distribution would itself be significantly modified from the homogeneous body case, and they introduced a novel piecewise linear representation of the tractions which is determined as part of the solution. This approach is very satisfactory and effective, but applies rigorously only to the case where the tyre is fully bonded.

The case depicted in Figure 1.7(ii) has received much attention as it corresponds to a class of contact problems which is also solved to study the indentation of coated surfaces. Two methodologies are conventionally employed to tackle these problems. The first is the finite element method (FEM). This technique has been extensively used in solid mechanics calculations since the 80s and it is commonly applied to analyse complex geometries and material constitutive laws. Many example cases can be found in the literature and for a more comprehensive review the reader should refer to (Nikas and Sayles, 2008). Komvopoulos (1988) devised a FE model of a rigid sphere indenting an elastic layered body under plane strain. More two-dimensional configurations were investigated (Ihara et al., 1986a and 1986b) and, subsequently, three dimensional contacts were studied (Tian and Saka, 1991a and 1991b; Lovell, 1998; Ye and Komvopoulos, 2003a and 2003b; Kral et al., 1995a and 1995b; and Kral and Komvopoulos, 1996a, 1996b and 1997). Anisotropic (Lovell, 1998), thermo-mechanical and roughness effects have also, more recently, been included in the models (Cole and Sayles, 1992; and Kadiric et al., 2008). Finally, more realistic models have been introduced (Nikas and Sayles, 2008 and 2009) with the intention of predicting life expectancy of coated surfaces (Oliveira and Bower, 1996; and Aslantas and Tasgetiren, 2002). Many commercial subroutines are also now available (Abaqus, 2007). The second technique is BIM (boundary integral method) which is generally preferred to the FE method when simplified elastic contact configurations are treated. Interesting studies can be found in (Johnson, 1985; Hills et al., 1993; Jaffar, 1988, 1989 and 1991; King and O'Sullivan, 1987; Polonsky and Keer, 2000 and 2001; Meijers, 1968; Chen, 1971; Chen and Engel, 1972; Chen et al., 2002; Eberhhardt et al., 1991; Keer and Guo, 1990 and Ma and Korsunsky, 2004). In the present study, given the relatively straigthfoward contact geometry (Fig. 1.6), a BIM technique was selected and validated for specific cases against a commercial FE code (Abaqus, 2007). As mentioned earlier, the BIM techniques just described imply that cases where the tyre, or layer, is in contact but not bonded to the substrate can only be solved when: (a) the interface is in compression at all points and (b) the limiting friction is not violated at any point.

A separate strand of investigation, in which the tyre/wheel interface is defined by conventional friction (Amonton-Coulomb's law) and the Signorini conditions, was undertaken by Comninou and others (Schmueser and Comninou, 1979; Comninou and Dundurs, 1978 and 1983c; Comninou et al. 1980; and Comninou and Barber, 1983a). This early work, shown schematically in Figure 1.7(iii) comprised an investigation of the layer/substrate interface conditions for the case when the elastic layer was subject to stationary line forces; first a normal load was applied and then a monotonically increasing shearing force was imposed. In this work, the concept of using a dislocation at the interface as the kernel in an integral equation formulation to restore unilateral conditions (i.e. Signorini-Coulomb) along the interface was first introduced. In later work, the same authors investigated scenarios in which the contact loads were held stationary in time, but moved along with respect to the layer (Chang et al., 1983; and Comninou et al., 1983b), as shown in Figure 1.7(iv). This represented a significant advance as it allowed investigating the "creep" of the layer along the substrate. However, the extremely idealised nature of the applied loads and the analysed contact conditions limited its practical application.

The present work aims to bring together these two strands of work (Fig. 1.7(v)) by including a realistic representation of the contact interface between the homogeneous roller and the layer, as well as the possibility of slip and separation along the tyre/roller interface. In general, for finite coefficients of friction, slip will always occur before separation, because separation is characterised by the interfacial direct traction moving smoothly towards zero. After implementation of this combined model, an investigation of the system at loads beyond the domain of validity of the bilateral solution (i.e. with finite regions of slip and possibly, also, separation) was undertaken. Problems of this type are inherently history-dependent, and various loading histories could be chosen. However, most wheel type problems are characterised by a load history of the following form: (1) the contact is initially stationary with an applied normal load; (2) a shear load is then gradually applied, representing the tractive effort of a vehicle, giving rise to the layered form of a Cattaneo (Cattaneo, 1938) problem.

(3) The vehicle may then move off giving rise to a transient problem, and where the steady state is the equivalent of the Carter problem (Carter, 1926). While for absolute realism each of these steps should be included, for speed and numerical efficiency (and also because it is of greater practical relevance) the steady state tractive rolling problem is studied principally. Indeed, establishing the steady state requirements constitutes an important part of the solution.

In much of the literature convering analyses of the slipping/separating layer problem, integral equation formulations of the dislocation densities, needed to establish slip and separation, were obtained and, then, solved by conventional inversion (Dundurs and Comninou, 1979). One feature of this approach is that it is necessary to identify a number of side conditions in order to determine the extent of slip/separation zone. When several such regions exist, it becomes increasingly impractical to find self-consistent values for the stick, slip and separation boundaries. This sets a limit to the complexity of the problem that can be treated using this method.

The present work is focused primarily on the associated challenging formulation with the case in which the elastic layer is mounted on a rigid substrate (Reina et al., 2010b). However, it should be noted that the same strategy could be identically applied to the solution of problems when the layer is mounted on an elastically similar substrate (Reina et al., 2010a). This will be treated separately in Chapter 3 where Carter-like contact problems are discussed.

1.2.3 Layered system - Modelling of gross sliding layers

The motivation for the current study is the observation of gross sliding in the tyre-rim assembly. Further work was required to enable investigation of this peculiar loading scenario (Reina et al., 2010c). In fact, under normal conditions it would be expected that the tyre/wheel interface would remain substantially stuck whilst the tyre/road approached the sliding condition. However, there are cases of severely loaded earth-moving machinery where incipient spinning of the tyre around the wheel rim may also be attained.

In the pioneering theoretical studies of slipping/separating layers, integral equation formulations of

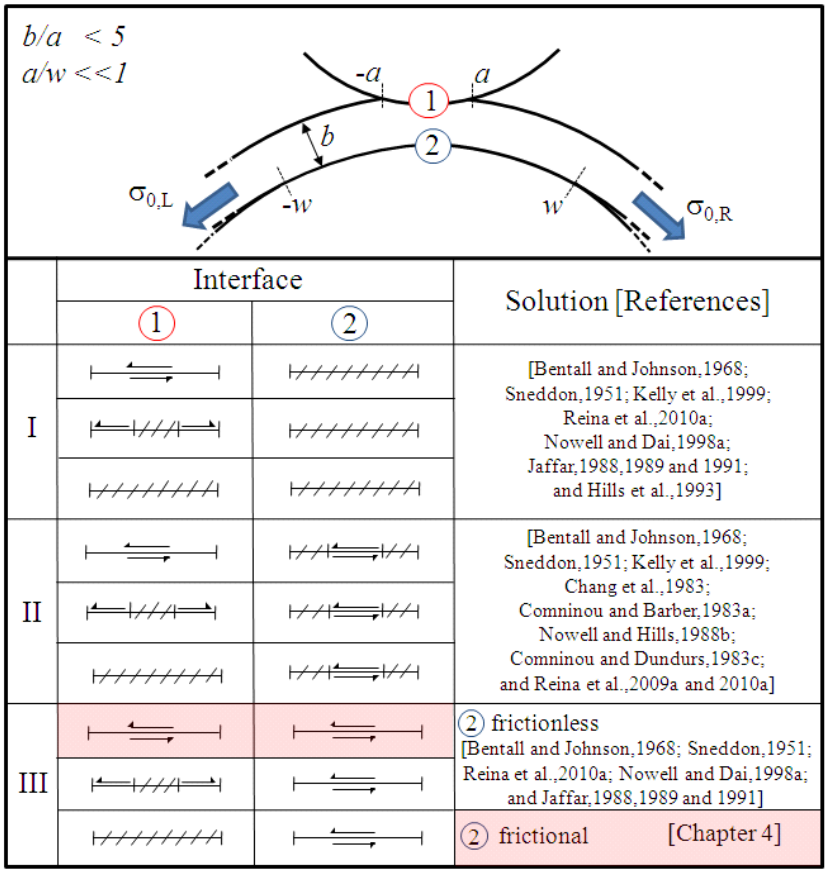


Figure 1.8. Schematic of the system, the possible interface regimes, and review of the approaches available in the literature for the case under investigation.

the dislocation densities, needed to establish slip and separation, were obtained and, then, solved by conventional inversion (Erdogan, 1971). This method is impractical when more than one slip or separation areas must be detected.

Many elastic contact problems are solved using half-space (or half-plane) theory. This idealization is inappropriate if one of the bodies is coated or has a tyre mounted on it, which has different elastic properties from the substrate, and where the thickness of the layer is comparable with the contact half-width (Bentall and Johnson, 1968). A typical schematic of this kind of contact problem is shown in Figure 1.8.

In this case it is customary to use an integral transform procedure, based on the pioneering work conducted by Sneddon in the 1950s (Sneddon, 1951). This procedure has been developed and

extended many times. One key improvement was the adoption of an influence function for a triangle of traction by Bentall and Johnson (1968). This advance allowed the solution to many practical contact problems which involve 'imposed displacement' boundary conditions. The resulting surface tractions are, of course, different from those arising with a geometrically and elastically similar indenter pressed onto a half-plane. There have also been many extensions designed to include the effects of multiple layers, e.g. Kelly et al. (1999). However, in all these analyses it is assumed that the layer is perfectly adhered to the substrate (Fig. 1.8 - case I). This is often appropriate and, when needed, the presence of finite zones of interfacial slip may be incorporated by arranging distributions of glide dislocations to permit localised slip (Fig. 1.8 - case II). Again, this has been described by several authors as mentioned in the previous sub-section and needs no further description here. However, the existing literature does not cover one class of practical problem in which the surface loading is capable of causing the layer to move along the substrate, therefore producing rigid body motion between the contacting parts. The case of a layer resting on a frictionless substrate (Fig. 1.8 - case III frictionless) was already solved to investigate the contact problem of a thin layer clamped by two cylinders or passing between two elastic bodies (Hills et al., 1993). When the interface between layer and substrate is frictional (Fig. 1.8 - case III frictional), in principle this could be tackled by distributing glide dislocations over the entire interface. However, this results in a problem that cannot be solved without iteration. A more satisfactory approach is to re-work the basic formulation for the layer problem but with a mixed condition applied along the interface. Continuity of normal displacement is imposed and the shear traction is proportional to the direct traction at all points. This implies that the direct traction is always compressive such that there is no tendency for separation to occur. Although this could, in principle, be handled by introducing climb dislocations under the same circumstances (Porter and Hills, 2002a and 2002b).

In this thesis the formulation for an elastic layer moving steadily over a *rigid* substrate is presented and an example application of this technique provided in Chapter 4 (Reina et al., 2010c).

1.2.4 Layered system - On the application of optimisation technique to elastic contact problems modelled using the distributed dislocation technique

Although the distributed dislocation technique has been successfully used to explain "interfacial micro slip" in layered frictional contacts (Chang et al., 1983; Comninou and Dundurs, 1978; Comninou et al. 1980; Comninou and Barber, 1983a; Comninou and Dundurs, 1983c; and Reina et al., 2010b), its applicability has been limited by the difficulties encountered when trying to simulate complex loading conditions, as these require convoluted iterative schemes (Reina et al., 2009) to ensure that all Signorini inequalities are satisfied throughout the interface. Furthermore, interfacial micro-slip is not easily captured using standard analytical and numerical tools, especially in the presence of complex loading scenarios, where simultaneous slip may occur at different locations along the mating surfaces (Ahn and Barber, 2008b). Finite element or boundary element approaches may be able to provide accurate results. However, computational time and solution convergence can be critical aspects for this type of analysis (Reina et al., 2009). In the approach advocated here, the advantages of the dislocation kernel (which maintains remote boundary conditions) are retained, however the problems associated with the integral equation are averted by formulating the contact problem in terms of a 'quadratic cost function' to be minimised. The problem can, therefore, be solved using quadratic programming techniques. In mathematics this way of solving problems is normally referred to as optimization or mathematical programming. Building on the suitability of linear programming for solving contact problems (*e.g.* see Kalker, 1971 and 1990), optimisation techniques have been widely applied in mechanics to solve problems with both linear or non-linear constraints. Its applicability to solve two and three dimensional elastic contact problems has been demonstrated by various authors in the '80s (Klarbring, 1986; and Klarbring and Björkman 1988). Later, Nowell and Dai (1998a) used quadratic programming to solve a fretting configuration. The technique is also well established within other areas of applied mechanics; for example, by the late '60s, Maier had already demonstrated its effectiveness in solving non-linear structural problems (1968a), elastic-perfectly plastic structures (1968b) and problems involving creep (1969a). Finally,

the quadratic programming technique has also been applied in combination with both FEM (Chand et al., 1976; and Su et al., 2002), or BEM (Matos and Nowell, 2007), to investigate problems related to fracture and contact mechanics.

In this thesis, the problem in which a layered system is mounted on a (elastic or rigid) substrate in the presence of friction and subjected to loading conditions giving rise to micro-slip or creep is formulated for the first time using the distributed dislocation technique within a quadratic programming framework. The usefulness of this solution for rolling contact problems in layered systems is then demonstrated. The development of an experimental technique to measure the extent of creep in layered rolling contact problems is also presented. A preliminary comparison between numerical and experimental results is performed to confirm the validity of the proposed numerical technique.

1.2.5 Frictional shakedown in frictional elastic contact problems

The behaviour of elastic systems with frictional interfaces under cyclic loading may be compared with the behaviour of monolithic bodies with elastic-plastic constituive behaviour. When slip ceases after a few cycles, elastic frictional systems are said to have shaken down. Specifically, we refer to frictional elastic shakedown when no cyclic slip occurs after a few loading cycles, whereas frictional plastic shakedown occurs when the amount of slip reduces after a few cycle but it does not cease. This second scenario is commonly associated with problems of wear and fretting. Frictional ratchetting implies cumulative slip which may lead to severe failures of mechanical assemblies. For instance, cumulative micro slip has been observed in conrod assemblies or in tyred systems. In this thesis, by adopting the optimisation technique introduced in the previous sub-section, a systematic approach to explore the applicability of plasticity theorem to frictional elastic systems is presented. In fact, many authors have speculated on the applicability of the Melan's theorem (Melan, 1936) to describe the behaviour of frictional elastic systems. The theorem, which is lower bound in nature, may be stated as follows: "If a set of time-independent tangential displacements at the interface can be identified such that the corresponding residual stresses when superposed on the time-varying

stresses due to the applied loads cause the interface tractions to satisfy the conditions for frictional stick throughout the contact area at all times, then the system will eventually shake down to a state involving no slip, though not necessarily to the state so identified" (Klarbring et al., 2007).

A brief summary of the recent progress on the study of frictional shakedown is reported here. For a more comprehensive review of shakedown for frictional elastic problems the reader should refer to (Klarbring et al., 2007). Drucker (Drucker, 1954) was the first author to note the analogy between the elastic-plastic behaviour of a monolithic body and frictional systems. He illustrated that the Melan's theorem does not apply in full generality for a one degree of freedom system because of the non associative nature of the 'flow rule'. In fact, Coulomb's law is non-associative in the sense that there is coupling between tangential displacement and normal traction. For cases where the pressure remains unaffected by the presence of relative displacement between the mating surfaces in the presence of cyclic loads (definition of an *uncoupled* frictional system), then the law becomes associative and the theorem holds (Fredriksson and Rydholm, 1981). This is true in the simple contact configuration investigated by Churchman and Hills (Churchman and Hills, 2006). Antoni (Antoni et al., 2007) investigated the artificial so called "Tresca friction criterion", for which shakedown theorems can be proved to hold. However, no additional information was provided for Coulomb frictional systems. The non associated flow law in perfect elastoplasticity was investigated by Maier (1969b). Its extension to elastic friction problems was explored by Klarbring and Björkman (Klarbring, 1986; and Klarbring and Björkman, 1988) who pointed out that the sufficient condition based on the "reduced elastic domain" introduced by Maier (1969b) cannot be extended to frictional elastic problems, whereas the necessary condition quoted above remains valid. More recent rigorous and structured analyses of frictional shakedown problems can be found in (Klarbring et al., 2007; Barber et al., 2008; Antoni et al., 2007; and Antoni and Nguyen, 2008), where the criteria required for Melan's theorem to hold were considered, with the analysis being restricted to complete contacts. In general, from the literature available on this topic, it appears that

Melan's theorem is not applicable to elastic frictional problems in full generality. However, its limit of applicability have not been yet defined. In this thesis, the applicability of Melan's theorem in predicting frictional shakedown is discussed by direct comparison with the exact marching-in-time solution (Reina et al., 2009 and 2010b), for the specific problem under investigation.

1.2.6 Frictional joints - on the possibility to measure the friction coefficient in partial slip condition

Another important aspect to be considered, together with its variability in time and space, is the friction coefficient at the interface between mating surfaces. With the exception of the gross sliding case, which is the consequence of severe loading conditions, the contact configurations so far discussed are characterized by partial slip. In this general context, it is difficult to predict the value of the friction coefficient at the mating surfaces a-priori. In fact, it is truism in physics that quantities cannot be measured without changing them (Heisenberg, 1927); a voltmeter draws current; the insertion of a load cell in a load path introduces compliance, and so forth. Similarly, the coefficient of friction is normally measured by sliding solid bodies pressed together, and the process of sliding normally causes significant surface modification, and, hence, a change in the coefficient of friction. It could be argued that conducting tests under an even lower normal force, and extrapolating back to zero, would circumvent the problem, but this presumes that the coefficient of friction is truly load independent, and it may be desirable to measure its value at representative contact pressures.

In this thesis an alternative source of quantitative evidence is used to deduce the coefficient of friction. Stationary contacts suffering partial slip occur in fretting experiments and merit a really detailed knowledge of the value of the coefficient of friction. Sliding is absent, but a large body of experimental data is readily available. It may seem contradictory to measure the coefficient of friction without sliding the bodies, however, in fact, a careful exploitation of the phenomenon of partial slip may reveal the value of the coefficient of friction. One attempt at this has already been made by Pasanen et al. (2010), who used visible evidence of surface damage caused by slip to

measure the extent of the slip annulus in a Cattaneo (1938) type experiment. Previous attempts to infer the friction from the hysteretic response of contact pairs subjected to partial slip include the work by Fouvry and co-workers (1998). A number of other authors have also developed techniques for estimating the slip zone friction coefficient from a measured mean values for different contact configurations (Araújo and Nowell, 1999; and Dini and Nowell, 2003).

The work carried out in this thesis aims at developing a new combined experimental and modelling methodology to measure friction in partial-slip contacts. The basic idea is to induce a cyclic set of loads which alternately inject a slip region into one end of the contact and abstract it at the other, so that, after each cycle of loading, there is, potentially, a net rigid body movement of the indenter. In many respects the idea was foreseen by Comninou and Dundurs (1978) in a paper in which they describe movement of a rug over a floor by inserting a 'ruche' or dislocation at one end which may emerge at the other. In the present work, a classical fretting fatigue test configuration (Mugadu, 2002) is used to produce the net rigid body movement of an indenter by modulating the loading histories applied to a fretting pair. The aim is to find a range of loads which causes, at some point during the loading cycle, every point to pass through the slip condition (though not all simultaneously!). If this is the case, it is important to check that the slip conditions are such that gradual rigid body displacement, or 'creep', occurs. Given this, it is possible to measure a significant rigid body movement over many cycles of loading, and from this infer the value of the interfacial coefficient of friction, f.

This can be achieved by comparison with a transient partial slip contact analysis. An attempt to solve the evolution of the stick slip regime for a wide range of fretting and rolling contacts was made using the classical integral equation formulation for half-planes in contact (Hills et al., 2003). However, this approach rapidly becomes unwieldy if the stick-slip regime is complex. A better approach is to devise a general procedure using a numerically defined shear traction distribution, and, then, apply optimisation techniques, pioneered in this context by Kalker (1971 and 1990) to

determine the evolving problem. This approach has been previously employed by Nowell and Dai (1998a). The essential point is that the distribution of shear tractions is spatially smooth, and falls continuously to zero at each end of the contact. An appropriate way to represent this is, therefore, a triangular distribution of traction and a corresponding influence function. Hence, an overlapping set of such triangles, as pioneered by Benthall and Johnson (1968), gives a very good piecewise-linear representation of the true solution. This means that the evolving array of stick and slip regions may be found with good accuracy at relatively little computational expense. It is also simple to determine the relative surface slip displacement in slip regions, and the associated residual interfacial shear tractions which remain when such regions become 'stuck', at points within the loading cycle (Qiu et al., 2008).

The use of a semi-analytical method allows investigation of the contact regimes arising at the interface between two bodies under fretting conditions. The exact form of the remote loading cycles are unimportant and have no bearing on the solution. The solution is defined only by maximum values of the applied loads at their turning points. If there is at least one particle within the contact which never slips, the contact undergoes no rigid body displacement. Conversely, if every particle slips at some point during the loading cycle, then the indenter may 'walk' (Mugadu et al., 2004; and Nowell, 2004). There is also the possibility that there will be no net movement over the cycle once the steady state regime is achieved. These two responses are analogous to the phenomena of creep and cyclic plasticity, respectively, in classical plasticity theory (Antoni et al., 2007; and Klarbring et al., 2007).

Preliminary results from this analysis and possible extensions will be discussed in this thesis.

1.3 Thesis outline

This thesis summarises the advances made in the basic understanding of layered contact problems during the author's PhD work. New semi-analytical, numerical and experimental techniques have been developed and applied to a wide range of systems, although particular attention is focussed on

tyre-wheel assemblies. The work is presented mostly to reflect the chronological sequence of the studies carried out, although adjustments have been made to group some of the material by subject topic.

The following chapters constitute the substructure of this thesis:

- Chapter 2 presents an investigation on layered systems using a conventional method to solve elastic contact problems modelled using the distributed dislocation technique;

- Chapter 3 investigates the onset of slip for the Carter type partial slip rolling problem;

- Chapter 4 investigates elastic contact problems in the presence of mixed boundary conditions at the interface between mating surfaces;

- Chapter 5 presents the application of quadratic programming technique to the class of elastic contact problems illustrated in Chapter 2;

- Chapter 6 investigates the frictional shakedown problem in layered elastic contacts;

- Chapter 7 presents a novel technique which may be applied to determine the friction coefficient in partial slip;

- Chapter 8 discusses the practicalities to be considered when the engineering scenario that prompted our studies is treated, and presents a 3D analysis of the prototype under investigation;

- Chapter 9 presents the main conclusions and discusses potential future research areas.

Chapter 2

Interfacial Slip and Creep in Tyred systems

2.1 Introduction

In this second chapter a systematic approach for investigating the interfacial behaviour of tyred systems is proposed. A simplified two-dimensional contact model of an elastic strip, shrink-fitted onto a wheel, and subjected to different rolling contact conditions, has been adopted to illustrate the method. The schematic of the contact problem is illustrated in Figure 1.6. The model combines existing techniques to explore individual elastic contact problems and it enables us to characterise the behaviour at the strip/substrate interface caused by loads induced by the quasi-static application of stationary and moving loads on the surface of the layer. The solution is compared to the stationary load case and regimes of local slip, full stick, separation and frictional creep are identified and collated for a variety of loading conditions, materials and geometries (Reina et al., 2010b).

2.2 Formulation - bilateral solution

The elastic contact problem between indenting cylinder and layer, under the assumption of Figure 1.7(ii), is first solved. This is done by following the approach proposed by Bentall and Johnson (1968) for which the contact tractions are discretised using overlapping triangles. Hence, the first step in the solution is to determine the influence function for a triangular distribution of traction, of half-width a_{tr} and height (p_i, q_i), on the surface normal displacement, v_{surf}, at a point x along the interface between the indenting roller and the elastic layer. Here p_i represents the contact pres-

sure and q_i the shear traction applied to the layer surface and located at point x_i. The problem potentially includes a large number of independent variables and, in order to reduce them by one, the contact is assumed to be *sliding* over the tyre, averting the analysis of a partial slip problem at the layer/indenter interface. The surface tangential displacement, u_{surf}, is therefore not needed. Further, it is assumed that the substrate to which the layer is bonded is rigid, and that the layer has a modulus of elasticity E and Poisson's ratio ν. Details of the calculation are given in Bentall and Johnson (1968), and Nowell and Hills (1988b), and here the effects of a distribution of triangles of traction may be simply written down in the form:

$$v_{surf}(x) = \frac{4(1-\nu^2)}{\pi E} \sum_{\text{contact}} p_i F^p(x, x_i) + \frac{2(1+\nu)}{\pi E} \sum_{\text{contact}} q_i F^q(x, x_i) . \tag{2.1}$$

where F^p and F^q are given in Appendix A. Given this, it is possible to solve the contact problem with bilateral or adhered conditions along the interface.

In the current study it is assumed that prior to the application of the contact load, a shrink fit is applied, giving rise to a constant pressure, p_0, along the entire interface. The load from the contacting wheel is then applied. The wheel is assumed to be rigid, and have an equivalent radius R^*. Because of the compliance mismatch between the tyre and the contacting surface, this results in the development of an antisymmetric shear traction distribution between the layer and the wheel in which the central portion is adhered, but fringes of slip of opposite sign may develop at the contact edges. However, this is not a principal concern in this analysis as the subsequent application of a shearing force sufficiently large to cause sliding dominates the steady state problem at the interface.

At this point the solution is controlled by a number of factors. (1) The ratio of the interfacial ('shrink fit') contact pressure to the equivalent maximum Hertzian[1] pressure which would be obtained under the same geometry and loading conditions, $\lambda = p_0/p_H$. (2) The geometry of the problem identified by the ratio between the layer thickness and the contact half-width, $B = b/a$, and (3) its elasticity

[1] It should be noted here that the Hertzian case has been chosen as a reference for the normalised variables as it corresponds to the case when the layer thickness $b \to \infty$. Both a_H and p_H are therefore easily computed once the geometry, the applied normal load and elastic properties of the layer are known.

by tyre Poisson's ratio, ν. (4) The coefficient of friction between the tyre and the surface of the contacting roller, μ. The formulation (2.1) is such that the boundary conditions outside the contact area between the indenting cylinder and the layer are satisfied. The solution to the contact problem is then obtained by finding the values of p_i that satisfy the appropriate boundary conditions within the contact. The reader is referred to Hills et al. (1993) for a comprehensive description of the solution to the contact problem. Once the contact tractions are found, the stress field within the layer and, therefore, the interfacial stress field between layer and substrate, can be calculated by superposition of the stress fields associated with each triangle of traction.

The resulting solution represents the (numerically) exact solution of the contact problem provided that, along the tyre/substrate interface $y = 0$, the tractions satisfy the following inequalities:

$$\sigma_{yy}^{bil}(x,0) \leq 0 \text{ and } \left|\sigma_{xy}^{bil}(x,0)\right| / f \leq -\sigma_{yy}^{bil}(x,0), \quad \forall x, \tag{2.2}$$

where the superscript bil refers to the components of the stress field evaluated solely by using the bilateral solution, and f is the coefficient of friction between the tyre and the substrate, not necessarily equal to μ. The presence of slip at the interface between the layer and the substrate implies the violation of the friction law.

2.3 Formulation - unilateral solution

Consider now when the shearing traction along the tyre/hub interface exceeds its limiting value at one or more points, and regions of slip occur. At this stage separation is not considered, and the analysis is stopped at the point where this is incipient. In order to introduce slip the state of stress induced by an edge dislocation at a layer/half-plane interface is first needed. As with the solution for the element of surface contact pressure, an integral representation of the state of stress induced is required. A full description of the process is provided by Comninou and Dundurs (1983c), so only results are given here. Note that the problem is coupled in the sense that the glide dislocation, having a Burgers vector b_x, induces both shear and direct tractions along the interface. The interfacial

tractions, σ_{yy}^{glide} and σ_{xy}^{glide}, induced by a glide dislocation situated at $(\xi, 0)$ are given by:

$$\begin{aligned}\sigma_{xy}^{glide}(x,\xi) &= \frac{Cb_x(\xi)}{\pi}\left(\begin{array}{c}\dfrac{1}{x-\xi}+\\ -\dfrac{1}{b}\int_0^\infty \dfrac{N_{22}}{D_{22}}e^{-\tau}\sin\left(\dfrac{(x-\xi)\tau}{b}\right)d\tau\end{array}\right) \\ &= G_{xy}(x,\xi)\,b_x(\xi)\end{aligned} \tag{2.3}$$

$$\begin{aligned}\sigma_{yy}^{glide}(x,\xi) &= \frac{Cb_x(\xi)}{\pi}\left(\begin{array}{c}-\pi\beta\delta(x-\xi)\\ +\dfrac{1}{b}\int_0^\infty \dfrac{N_{12}}{D_{12}}e^{-\tau}\cos\left(\dfrac{(x-\xi)\tau}{b}\right)d\tau\end{array}\right) \\ &= G_{yy}(x,\xi)\,b_x(\xi)\end{aligned} \tag{2.4}$$

where the kernels N_{12}, N_{22}, together with D_{12} and D_{22}, are given in Appendix A, and $\delta(\cdot)$ is Dirac's delta function. Standard nomenclature α, β, κ, C for the Dundurs' constants, Kolosov's constant and the 'stiffness', respectively, is retained. For the case of an elastic layer bonded to a rigid half-plane these reduce to the following simplified forms:

$$\alpha = -1 \tag{2.5}$$

$$\beta = -\frac{1-2\nu}{2(1-\nu)} \tag{2.6}$$

$$\kappa = 3-4\nu \text{ - Kolosov's constant - plane strain} \tag{2.7}$$

$$C = \frac{2G(1-\alpha)}{(\kappa+1)\left(1-\beta^2\right)} = \frac{G}{(1-\nu)\left(1-\beta^2\right)}. \tag{2.8}$$

where G is the shear modulus of the layer.

Note that the state of stress everywhere (and including, therefore, also the interfacial tractions) is dependent only on the value of Poisson's ratio of the tyre, and the modulus of rigidity enters the solution only insofar as it controls the displacement field, and therefore, ultimately, the slip displacement and creep.

The tractions $\sigma_{yy}(x), \sigma_{xy}(x)$ present along the interface can then be written in terms of the three contributions - the effect of shrink fit, i.e. the contact pressure, p_0, the tractions induced by the contact tractions as implied by the bilateral solution, σ_{iy}^{bil} (with $i = x$ or y), and the influence of

dislocation arrays, so that:

$$\sigma_{yy}(x) = -p_0 + \sigma_{yy}^{bil}(x,0) + \int_{\text{slip region}} G_{yy}(x,\xi)\, B_x(\xi)\, d\xi \tag{2.9}$$

$$\sigma_{xy}(x) = \sigma_{xy}^{bil}(x,0) + \int_{\text{slip region}} G_{xy}(x,\xi)\, B_x(\xi)\, d\xi \tag{2.10}$$

where $B_x(\xi)$ ($db_x(\xi) = B_x(\xi)\, d\xi$) is the unknown dislocation density, and is physically the derivative of the interfacial slip displacement with respect to position. Note that the solution presented is for a single slip region as this is the simplest scenario which can be analysed and constitutes an ideal vehicle for describing the salient features of the solution. The formulation can, however, be easily extended to the case of two slip regions simultaneously nucleating and evolving along the layer/substrate interface as shown by (Chang et al., 1983; and Comninou and Barber, 1983a).

The conditions at the interface are therefore:

$$\sigma_{yy}(x) < 0 \qquad \forall x \tag{2.11}$$

$$|\sigma_{xy}(x)| = \pm f\sigma_{yy}(x) \qquad sgn(\sigma_{xy}(x)) = sgn(V(x)) \qquad x \in \text{ slip regions} \tag{2.12}$$

$$|\sigma_{xy}(x)| < -f\sigma_{yy}(x) \qquad B_x(x) = 0 \qquad x \notin \text{ slip regions.} \tag{2.13}$$

where $V(x)$ is the interfacial relative velocity.

Each of these conditions is necessary to determine the complete interfacial traction distribution, however they are insufficient, and an extra condition is required to fully define the problem. The nature of such a condition depends on the kinematics of the problem which may be divided into two distinct "scenarios":

1. When the contact is stationary, or sliding along a layered body, such that it is always moving into initially unstressed virgin material, slip regions develop in areas where, exterior to them points either side the interface remain in the same position that they were in before the assembly was loaded. This means that, within each slip region, the net tangential (slip) displacement between the tyre and the substrate must return to zero, and, therefore, that not only must $sgn(\sigma_{xy}(x)) = sgn(h(x))$ since $sgn(V(x) = sgn(h(x))$, where $h(x)$ is the tangential shift due to the distributed dislocations, but

additionally:

$$\int_{\text{slip region}} B_x(\xi)\, d\xi = 0, \tag{2.14}$$

to ensure uniqueness of the displacement field.

2. Rotating wheels in contact. In this scenario, when material moves through the contact slip regions can develop which then leave both a residual slip displacement, and a residual state of stress. These become the 'starting' conditions for material re-entering the contact. In the steady state, material exiting the contact and material entering this neighbourhood must be in the same state of residual stress. Thus, it is no longer the case that particles just within the tyre and just within the substrate must remain opposite each other in the loaded state. In fact, the tyre is expected to have a slightly lower rigid body velocity than the periphery of the substrate beneath. This is the phenomenon known as creep. In the current model, this means that, as material flows through the contact, the slip dislocations present become 'locked' as adjacent material passes into stick regions, and their presence is manifested as the rigid body motion being sought. It is no longer true to say that, within the stick regions, the net dislocation must vanish, but simply that, in the steady state, they must be the same at all points along the adhered part of the boundary. Therefore, whilst the left hand set of requirements of Equations (2.12) is preserved, the following must be replaced

$$sgn(\sigma_{xy}(x)) = sgn(h(x)) \qquad \text{by} \qquad sgn(\sigma_{xy}(x)) = sgn(V(x)) \qquad x \in \textit{slip regions} \tag{2.15}$$

where the sign of the slip velocity, $V(x)$, is given by

$$sgn(V(x)) = sgn\left(\frac{dh}{dx}\right) = c\; sgn(B_x(x)), \tag{2.16}$$

and c is the creep velocity.

Further, the auxiliary condition stated before in order to avoid multivalued displacements is here replaced by:

$$\int_{\text{slip region}} B_x(\xi)\, d\xi = d. \tag{2.17}$$

where the integral of the dislocation density now represents the net relative shift, d, between the layer and the substrate. The differences between the two formulations adopted to solve the stationary problem and the moving load scenario have already been discussed by Comninou et al. (1983b) and are here briefly summarised. In the static solution d must vanish so that (2.14) is an auxiliary condition required by the solution. This, together with the modified condition imposed by Equation (2.15), implies that the condition $d = 0$, no longer valid in the moving load problem, needs to be replaced by a condition obtained from the inequalities. The study of the asymptotics of the transition between stick and slip is essential to assess the strength of the inequalities (Comninou et al., 1983b; and Dundurs and Comninou, 1979). It is found that, as already discussed by Comninou et al. (1983b) for simpler configurations, the slip zone moving between two stick areas implies that Equations (2.13) and (2.15) provide a stronger result with respect to the static case at the trailing edge of the slip zone. This enforces the shear tractions at the trailing edge to have continuous derivative. This is not the case for the leading edge, where discontinuous derivatives result in "hooks" which are typical of both trailing and leading edges for the stationary case. This will become apparent when the two solutions are compared in Section 2.4.3.

2.4 Results

2.4.1 Limits implied by the validity of the bilateral solution: first point of slip and separation

It is necessary to study the domain of validity of the bilateral solution. It is very important to note that, if the inequalities defining a bilateral response, stated by Equation (2.2), are always satisfied, the solution is independent of the load path. It is therefore valuable to probe the limitations of this requirement. Once the normal and tangential stresses have been obtained along the interface $y = 0$, the minimum friction coefficient needed to guarantee adhesion between layer and substrate may be determined by determining when the tractions at the layer/substrate interface violate the inequalities in Equation (2.2). Figure 2.1 provides a "first point of slip" threshold map illustrating the minimum

friction coefficient needed to guarantee adhesion between the elastic layer and the rigid substrate when the two rollers are pressed together and are fully sliding with respect to each other. Figure 2.1 shows the threshold for $\nu = 0.3$ and $\lambda = 1$ and Figure 2.2 for $\nu = 0.5$ and $\lambda = 1$, for different values of μ. The method developed is not restricted to sliding problems, but this is chosen simply to remove one independent variable.

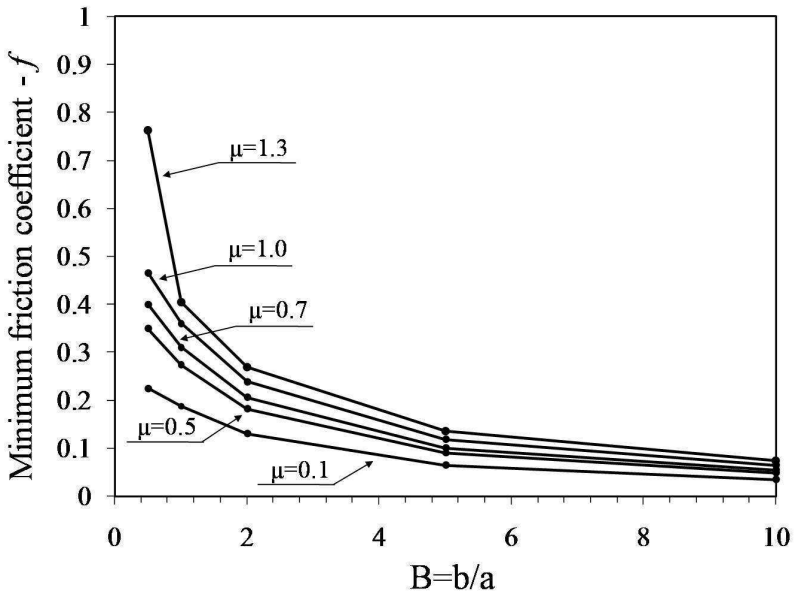


Figure 2.1. Minimum friction coefficient *f* to guarantee adhesion as a function of the normalised layer thickness *B* for various friction coefficients μ and ν = 0.3 – full sliding of external contact over layer surface.

The threshold maps in Figures 2.1 and 2.2 refer solely to the loading conditions under which the applied torque is sufficient for sliding to occur at the cylinder/tyre interface (see Fig. 1.6). However, it is also important to display these limits for different sets of loading conditions. In particular, it is of interest to show when the "first point of slip" is reached when the normal load, N, is applied in the absence of torque, T. The results shown in Figure 2.3(a) present the comparison of the interfacial response both in the presence and in the absence of applied torque for a given example set of parameters: $\lambda = 1, \nu = 0.3$. Two sets of lines are included and each shows, for a given dimensionless layer thickness, b/a, the minimum interfacial coefficient of friction, f, to maintain full adhesion between tyre and wheel. The two cases looked at are (a) when the bodies are pressed

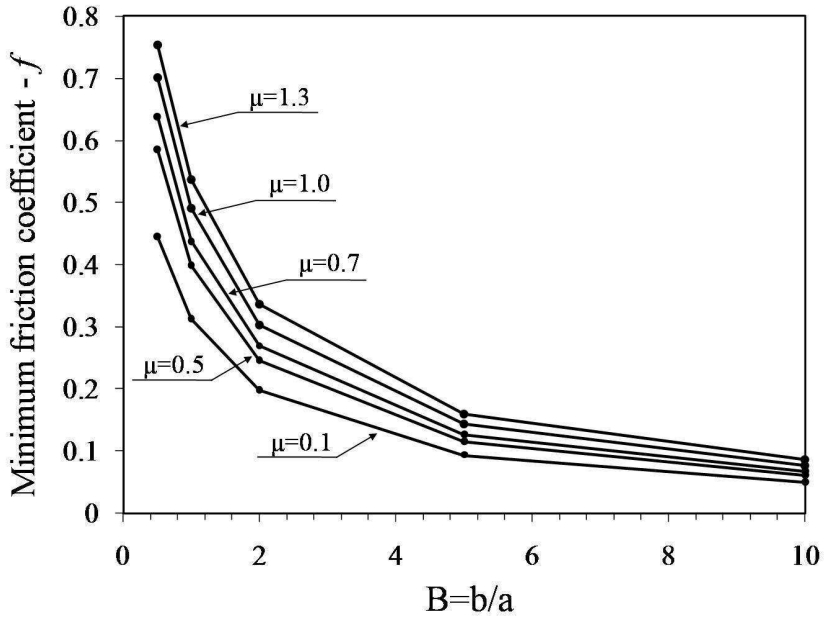


Figure 2.2. Minimum friction coefficient f to guarantee adhesion as a function of the normalised layer thickness B for various friction coefficients μ and ν = 0.5 – full sliding of external contact over layer surface.

together under a normal load *alone*, and a second line, denoted (b) for the case when the disks are in sliding contact, with $\mu = 0.7$. In case (a) the tyre-substrate interfacial shear traction is antisymmetric but the contact pressure is symmetric, whilst in case (b) the interfacial traction possess neither symmetry nor anti-symmetry.

At this point it is worth considering the possibility that separation, as implied by the violation of the first of the two inequalities (2.2), precedes slip. Figure 2.3(b) shows the "separation limit", i.e. the minimum interfacial contact pressure (usually due to interference), needed to maintain full contact when the top disk is fully sliding over the elastic layer (the only case when separation may occur). Furthermore, the limit for separation is in general weakly dependent on local violations of the bilateral solution and, consequently, it is here plotted as a function of the dimensionless layer thickness, b/a, only. By combining the results shown in Figures 2.3(a) and 2.3(b), it can be noted that the necessary value of interfacial contact pressure to maintain full contact is usually not more than about 10% of that used in the 'no slip' calculation, so that slip would precede separation by a

large margin.

Finally, it is useful to establish the conditions under which, *in the steady state*, there is no tyre-substrate slip, and that therefore all creep ceases. This is, apparently, a less stringent condition than (Fig. 2.3a - *(b)*) above, and corresponds to a frictionally shaken down state (Ahn et al., 2008a; and Barber et al., 2008). However, the dislocation density passing out of the contact region is constant (i.e. it does not vary with x), and so there can be no corresponding residual stress field, because there are no gradients. A consideration of equilibrium in the $x-y$ plane leads to the same conclusion: the state of stress for large x is independent of x, and so it follows that neither σ_{yy} nor σ_{xy} can vary with y. Thus, as the free surface is free of shearing traction so must be the tyre-substrate interface. It follows immediately that, for this problem, the tyre will either remain fixed with respect to the substrate or it will rotate steadily with respect to its hub, and there is no loading regime where there is initially creep but which subsequently gives rise to an adhered state.

2.4.2 The use of the unilateral solution to study interfacial slip: Stationary loading

Turning, now, to a consideration of what happens when the conditions for the bilateral solution to hold are violated, an example case is studied in detail in order to gain insight into anticipated behaviour. Start with the bilateral formulation, and assume that a normal load, alone, has been imposed on the contact, taking the configuration to Point A on Figure 2.3 ($B = 1$, $\lambda = 1$). An interfacial friction coefficient of 0.2 is clearly sufficient to maintain full adhesion at this stage, but suppose, now, that a shear force sufficient to cause sliding is imposed, and that the inter-body coefficient of friction, μ, is 0.7. The value of f is now insufficient to guarantee full adhesion between layer and substrate when torque is applied, and therefore the threshold for case (Fig. 2.3a - *(b)*) need to be considered as the limiting value.

The effects of slip on the stress field may be found by deploying distributed edge dislocations where slip occurs. Specifically, the location and size of the slip region (and therefore its leading and trailing

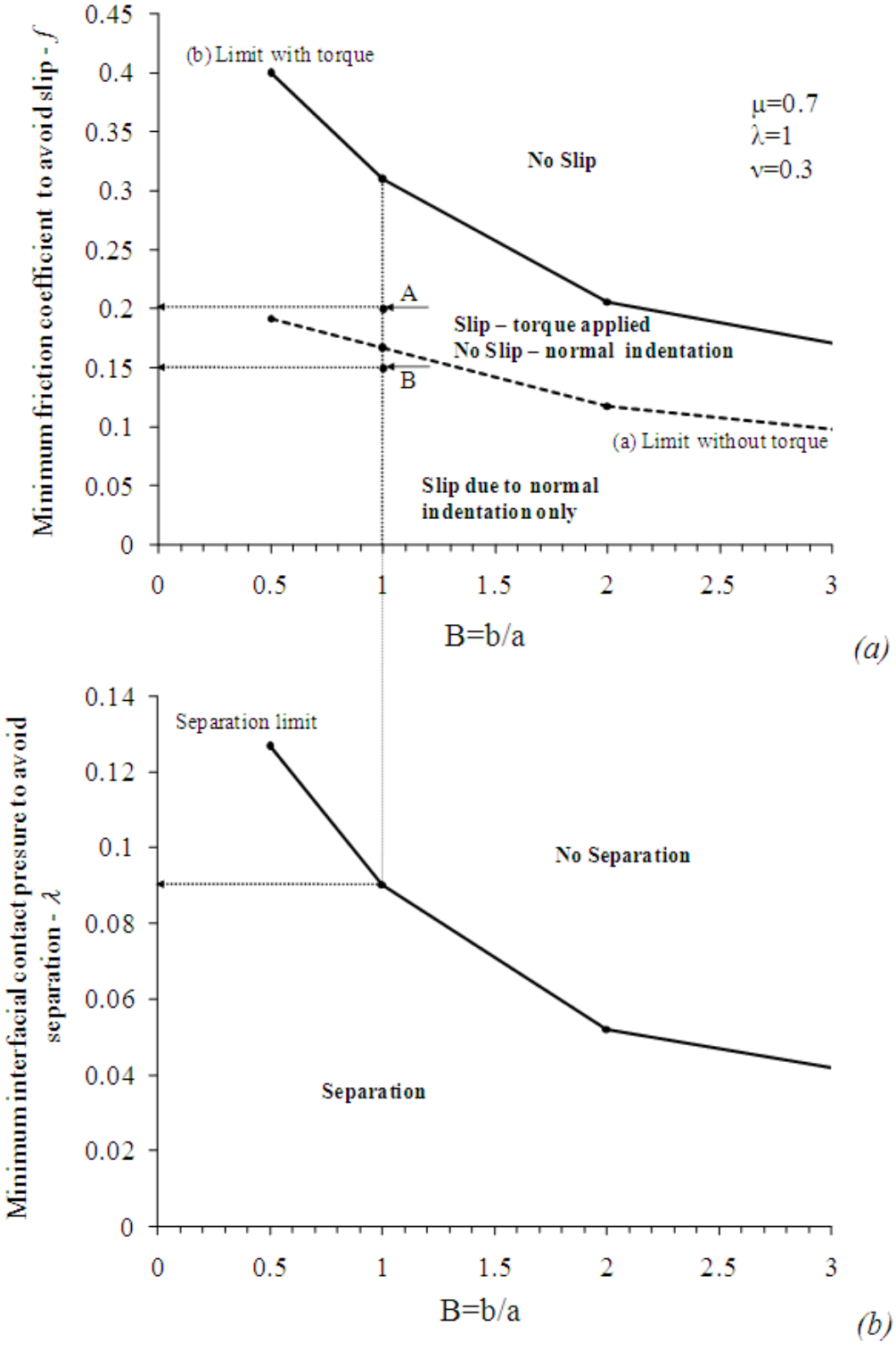


Figure 2.3. (a) Minimum friction coefficient f to guarantee adhesion with and without the application of tangential forces (induced by an applied torque sufficient to cause full sliding of external contact over the layer surface) and (b) separation limit and as a function of the normalised layer thickness B for $\mu = 0.7$ and $\nu = 0.3$.

edge, n and m in Figure 1.6, respectively) are first estimated by identifying the area where the bilateral solution is violated and then the solution is refined by solving an integral equation obtained by substituting (2.9) and (2.10) into (2.12) over the candidate slip zone until (2.14) is satisfied. For point A on Figure 2.3, where the normal load and the subsequent shear force are sufficient to cause sliding, Figure 2.4 shows how the normal and tangential tractions at the layer/substrate interface are modified by the presence of slip. In this case the external contact load is suffering incipient sliding, but is *stationary*, and the specific parameters prevalent are: $B = 1$, $\nu = 0.3$, $\mu = 0.7$, $\lambda = 1$, $f = 0.2$. Discontinuous derivatives appear at both edges of the interfacial slip region when slip is permitted, although the tractions are required to be smooth and continuous. This is a distinctive characteristic of the stationary loading case as the asymptotic behaviour of stress and displacement fields ($d = 0$ - transition between stick and slip) is such that discontinuous derivatives in the shear tractions are present at both sides of the slip area (Comninou et al., 1980). The shaded area shows the extent of the slip region and the red line shows the tangential relative slip displacement across the interface. Results of many calculations such as the one just described, and with the same B, ν, μ, f values, but variable clamping pressure, λ, are summarised in Figure 2.5, which shows the extent of slip for different values of λ. The results obtained using the semi-analytical technique described have been compared to the solution obtained using the commercial FE software ABAQUS (Abaqus, 2007) to model the same contact problem. A very accurate match between the two solutions in terms of interface stresses is achieved, Figure 2.4, confirming the validity of the proposed approach.

The loading scenario and the kinematic constraints considered in the example problem are such that only one slip zone appears at the layer/substrate interface. Different loading regimes and geometries will lead to the formation of multiple slip regions and this can also be addressed within the current formulation (Comninou and Barber, 1983a). However, extra dependent variables will be introduced and this makes the rate of convergence of the solution dependent on the initial guess of location and extension of the slip and opening regimes, which are difficult to locate rigorously. A

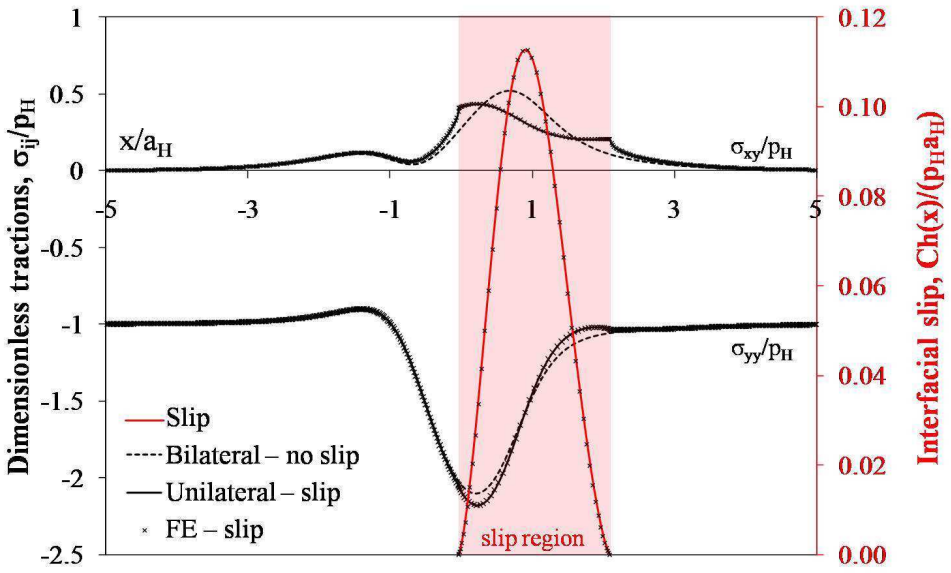


Figure 2.4. Normal, tangential tractions and tangential shift for B=1, ν=0.3, μ=0.7, λ=1 and f=0.2 - stationary case - full sliding of external contact over layer surface.

quadratic programming formulation which enables to overcome this problem by employing optimisation techniques is presented in Chapter 5 (Reina et al., 2009).

2.4.3 The use of the unilateral solution to study interfacial slip: Moving loading

A steady state problem in which the homogeneous roller is sliding over the tyred roller is now considered. The formulation is, of course, quasi-static, and the frame of reference is fixed in the contact patch, so that the layered material passes through the field of view, Figure1.6(b), at a constant velocity, c. The main difference between the stationary solution and the moving load solution is that the latter allows introducing the possibility of frictional creep. The net cumulative tangential shift, d, between the layer and the substrate induced by the relative displacement of the indenting bodies (see Fig. 1.6(b) – case (iii)) can be computed in closed form using the formulation presented above. Figure 2.6 displays results for a contact configuration exhibiting the same properties as that in Figure 2.4 (the same values of B, ν, μ, λ, f) but with the conservation of displacement side condition now removed, as explained earlier, and replaced with a requirement that the material entering the

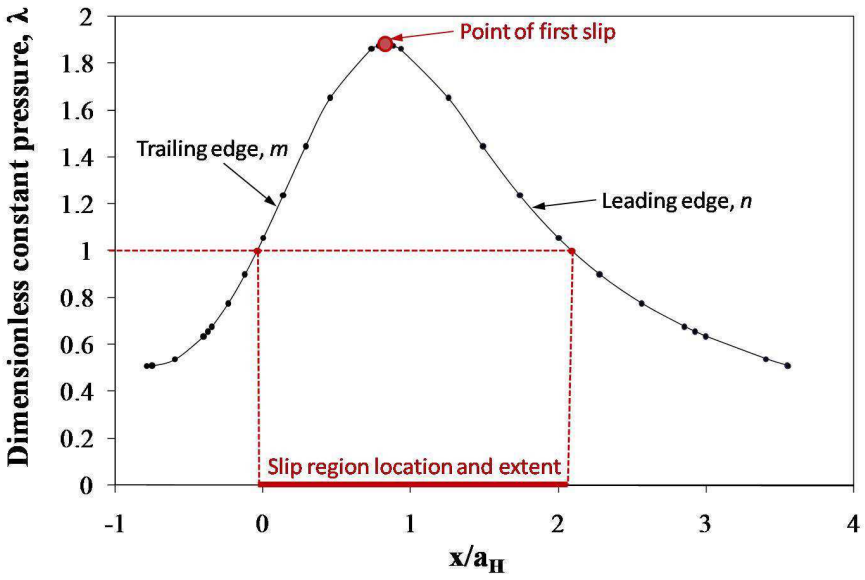


Figure 2.5. Slip region location and extent for B=1, ν=0.3, μ=0.7, f=0.2 and different values of the dimensionless constant pressure, λ=1 - stationary case (*traslational velocity=0*) - full sliding of external contact over layer surface.

contact neighbourhood is in the same state of stress as the material leaving it. As anticipated earlier, it is evident how the derivatives of the shear tractions are now continuous at the trailing edge of the slip area. The tractions are qualitatively similar (though by no means the same), and the accumulated slip displacement built up during the slip process is highlighted. Figure 2.7 illustrates how both location and extent of the slip area vary as a function of the loading parameter, λ, and provides the values of net slip displacement corresponding to a number of loading scenarios. The extent of the slip area is identified (by analogy with the plot displayed in Figure 2.5 for the stationary case) by the two curves on the plot which represent the "moving crack" trailing and leading edge location respectively. It should be noted that, as already observed by (Chang et al., 1983), the value of d is negative in the moving frame of reference as the layer creeps backwards with respect to the contact.

The results obtained by the authors to reproduce the steady state solution in the presence of moving loads were also checked using the FE package ABAQUS (Abaqus, 2007) to model the problem in Figure 1.6(a). After initial application of the normal load to the top cylinder the driving torque was

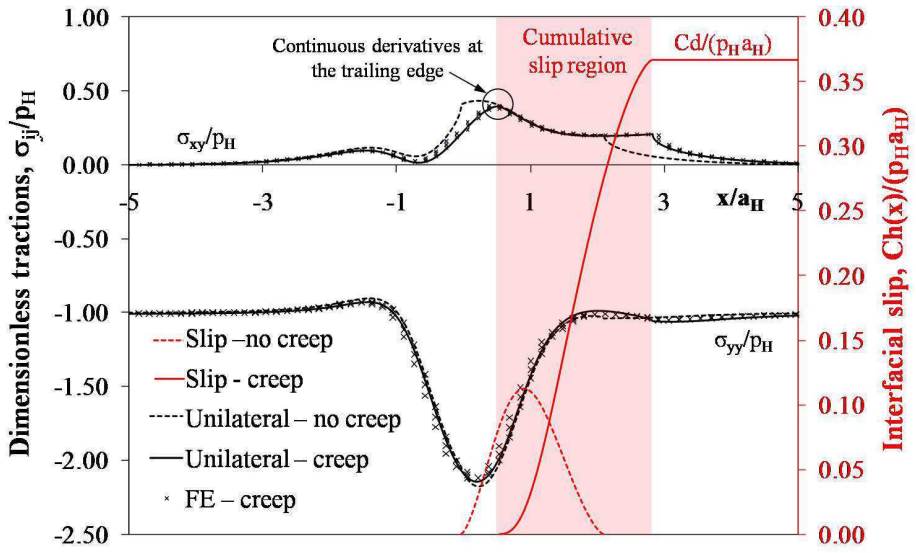


Figure 2.6. Tangential tractions, normal tractions and dimensionless net tangential shift per cycle for B=1, ν=0.3, μ=0.7, λ=1 and f=0.2 - steady state solution for the moving load case - full sliding of external contact over layer surface.

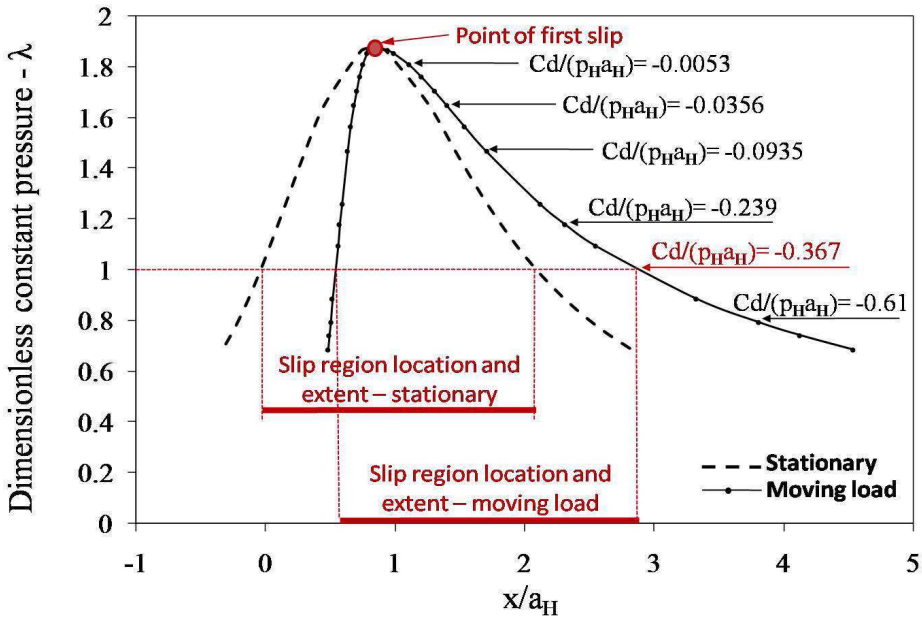


Figure 2.7. Slip region location and extent for B=1, ν=0.3, μ=0.7, λ=1 and f=0.2 and different values of λ - steady state solution for the moving load case - full sliding of external contact over layer surface. The accumulated net displacement per cycle, $Cd/(a_H p_H)$, is also reported for some example cases in full sliding condition.

applied and then roller 2 is rotated at a constant speed, c, to reproduce the moving load scenario modelled above. The results are analysed at different times and locations along the layer/substrate interface and Figure 2.8 shows the outputs in terms of normal tractions at the time-step when roller one first reaches position P2 in Figure 1.6(a) during the relative rotation of the two rollers. Here two horizontal axes are used to distinguish between the normalised coordinates: (i) x_d/a_H, represents the location of a point belonging to the layer/substrate interface in the fixed frame of reference (and whose origin is along the line of initial application of the normal load - see inset to Figure 2.8) and (ii) x/a_H, is a moving abscissa which follows the centre of the contact during the relative rotation of the two rollers, and with respect to which the steady-state solution is computed (i.e. the same used in Figure 2.6).

In the region immediately beneath the area where the normal load is initially applied (around P1 in Figure1.6(a)), locked-in residual stresses are generated during the first loading cycle. This is because, before the substrate is moved (and therefore the results obtained for the stationary loading configuration apply), the layer shifts locally in the direction corresponding to the application of the tangential force caused by the transmission of the torque, as shown in Figure 2.4, and the interfacial shear stresses consequently generated have opposite sign with respect to the local tangential velocity of the top roller at the layer surface. As soon as the bottom roller starts moving, the layer tends to rotate and creep around the substrate reversing the shear traction direction, as predicted by our semi-analytical model. The abrupt inversion of the direction of the tangential stresses associated with slip leaves some locked-in residual stresses which will be modified, and ultimately removed, during subsequent passages of the load over this region.

The second location of interest is the region around point P2 in Figure1.6(a). This area was chosen to be at a distance from P1 (approximately four contact lengths) such that the residual shear tractions developed at the beginning of the rotation of roller 2 would not affect the stress and strain field developed in its neighborhoods and therefore direct comparisons can be made with the semi-

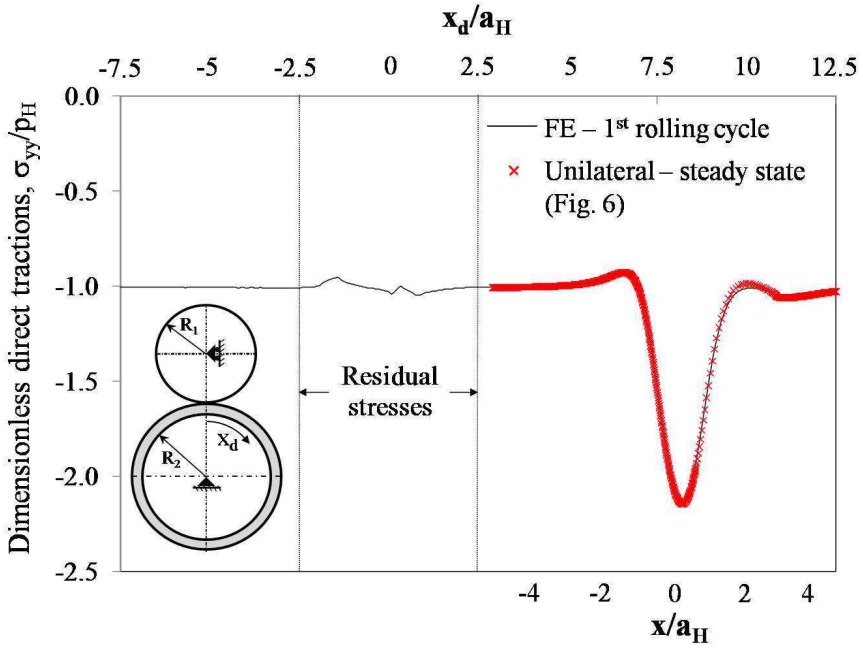


Figure 2.8. Snapshot of the transient FE solution: normal tractions at the layer/substrate interface for B=1, ν=0.3, μ=0.7, λ=1 and f=0.2 - moving load case - full sliding of external contact over layer surface. The comparison with the steady state solution displayed in Fig. 2.6 is also presented.

analytical solution obtained for the moving load scenario. Such a comparison is shown in Figure 2.8 for the normal component of stress and it confirms the accuracy of the model in reproducing the stress field accurately already after small rotations.

Finally, Table 2.1 shows the evolution of the net displacement per cycle obtained using the FE code and the steady-state value calculated using the proposed formulation. The relatively small discrepancy between the two sets of results after the first loading cycle is caused by the locked-in residual stresses generated at the beginning of the moving loading scenario, as simulated using FE. They affect the total cyclic net displacement as well as the local state of stress in the region surrounding P1. In fact, the steady state solution cannot be reached instantaneously and this results in the discrepancy between the solution obtained using the formulation for the unilateral problem proposed by the author, which represents the steady state solution, and the values obtained from the FE model. The table also shows the value of the net displacement after the second loading cycle. The discrepancy between the numerical and the semi-analytical results decreases during the second

loading cycle (to less than 5%) after that the second passage of the load over the region around P1 has modified and almost completely removed the residual stress field generated during the first loading cycle. A steady state condition should be, practically, achieved after three or four passages of the load, although this has not been fully verified due to the fact that the finite element numerical solution obtained using ABAQUS was very demanding in terms of computational resources (over one week on a 4 CPU cluster was required to obtain an accurate solution for the two loading cycles for the moving loading). This emphasises the usefulness of the semi-analytical method developed: its efficiency (only a few minutes of CPU time required to study the steady-state regime under moving loading) and its accuracy in predicting immediately the creep rate of the layered system under investigation renders the tool very powerful.

$Cd/p_H a_H$	FE	Unilateral solution
First cycle	-0.39	...
Second cycle	-0.384	...
...	...	...
Steady state	...	-0.367

Table 2.1: Evolution of the net displacement per cycle and comparison with the steady state semi–analytical solution obtained using the formulation for the unilateral problem - full sliding of external contact over layer surface.

2.5 Further Properties

2.5.1 Development of residual shear stresses and time history dependence

The results shown so far refer to combinations of geometries, loading conditions and friction coefficient that give an operating point (*e.g.* point A in Figure 2.3) in the area above the threshold for case (a) in Figure 2.3, which corresponds to loading scenarios where the layer sticks everywhere during normal indentation. If this condition is not fulfilled and the operating condition (*e.g.* point B in Figure 2.3) is such that interfacial slip occurs during the indentation process, the stress field is affected by the nucleation of slip areas during the normal loading phase. This implies that the effect of the bilateral stress field modifications occurring need to be considered in the subsequent

application of the tangential force. The error arising by neglecting the formation of slip areas during normal loading is non trivial, as shown in Figure 2.9, where the solutions for the configuration identified by the dimensionless parameters $B = 1$ and $\lambda = 1$ and by interfacial friction coefficient $f = 0.15$ (point B in Figure 2.3) are plotted for both the case when the layer is considered adhered to the substrate before the application of the tangential force and for the case when the development of slip zones is tracked during and after indentation.

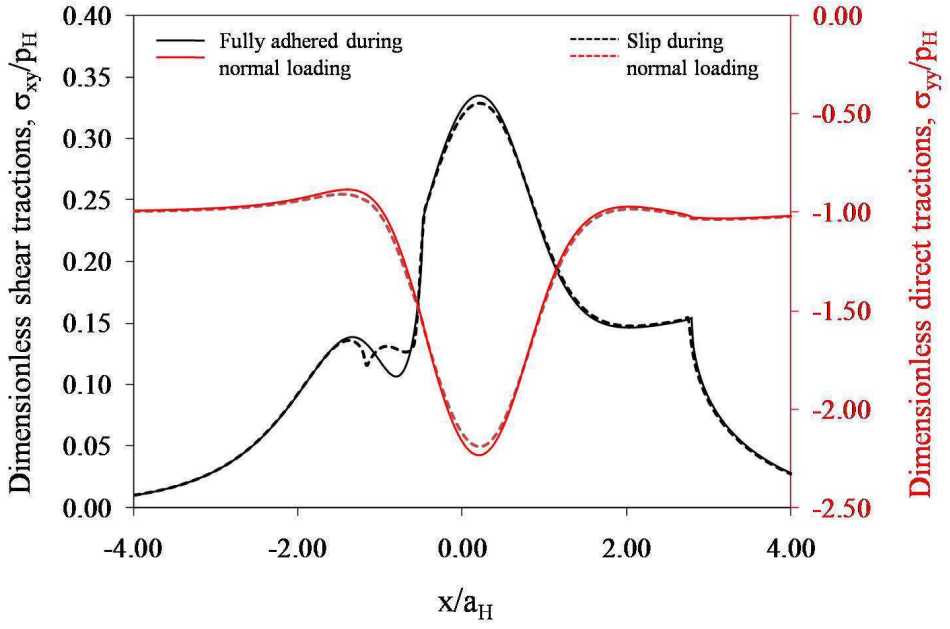


Figure 2.9. Normal and tangential tractions for B=1, ν=0.3, μ=0.7, λ=1 and f=0.15 - stationary case - full sliding of external contact over layer surface.

This example shows the importance of the "system memory" contained in the locked-in displacements stored in the stick regions, already discussed in detail by Barber and co-workers (*e.g.* Reina et al., 2010b; Barber et al., 2008; and Klarbring et al., 2007). The overall behavior of the system is affected not only when loads are applied monotonically (e.g. Fig. 2.9), but also when the system is subjected to cyclic loading, where the steady state solution of the problem (e.g. frictional shakedown or any other cyclic frictional response) induced by the loading history, also depends heavily

on the locked-in residual shear stresses developed during the first few loading cycles. This topic will be treated separately in Chapter 6.

2.6 Summary

A general systematic approach based on existing techniques, but never before combined, has been proposed to explore the behavior of elastic layered systems. A simplified contact problem was presented and solved in three different stages: (a) "first slip point" thresholds - the region of validity of the bilateral solution to the problem was found and the condition for incipient slip determined; (b) monotonic application of stationary forces - the implementation of the distributed dislocation technique for modelling slip and separation was demonstrated as being suitable to model the application of stationary loads; and (c) monotonic application of moving loads was studied. Results were discussed for a series of example problems focussing on systems where only one slip region nucleated at the layer/substrate interface and both stationary and moving loading conditions were successfully modelled. Finally, the importance of the time history on the solution of the problem was emphasised.

Chapter 3

Incipient slip conditions in rolling contact of tyred wheels

3.1 Introduction

In this chapter, the contact problem of a driving tyred wheel, pressed and rolling over an elastically similar half-plane, is considered. Although applicable to a wide range of shrink-fitted assemblies, the simplified model is solved to study the practical case of an elastically similar steel tyre mounted on a locomotive steel wheel subjected to tractive rolling (Reina et al., 2010a). A distinction between the *onset* of interfacial slip which is necessary to avoid all interfacial degradation, and the less restrictive requirement that the evolution of microslip inhibits creep is drawn here. It would seem possible, for the case of a tyre fitted to an elastically similar wheel, to abstract the conditions needed for the avoidance of all interfacial slip. It might be added that, although circumferential creep is not necessarily disastrous in its consequences, the presence of any slip region introduces the possibility of a more complex slip regime developing, including axial creep of the tyre, and which would have very serious consequences, in addition to more general degradation. In Chapter 2 the general case of a tyre mounted on a rigid disc and rolling rolling over an elastically dissimilar countersurface was studied. In such circumstances, the slip regime between the tyre and the named counterface would, necessarily, be rather complicated (Reina et al., 2010b; Hills et al., 1993; Barber, 2002; Carter, 1926; Munisamy et al., 1991; Nowell and Hills, 1988a; and Nowell et al. 1988c), and it is

felt that, in practical applications of the problem to the locomotive driving wheel, the countersurface will itself invariably be steel, and this renders the problem capable of solution in closed form. In this chapter, the behaviour of the system at the tyre/substrate interface is studied using closed form solutions to calculate the state of stress within the tyre. Conditions leading to incipient slip and/or plasticity are identified and mapped for different loads and geometries.

3.2 Formulation

Figure 3.1(a) depicts the problem to be analysed. A disk of radius R_1 indents a second disc, of radius R_2, carrying a tyre of thickness b. The case corresponding to $R_1 \to \infty$ represents the idealisation of the railway locomotive wheels scenario. Figure 3.1(b) shows the equivalent problem of a disc of outer radius R^* pressed into contact with an elastically similar half-plane by a normal line load, N. It should be noted that the layer can be transferred to the flat substrate within a half-plane formulation without loss of accuracy.

The application of the normal load gives rise to a classical Hertzian contact of half-width $a = a_H$, which is given by (Barber, 2002):

$$a_H^2 = \frac{8NR^*\left(1-\nu^2\right)}{\pi E}, \tag{3.1}$$

where E is Young's modulus, ν Poisson's ratio, and N is the load per unit width of the disc, whilst the contact pressure distribution, $p(x)$, is given by:

$$\frac{p\left(x\right)}{p_H} = \sqrt{1-\left(\frac{x}{a_H}\right)^2}, \qquad \text{where} \qquad p_H = \sqrt{\frac{NE}{2\pi R^*\left(1-\nu^2\right)}}. \tag{3.2}$$

Let us suppose that the coefficient of friction between the tyre and the disc (see Fig. 3.1) is μ, that the tractive force developed by the locomotive at this wheel is Q, and that the disk is rolling under steady state conditions. In this case a partial slip regime, first analysed by Carter (Carter, 1926; and Munisamy et al., 1991) exists. A stick zone of length $2c_{stick}$ is attached to the leading edge, where:

$$\frac{c_{stick}}{a_H} = 1 - 2\sqrt{1-\frac{Q}{\mu N}}, \tag{3.3}$$

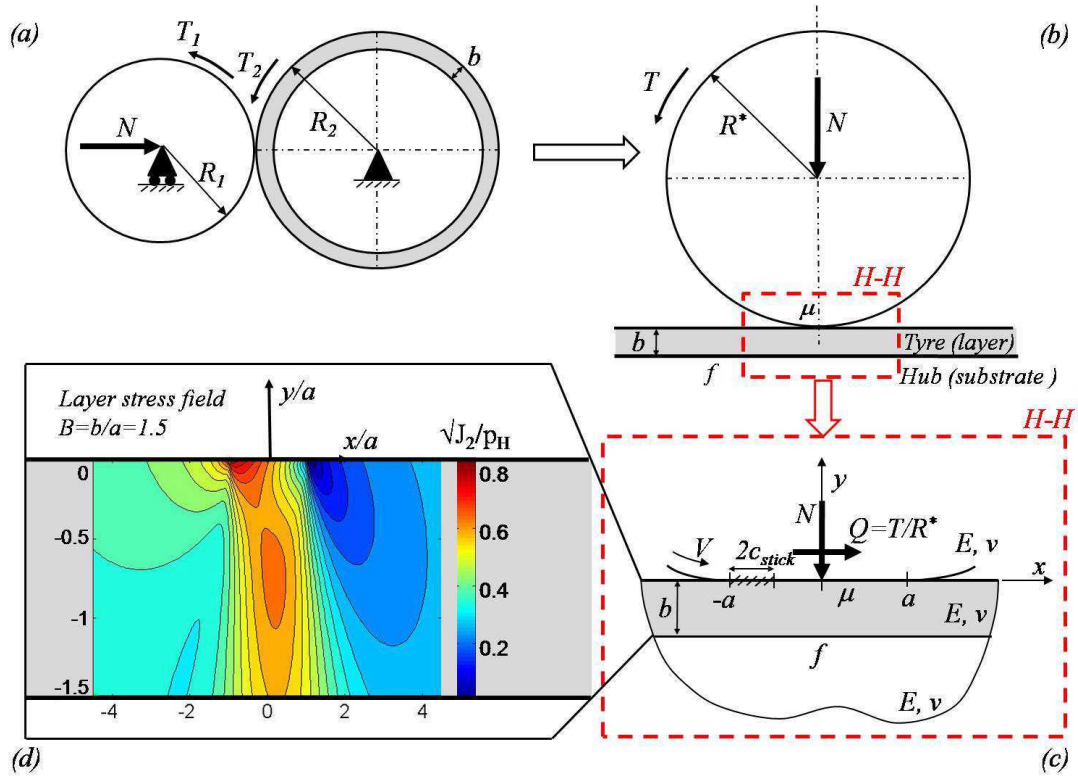


Figure 3.1. Schematic of the problem: (a) Layered cylinder indenting a homogeneous cylinder; (b) Equivalent problem – cylinder rolling on a layered substrate; (c) Zoom-in showing the contact area and the salient parameters; (d) Example plot of the von Mises stresses induced by the application of the external loads. Note that for $R_1 \to \infty$ the schematic in (a) represents a typical wheel/rail contact.

and the shearing traction, $q(x)$, is given by (Barber, 2002):

$$\frac{q(x)}{p_H} = f\left[\sqrt{1-\left(\frac{x}{a_H}\right)^2} - H\left(x-c_{stick}\right)\sqrt{\left(1-\frac{x}{a_H}\right)\left(\frac{x}{a_H}-\frac{c_{stick}}{a_H}\right)}\right], \tag{3.4}$$

where $H(\cdot)$ is the Heaviside's step function. The surface tractions are fully specified, and the internal state of stress induced may now be found using the standard results for the state of stress associated with a sliding Hertzian contact (Hills et al., 1993), and using superposition to make the adjustment needed for the Carter shear traction distribution.

In addition to the contact loading, there will be a radial direct stress (which is locally in the y direction) of magnitude p_0, generated by the shrink fit process. Thus, the total state of stress along the interface between the tyre and the substrate may be found by standard superposition as the sum of the stress induced by contact loading and the (constant) direct traction induced by shrink-fit. The

requirement that there be no interfacial slip is, therefore, that:

$$\frac{|\sigma_{xy}(x,b)|}{-(\sigma_{yy}(x,b)+p_0)} < f \qquad \forall x, \tag{3.5}$$

where f is the coefficient of friction between the tyre and the substrate, and σ_{xy} and σ_{yy} denote the shear and normal stress components, respectively.

The stick-slip regime associated with a Carter-type partial slip rolling problem is shown within the dotted line box in Figure 3.1(c), and, finally, a schematic sample contour plot of Von Mises' parameter is shown in Figure 3.1(d), embedded in the layer. Plots of this kind will be used to infer the elastic limit. Further, due to the fact that the contact problem is solved using linear elasticity, a practical limitation is that the state of stress present everywhere must be sufficiently mild for it to remain within the yield condition. Here, Von Mises yield criterion will be used to assess the likelihood of plasticity to occur, and the material is assumed to have a yield strength in pure shear k. There are three key physical locations where the elastic limit could be reached and which must be monitored: a subsurface general point and the trailing edge of the contact at the surface, as is well known from standard homogeneous Hertz results, and, in addition, here, a point at the tyre/wheel interface. The treatment of local plastic deformations, which may occur under certain loading conditions, is outside the scope of the present contribution.

3.3 Results

The first result, which quoted without illustration, is that, for all practical values of μ, f, $B = b/a$ ($a = a_H$), the severest interfacial tractions invariably arise when $Q/\mu N \to 1$, i.e. when the wheel is in an incipient sliding state. As this is a circumstance which can always arise in practice, the wheel is assumed, from now on, to be sliding along the rail, as this removes one independent variable from the problem. This means that the conditions which guarantee no interfacial slip between tyre and substrate can be mapped out by varying the dimensionless stress parameter, $\lambda = p_0/p_H$, the dimensionless length, B, which carries informations about load, geometry and material properties,

and the coefficient of friction at the interface between the disc and the tyre, μ.

The example corresponding to values of the parameters $\lambda = 0.05$ (a moderately high value of shrink fit pressure) and $B = 1.5$ (i.e. quite a thin tyre) is first used as a vehicle to illustrate the features of the solution to the problem under investigation. Results for this case are shown in Figure 3.2.

The plot includes two lines: the solid one relates to tendency for interfacial slip, and should be read in conjunction with the left hand axis, while the broken line relates to the strength condition, and should be read in conjunction with the right hand axis. To be more specific, the solid line represents the minimum value of f needed to avoid slip everywhere at the tyre/wheel interface, while the broken line provides the maximum dimensionless value of the deviatoric invariant of the stress tensor, $\sqrt{J_2}/p_H$, within the layer. By comparing this value and the dimensionless value of the yield stress in pure shear, k/p_H, one can assess if the elastic limit is locally exceeded. Also included in the figure are a family of five inset diagrams, which represent the behaviour of the contact. The physical region of the cross section they represent is the depth of the layer ($0 \leq y/a \leq 1.5$), and a short distance spanning the contact ($-4 \leq x/a \leq 4$). The contours themselves represent normalised values of the deviatoric invariant, and the key to this is provided within the figure, together with 'spots' which indicate where the severest state of stress arises. A second 'spot ' (or, in the case of inset 1 only, two spots) is shown at the interface between the tyre and the substrate at the point where the maximum ratio of the shear to direct traction occurs, i.e. where slip is most likely to start. Consider, first, the case of frictionless contact, where either the wheel-rail interface is perfectly lubricated or, more likely the vehicle is rolling without a tractive force being applied, Case 1. The severest state of stress is, here, on the centreline of contact ($x/a = 0$) and at a depth of about ($y/a = 0.9$), whilst the antisymmetric shear tractions arising along the wheel-rim interface imply two symmetrically disposed severe points (at $y/a \sim \pm 2.3$). If the wheel-rail coefficient of friction (corresponding to μ in Figure 3.1), is increased, the magnitude of the shear/direct traction ratio arising along the interface steadily rises, whilst the severest state of stress remains substantially

unchanged, until μ reaches a value of about 0.305, Case 2. At that point, a second maximum in the magnitude of the deviatoric stress, which has been steadily developing at the surface for increasing coefficient of frictions corresponding to larger shear tractions, starts to dominate. This is located at the trailing edge of the contact, and for all higher coefficients of friction (Cases 2-5) it is this which is the controlling point; the magnitude of the stress state rises steadily with coefficient of friction. It will also be noted that the location of the maximum tyre-wheel traction ratio has also moved slightly, migrating gradually forward well beyond the leading edge of the wheel contact point (to $x/a \sim 2.63$, Case 2) and further to (to $x/a \sim 3.05$, Case 3), by which time the value of μ has increased to about 0.8. A further increase in μ then causes a second maximum in the interfacial traction ratio, located at $x/a \sim -3.02$ to dominate, and this is the location which continues to control the problem for subsequent increases in μ, whilst the traction ratio rises very steeply. This, then summarises the response of the contact, and gives a general trend. Overall, it may be noted that: (a) the severity of the state of stress is rather greater than in the residual stress free cases (Hills et al., 1993) and that, for low coefficients of wheel-rail friction, it is substantially independent of the coefficient of friction there, and (b) with a tyre this thin it is, for practical purposes, impossible to inhibit the development of a slip region.

A reduction in the value of the interfacial pressure to $\lambda = 0.005$, makes the problems even worse, as shown in Fig. 3.3.

This includes lines giving the behaviour of the contact for a number of tyre thicknesses ($0.5 \leq B \leq 30$), and, for the comparable case ($B = 1.5$) to that displayed in detail in Figure 3.2 it may be noted that: (a) an even higher shear/direct traction ratio along the tyre/wheel interface arises and (b) if $\mu \gtrsim 0.55$ the interfacial direct traction becomes vanishingly light, and separation arises. On the other hand, the general trend is that, as B is increased (the tyre is made thicker) the coefficient of friction needed to maintain full adhesion becomes lower, whilst the risk of separation is, of course reduced. Nevertheless, this interference fit contact pressure is clearly too small in magnitude. In

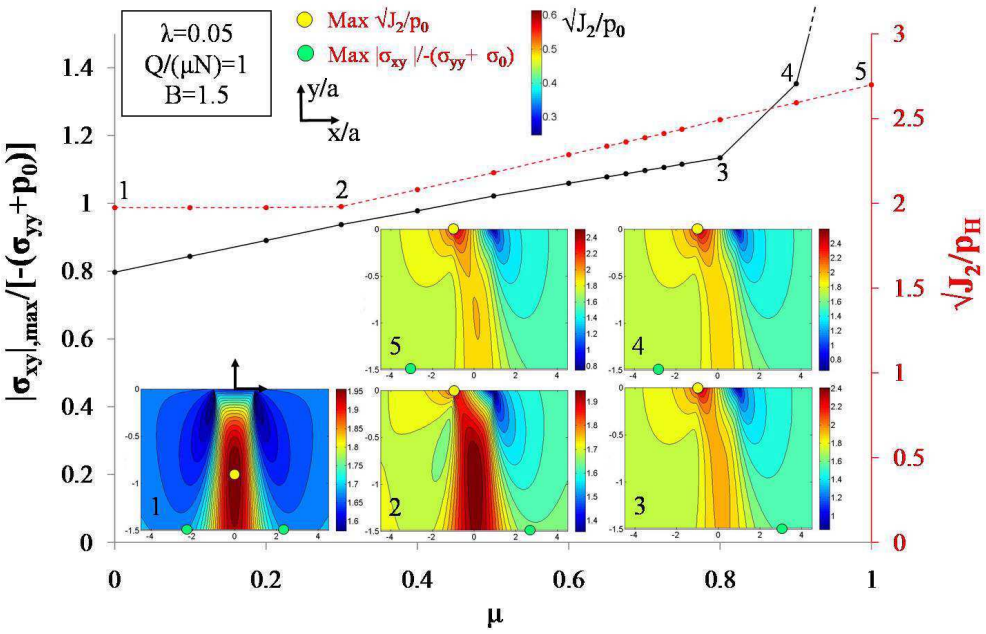


Figure 3.2. Minimum interfacial friction coefficient f to guarantee adhesion for B = 1.5, ν = 0.3, λ = 0.05 (dimensionless constant pressure) and various surface friction coefficients, μ.

Figure 3.4, therefore, reverting to a dimensionless interference contact pressure of $\lambda = 0.01$, the influence of tyre thickness, B, is explored again.

Separation now occurs only at higher values of μ, and, of course, for the thinner tyres. Very high interfacial residual stresses incur the risk of yielding, and a sensible maximum for λ might be 0.05 (see Figure 3.5). This makes a tremendous difference in the requirement for the avoidance of tyre/wheel localised slip and fretting. The impediment of slip everywhere within the tyre/wheel contact interface is clearly a real possibility. At the same time, the likelihood of there being plastic deformation is increased.

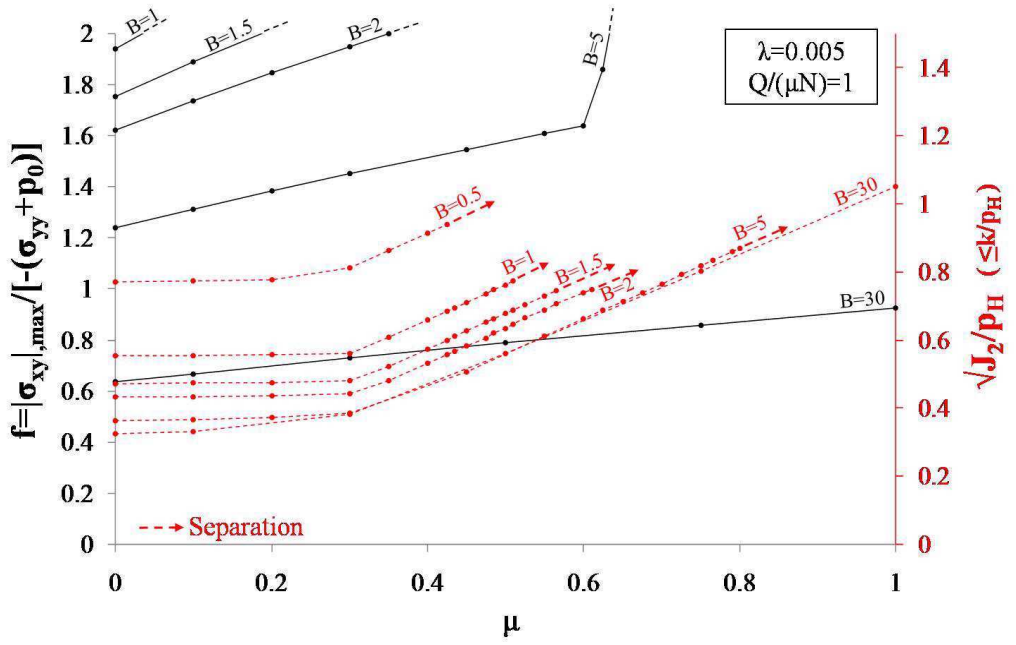


Figure 3.3. Minimum interfacial friction coefficient f to guarantee adhesion for $\nu = 0.3$, $\lambda = 0.005$ and various surface friction coefficients, μ, and layer thicknesses, B.

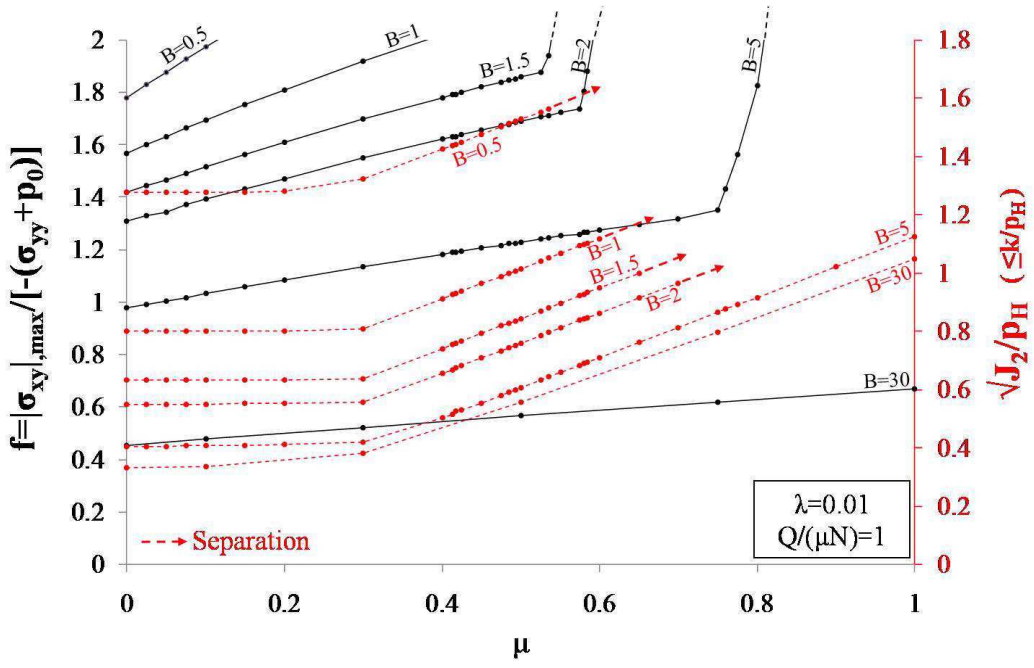


Figure 3.4. Minimum interfacial friction coefficient f to guarantee adhesion for $\nu = 0.3$, $\lambda = 0.01$ and various surface friction coefficients, μ, and layer thicknesses, B.

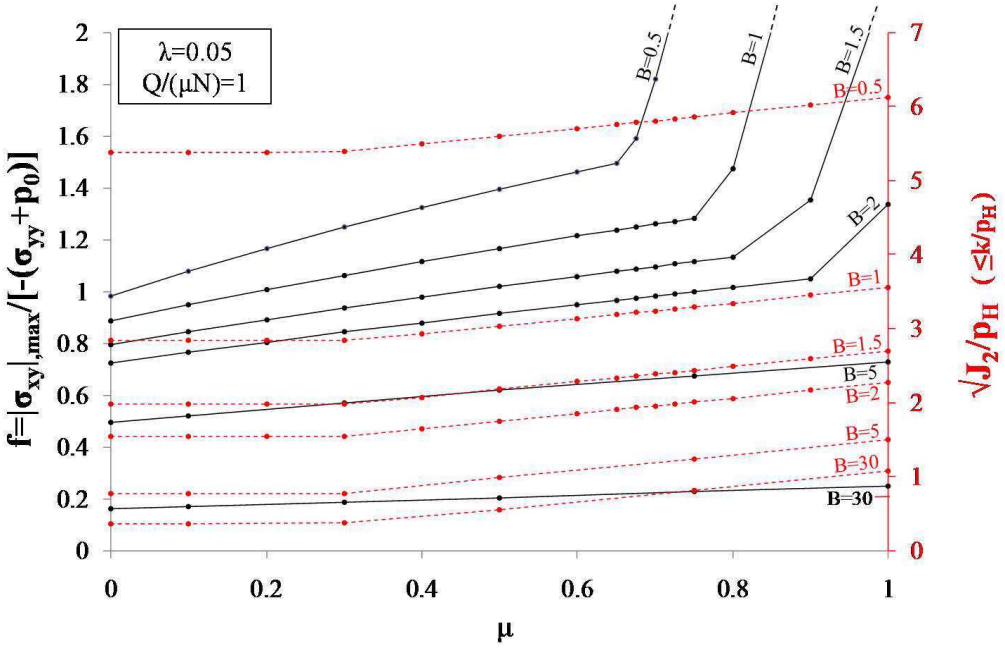


Figure 3.5. Minimum interfacial friction coefficient f to guarantee adhesion for $\nu = 0.3$, $\lambda = 0.05$ and various surface friction coefficients, μ, and layer thicknesses, B.

3.4 Summary

In this chapter, a closed form solution has been derived to investigate the onset of interfacial slip and the strength of the contact in tyred wheels rolling over an elastically similar body. The problem has direct implication to the design of locomotive wheels. The principal conclusion is that, if it is necessary to use a replaceable tyre, its thickness should be as great as possible in relation to the contact size in order to avoid the possibility of fretting. Also, the larger the shrink-fit contact pressure achievable the better, but the other side to this coin is that the strength of the contact will be severely reduced as plasticity is more likely to take place.

Chapter 4

The case of an elastic layer sliding over a rigid substrate

4.1 Introduction

In this chapter the extreme case of a tyre skidding around the wheel is discussed (Reina et al., 2010c). In Chapter 1 this scenario has been explained as being experienced in the tyre-rim assembly for severely loaded earth-moving machinery. Using the simplified two-dimensional problem described in the previous chapters as a vehicle, in this chapter the integral transform solution of the state of stress induced by external loading in a layer resting on but *sliding* over a rigid substrate is studied. The interface between the layer and the substrate is considered to be frictional. An overview of the formulation available in the literature to tackle similar problems has already been presented in Chapter 1 and, therefore, here attention will be given to the general formulation of the problem, which is then solved semi-analytically. The demonstration of the suitability of the proposed approach to solve this class of problems is then followed by the application of the newly developed technique to our particular application.

4.2 Formulation for unit tractions

Consider the contact problem in Figure 1.8. The problem is clearly best considered in a frame of reference attached to the contact itself, Figure 4.1. Thus, in this axis set the contacting component and the layer are both spatially fixed, and the layer moves steadily through the figure, with

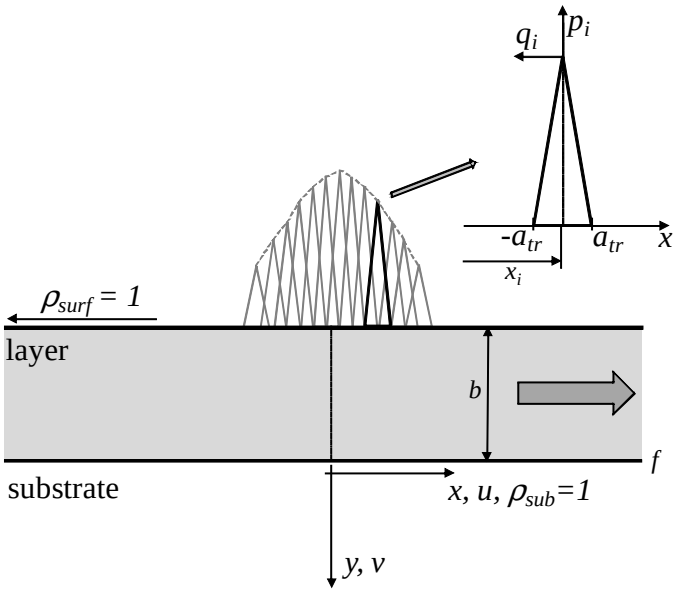


Figure 4.1. Reference system and triangular traction elements applied to discretise generic traction distributions at the layer surface; sign conventions are shown (positive directions).

frictional conditions maintained along the layer/substrate interface. Figure 4.1. also illustrates the discretisation scheme adopted to reproduce the loading condition to which the layer is subject. The procedure, as explained in Section 1.2.3, consists of employing overlapping trangles of traction and their influence functions to reproduce tractions and displacements induced by an external contacting body (Bentall and Johnson, 1968).

The first step in the solution is to establish a general representation of the state of stress within the layer, Figure 4.1, which is of thickness b, and extends indefinitely in the $\pm x$ directions. An Airy function, χ, is employed which is connected to the stress components by the following expressions

$$\sigma_{xx}(x,y) = \frac{\partial^2 \chi(x,y)}{\partial y^2}, \sigma_{yy}(x,y) = \frac{\partial^2 \chi(x,y)}{\partial x^2}, \sigma_{xy}(x,y) = -\frac{\partial^2 \chi(x,y)}{\partial x \partial y} \tag{4.1}$$

and automatically satisfies the equilibrium requirements. The application of Hooke's law yields the strain components and, if compatibility is to be satisfied, the function χ must be a solution of the biharmonic equation

$$\nabla_1^4 \chi = 0, \tag{4.2}$$

where $\nabla_1^2 \equiv \partial^2/\partial x^2 + \partial^2/\partial y^2$. An integral representation of the stress function is expected to be emplyed in order to satisfy all the boundary conditions, and hence write

$$\Gamma(y,\phi) = \int_{-\infty}^{+\infty} \chi(x,y) e^{i\phi y} dx. \tag{4.3}$$

Thus, if χ is to be a solution of the biharmonic equation then Γ must satisfy the requirement

$$\left(\frac{d^2}{dy^2} - \phi^2\right)^2 \Gamma(y,\phi) = 0, \tag{4.4}$$

so that the general solution may be written as follows

$$\Gamma(y,\phi) = (A_\Gamma + B_\Gamma y)\, e^{-|\phi| y} + (C_\Gamma + D_\Gamma y)\, e^{+|\phi| y}. \tag{4.5}$$

The four constants, A_Γ, B_Γ, C_Γ and D_Γ, are general functions of ϕ and are determined from the boundary conditions imposed on the problem under investigation. To do this Fourier's inversion theorem (Sneddon, 1951) must be applied. The theorem states

$$\chi(x,y) = \frac{1}{2\pi} \int_{-\infty}^{+\infty} \Gamma(y,\phi)\, e^{-i\phi x} d\phi, \tag{4.6}$$

so that the stress components are given by:

$$\sigma_{yy}(x,y) = -\frac{1}{2\pi} \int_{-\infty}^{+\infty} \phi^2 \Gamma(y,\phi)\, e^{-i\phi x} d\phi \tag{4.7}$$

$$\sigma_{xx}(x,y) = \frac{1}{2\pi} \int_{-\infty}^{+\infty} \frac{\partial^2 \Gamma(y,\phi)}{\partial y^2} e^{-i\phi x} d\phi \tag{4.8}$$

$$\sigma_{xy}(x,y) = \frac{1}{2\pi} \int_{-\infty}^{+\infty} i\phi \frac{\partial \Gamma(y,\phi)}{\partial y} e^{-i\phi x} d\phi \tag{4.9}$$

whilst the displacements are found by first writing the displacement derivatives in plane strain, for example:

$$\frac{E}{1+\nu} \frac{\partial u(x,y)}{\partial x} = \sigma_{xx}(x,y) - \nu\left(\sigma_{xx}(x,y) + \sigma_{yy}(x,y)\right). \tag{4.10}$$

Hence, after multiplying by $e^{i\phi y}$, integrating over y and applying Fourier's inversion theorem (Sneddon, 1951), we obtain:

$$u(x,y) = \frac{1+\nu}{2\pi E}\int_{-\infty}^{+\infty}\left[\frac{\partial^2\Gamma(y,\phi)}{\partial y^2}(1-\nu)+\nu\phi^2\Gamma(y,\phi)\right]ie^{-i\phi x}\frac{d\phi}{\phi}, \tag{4.11}$$

and, in a similar fashion,

$$v(x,y) = \frac{1+\nu}{2\pi E}\int_{-\infty}^{+\infty}\left(\frac{\partial^3\Gamma(y,\phi)}{\partial y^3}(1-\nu)+(\nu-2)\phi^2\frac{\partial\Gamma(y,\phi)}{\partial y}\right)e^{i\phi x}\frac{d\phi}{\phi^2}. \tag{4.12}$$

4.2.1 Imposition of the boundary conditions

Conditions along both surfaces of the layer need to be imposed, i.e. along the interface with the substrate and along the upper surface. Along the interface, assuming that the substrate is rigid, we may write:

$$y=0,\forall x\begin{cases} v(x,0)=0 \\ \sigma_{xy}(x,0)=\rho_{sub}f\sigma_{yy}(x,0)\end{cases} \tag{4.13}$$

where f is the coefficient of friction between the two surfaces, v is the surface normal displacement and ρ_{sub} (Fig. 4.1) assumes the values ±1 depending on the sign of the relative velocity between layer and substrate. Throughout this model a Coulomb-Amonton's friction law is adopted and, hence, the coefficient of friction is independent of the slip-velocity. The value of ρ_{sub} must be taken such that tangential tractions oppose relative slip velocity. Start by multiplying boundary conditions (4.13) by $e^{i\phi y}$ to obtain, on integrating over y,

$$y=0,\forall x\begin{cases} \displaystyle\int_{-\infty}^{+\infty} v(x,0)\,e^{i\phi x}dx=0 \\ \displaystyle\int_{-\infty}^{+\infty}\sigma_{xy}(x,0)\,e^{i\phi x}dx=\int_{-\infty}^{+\infty}\rho_{sub}f\sigma_{yy}(x,0)\,e^{i\phi x}dx\end{cases}. \tag{4.14}$$

Thus, by substituting (4.5) into (4.14) and applying Fourier's theorem (Sneddon, 1951), the boundary conditions become

$$y=0,\forall x\begin{cases} \dfrac{1+\nu}{\mu\phi^2}\begin{pmatrix}(1-\nu)(-|\phi|^3A_\Gamma+3B_\Gamma\phi^2+|\phi|^3C_\Gamma+3D_\Gamma\phi^2)+\\ +\phi^2(\nu-2)(-|\phi|A_\Gamma+B_\Gamma+|\phi|C_\Gamma+D_\Gamma)\end{pmatrix}=0 \\ i\phi(-|\phi|A_\Gamma+B_\Gamma+|\phi|C_\Gamma+D_\Gamma)=-\rho f\phi^2(A_\Gamma+C_\Gamma)\end{cases}. \tag{4.15}$$

Attention is now turned to the free surface of the layer, and assume *pro tem* that the surface tractions are given everywhere. First, consider the direct traction, and start by writing

$$y=-b,\forall x\begin{cases}\sigma_{xy}(x,-b)=0\\ \sigma_{yy}(x,-b)=p(x)\end{cases}. \tag{4.16}$$

By multiplying by $e^{i\lambda y}$ we obtain, on integrating over y,

$$y=-b,\forall x\begin{cases}i\phi\left.\dfrac{\partial\Gamma}{\partial y}\right|_{y=-b}=0\\ -\phi^2\Gamma|_{y=-b}=\tilde{p}(\phi)\end{cases}, \tag{4.17}$$

where $\tilde{p}(\phi)$ represents the Fourier transform of the pressure distribution. Finally, by substituting (4.5) into (4.17), the boundary conditions become:

$$y=-b,\forall x\begin{cases}i\phi(-|\phi|A_{\Gamma=p}e^{|\phi|b}+B_{\Gamma=p}(1+|\phi|b)e^{|\phi|b}+\\ +|\phi|C_{\Gamma=p}e^{-|\phi|b}+D_{\Gamma=p}(1-|\phi|b)e^{-|\phi|b})=0\\ (A_{\Gamma=p}-B_{\Gamma=p}b)e^{|\phi|b}+(C_{\Gamma=p}-D_{\Gamma=p}b)e^{-|\phi|b}=-\dfrac{\tilde{p}(\phi)}{\phi^2}\end{cases}. \tag{4.18}$$

The four constants, A_p,B_p,C_p and D_p, needed to evaluate (4.5) for a given general direct traction distribution, can be obtained by solving the system of equations obtained by combining (4.15) and (4.18), giving

$$\begin{bmatrix}-i\phi|\phi|+\rho f\phi^2 & i\phi & i\phi|\phi|+\rho f\phi^2 & i\phi\\ |\phi|^3 & \phi^2(1-2\nu) & -|\phi|^3 & \phi^2(1-2\nu)\\ -|\phi|e^{|\phi|b} & (1+|\phi|b)e^{|\phi|b} & |\phi|e^{-|\phi|b} & (1-|\phi|b)e^{-|\phi|b}\\ e^{|\phi|b} & -be^{|\phi|b} & e^{-|\phi|b} & -be^{-|\phi|b}\end{bmatrix}\begin{Bmatrix}A_p\\ B_p\\ C_p\\ D_p\end{Bmatrix}=\begin{Bmatrix}0\\ 0\\ 0\\ -\dfrac{\tilde{p}(\phi)}{\phi^2}\end{Bmatrix}, \tag{4.19}$$

where the subscript p, added to the four constants, stands for pressure distribution. Similarly, a general surface shearing traction distribution, $q(x)$, acts over the surface, $y=-b$, of the layer, giving:

$$\begin{bmatrix}-i\phi|\phi|+\rho f\phi^2 & i\phi & i\phi|\phi|+\rho f\phi^2 & i\phi\\ |\phi|^3 & \phi^2(1-2\nu) & -|\phi|^3 & \phi^2(1-2\nu)\\ -i\phi|\phi|e^{|\phi|b} & i\phi(1+|\phi|b)e^{|\phi|b} & i\phi|\phi|e^{-|\phi|b} & i\phi(1-|\phi|b)e^{-|\phi|b}\\ e^{|\phi|b} & -be^{|\phi|b} & e^{-|\phi|b} & -be^{-|\phi|b}\end{bmatrix}\begin{Bmatrix}A_q\\ B_q\\ C_q\\ D_q\end{Bmatrix}=\begin{Bmatrix}0\\ 0\\ \tilde{q}(\phi)\\ 0\end{Bmatrix} \tag{4.20}$$

where the subscript q, added to the four constants, stands for shear distribution. The eight constants in Equations (4.19) and (4.20) depend on the functions $\tilde{p}(\phi)$ and $\tilde{q}(\phi)$, which represent the Fourier's transform (Sneddon, 1951) of the direct and shearing traction distributions applied to the layer surface.

4.2.2 Influence Function for a Triangle of Surface Traction

The contact problem on the surface $y = -b$ must, itself, be solved. Usually, the surface tractions are not known, but the normal displacement imposed by the indenter is. In order to find the contact pressure a piecewise-linear representation of the actual traction, Figure 4.1, is employed, which consists of an array of overlapping triangles whose altitude, p_i, is initially unknown. If the influence function has a base width of $2a_{tr}$ we may write:

$$p(x) = \begin{cases} p_i \left(1 - \left|\dfrac{x}{a_{tr}}\right|\right), & \left|\dfrac{x}{a_{tr}}\right| \leq 1 \\ 0, & \left|\dfrac{x}{a_{tr}}\right| > 1 \end{cases} \tag{4.21}$$

so that the Fourier transform of the load function is given by

$$\tilde{p}(\phi) = \int_{-\infty}^{+\infty} p(x)\, e^{-i\phi x} dx \tag{4.22}$$

or, after some algebra:

$$\tilde{p}(\phi) = -\frac{2p_i}{a_{tr}} \left.\frac{\cos(\phi x)}{\phi^2}\right|_0^c = \frac{2p_i}{\phi^2 a_{tr}} \left(1 - \cos(\phi a_{tr})\right) = \frac{4p_i}{\phi^2 a_{tr}} \sin^2\left(\frac{\phi a_{tr}}{2}\right). \tag{4.23}$$

The analysis for an element of shear traction follows the same process, *mutatis mutandis*.

4.2.3 Results

A series of key points must be discussed before applying this formulation to practical cases. First, the formulation has to be validated by using a different numerical method, which in this case is an equivalent FE model, using the commercial programme, ABAQUS. Secondly, overall equilibrium of the system will be examined, because this shows some unexpected properties. In fact, the formulation as described above provides a solution which is not obviously in overall equilibrium, *per se*. It may have been noted that conditions relating to the equilibrium of the system are absent in the formulation of the problem (Hills et al., 1993) and, consequently, remote forces must be added to compensate the tension imbalance associated with the mixed boundary condition (4.13).

Also, it has been noted that a strict proportionality between the shear and direct tractions has been chosen. Under some conditions, for example with the shear traction triangular influence function,

the direct interfacial traction can become tensile locally and, hence, the sign of the shear reversed. Physically, this has no meaning, but when the triangle is used to build up the solution for a distributed contact (and where there may also be a clamping pressure imposed, as in the example to be presented), the net direct traction may subsequently become negative everywhere. Thus, it is a legitimate procedure to use superposition, provided only that the *resultant* direct traction is negative everywhere. This should be borne in mind when the solution for the effect of an individual triangle of surface traction is considered.

A triangle of direct/shear traction was applied to the free surface, over a length $-a_{tr} \leq x \leq a_{tr}$, and $b/a_{tr} = 1$ and the interfacial friction coefficient set to 0.2. Figure 4.2 shows the tractions induced along the interface for a triangle of direct and shear traction.

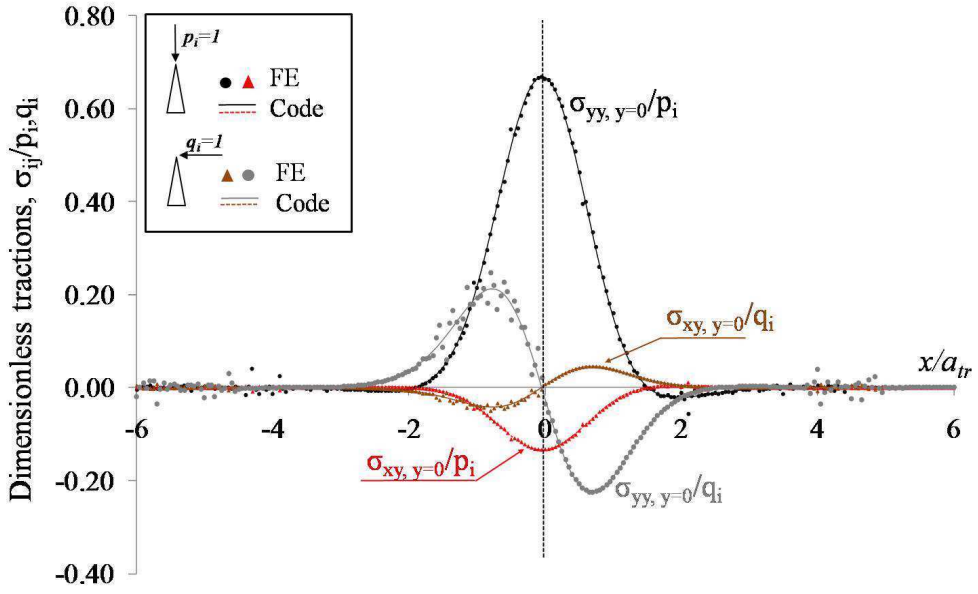


Figure 4.2. Normal and shear tractions induced along the layer-substrate interface by a triangle of direct and shear traction imposed on the free surface, $-1 < x/b < 1$ ($b/a_{tr} = 1$ and $f = 0.2$).

Similarly, Figure 4.3 shows the stress component acting parallel with the interface at two depths - the surface and immediately above the interface.

In each case the solution obtained by using the Fourier representation agrees very well with the

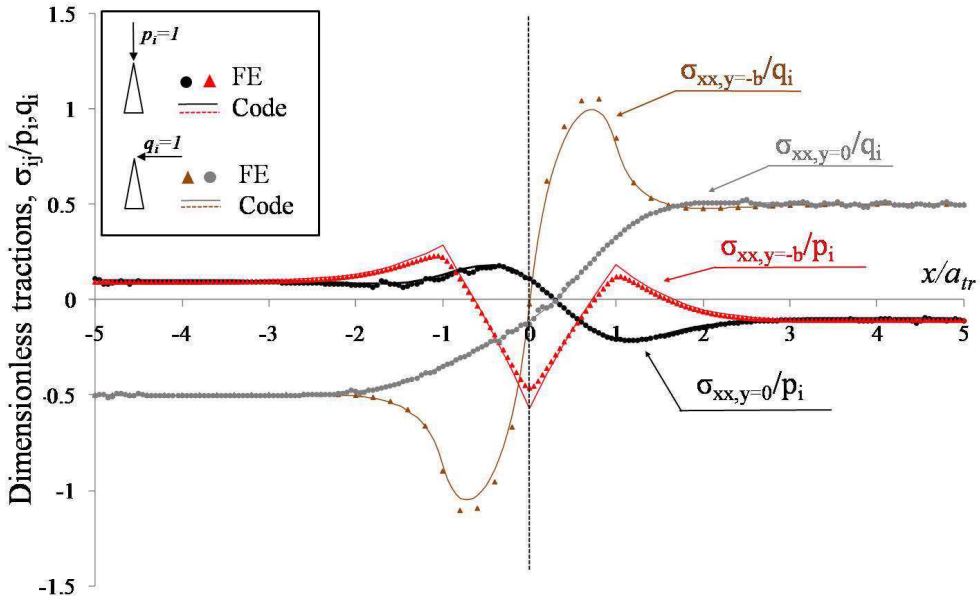


Figure 4.3. Bulk stresses associated with the tension imbalance present in the system for a triangle of direct and shear traction imposed on the free surface, $-1 < x/b < 1$ ($b/a_{tr} = 1$ and $f = 0.2$).

finite element model. The FE solution shows oscillations at the trailing edge of the contact that we believe due to numerical noise introduced by the full sliding condition.

For each surface loading case, equilibrium of the system merits comment. It is clear that, if forces acting along the free surface and interface alone are considered, equilibrium in the *x*-direction is not maintained. This can be easily seen from the fact that the mixed boundary condition (4.13) introduces a tension imbalance. Equilibrium is restored by the presence of direct stress, σ_{xx}, throughout the thickness of the layer, which becomes more uniform with depth as the observation point becomes more remote ($x/b \to \pm\infty$).

For a triangle of direct traction, the average remote value of the 'bulk stress' is defined by

$$\sigma_{xx,j,\,|x|\to\infty} = \frac{1}{b}\int_{-b}^{0} \sigma_{xx}\left(\infty, y\right) dy \tag{4.24}$$

with $j = p, q$. Thus, as shown schematically in Figure 4.4, the remote tensions needed to attain

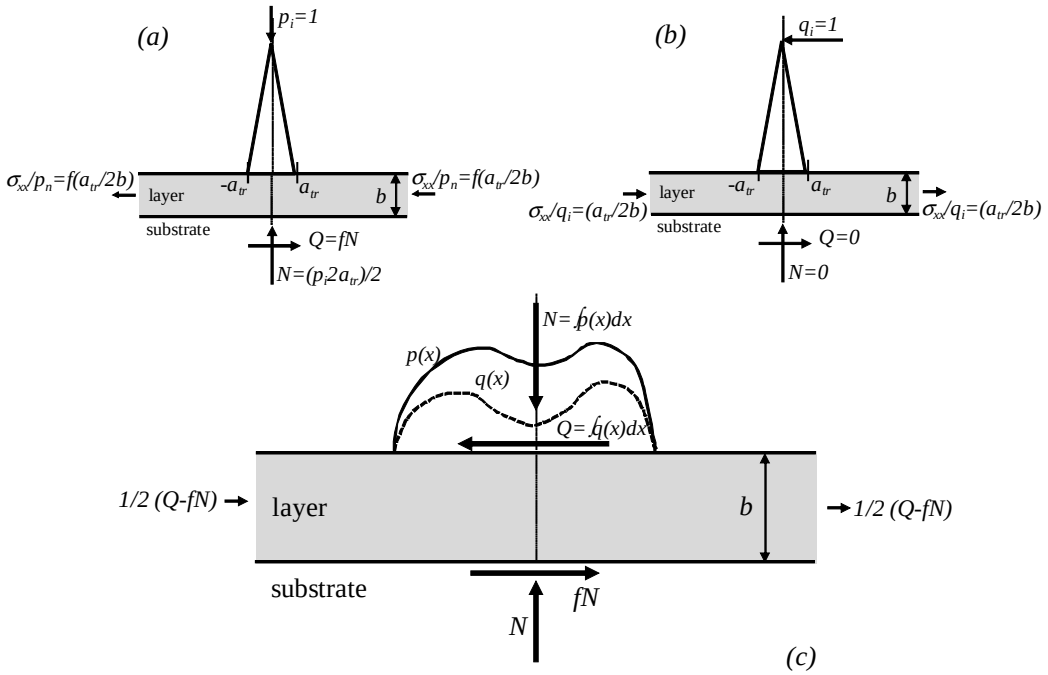


Figure 4.4. (a) free body diagram for a triangle of direct traction - (b) free body diagram for a triangle of shear traction - (c) free body diagram for a generic induced traction distribution at the layer surface.

equilibrium are clearly

$$\frac{\sigma_{xx,p,\,|x|\to\infty}}{p_i} = \pm f\frac{a_{tr}}{2b} \qquad \frac{\sigma_{xx,q,\,|x|\to\infty}}{q_i} = \pm\frac{a_{tr}}{2b}. \tag{4.25}$$

When the interfacial friction coefficient is set to zero, the contact problem illustrated in Figure 1.8 - *case III frictionless* is recovered, and the formulation for this case is given in (Hills et al., 1993). For this special case Figure 4.5 provides a further comparison with the existing results (Hills et al., 1993) and the agreement is excellent. Figure 4.6 and 4.7 highlight the effect of the interfacial coefficient of friction on the interfacial direct tractions, excited by both a normal surface triangle of traction (Fig. 4.6), and a shear surface triangle of traction (Fig. 4.7), for the case when $b/a_{tr} = 1$.

When the friction coefficient increases, then the term of comparison may be the influence functions for the adhered case (Figure 1.8 - *case I adhered*) which are reported in (Hills et al., 1993). In this case, the influence functions for the bonded case are such that no tension imbalance is generated at the layer extremities as it is compensated by the reaction forces at the layer-substrate interface.

Consequently, the influence functions for the adhered case differ significantly with respect to the influence functions for the frictional problem, regardless the value of the interfacial friction coefficient, f. Figures 4.8 and 4.9 illustrate this aspect for a triangle of direct and shear traction, respectively. Figures 4.10 and 4.11 display the 'diffusion' of the surface tractions outwards as the layer thickness is increased.

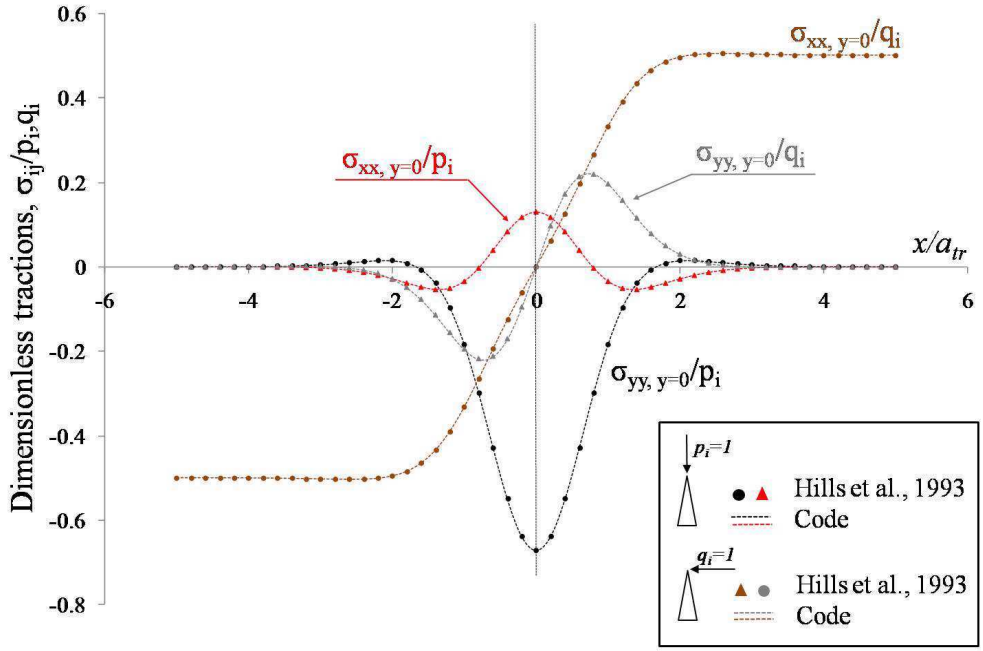


Figure 4.5. Comparison between the influence functions for a triangle of direct and shear traction formulated for the case of a layer resting on a substrate in frictionless condition and the influence functions devised for the frictional problem for f set to 0.

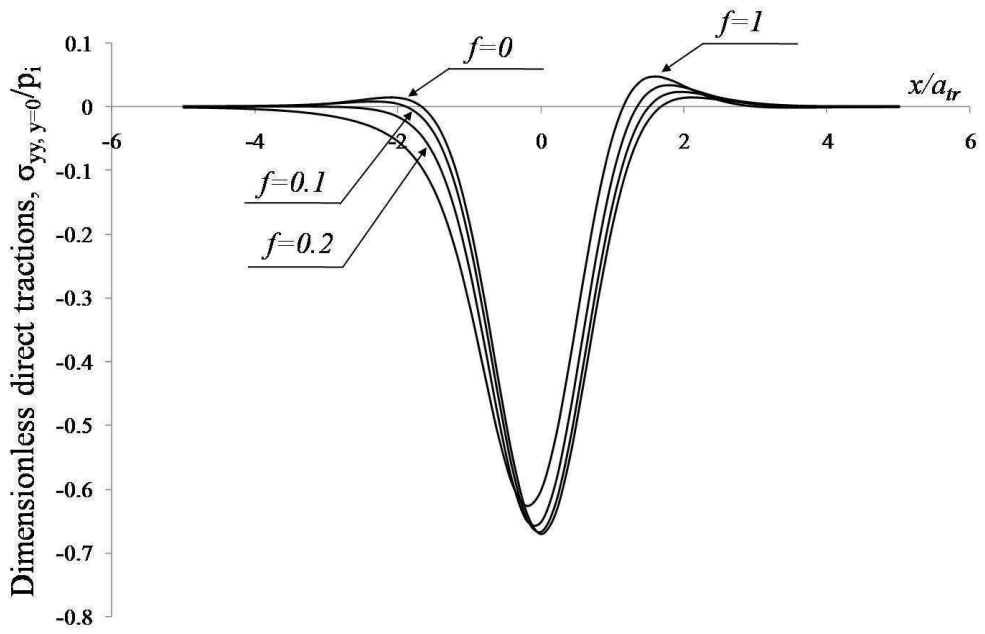


Figure 4.6. Normal tractions at the interface between layer and substrate for a triangle of direct traction for different values of the interfacial friction coefficient, *f*, and $\nu_1 = 0.3$.

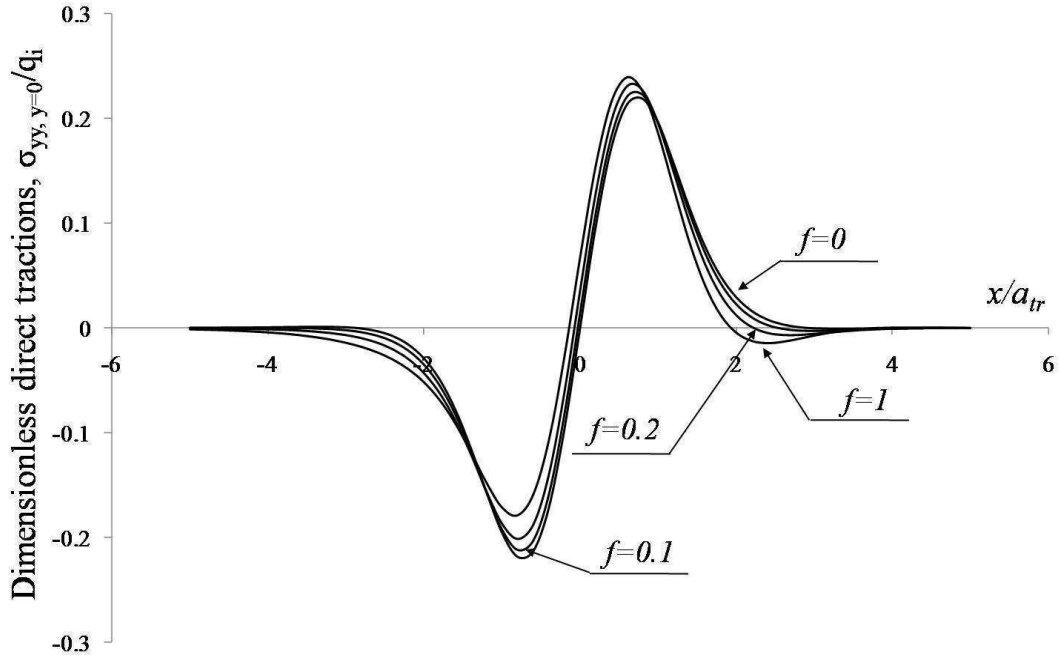


Figure 4.7. Normal tractions at the interface between layer and substrate for a triangle of shear traction for different values of the interfacial friction coefficient, *f*, and $\nu_1 = 0.5$.

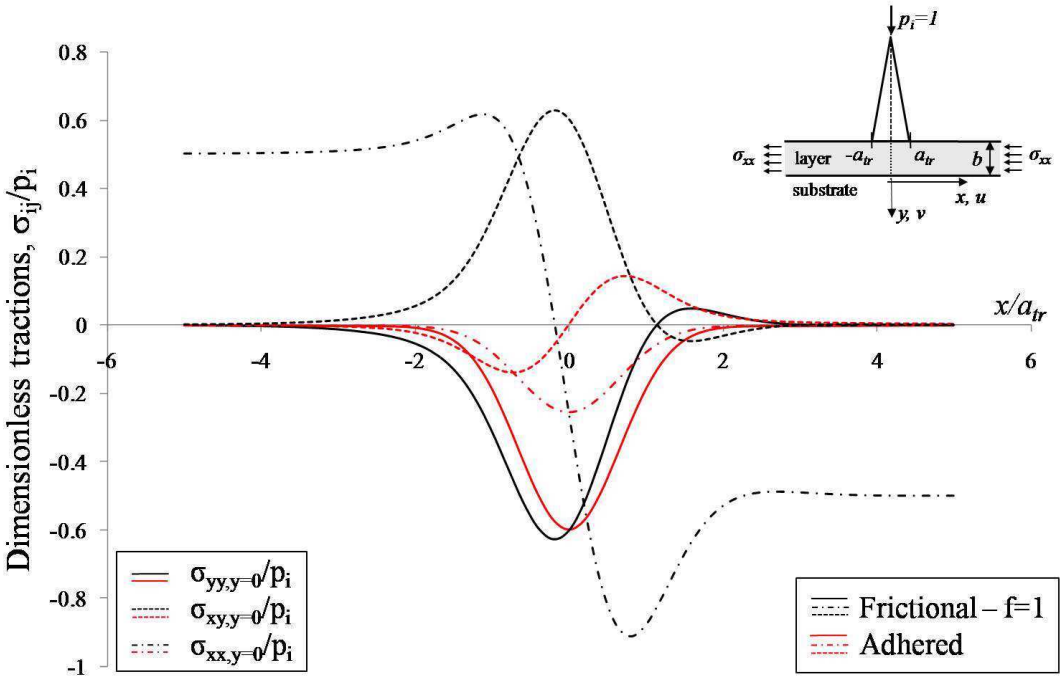


Figure 4.8. Comparison between the state of stress induced at the layer/substrate interface by a triangular influence function of direct tractions formulated for the case of a layer bonded to a substrate and that induced by the same influence function for the sliding frictional problem for f=1.

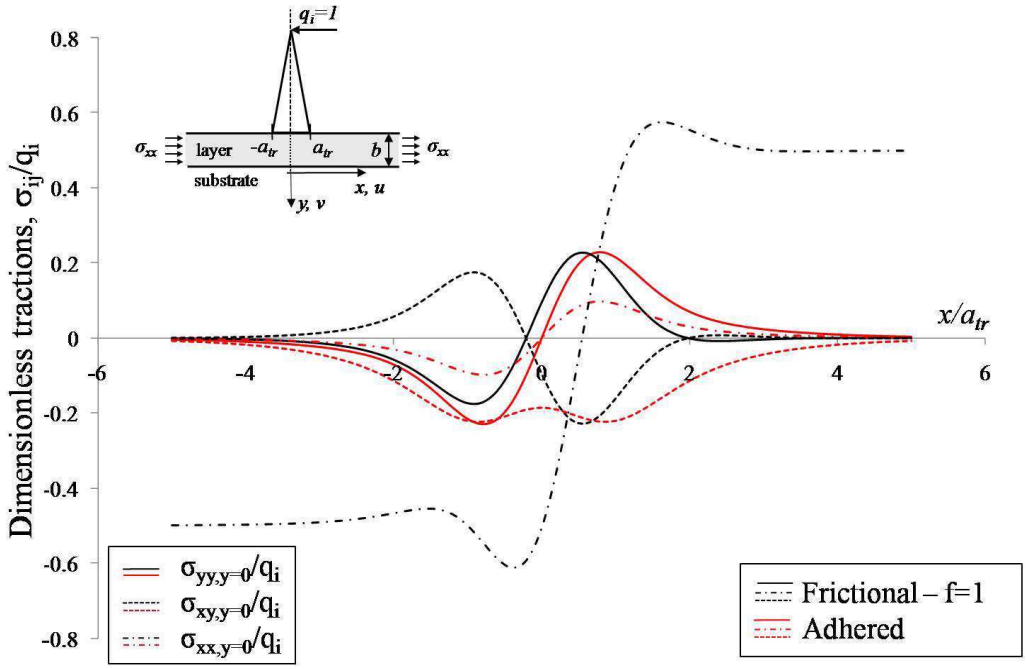


Figure 4.9. Comparison between the state of stress induced at the layer/substrate interface by a triangular influence function of shear tractions formulated for the case of a layer bonded to a substrate and that induced by the same influence function for the sliding frictional problem for f=1.

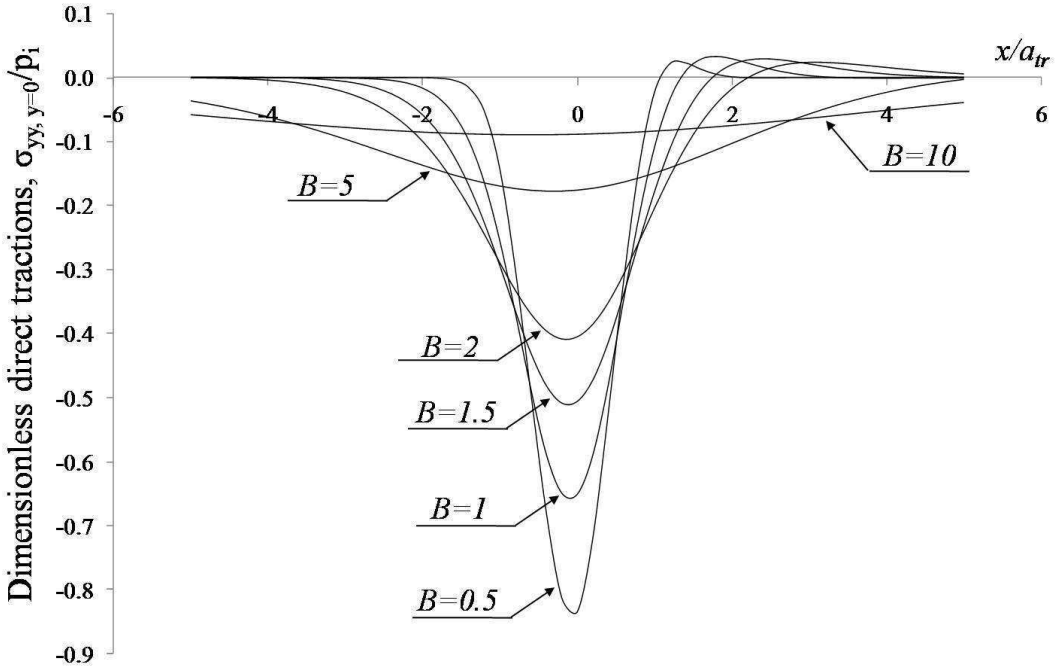


Figure 4.10. Normal tractions at the interface between layer and substrate for a triangle of direct traction for different values of the ratio b/a_{tr}, B, and $\nu = 0.3$.

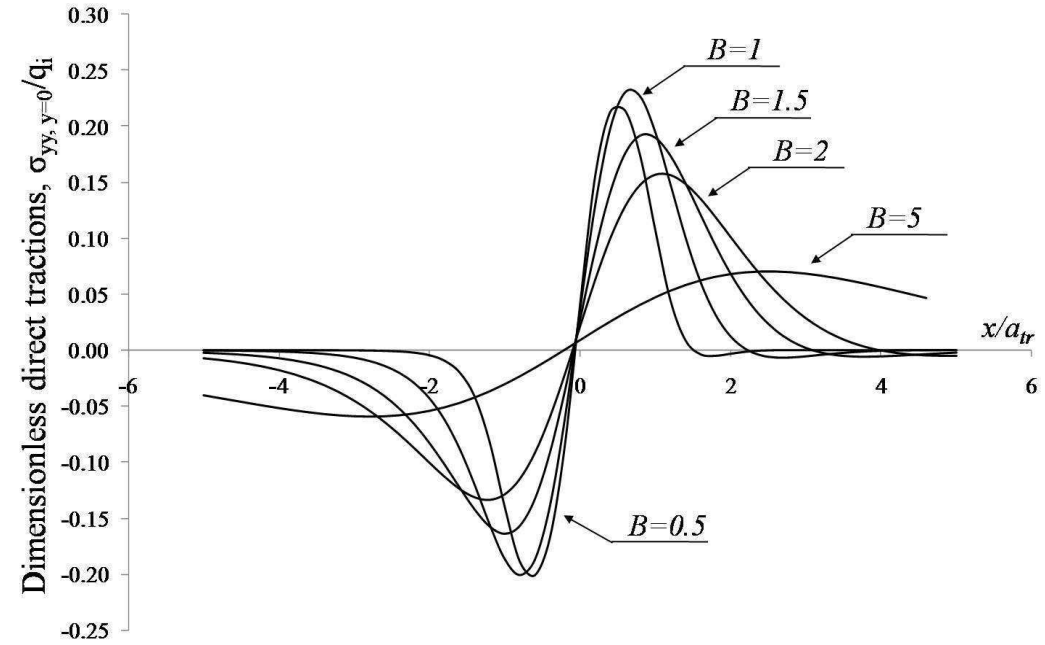


Figure 4.11. Normal tractions at the interface between layer and substrate for a triangle of shear traction for different values of the ratio b/a_{tr}, B, and $\nu = 0.3$.

4.3 Example Application

It is now clear from our considerations of the equilibrium of the influence functions that, although the 'sliding layer' influence function is, potentially, a very valuable general solution, care needs to be exercised in its application, and the presence of tension effects in the strip are very important. If a partial slip contact problem is analysed which starts from rest, and then an overall motion is imposed, a transient state will be experienced and then a steady state attained; this is not associated with inertia effects but the removal from the system of the locked-in residual shearing tractions associated with the initial phase of loading. When once such a system is in the steady state, the effects of any pre-existing tension applied to the strip ends will disappear, and it is only the *difference* in bulk tension between the strip ends, σ_o, which enters the solution. The most general problem solved is therefore of the kind shown in Figure 1.8 in Chapter 1: a contact of width $2a$ (where $a/b \sim 1$, and which may, in general, be adhered, in partial slip, or sliding) is applied to the upper surface of a strip, in intimate contact with a semi-infinite rigid counter surface, along which it is sliding, and where the difference in end tensions is $\sigma_o = \sigma_{0,R} - \sigma_{0,L}$. The formulation may therefore be used to solve, for example, the action of the capstan and pinch wheel in controlling tape motion in a traditional tape recorder, and mechanically equivalent mechanisms. But the motivation for the present study was a consideration of what happens when a tyred wheel (this corresponds to the case when the layer cannot undergo any tension unbalance $\sigma_o = 0$) is pressed onto a road and a torque gradually applied to the wheel, inducing shearing tractions both along the tyre/wheel interface, and between the tyre and the road (see Fig. 4.12).

Under normal conditions one would expect that the tyre/wheel interface would remain substantially stuck whilst the tyre/road approached the sliding condition, but there are cases of severely loaded earth-moving machinery where incipient spinning of the wheel within the tyre may also be attained. If the coefficient of friction between the tyre and the pavement is μ (see Fig. 4.12a), whilst the imposition of shrink fit conditions produces an interfacial contact pressure p_0, the condition for spin

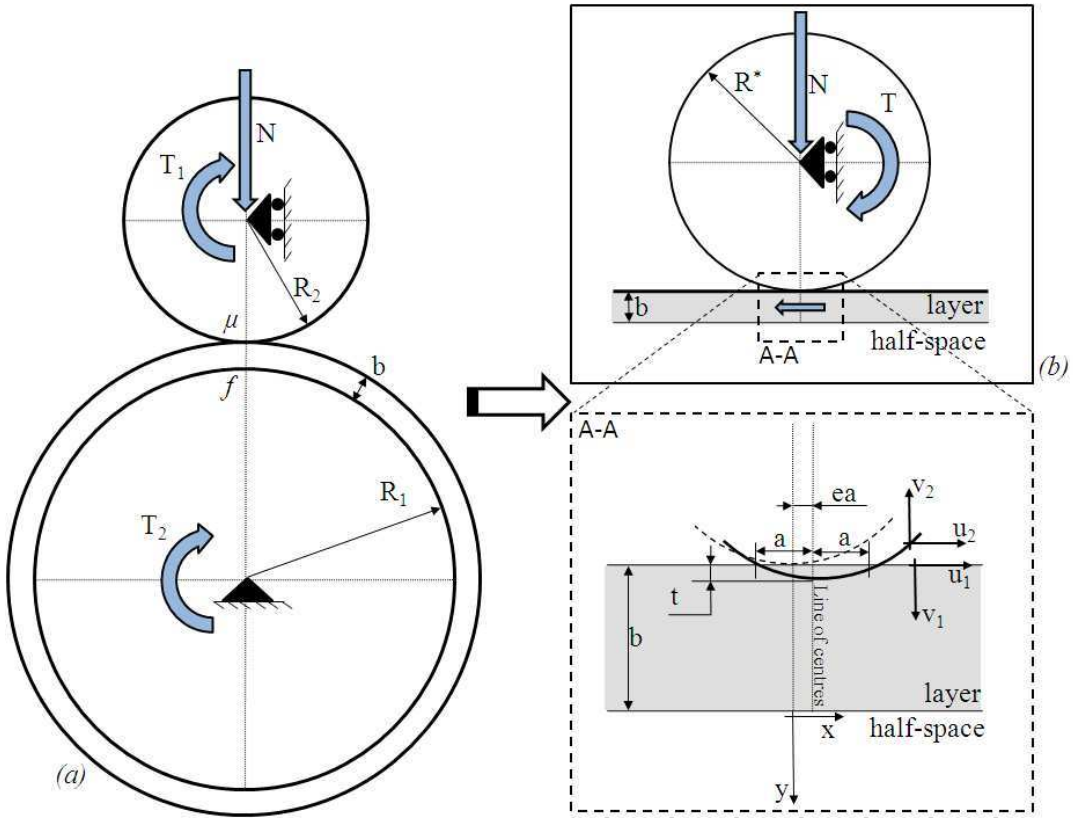


Figure 4.12. (a) Schematic of the example application, and (b) equivalent contact model. The inset to figure (b) shows the problem variables and the undeformed and deformed configurations.

between the tyre and wheel is

$$T_H = 2\pi R_1^2 f p_0, \tag{4.26}$$

where T_H is the applied torque per unit width, and this condition is independent of the normal line-load carried by the wheel, N, *provided only that no separation occurs*. On the other hand, the condition for sliding between the tyre and the pavement is that this will occur when

$$T_P = \mu(R_1 + b)N, \tag{4.27}$$

where T_P is the applied torque per unit width. The requirement that pavement slip occurs before spinning is therefore given by

$$\frac{f}{\mu} > \frac{1 + b/R_1}{2\pi} \frac{N}{p_0 R_1} \tag{4.28}$$

and this is an extremely easy condition to evaluate. However, what it does not do is to determine

whether the requirement for full wheel/tyre contact is maintained. The problem is therefore evaluated by the procedure described above, with a view to testing this condition. Also, to render the problem simpler incipient sliding between the tyre and the pavement is assumed.

The outer surface of the tyre is, of course, circular, but, as the contact half-width is small compared with the radius, it may be reduced to a straight line and the interior (the wheel) to a half-plane: this is because the contact itself must be capable of idealisation within a half-plane approach (see Fig. 4.12b). Thus, exterior to the contact we have

$$\begin{array}{l} p\left(X\right)=0 \\ q\left(X\right)=0 \end{array} \qquad |X| \notin \text{contact } (>1) \tag{4.29}$$

where $X = x/a$ and a is the contact half-width. Within the contact, the surface normal displacement is specified by the profile of the relative curvature of the tyred roller and the countersurface and is given by:

$$V_1 + V_2 = D_{ind} + Xe\frac{a}{R^*} - X^2\frac{a}{2R^*} \qquad X \in \text{ contact } (\leq 1), \tag{4.30}$$

where $R^* = R_1R_2/(R_1+R_2)$, $V_1 = v_1/a$, $V_2 = v_2/a$ ($= 0$ - *when the top roller, or pavement, is assumed to be rigid*), $D_{ind} = t/a$ and ea is the eccentricity of the contact (see Fig. 4.12(b)). Subscripts 1 and 2 refer to the strip (tyre) and the 'top roller' respectively. The top roller is assumed here to be rigid and, therefore, V_2 is equal to zero. In such configuration (see Figure 4.12b), the surface (of the tyre) displacements induced by general distribution of tractions are given by

$$u_1\left(x,-b\right) = \frac{1+\nu_1}{2\pi E_1}\int_{-\infty}^{+\infty}\left[I_{u_p}\tilde{p}\left(\phi\right) + I_{u_q}\tilde{q}(\phi)\right] ie^{-i\phi x}\frac{d\phi}{\phi}, y=-b, \forall x \tag{4.31}$$

$$v_1\left(x,-b\right) = \frac{1+\nu_1}{2\pi E_1}\int_{-\infty}^{+\infty}\left[I_{v_p}\tilde{p}\left(\phi\right) + I_{v_q}\tilde{q}(\phi)\right] e^{-i\phi x}\frac{d\phi}{\phi^2}, y=-b, \forall x \tag{4.32}$$

where the integrals I_{u_ij}, with $j = p, q$, are given in Appendix B, and the tractions are, at this stage, still general. Focussing on the normal displacement, the traction distribution is linearised and hence the integrals are replaced with a summation whose kernel is the influence function for a triangle of

traction, thereby giving:

$$\frac{t}{\bar{p}} + Xe\frac{a}{\bar{p}R^*} - X^2\frac{a}{2R^*\bar{p}} = \frac{2\left(1+\nu_1\right)}{\pi E_1}\sum_{n=-(S-1)}^{S-1}\left(\frac{p_n}{\bar{p}}I\tilde{V}1\left[i_m - i_n\right] + \frac{q_n}{\bar{p}}I\tilde{V}2\left[i_m - i_n\right]\right) \quad (4.33)$$

where $I\tilde{V}1$ and $I\tilde{V}2$ are also given in Appendix B. Now, use a reference solution for an infinitely thick strip where the contact width (as in the Hertz case), $2a_H$, is given by

$$a_H = \frac{4NR^*}{\pi}\left(\frac{1-\nu_1^2}{E_1} + \frac{1-\nu_2^2}{E_2}\right) = \frac{8}{\pi}\frac{1-\nu_1^2}{E_1}a\bar{p}R^*, \quad (4.34)$$

where N is the normal load per unit width, $\bar{p} = N/2a$ the mean pressure. The mean pressure may be rewritten as follows:

$$\bar{p} = \frac{\pi a_H^2}{4\tilde{A}aR^*} \quad (4.35)$$

where:

$$\tilde{A} = \frac{2\left(1-\nu_1^2\right)}{E_1} \quad (4.36)$$

Thus (4.33) can be rewritten as follows:

$$\frac{2R^*D_{ind}A}{a_H} + \frac{2i_m}{S}eA^2 - \frac{i_m^2}{S^2}A^2 = \frac{B}{2\left(1-\nu_1\right)}\sum_{n=-(S-1)}^{S-1}\left(P_nI\tilde{V}1\left[i_m - i_n\right] + Q_iI\tilde{V}2\left[i_m - i_n\right]\right). \quad (4.37)$$

Here $P_n = p_n/\bar{p}$, $Q_n = q_n/\bar{p}$ and $A = a/a_H$. This is rewritten in a final, normalised form as:

$$\frac{2R^*}{a_H}X_1 + \frac{2i_m}{S}X_2 - \frac{i_m^2}{S^2}X_3 = \frac{B}{2\left(1-\nu_1\right)}\sum_{n=-(S-1)}^{S-1}\left(P_nI\tilde{V}1\left[i_m - i_n\right] + Q_nI\tilde{V}2\left[i_m - i_n\right]\right), \quad (4.38)$$

where $X_1 = D_{ind}/A, X_2 = eA^2, X_3 = A^2$.

In a similar fashion, the tangential displacement can be expressed in a linear dimensionless form as follows:

$$\frac{2i_mR}{a_HS}X_4 + \frac{2R}{a_H}X_5 = \frac{B}{2\left(1-\nu_1\right)}\sum_{n=-(S-1)}^{S-1}\left(P_nI\tilde{U}1\left[i_m - i_n\right] + Q_nI\tilde{U}2\left[i_m - i_n\right]\right), \quad (4.39)$$

where $X_4 = \xi_{creep}A$ and $X_5 = C_{slip}A$ and where $I\tilde{U}1$ and $I\tilde{U}2$ are also given in Appendix B.

To summarise, the matching Equations (4.38) and (4.39) can be satisified throughout the contact region which is made of *2S+1* points, so that i_m goes from -*S* to *S*. Finally, normal and tangential

equilibrium requirements are expressed by the equations:

$$\sum_{n=-(S-1)}^{S-1} P_n = \sum_{n=-(S-1)}^{S-1} \frac{p_n}{\bar{p}} = \sum_{n=-(S-1)}^{S-1} \frac{p_n}{\frac{N}{2Sa_{tr}}} = -\frac{\frac{N}{c}}{\frac{N}{2Sa_{tr}}} = -2S \tag{4.40}$$

$$\sum_{n=-(S-1)}^{S-1} Q_n = \sum_{n=-(S-1)}^{S-1} \frac{q_n}{\bar{p}} = \sum_{n=-(S-1)}^{S-1} \frac{q_n}{\frac{N}{2Sa_{tr}}} = -\frac{\frac{Q}{c}}{\frac{N}{2Sa_{tr}}} = 2S\frac{Q}{N}. \tag{4.41}$$

with N and Q representing the normal and tangential load transmitted at the roller/layer interface.

4.4 Results

The first case treated is frictionless contact between the layer and indenter, so that all tangential tractions vanish at the interface. The interfacial coefficient of friction, μ is set to zero and clearly:

$$Q_n = 0, \forall x \tag{4.42}$$

Combining Equations (4.38) and (4.40) a determinate problem is obtained. The number of equations is $2S + 2$ in as many unknowns, viz. $2S - 1$ values of the contact pressure P_n, together with D_{ind} (a measure of the rigid body indentation), A (a measure of the contact width) and the eccentricity e (which here is clearly zero because the problem is inherently symmetrical). The equations are linear and they can be solved with standard computer library routines. The formulation has also been used to study the case for which full sliding takes place at the layer/indenter interface. In this case, the shear traction is simply proportional to the normal pressure, so that, for each element:

$$|Q_n| = \mu |P_n|, \forall x \tag{4.43}$$

Equations (4.38) then become:

$$\frac{2R^*}{a_H}X_1 + \frac{2i_m}{S}X_2 - \frac{{i_m}^2}{S^2}X_3 = \frac{B}{2(1-\nu_1)} \sum_{n=-(S-1)}^{S-1} P_n \left(I\tilde{V}1\left[i_m - i_n\right] + \rho_{sub}\mu I\tilde{V}2\left[i_m - i_n\right] \right). \tag{4.44}$$

The problem of the interfacial contact pressure distribution when a roller is slid over a second layered body has been examined already (e.g. see Nowell and Hills, 1988b and Hills et al., 1993). The solution has, therefore, first been validated using the existing semi-analytical solutions by com-

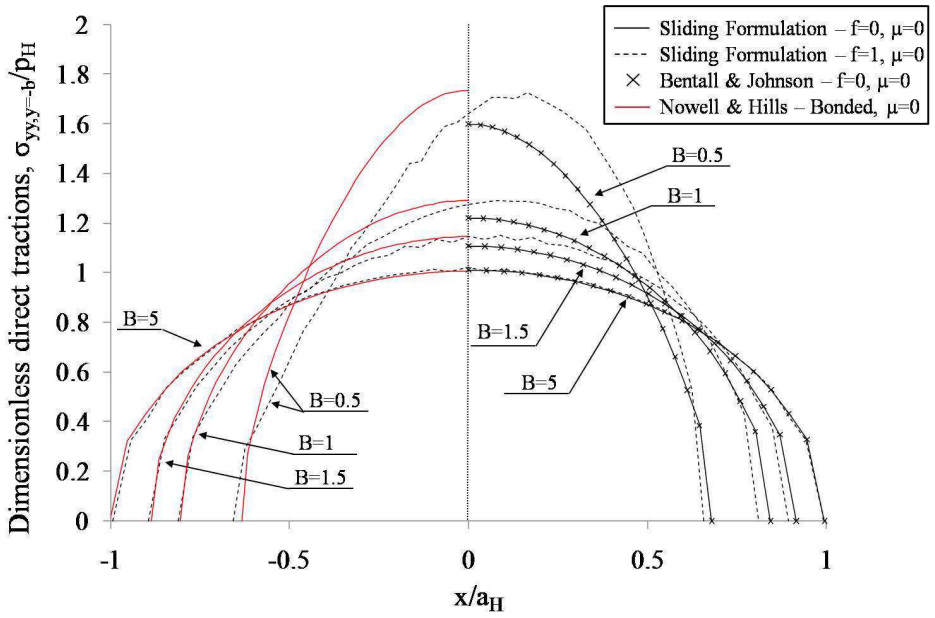


Figure 4.13. Comparison between the pressure distributions for the sliding frictional formulation for f=0 and f=1 and the solution for the frictionless layer problem (Bentall, 1968) and the bonded layer problem (Nowell, 1988b). The solutions are computed for the frictionless contact configuration ($\mu = 0$) and various values of B. It should also be noted that the solution is only plotted along the contact half-width for the three problems which produce symmetric distributions to improve the diagram's legibility.

paring the contact pressure distribution for various dimensionless contact widths (B), for the frictionless case, $\mu = f = 0$ (as already done for the influence functions - see above). A very good agreement (see Fig. 4.13) was achieved between the frictionless formulation for rigid rollers described in (Bentall and Johnson, 1968) and the sliding formulation when f is set to zero.

A comparison between the sliding solution in the presence of strong friction and the bonded layer case (Nowell and Hills, 1988b) has been also performed showing that, as expected, the solution for the bonded case differs significantly from that for the sliding frictional problem, regardless the value of the interfacial friction coefficient, f, especially for small values of B. This is shown in Figure 4.13, where the bonded layer solution and the results from the frictional sliding formulation for a relatively high value of friction coefficient, $f = 1$, are also compared. In every case the layered contact gives rise to a reduced contact patch with higher peak pressure, and it is seen that the localisation of contact load is greater when the tyre is adhered than when it is unconstrained from

lateral expansion of the rigid substrate, as might be anticipated. The solutions obtained using the present formulation have been further corroborated using equivalent FE models for the cases where benchmark semi-analytical solutions could not be found. Sample results are shown in Figures 4.14 and 4.15 for a value of the interfacial friction coefficient $f = 0.2$ and, respectively, Poisson's ratio $\nu_1 = 0.3$ and $\nu_1 = 0.5$. Once again, the appropriate half-plane solutions are recovered for large tyre thickness and results are satisfactorily validated using the equivalent FE model for the case of $B = 1$.

We turn, now, to an examination of the conditions along the interface, which effectively define the conditions under which a simple limit-state analysis, as described above, apply. This is done by taking a particular set of conditions (defining geometry and dimensionless pressure), and scanning the interface to find when σ_{yy} incipiently becomes positive. It is this point which defines the limit of the simple 'bilaterally' defined spinning condition, Equation (4.28). The results of the detailed calculations using the method developed here are shown in Figure 4.16. The solid lines define the 'limit state' sliding condition developed using the simple bilateral assumptions stated. If, however, the coefficient of friction, μ, is too low or the contact pressure, p_0/p_H, is too low, a region of separation occurs (dotted lines) and the simple calculation which hinges on the application of superposition fails. Further, if the point respresenting the actual set of onditions lies *above* the relevant line in the figure, there is partial slip at interface 1 (between the tyre and contacting component), whilst if the point lies *below* the relevant line equilibrium is not maintained - either there are inertia forces present or there must be a tension gradient within the tyre. The case where interface 1 undergoes partial slip can also be solved using the current formulation but its treatment is outside the scope of the present contribution.

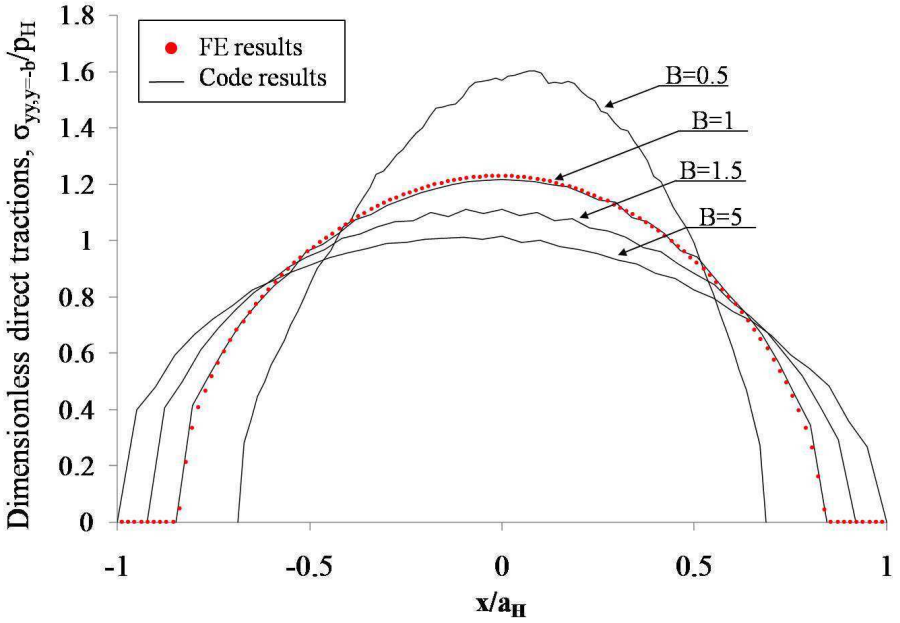


Figure 4.14. Normal traction at the interface between layer and indenter for a pure sliding contact ($\mu = 0.5$) for different values of B, $\nu = 0.3$ and $f = 0.2$.

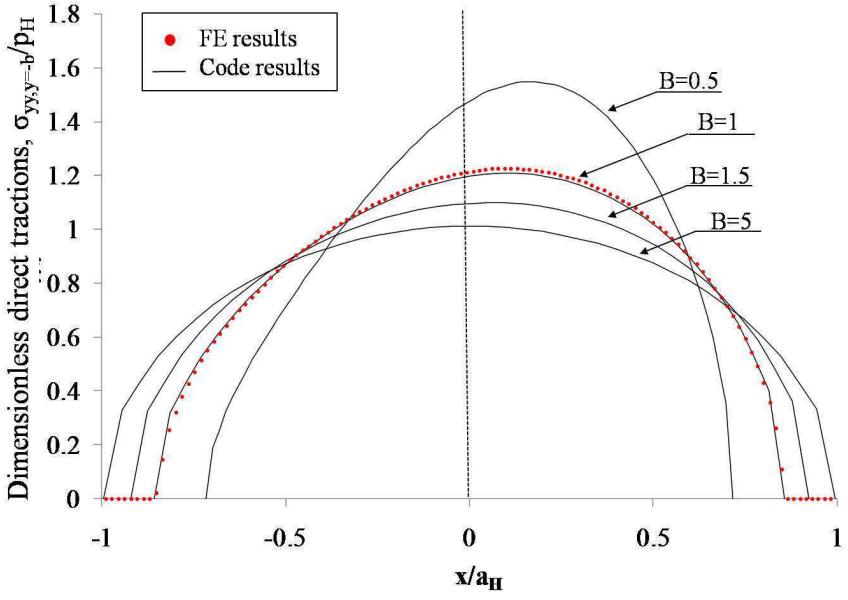


Figure 4.15. Normal traction at the interface between layer and indenter for a pure sliding contact ($\mu = 0.5$) for different values of B, $\nu = 0.5$ and $f = 0.2$.

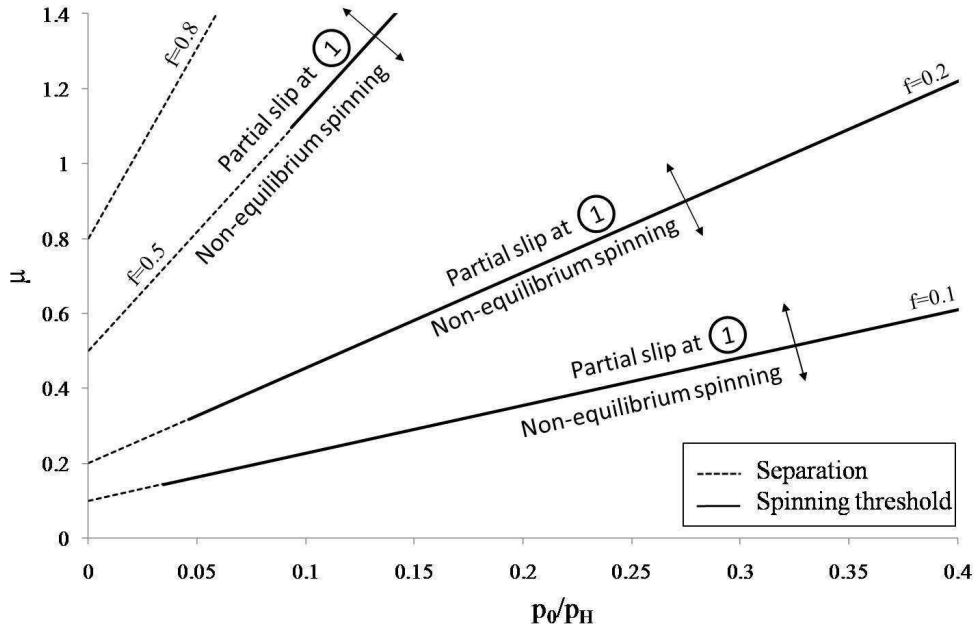


Figure 4.16. "Limit state" sliding condition. The solid line represents the layer/indenter friction coefficient, μ, required to guarantee the equilibrium of the system while spinning for $B = 1$, $R/b = 10$, and for different values of f. The dotted lines represent the values for which separation between the layer and the substrate occurs. The behaviour of the contact problem above and below the limit states is also schematically shown.

4.5 Summary

A formulation for an elastic layer, pressed onto a rigid substrate, and slid along by a local external contact, has been described. The output of this phase of the solution is an influence function for a triangle of direct and shearing traction applied over the external, free surface. These influence functions have been combined to form a piecewise linear representation of the actual contact traction distribution. The approach has then been applied to study the problem of a layer pressed and sliding onto a flat rigid surface, and indented by a rigid cylinder, with the cylinder being subject to a major torque. The torque is then steadily increased, and a complicated system of slip zones develops at the point where the tyre is in contact with the ground, and gradually spreads. The details of this transition problem are not considered, but the limit state condition, when the cylinder spins within the tyre is studied in detail. It is shown that the formulation accurately captures the behaviour of skidding layer mounted on rolling systems in terms of traction distribution at the layer/indenter

interface. This proves the viability of the proposed semi-analytical formulation to study layered contact problems in the presence of sliding.

Chapter 5

Analysis of interfacial slip using quadratic programming

5.1 Introduction

Interfacial micro-slip is not easily captured using standard numerical design tools, especially if the loading history is complicated, and where slip may simultaneously occur at different locations along the mating surfaces (Ahn and Barber, 2008b/Reina et al., 2009). A semi-analytical procedure normally referred to as the distributed dislocation technique has been comprehesively illustrated in Chapter 2 and successfully used to analyse microslip in layered frictional contacts (Reina et al., 2010b). However, its principal limitation is that, if the classical integral equation procedure is adopted, it is extremely difficult to determine the locations of the stick/slip transition points systematically (Chang et al., 1983) and, if there are several such points, long-winded iterative schemes may be needed (Chang et al., 1983 and Reina et al., 2010b). In the approach presented in this chapter, the advantages of the distributed dislocation technique are preserved but the problems of the integral equation are averted by formulating the contact problem in terms of a 'quadratic cost function' to be minimised. This is normally referred to as mathematical programming, among which quadratic programming is one of the most important.

5.2 Stationary loads

Figure 5.1 shows a generic elastic layer problem, under transverse plane strain, that may be treated

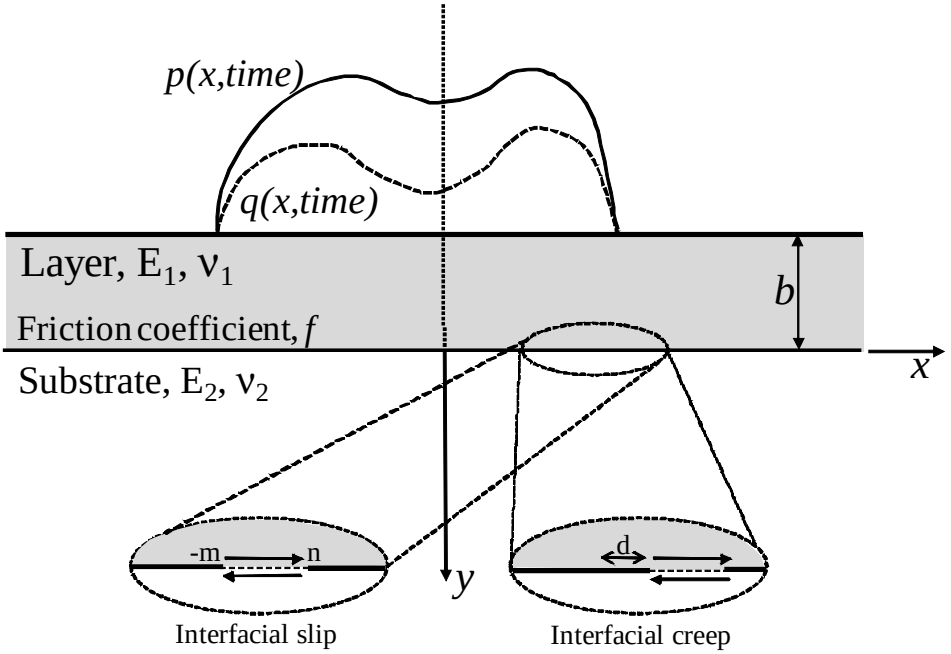


Figure 5.1. Schematic of the layered contact problem and possible interface regimes.

using the formulation proposed here. This problem may be seen as generalization of the contact problem extensively discussed in Chapter 2 and (Reina et al., 2010b).

The coordinate origin is positioned on the interface, and the Coulomb-Amontons friction law is adopted so that the coefficient of friction is independent of the slip-velocity. The solution to the 'bilateral' problem (coefficient of friction sufficiently high to prevent all slip) is found first, and denoted with $\sigma_{xy}^{bil}(x)$ and $\sigma_{yy}^{bil}(x)$ for shear and direct tractions, respectively. Slip along the interface is subsequently introduced by distributing dislocations within slip region(s), and the corrective solution denoted by $\sigma_{xy}^{corr}(x)$ and $\sigma_{yy}^{corr}(x)$ for shear and direct tractions, respectively. The direct, $\sigma_{yy}(x,0)$, and shear, $\sigma_{xy}(x,0)$, tractions are then given by

$$\begin{bmatrix}\sigma_{yy}(x,0)\\ \sigma_{xy}(x,0)\end{bmatrix} = \begin{bmatrix}\sigma_{yy}^{bil}(x)\\ \sigma_{xy}^{bil}(x)\end{bmatrix} + \begin{bmatrix}\sigma_{yy}^{corr}(x)\\ \sigma_{xy}^{corr}(x)\end{bmatrix}, \tag{5.1}$$

and the corrective terms are given by

$$\begin{bmatrix}\sigma_{yy}^{corr}(x)\\ \sigma_{xy}^{corr}(x)\end{bmatrix} = A_{SM,DM}\int_{-\infty}^{+\infty} B_x(\xi)\begin{bmatrix}G_{yy}(x,\xi)\\ G_{xy}(x,\xi)\end{bmatrix}d\xi \tag{5.2}$$

where A is the contact compliance, the subscripts SM and DM refer, respectively, to similar

($E_1 = E_2$ and $\nu_1 = \nu_2$) and dissimilar ($E_1 \neq E_2$ and/or $\nu_1 \neq \nu_2$) material pairs, $B_x(\xi)$ is the dislocation density and $G_{yy}(x,\xi)$ and $G_{xy}(x,\xi)$ are the influence functions associated with the glide dislocations (see Appendix C). Conditions of separation between the layer and the substrate are not considered.

The interface conditions are now defined. Where the frictional law is not violated, stick occurs and this means that

$$h(x) = 0 \tag{5.3}$$

and

$$|\sigma_{xy}(x,0)| \leq -f\sigma_{yy}(x,0) \tag{5.4}$$

where $h(x)$ is the relative displacement between the bodies in contact defined by

$$h(x) = u_{layer}(x) - u_{substrate}(x) \tag{5.5}$$

and $u_{layer}(x)$ and $u_{substrate}(x)$ represent, respectively, the upper body and the lower body surface tangential displacement. Where the friction law is violated, slip takes place and

$$|\sigma_{xy}(x,0)| = f|\sigma_{yy}(x,0)| \tag{5.6}$$

whilst the sign of the shear is dictated by the requirement that it opposes the first derivative of slip in time, so that

$$sgn(\sigma_{xy}(x,0)) = sgn\left(\dot{h}(x)\right). \tag{5.7}$$

Here, the sign of the relative slip and its first derivative in time coincide (Chang et al., 1983)

$$sgn\left(\dot{h}(x)\right) = sgn(h(x)) \tag{5.8}$$

so that the final expression for the shear traction in presence of slip is

$$\sigma_{xy}(x,0) = -f\sigma_{yy}(x,0)\frac{h(x)}{|h(x)|}. \tag{5.9}$$

Lastly, uniqueness demands that

$$\int_{-\infty}^{+\infty} B_x(\xi)\, d\xi = 0 \tag{5.10}$$

although, of course, the integrand is zero everywhere except in the slip regions.

The classic way of solving the problem requires guessing the location and extent of each slip area present and iterating the solution until Equation (5.10) is satisfied, but this can easily become very cumbersome (Chang et al., 1983), and the formulation developed below relies on the use of optimisation strategies to avoid this. As explained in Section 1.2.4, these strategies have been applied to tackle contact problems (Kalker, 1971) and the quadratic programming procedure illustrated by Nowell and Dai (1998a) was extended to model interfacial slip in layered systems.

If both sides of the equation for slip (5.9) are multiplied by $h(x,0)$, we have

$$\sigma_{xy}(x,0)\, h(x) = -f\sigma_{yy}(x,0)\, \frac{h(x)}{|h(x)|} h(x), \tag{5.11}$$

which may be simplified to give

$$\sigma_{xy}(x,0)\, h(x) + f\sigma_{yy}(x,0)\, |h(x)| = 0, \tag{5.12}$$

but it will be noted that this also applies where stick occurs. Thus, the above boundary condition is valid along the whole interface, with no distinction made between stick and slip areas (Kalker, 1971). If Equation (5.12) is integrated along the entire interface, the functional of our layered elastic problem, $\tilde{F}$, can be defined as follows

$$\tilde{F} = \int_{-\infty}^{+\infty} \left\{ -\left[\sigma_{xy}(x,0)\, h(x) + f\sigma_{yy}(x,0)\, |h(x)|\right] \right\} dx \tag{5.13}$$

The minus sign was added in front of the integrand as this makes it always positive. This property can be easily proved, because

$$-\sigma_{xy}(x,0)\, h(x) - f\sigma_{yy}(x,0)\, |h(x)| \geq -|\sigma_{xy}(x,0)|\, |h(x)| - f\sigma_{yy}(x,0)\, |h(x)| \geq 0 \tag{5.14}$$

where the first inequality becames an equality if and only if slip vanishes or traction has the same sign direction as slip, whilst the second inequality turns into an equality if and only if the shear traction are f times $\sigma_{yy}(x,0)$ or slip vanishes (Kalker, 1971). Now, if the solution to the layer problem

is substituted in (5.13), the functional goes to zero. On the other hand, if any other combination of pressure, tangential tractions and displacement is substituted in (5.13), the value of the functional is strictly positive. Hence, the solution to the problem may be found by minimizing the value of the functional, taking into account the frictional law adopted together with the condition for uniqueness of elastic solution. This is the principle on which the formulation is built (Kalker, 1971; Nowell and Dai, 1998a; and Nowell, 2004). The attention is now focussed on how the functional and the boundary conditions can be discretised.

The integral representing the functional is improper as the integration domain is unbounded. However, the integration interval may be truncated as no slip is permitted as x goes to $\pm\infty$. The interval of integration may therefore be reduced until it just includes all slip areas. In order to compute the value of Equation (5.13), traction and displacement fields are sampled at a finite number of points n_p, indicated with the letter j, with $j = 1, ..., n_p$. The supports are equally spaced, with the distance between adjacent supports indicated with the letter d_{sup} (see Fig. 5.2). Thus, the integration in Equation (5.13) can be replaced by a summation and, consequently, the functional rewritten as follows

$$\tilde{F} = -\sum_{j=1}^{n_p} \left[\left(\sigma_{xy,j}^{bil} + \sigma_{xy,j}^{corr} \right) h_j + f \left(\sigma_{yy,j}^{bil} + \sigma_{yy,j}^{corr} \right) |h_j| \right]. \tag{5.15}$$

The presence of the absolute value of the relative displacement, $h\,(x)$, complicates the formulation. A similar problem was first faced and solved by Kalker (1971) who proposed that the absolute value could be substituted with the sum of two positive quantities, and that the term within the sign of absolute value with the difference between the same quantities. This transformation is applied here by replacing the displacement term, h_j, and its absolute values, $|h_j|$, as follows

$$h_j = h'_j - h''_j \tag{5.16}$$

$$|h_j| = h'_j + h''_j \tag{5.17}$$

where h'_j are h''_j are positive quantities, so that the final discretised form of the functional is

$$\tilde{F} = -\sum_{j=1}^{n_p} \left[\left(\sigma_{xy,j}^{bil} + \sigma_{xy,j}^{corr} \right) \left(h'_j - h''_j \right) + f \left(\sigma_{yy,j}^{bil} + \sigma_{yy,j}^{corr} \right) \left(h'_j + h''_j \right) \right]. \tag{5.18}$$

Attention is now focussed on the corrective terms. The dislocation density is related to the slip displacement by (Hills et al., 1996)

$$B_x(\xi) = -\frac{dh(\xi)}{dx}. \tag{5.19}$$

The gradient of the slip displacement may be calculated using the finite difference method. The position of a generic midpoint coordinate, k, where the dislocation density is sampled, can be expressed as follows

$$x_k = \frac{x_j}{2} + \frac{x_{j+1}}{2} \tag{5.20}$$

and the discretised form of (5.19) is therefore

$$B_{x_k} = -\frac{h_{j+1} - h_j}{d_{\sup}} = \frac{h_j - h_{j+1}}{d_{\sup}}. \tag{5.21}$$

Had the density been sampled at the supports where the displacement is computed, the equivalent discretised form of Equation (5.21) would have had $2d_{\sup}$ at the denominator, reducing the accuracy of the numerical scheme. The integral in (5.2) is discretised by representing the density function using overlapping triangles (Qiu et al., 2008), which provides a piecewise linear approximation of its distribution. Figure 5.2 shows a typical element with a triangular distribution of dislocation density, located at x_k.

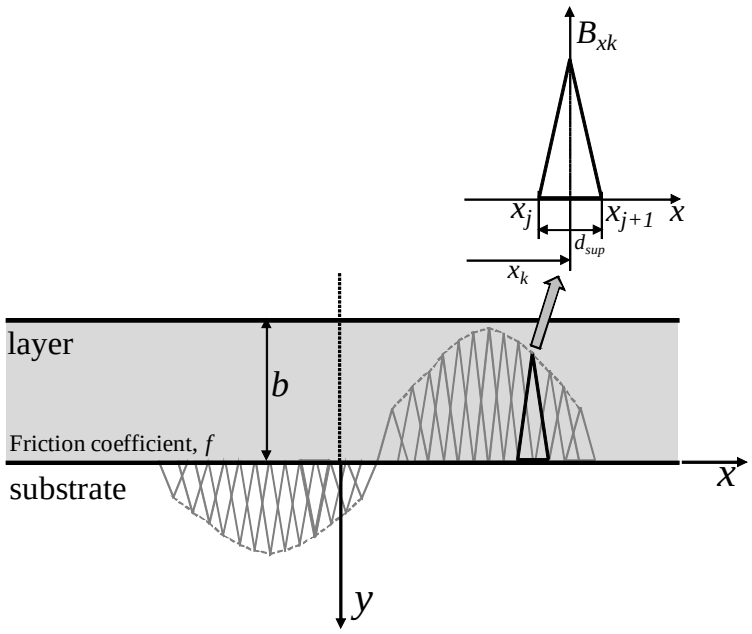


Figure 5.2. Schematic of the layered system and piecewise linear representation of the dislocation density.

Hence, the corrective terms, $\sigma_{yy}^{corr}(x)$ and $\sigma_{xy}^{corr}(x)$ are given by

$$\begin{bmatrix}\sigma_{yy,j}^{corr}\\ \sigma_{xy,j}^{corr}\end{bmatrix} = A_{SM,DM}\sum_{k=1}^{n_p}\int_{x_k-d_{\sup}}^{x_k+d_{\sup}} B_{x_k}(\xi,x_k)\begin{bmatrix}G_{yy}(x_j,\xi)\\ G_{xy}(x_j,\xi)\end{bmatrix}d\xi. \tag{5.22}$$

This can be further simplified to obtain

$$\begin{aligned}\begin{bmatrix}\sigma_{yy,j}^{corr}\\ \sigma_{xy,j}^{corr}\end{bmatrix} &= A_{SM,DM}\sum_{k=1}^{n_p}B_{x_k}\int_{x_k-d_{\sup}}^{x_k}\left(1+\frac{x_k}{d_{\sup}}\right)\begin{bmatrix}G_{yy}(x_j,\xi)\\ G_{xy}(x_j,\xi)\end{bmatrix}d\xi + \\ &+A_{SM,DM}\sum_{k=1}^{n_p}B_{x_k}\int_{x_k}^{x_k+d_{\sup}}\left(1-\frac{x_k}{d_{\sup}}\right)\begin{bmatrix}G_{yy}(x_j,\xi)\\ G_{xy}(x_j,\xi)\end{bmatrix}d\xi\end{aligned} \tag{5.23}$$

where the only unknowns are the triangle heights, B_{x_k}, and hence

$$\begin{bmatrix}\sigma_{yy,j}^{corr}\\ \sigma_{xy,j}^{corr}\end{bmatrix} = A_{SM,DM}\sum_{k=1}^{n_p}B_{x_k}\begin{bmatrix}F_{xyjk}\\ F_{yyjk}\end{bmatrix} \tag{5.24}$$

where F_{xyjk} and F_{yyjk} are

$$\begin{aligned}\begin{bmatrix}F_{xyjk}\\ F_{yyjk}\end{bmatrix} &= \int_{x_k-d_{\sup}}^{x_k}\left(1+\frac{x_k}{d}\right)\begin{bmatrix}G_{yy}(x_j,\xi)\\ G_{xy}(x_j,\xi)\end{bmatrix}d\xi + \\ &+\int_{x_k}^{x_k+d_{\sup}}\left(1-\frac{x_k}{d}\right)\begin{bmatrix}G_{yy}(x_j,\xi)\\ G_{xy}(x_j,\xi)\end{bmatrix}d\xi.\end{aligned} \tag{5.25}$$

F_{xyjk} and F_{yyjk} represent the influence functions of a dislocation triangle centred at x_k and of unit height. These functions can be computed and stored at the outset as they depend only on the density grid, x_k.

The condition for the solution of the problem to be unique Equation (5.10), can be expressed in its discretised form as follows

$$\sum_{k=1}^{n_p} B_{x_k} d_{\sup} = 0. \tag{5.26}$$

Now that all element of the layered elastic problem have been discretised, the problem to be solved can be written as follows

$$\underset{\min}{\tilde{F}} = -\sum_{j=1}^{n_p} \left[\left(\sigma_{xy,j}^{bil} + \sigma_{xy,j}^{corr} \right) \left(h'_j - h''_j \right) + f \left(\sigma_{yy,j}^{bil} + \sigma_{yy,j}^{corr} \right) \left(h'_j + h''_j \right) \right], \tag{5.27}$$

where

$$\begin{aligned} \begin{bmatrix} \sigma_{yy,j}^{corr} \\ \sigma_{xy,j}^{corr} \end{bmatrix} &= A_{SM,DM} \sum_{k=1}^{n_p} B_{x_k} \int_{x_k - d_{\sup}}^{x_k} \left(1 + \frac{x_k}{d_{\sup}} \right) \begin{bmatrix} G_{yy}\left(x_j, \xi\right) \\ G_{xy}\left(x_j, \xi\right) \end{bmatrix} d\xi + \\ &+ A_{SM,DM} \sum_{k=1}^{n_p} B_{x_k} \int_{x_k}^{x_k + d_{\sup}} \left(1 - \frac{x_k}{d_{\sup}} \right) \begin{bmatrix} G_{yy}\left(x_j, \xi\right) \\ G_{xy}\left(x_j, \xi\right) \end{bmatrix} d\xi, \end{aligned} \tag{5.28}$$

subject to

$$\sum_{k=1}^{n_p} B_{x_k} = 0 \tag{5.29}$$

and

$$h'_j, h''_j \geq 0 \tag{5.30}$$

The $5n_p$ unknowns of the layered elastic problem are h'_j, h''_j,$\sigma_{xy,j}^{corr}, \sigma_{yy,j}^{corr}, B_{x_k} (= B_{x_{j+1}}/2 + B_{x_j}/2)$, all over range $j = 1..n_p$, and which may be grouped in a vector, $\underline{x}_{qp}$, as follows

$$\underline{x}_{qp}^T = \left[h'_1 \ldots h'_{n_p}, h''_1 \ldots h''_{n_p}, \sigma_{xy,1}^{corr} \ldots \sigma_{xy,n_p}^{corr}, \sigma_{yy,1}^{corr} \ldots \sigma_{yy,n_p}^{corr}, B_{x_1} \ldots B_{x_{n_p}} \right] \tag{5.31}$$

The typical quadratic form of the problem can be expressed as follows

$$\min_{\underline{x}_{qp}} \frac{1}{2}\underline{x}_{qp}^T H_{qp}\underline{x}_{qp} + \underline{f}_{qp}^T \underline{x}_{qp} \tag{5.32}$$

where the square matrix H_{qp} includes the quadratic terms of the formulation and the vector $\underline{f}_{qp}$ the linear terms. This way of writing the problem is useful when commercial subroutines (MATLAB, 2009) are applied to find the solution to the problem.

5.3 Moving loads

When the applied loads are stationary, it is impossible for slip displacement to accumulate, but when the applied loads move, this is no longer true. The formulation differs only in Equations (5.8) and (5.10). In fact, the sign of the relative velocity between layer and substrate, $\dot{h}$, is now the same as the sign of the dislocation density. This implies that the functional for the moving load scenario, $\tilde{F}_M$, can be written as

$$\tilde{F}_M = \int_{-\infty}^{+\infty} \left\{ -\left[\sigma_{xy}\left(x,0\right) B_x\left(x\right) + f\sigma_{yy}\left(x,0\right) \left| B_x\left(x\right) \right| \right] \right\} dx. \tag{5.33}$$

This can also be shown to be positive definite, but it requires a different discretisation in order for the problem to be formulated in a quadratic programming form. The discretised form of our functional may be formulated as follows:

$$\tilde{F}_M = -\sum_{k=1}^{n_p} \left[\left(\sigma_{xy,k}^{bil} + \sigma_{xy,k}^{corr} \right) B_{x_k} + f\left(\sigma_{yy,k}^{bil} + \sigma_{yy,k}^{corr} \right) \left| B_{x_k} \right| \right], \tag{5.34}$$

where

$$\begin{bmatrix} \sigma_{yy,k}^{corr} \\ \sigma_{xy,k}^{corr} \\ \sigma_{yy,k}^{bil} \\ \sigma_{xy,k}^{bil} \end{bmatrix} = \frac{1}{2} \begin{bmatrix} \sigma_{yy,j}^{corr} \\ \sigma_{xy,j}^{corr} \\ \sigma_{yy,j}^{bil} \\ \sigma_{xy,j}^{bil} \end{bmatrix} + \frac{1}{2} \begin{bmatrix} \sigma_{yy,j+1}^{corr} \\ \sigma_{xy,j+1}^{corr} \\ \sigma_{yy,j+1}^{bil} \\ \sigma_{xy,j+1}^{bil} \end{bmatrix}. \tag{5.35}$$

Then, the discretised form of the dislocation density (5.21) is substituted into (5.33) to obtain:

$$\tilde{F}_M = -\sum_{k,j=1}^{n_p} \left[\left(\sigma_{xy,k}^{bil} + \sigma_{xy,k}^{corr} \right) \frac{h_j - h_{j+1}}{d_{\sup}} + f\left(\sigma_{yy,k}^{bil} + \sigma_{yy,k}^{corr} \right) \left| \frac{h_j - h_{j+1}}{d_{\sup}} \right| \right]. \tag{5.36}$$

The difference $h_j - h_{j+1}$ can be replaced by ζ_j and, as $d_{\sup}$ is a positive parameter, it can be

removed from the functional, giving

$$\tilde{F}_M = -\sum_{k,j=1}^{n_p} \left[\left(\sigma_{xy,k}^{bil} + \sigma_{xy,k}^{corr} \right) \zeta_j + f \left(\sigma_{yy,k}^{bil} + \sigma_{yy,k}^{corr} \right) |\zeta_j| \right]. \tag{5.37}$$

This time it is the presence of the absolute value of the relative displacement, ζ_j which complicates the formulation and it is replaced using the same procedure as that described in the previous section, *mutatis mutandis*, so that the problem can be written as follows:

$$\underset{\min}{\tilde{F}_M} = -\sum_{k,j=1}^{n_p} \left[\left(\sigma_{xy,k}^{bil} + \sigma_{xy,k}^{corr} \right) \left(\zeta_j' - \zeta_j'' \right) + f \left(\sigma_{yy,k}^{bil} + \sigma_{yy,k}^{corr} \right) \left(\zeta_j' + \zeta_j'' \right) \right] \tag{5.38}$$

where

$$\begin{aligned} \begin{bmatrix} \sigma_{yy,j}^{corr} \\ \sigma_{xy,j}^{corr} \end{bmatrix} &= A_{SM,DM} \sum_{k,j=1}^{n_p} \frac{\zeta_j}{d_{\sup}} \int_{x_k - d_{\sup}}^{x_k} \left(1 + \frac{x_k}{d_{\sup}} \right) \begin{bmatrix} G_{yy}(x_j, \xi) \\ G_{xy}(x_j, \xi) \end{bmatrix} d\xi + \\ &+ A_{SM,DM} \sum_{k,i=1}^{n_p} \frac{\zeta_j}{d_{\sup}} \int_{x_k}^{x_k + d_{\sup}} \left(1 - \frac{x_k}{d_{\sup}} \right) \begin{bmatrix} G_{yy}(x_j, \xi) \\ G_{xy}(x_j, \xi) \end{bmatrix} d\xi \end{aligned} \tag{5.39}$$

subject to

$$\sum_{k=1}^{n_p} B_{x_k} d_{\sup} = d \tag{5.40}$$

$$\zeta_j', \zeta_j'' \geq 0 \tag{5.41}$$

where d is the net slip accumulated after one passage of the load. Following the same procedure described in the previous section, the problem can be rewritten in a quadratic form and solved using commercial subroutines.

5.4 Numerical model validation

Extensive comparisons and test cases have been performed, to check the correctness of the formulation and its implementation. These include, for example, the problem of uniform compression, everywhere, applied to the surface of a strip pressed onto an elastically similar half-plane, and with a supplementary line force applied to the free surface, at the origin of the coordinate system shown in Figure 5.3.

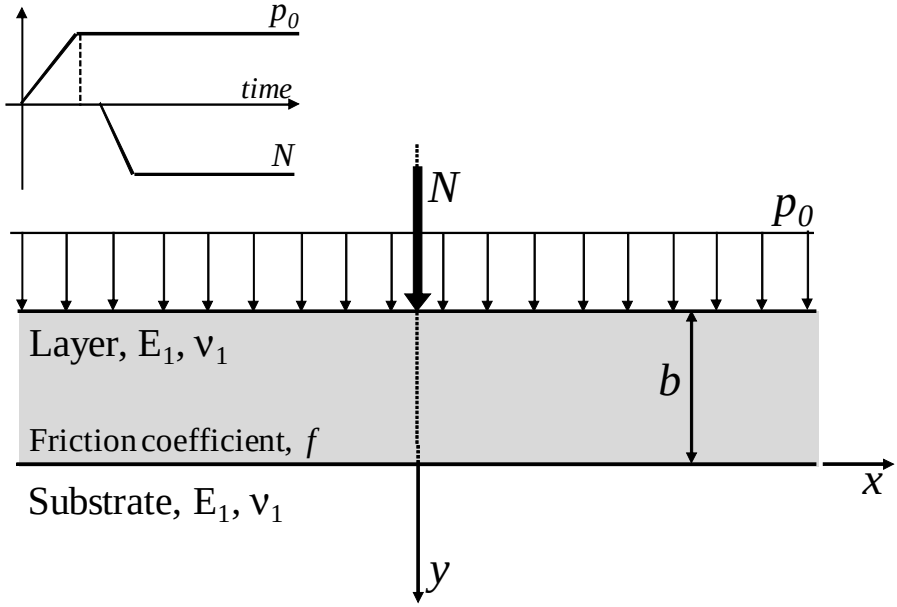


Figure 5.3. Geometry of the present problem and loading conditions.

The bilateral solution to the elastic problem (Timoshenko and Goodier, 1970) is

$$\sigma_{xy}^{bil}(x) = +\frac{2N}{\pi b}\frac{b^3 x}{\left(b^2+x^2\right)^2} \tag{5.42}$$

$$\sigma_{yy}^{bil}(x) = -\frac{2N}{\pi b}\frac{b^4}{\left(b^2+x^2\right)^2} - p_0, \tag{5.43}$$

where b is the layer thickness, N, the normal load per unit depth applied to the system and p_0 the uniform constant pressure, or, in dimensionless terms

$$\frac{b\sigma_{xy}^{bil}(\tilde{x})}{N} = +\frac{2}{\pi}\frac{\tilde{x}}{\left(1+\tilde{x}^2\right)^2} \tag{5.44}$$

$$\frac{b\sigma_{yy}^{bil}(\tilde{x})}{N} = -\frac{2}{\pi}\frac{1}{\left(1+\tilde{x}^2\right)^2} - \frac{1}{\lambda_N} \tag{5.45}$$

where $\tilde{x} = x/b$ and $\lambda_N = N/\left(bp_0\right)$. It is assumed that the surface pressure is applied first and then the line force increased from zero to a particular value. Figure 5.4 shows the slip regions predicted with the formulation described, for $f = 0.25$ and $\lambda_N = 2$, compared with the results achieved with a classical iterative scheme where the symmetry in x was used to avoid treating the simulatenous

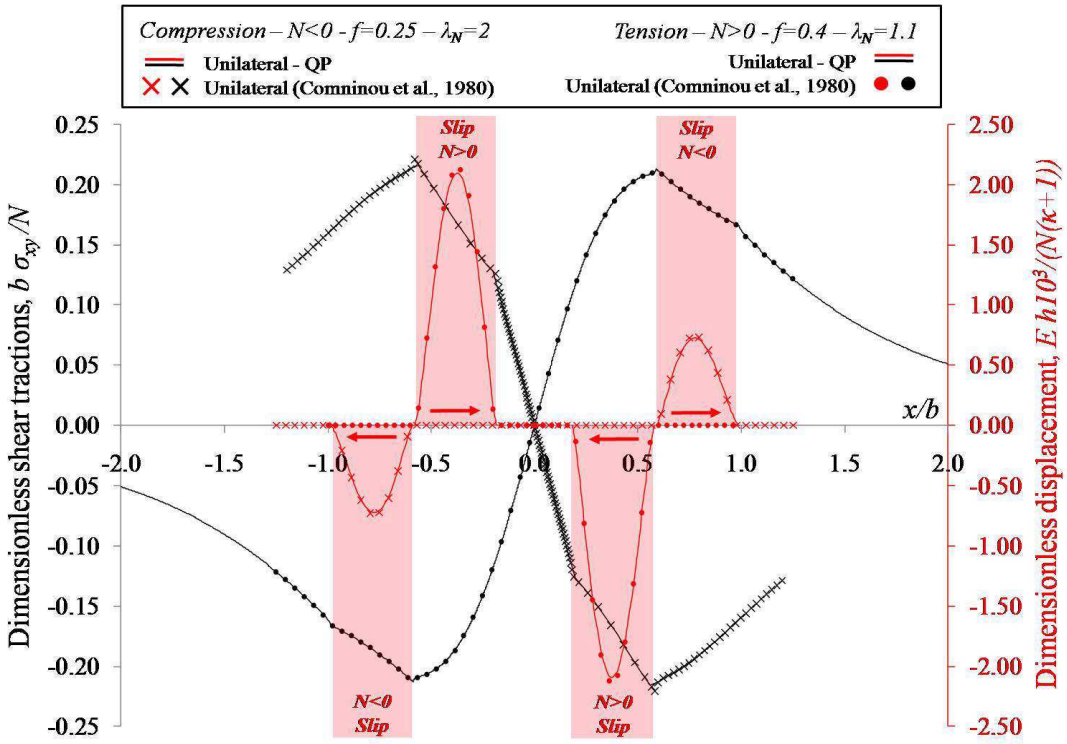


Figure 5.4. Shear tractions and relative displacement between layer and substrate for f=0.25, $\lambda_N = 2$ ($N < 0$) and f=0.4, $\lambda_N = 1.1$ ($N < 0$) - stationary case.

presence of multiple slip areas (Comninou et al., 1980). λ_N is here treated as un unknown of the problem (Comninou et al., 1980). On the same graph, results for a tensile force, where $\lambda_N = 1.1$ and $f = 0.4$, are plotted (Comninou et al., 1980). The figure shows the accuracy of the numerical scheme in capturing the location and the extent of the slip region, the local relative displacement and the shear stress distribution at the layer/substrate interface.

A variant on this problem is to apply a surface shearing force (Timoshenko and Goodier, 1970), Q, and this gives a state of interfacial tractions, in the same dimensionless variables, as

$$\frac{b\sigma_{xy}^{bil}(\tilde{x})}{Q} = +\frac{2}{\pi}\frac{\tilde{x}^2}{(1+\tilde{x}^2)^2} \tag{5.46}$$

$$\frac{b\sigma_{yy}^{bil}(\tilde{x})}{Q} = -\frac{2}{\pi}\frac{\tilde{x}}{(1+\tilde{x}^2)^2} - \frac{1}{\lambda_Q} \tag{5.47}$$

where now $\lambda_Q = Q/bp_0$. Figure 5.5 shows the results obtained with our formulation for $\lambda_Q = 2.36$

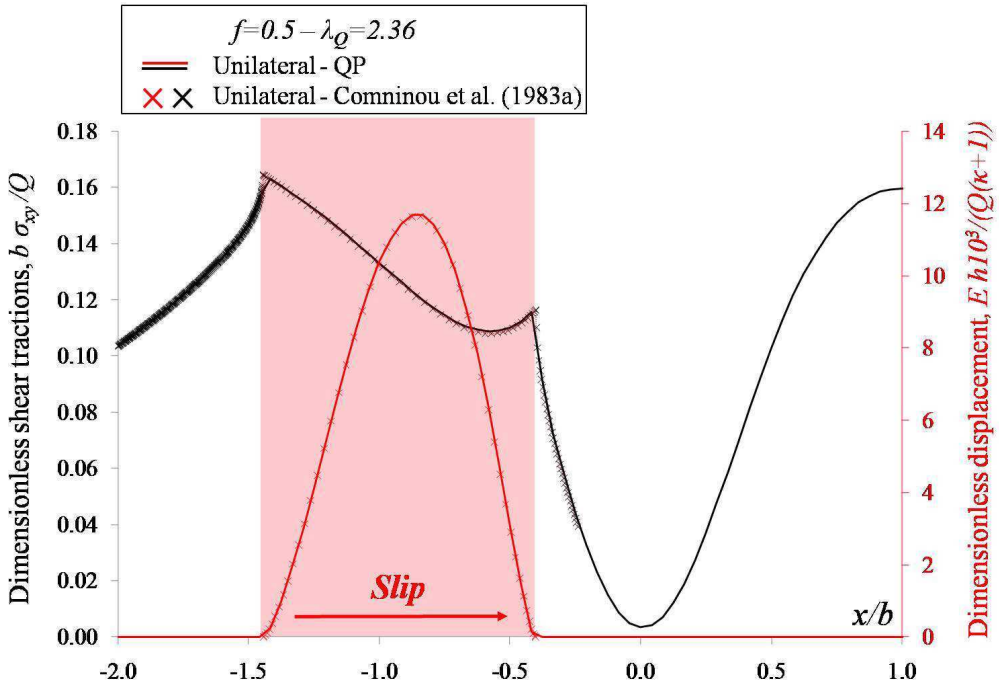


Figure 5.5. Shear tractions and relative displacement between layer and substrate for f=0.5, $\lambda_Q = 2.36$ - stationary case.

and $f = 0.5$, plotted together with the results calculated with the classical semi-analytical iterative scheme. Also in this case the results were shown to match the semi-analytical results obtained using the formulation in Comninou et al. (1980).

5.4.1 Cyclic loading - Tangential load - similar materials

So far, the load has been increased monotonically. In the following case, the tangential load of the example case shown in Figure 5.5 ($\lambda_Q = 2.36$ and $f = 0.5$) is first fully reversed ($\lambda_Q = -2.36$) and then cycled ($\lambda_Q = -2.36 \leftrightarrows 2.36$). This example enables us to show how the novel method allows us to track the "marching in time" solution. The same loading scenario was explored by Comninou and Barber (1983a), who, based on the numerical results obtained during their investigation, first introduced the frictional shakedown concept - and its analogy with plastic shakedown - in the context of layered frictional systems.

The tractions at the interface when the load is monotonically increased are given in the previous

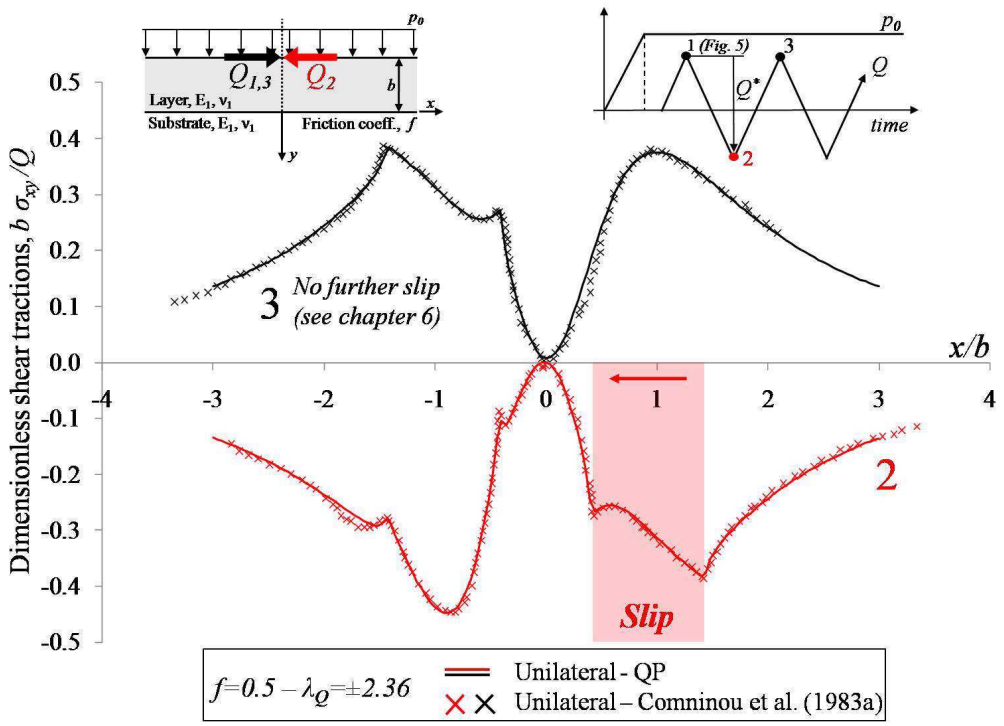


Figure 5.6. Shear tractions for f=0.5 and $\lambda_Q = \pm 2.36$ (cyclic tangential load) - stationary case.

case and they are here referred to with the index 1 (point 1- Figure 5.6). When the tangential load is reduced, the solution to the problem (point 2 in the top-right inset to Figure 5.6) can be written in dimensionless form, as follows

$$\begin{bmatrix} \frac{b\sigma^2_{yy}(\tilde{x},0)}{Q_1} \\ \frac{b\sigma^2_{xy}(\tilde{x},0)}{Q_1} \end{bmatrix} = \begin{bmatrix} \frac{b\sigma^1_{yy}(\tilde{x},0)}{Q_1} \\ \frac{b\sigma^1_{xy}(\tilde{x},0)}{Q_1} \end{bmatrix} + \begin{bmatrix} \frac{2}{\pi}\Delta Q \frac{\tilde{x}^2}{(1+\tilde{x}^2)^2} \\ -\frac{2}{\pi}\Delta Q \frac{\tilde{x}}{(1+\tilde{x}^2)^2} \end{bmatrix} + \begin{bmatrix} \sigma^{corr,2}_{yy}(\tilde{x}) \\ \sigma^{corr,2}_{xy}(\tilde{x}) \end{bmatrix} \tag{5.48}$$

where ΔQ is the difference between Q_1 and Q^*, with Q^* being $2Q_1$ (see Figure 5.6), $\sigma^1_{yy}(\tilde{x},0)$ and $\sigma^1_{xy}(\tilde{x},0)$ are the corrected stress field for the condition 1, and $\sigma^{corr,2}_{yy}(\tilde{x})$ and $\sigma^{corr,2}_{xy}(\tilde{x})$ the corrective terms to be superposed to modify the Flamant solution (Timoshenko and Goodier, 1970) introduced for the condition 2. The solutions for successive time steps can be calculated following exactly the same procedure.

Figure 5.6 shows the results calculated with our numerical scheme for $\lambda_Q = 2.353$ and $f = 0.5$ plotted along with the results achieved with the classic iterative scheme. As can be seen from the figure, the match between the results is very satisfactory.

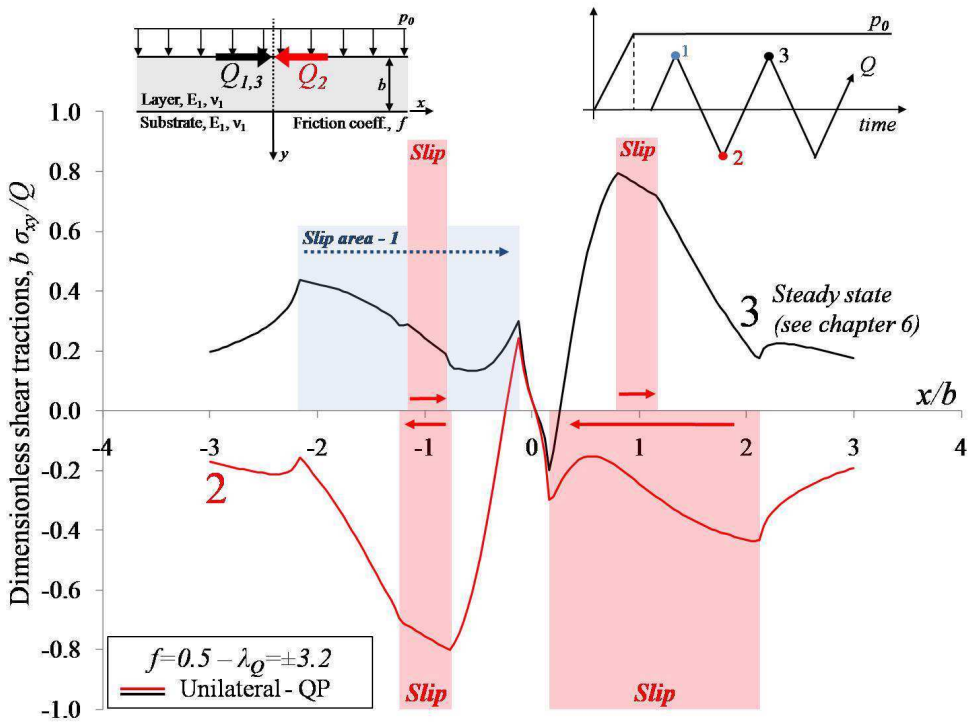


Figure 5.7. Shear tractions for f=0.5 and $\lambda_Q = \pm 3.2$ (cyclic tangential load) - stationary case.

As already mentioned, results reported in (Comninou and Barber, 1983a) were calculated for values of pressure such that the frictional law was violated at along the layer/substrate interface at only limited positions throughout the cycle. Subsequently, further investigations were limited to simplified loading scenarios. This limitation is here circumvented by our numerical scheme and many other loading regimes can be investigated. Figure 5.7 shows an example case where multiple slip areas are simultenously present during the loading and the unloading phases.

More complex regimes of frictional creep and frictional shakedown may be now investigated and this aspect will be extensively discussed in Chapter 6.

The numerical scheme proposed has also been applied to the more practical contact problem illustrated in Chapter 2. An example case is shown in Figure 5.8 where f=0.2, $\mu = 0.7$ and $\lambda = 1$. In this case the layer is elastic whilst the substrate is rigid. As can be seen from the figure, the match between the results is also very satisfactory for this case.

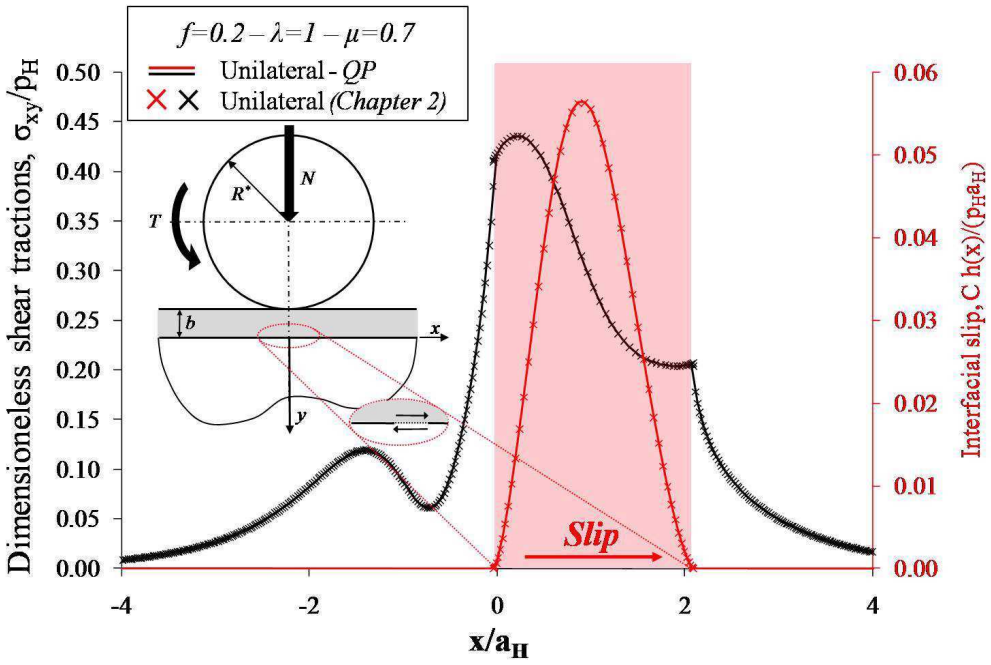


Figure 5.8. Shear tractions and relative displacement between layer and substrate for B=1, f=0.2, $\mu = 0.7$, $\lambda = 1$ and $\nu = 0.3$ - stationary case - full sliding of external contact over layer surface.

5.4.2 Moving load

The extension of the technique described above to model the effect of stationary loads to model moving load scenarios (section 5.3) was also tested.

The numerical scheme has been first validated against the case shown in Figure 5.3, where the compressive normal load is now moved along the layer surface at constant speed. The case was treated by Chang et al. (1983) who showed that, in general, two slip zones are always present at the interface between layer and substrate. The displacements accumulated in the two slip zones are opposite in sign, and Figure 5.9 shows an example case where the results obtained with our formulation for $\lambda_N = 8$ and $f = 0.5$ are plotted together with the results calculated with the classical semi-analytical iterative scheme (Chang et al., 1983). Moreover, Figure 5.10 shows the net displacement accumulated between layer and substrate as a function of the dimensionless contact pressure, λ_N, for f=0.5. As can be seen from the figures, the match between the results is satisfactory.

The numerical scheme has also been validated against the equivalent results in Chapter 2 achieved

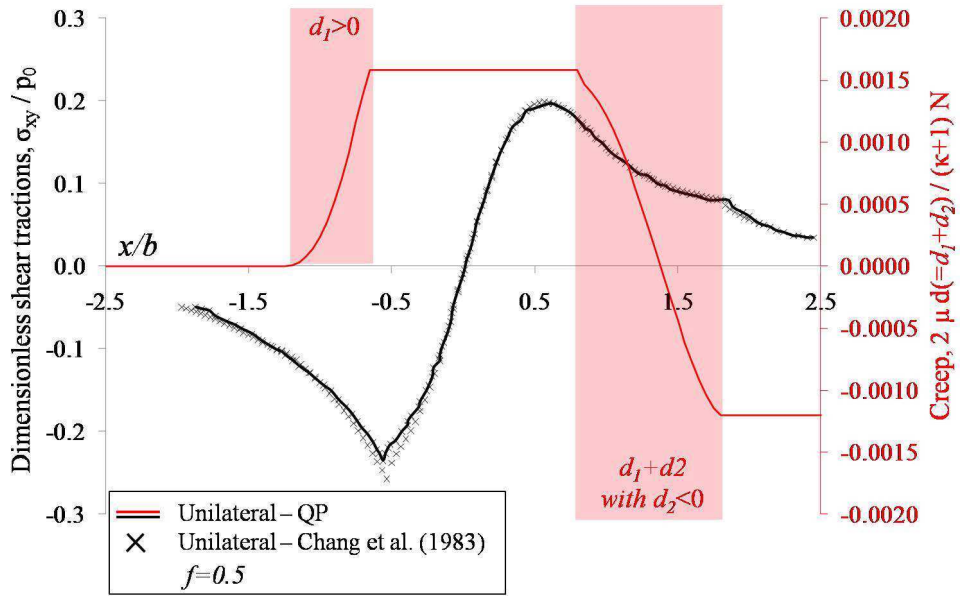


Figure 5.9. Shear tractions and relative net displacement between layer and substrate, d, for λ_N=8, for f=0.5.

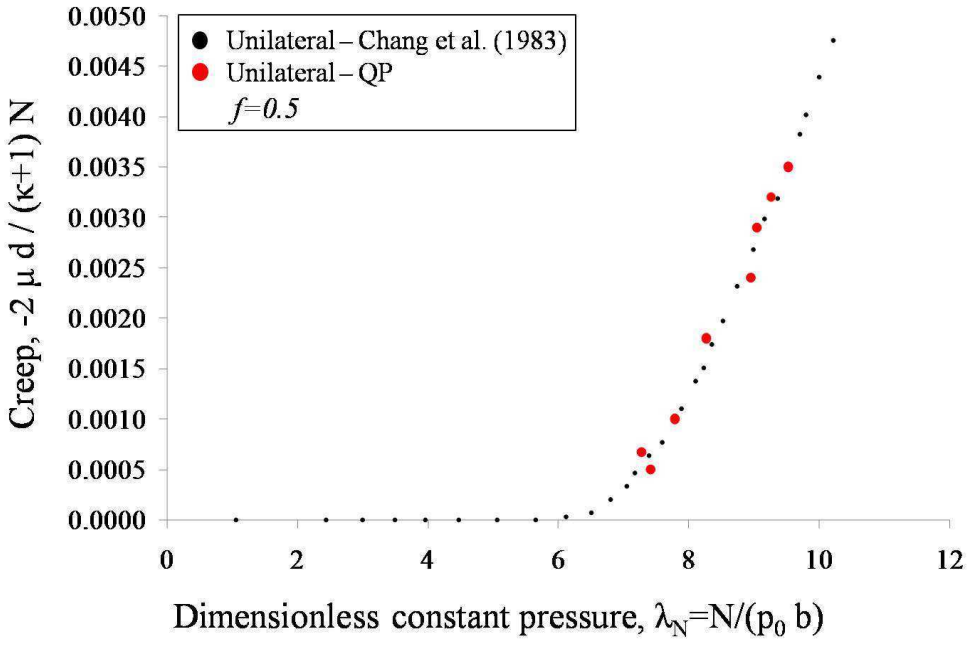


Figure 5.10. Relative net displacement, d, between layer and substrate as a function of the dimensionless constant pressure, λ_N, for f=0.5.

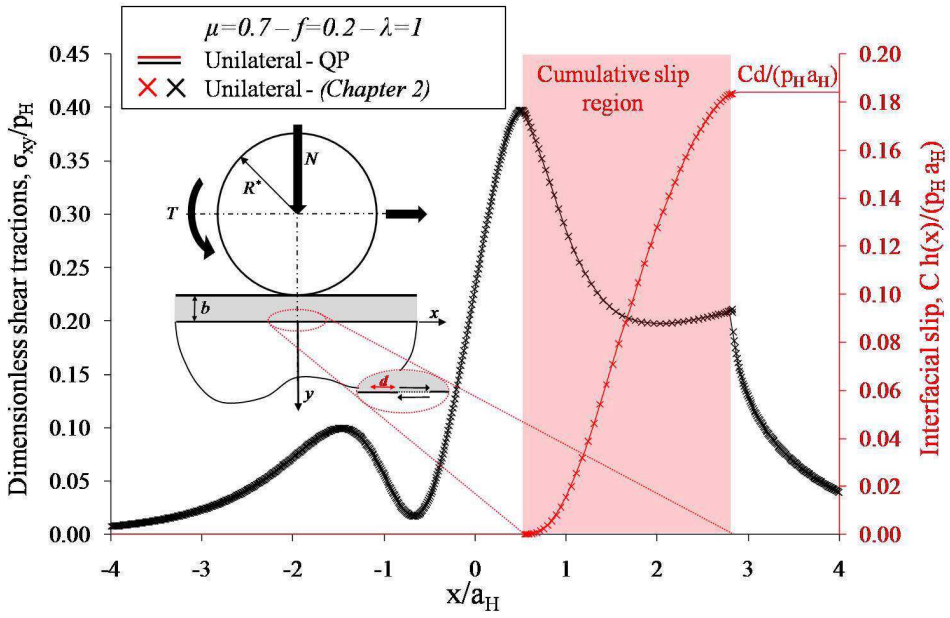


Figure 5.11. Shear tractions and relative net displacement, d, between layer and substrate for B=1, f=0.2, $\mu = 0.7$, $\lambda = 1$ and $\nu = 0.3$ - steady state solution for the moving load case - full sliding of external contact over layer surface.

using a semi-analytical approach. Figure 5.11 shows the results obtained with our formulation for a net displacement $d = 0.184$, $\mu = 0.7$, $f = 0.2$ and $\lambda = 1$. The comparison betwen the two sets of results shows again the accuracy of the proposed numerical scheme.

5.5 Experimental validation

The novel numerical tool has proved to be accurate and capable of resolving different loading scenarios.

An experimental investigation was deemed necessary to prove the technique here applied to model creep between a tyre and a wheel. The experimental work to be presented was carried out in collaboration with Dr. Yusuke Iida and Mr. Byron Po (Po, 2009). An experimental configuration is described which is capable of reproducing loading conditions simulated in our semi-analytical model (Chapter 2). Tests were performed by modifying an apparatus conventionally adopted to study micropitting (Lainé et al., 2008). The rig is shown in Figure 5.12 and is characterised by two main rotating shafts. The first shaft carries a large disk which drives three smaller shafts on

which layered rollers were mounted. The rollers were made of mild steel (*178HV*) and had shrink fitted steel tyres. The tyred rollers were denoted top ring, left ring and right ring (*ring internal radius=26.30mm; thickness=0.08mm*; *width=5mm*; *and average interference= 30-50*μm). This recalls the cases investigated before where an elastic layer was pressed onto an elastically similar substrate. The components were accurately manufactured so to guarantee a well controlled interference fit between roller and tyre ($R_{a,disk}$=0.82 μm; $R_{a,ring}$=1.31 μm). The second shaft drives the central roller against which the three tyred rollers are pressed. Torque-meters are mounted on the two main shafts in order to monitor and regulate the torque applied to the three rollers and to the central roller. The tests were run in pure rolling condition (Chang et al., 1983; and Anscombe and Johnson, 1974). Frictional properties of the layer-substrate interface have been investigated and the interfacial friction coefficient was measured by using a compressive test (INSTRON test apparatus - www.instron.co.uk) adapted to press the rings onto the discs. During the fitting process, the relative displacement between disk and ring was carefully recorded, together with the pressing force. The friction coefficient was then estimated by dividing the resultant radial force found from intereference calculations by the measured load used to press-fit the tyred disks. Figure 5.13 shows an example case where the friction coefficient was measured during the fitting process. As can be note from Figure 5.13, the friction coefficient levels off towards the end of the mounting process (therefore after that the instabilities linked to the mounting process are overcome). The final value corresponds to the elastic layer fully mounted on the roller and, therefore, is the coefficient of friction that characterises the coupling. Hence, this is the value to be used to simulate the system using analytical or numerical simulations. It should be also noted here that, in order to reduce the friction coefficient between ring and shaft, so to produce creep between the mating surfaces under the loading conditions that can be applied using the MPR test apparatus, a layer of dry spray coating (Molycote D321 - www.dowcorning.com) was applied at the contact interface

Figure 5.14 shows a series of experimental results where the incremental creep, d obtained for

different values of the layer/substrate friction coefficient, f, is plotted against, λ_N, a function of the constant pressure uniformly applied to the layer, p_0. The quantities d (*3-4μm/cycle on average*) and p_0 (*5-10 MPa on average*) are normalized with respect to the normal load applied to the counter-disc, *N* (*load=120N/mm*), the Young's modulus of the material, E, the Kolosov's constant, κ, and the layer thickness, b *(0.08mm)*. Also reported in Figure 5.14 are the predictions obtained using the newly developed numerical techniques presented in this chapter. The qualitative agreement between the model and the experiments demonstrates that the model is able to capture the behavior of the system. The discrepancies in the results are mainly due to the uncertainties in the measurement of the coefficient of friction between the layer and the substrate. Moreover, experimental results obtained by Anscombe and Johnson in 1974 for the same kinematic configuration, pure rolling, are plotted in the inset to Figure 5.14 (Anscombe and Johnson, 1974). As already shown by Chang et al. (1983), Johnson's experiments are not in line with the model predictions. The main causes are the presence of plasticity effects together with misalignments occured during the tyre fitting process. The latter aspect resulted being the most critical in our experimental work. In fact, misalignments during the fitting process may cause permanent deformation in the ring and, consequently, creep is accumulated at a higher rate with respect to the model predictions. This is because the interference pressure is reduced by local increase in the ring diameter due to plasticity effects.

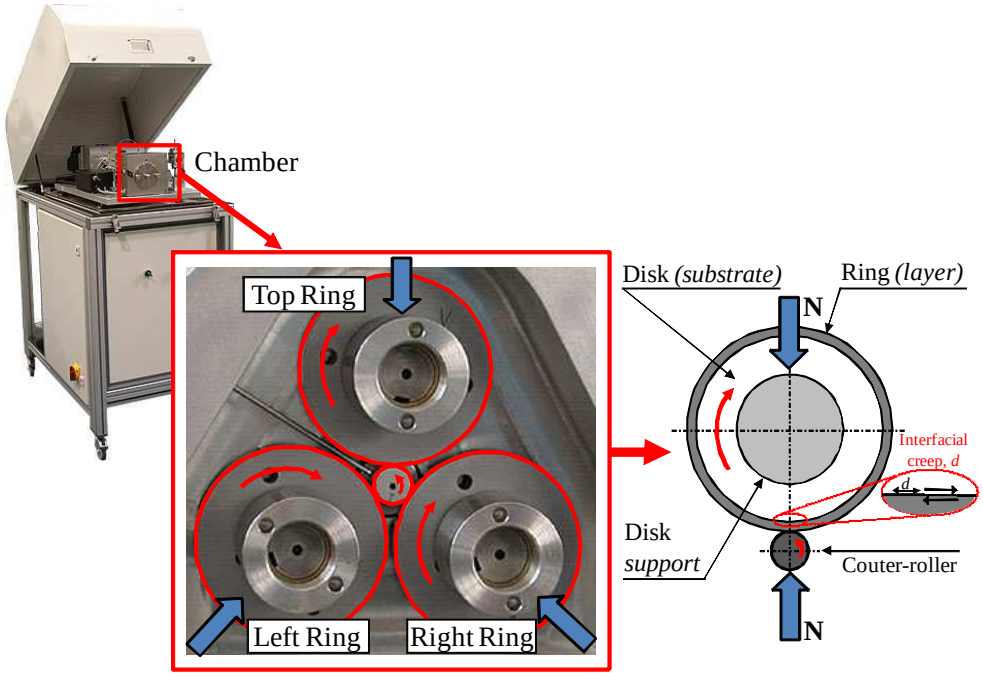


Figure 5.12. PCS MPR (*www.pcs-instruments.com/mpr*) experimental apparatus consisting of three tyred rollers and a central roller and schematic of the loading system.

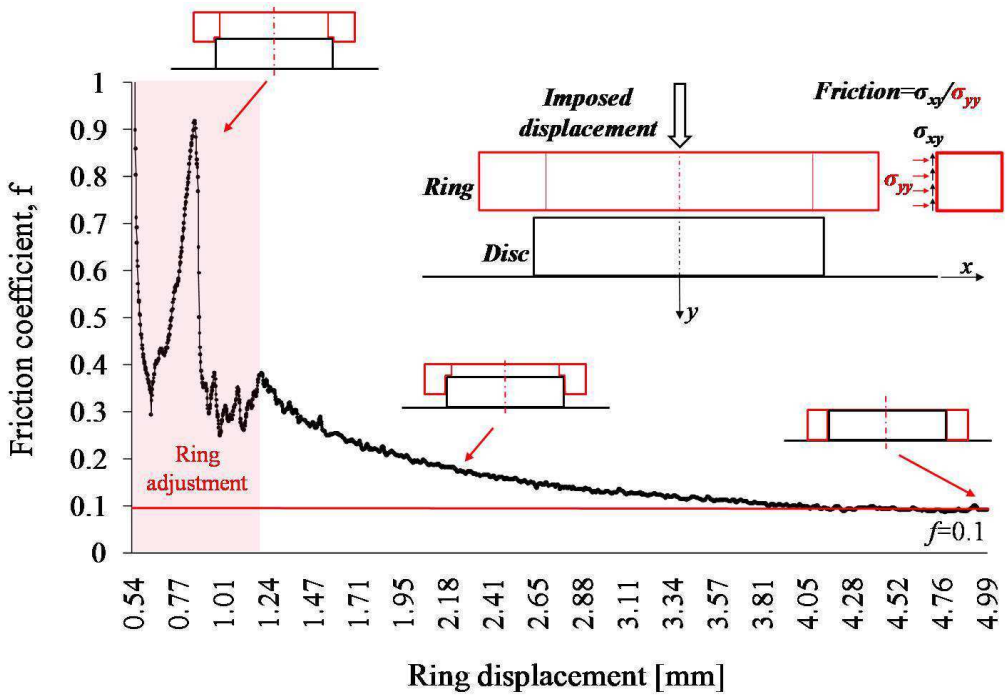


Figure 5.13. Friction coefficient versus ring displacement measured in the compression test.

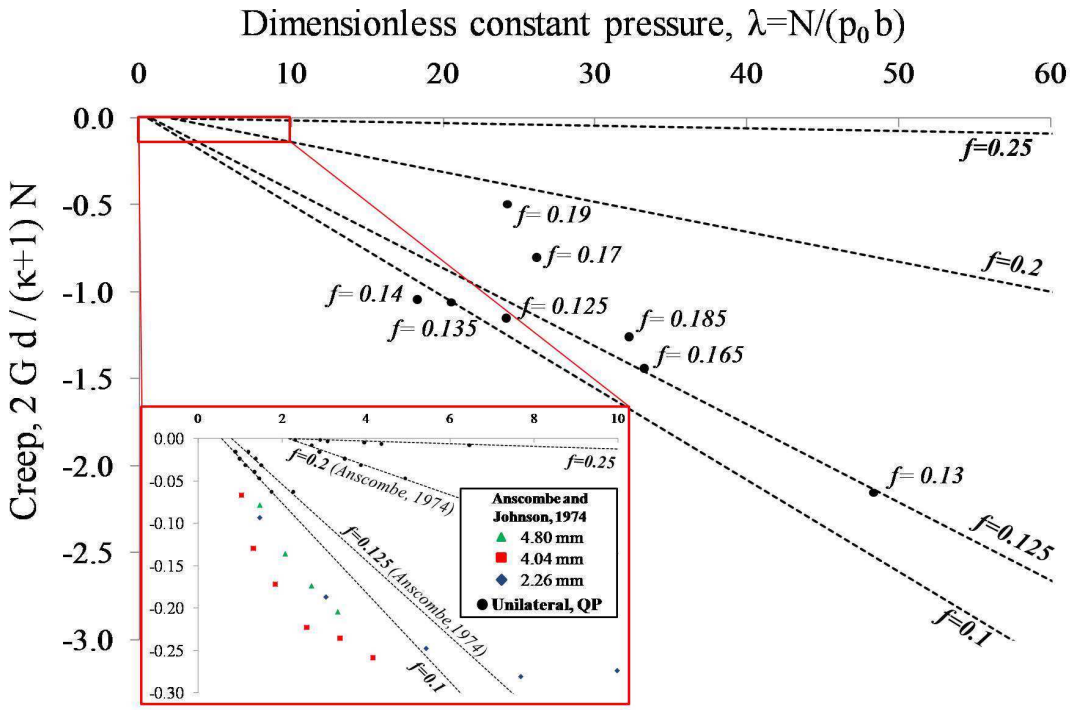


Figure 5.14. Net displacement, *d*, per revolution as a function of the dimensionless constant pressure, λ, and of the interfacial friction coefficient, *f*. In the same graph, comparison with experimental results and, in the inset, with Anscombe's original data classified based on ring thickness (Anscombe et al., 1968 and Chang, 1983).

5.6 Summary

A novel numerical method previously applied to track the "marching in time" solution for incomplete contact problems has been here modified and extended to investigate interfacial slip modelled using the distributed dislocation technique. The numerical scheme has been shown to be accurate and efficient, and, therefore, it enables us to extend the applicability of the distributed dislocation technique to the solution of complex two-dimensional layered systems when slip is present at the mating interfaces. A series of complex scenarios is indeed considered in Chapter 6 to study the frictional shakedown characteristics of these assemblies.

Chapter 6

Frictional shakedown of layered systems

6.1 Introduction

This chapter presents a preliminary investigation of frictional shakedown in layered systems using the quadratic programming technique outlined in Chapter 5. As explained in Chapter 1, micro-slip between mating surfaces often occurs in the presence of a periodic loading conditions. This can either cease after a few cycles or, eventually, lead to system failures (Antoni et al., 2007). When slip ceases after a few cycles, the system is said to have shaken down (Barber et al., 2008). Given the potential implications to design improvements a better understanding of this phenomenon would yield, an investigation of this important aspect of the tribological behaviour of elastic frictional layered systems is undertaken in this chapter. Specifically, an energy parameter has been proposed and here adopted to analyse shakedown of such frictional systems. The possibility of extending plasticity theorems to frictional contact has also been contemplated. At this point it is important to acknowledge that the energy parameter was proposed by Prof. J.R. Barber during our long and fruitful discussions on the problem and most of the work presented in this chapter has greatly benefited from his insightful suggestions.

6.2 Description of the problem

The possibility of accumulating relative local micro-slip between frictional surfaces depends on the loading conditions to which the system is subjected, the coefficient of friction and the resid-

ual stresses which are generated cyclically when interfacial displacements occur. The presence of interfacial residual stresses associated with cyclic slip prompted many authors to develop an analogy between the plastic behaviour within monolithic bodies and the frictional behaviour of elastic frictional systems (Drucker, 1954). As previously explained in Chapter 1, this analogy has led to the following classification of the response of contact problems with frictional interfaces subject to periodic loading: (i) elastic frictional shakedown: adhesion is recovered after relative micro-slip occurs after a few loading cycles; (ii) plastic frictional shakedown: this implies the presence of constant but confined slip at the end of every loading cycle with no rigid body motion (iii) frictional ratchetting: micro-slip is progressively accumulated at every cycle. The scope of the current work is to systematically investigate the first two responses and the applicability of plasticity theorems to frictional shakedown problems in layered systems. Cyclic energy dissipation is used as a measure of the different regimes occuring during application of the oscillating loads.

In order to understand the frictional behaviour of layered systems, a 2D model consisting of an elastic layer uniformly pressed onto a half-plane and subject to different loading histories has been developed. In the current study, this model has been chosen to further investigate the behaviour of the type of mechanical couplings which have been analysed in this thesis. Figure 6.1 shows a schematic of the layered system under investigation together with the potential frictional responses of the assembly.

The contact between layer and substrate is guaranteed by the application of a uniform pressure, p_0. The interface between the mating surfaces is frictional, and considered to be characterised by a coefficient of friction, f. The Coulomb-Amonton's frictional law is adopted and the coefficient of friction is, therefore, assumed to be independent of the slip velocity. If the frictional law is locally violated, slip arises and may be accounted for by introducing a dislocation distribution at the layer/substrate interface using the optimisation technique described in Chapter 5. Separation may also occur but this is not considered in the current model. As already discussed by many authors

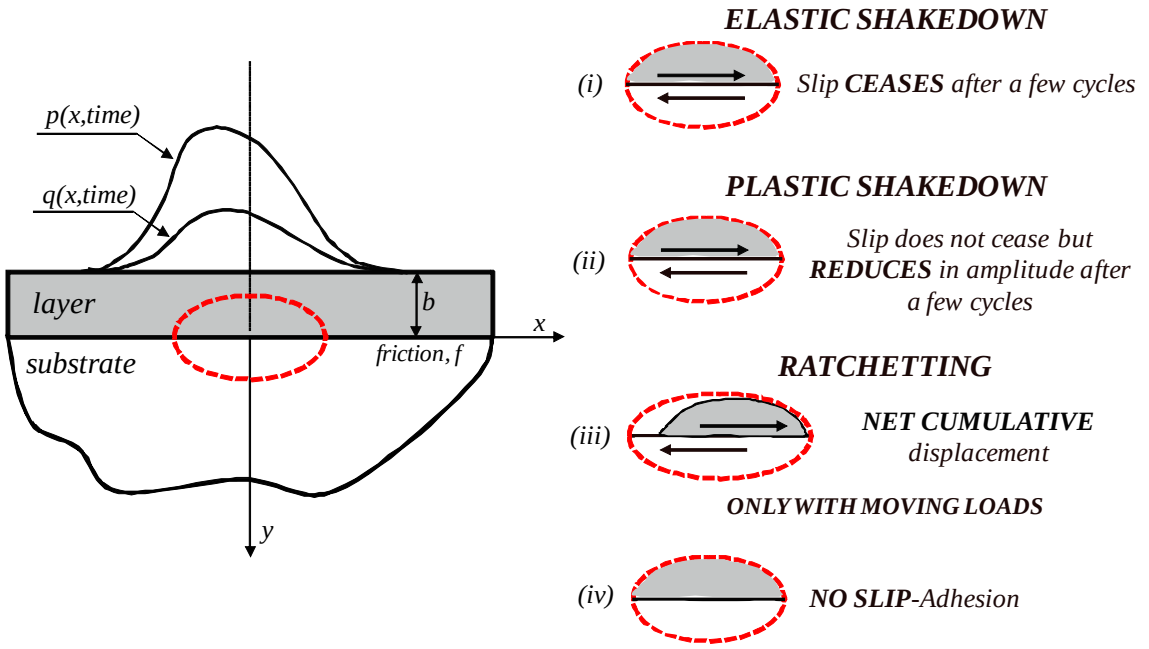


Figure 6.1. Schematic of the elastic contact problem and potential frictional shakedown responses.

(Antoni et al., 2007 and Barber et al., 2008), the final frictional response of the assembly depends on the inherent coupling present within the system. Coupling in the current context is defined as the direct influence of tangential displacements on the distribution of normal tractions. The system considered in this study is inherently coupled because the layer is allowed to slip and any area of slip always modifies the distribution of normal tractions. This can be explained by looking at the change in the normal tractions at the layer interface when glide dislocations are deployed to account for slip (see Chapter 2 - Section 2.4.2). Furthermore, for our problem different elements contribute to the coupling, which leads to the follow simplistic classification: (i) material coupling: when there is a difference between the elastic properties of layer and substrate; (ii) geometric coupling: when the layer surface normal and shear tractions depend on the layer thickness. In this chapter an attempt to single out and investigate the role of these contributions to the coupling on the steady state frictional response of the system in terms of "elastic" and "plastic" frictional shakedown is made. The idea is to tune the coupling by independently activating or modifying material and geometric effects either by changing the mechanical properties of layer and substrate or by adopting loading

boundary conditions which vary with the layer thickness.

The tribological response of the system as classified in Figure 6.1 can be monitored using the frictional energy dissipated per loading cycle. In particular, the dissipated energy is computed as the integral of the work done by the shear tractions along the interface in the presence of relative interfacial displacements. Its value goes to zero when adhesion occurs at all points within the contact and it has a finite value when slip occurs. This means that when "elastic" shakedown occurs the energy goes to zero after a few cycles, whilst it is finite in case of either "plastic" shakedown or "ratchetting". The reader should note that "ratchetting" may occur only in presence of moving loads.

Regarding the possibility of using plasticity theorems to predict the steady state response of the system, the range of applicability of Melan's lower bound shakedown theorem to this class of contacts has been contemplated. Barber et al. (2008) proved that, in general, for systems with coupling between slip displacements and normal contact tractions, such as that discussed here (Fig. 6.1), which is inherently coupled, and those in Chapters 2 and 5, Melan's theorem does not apply due to the non associative nature of the frictional law. A counter example, which disproves it, can always be found. In such circumstances the error that one would commit when applying Melan's theorem out of context is aimed to be measured.

The main advantage of using the theorem (if, indeed, it does apply) is that the shakedown condition can be determined from the bilateral solution alone. The shakedown limit may then be found following the same method implemented by Churchman and Hills (2006), where it is assumed that the Melan's theorem applies to frictional interfaces. A residual shear traction, $\sigma_{xy,res}(x)$, is assumed such that at a critical point the interface is about to slip in one direction at one end of the loading cycle and in the opposite direction at the other end of the cycle. This point is unknown *a priori* but can be located numerically following the procedure outlined below. The minimum value of friction coefficient, f_{Melan}, needed for the system to shake down to a state of no slip between the layer and

the substrate at a generic point along the interface can be determined as follows:

$$f_{Melan}(x) = (\sigma^{bil}_{xy,\max}(x) + \sigma_{xy,res}(x))/(\sigma^{bil}_{yy,\max}(x) + p_0) \quad (6.1)$$

$$= -(\sigma^{bil}_{xy,\min}(x) + \sigma_{xy,res}(x))/(\sigma^{bil}_{yy,\min}(x) + p_0) \quad (6.2)$$

The right hand side of equation (6.1) is first found along the layer/substrate interface to determine $\sigma_{xy,res}(x)$. The residual shear stress distribution is then substituted back into the same equation to find:

$$f_{Melan}(x) = (\sigma^{bil}_{xy,\max}(x) - \sigma^{bil}_{xy,\min}(x))/(\sigma^{bil}_{yy,\max}(x) + \sigma^{bil}_{yy,\min}(x) + 2p_0), \quad \forall x. \quad (6.3)$$

The thing which is so "useful" about this is that, unlike elastic shakedown in plastically deformed bodies, where the residual stress field postulated must satisfy the field equations, there is a free choice of $\sigma_{xy,res}(x)$.

In the following sections, a series of simplified contact problems are presented with the aim of quantifying the effect of the coupling on shakedown thresholds.

6.3 Results

6.3.1 Simplified loading cases - Flamant's problem

Consider the frictional shakedown behaviour of the contact problem illustrated in Figure 6.2. This system is adopted to quantify the effect of coupling induced by the material dissimilarity between layer and substrate. In terms of elastic shakedown, this is carried out by first applying Melan's theorem "out of context" and measuring the discrepancy with the actual response of the system computed using a marching-in-time formulation. This is followed by the application of different initial boundary conditions obtained by applying a pre-load to the system (see Figure 6.2(ii) and 6.2(iii)). This test is important in assessing if Melan's theorem can be applied approximately and

with a certain degree of confidence to weakly coupled systems. In fact, a corollary of Melan's theorem is that if it does apply, the solution of the problem does not depend on the initial boundary or loading conditions applied to the system. However, this should not be the case because of the presence of a coupled system.

The steady state response will be assessed in terms of elastic and plastic shakedown. A preliminary investigation had been carried out by Comninou and Barber (1983a) for the case of a concentrated cyclic tangential force applied to an elastic layer pressed onto an elastically similar substrate (Fig. 6.2(i)). For that case, the bilateral solution to the contact problem is available in closed form (Timoshenko and Goodier, 1970) and the frictional response of the system depends on both the interfacial friction coefficient and on the constant pressure applied to the layer (Comninou and Barber, 1983a). The constant pressure can be expressed in dimensionless form as $\lambda_Q = Q/(p_0 b)$ using the notation adopted in Chapter 5. This term sums up the loading boundary conditions to which the system is subject (Comninou and Barber, 1983a). This case provides a foundation on which to expand the preliminary analysis of the problem. The energy parameter introduced above is here applied to characterise the tribological response of the assembly.

In order to demonstrate the use of the energy parameter, two example loading conditions were chosen. In the first case $f = 0.5$ and $\lambda_Q = 3.1$ whilst in the second $f = 0.5$ and $\lambda_Q = 4$. Figure 6.3 shows the response of the system for the two cases in terms of energy dissipated at the interface between layer and substrate. It can be seen that when $\lambda_Q = 3.1$, elastic shakedown results (i.e. no energy dissipation in the steady state), whilst the energy profile for $\lambda_Q = 4$ is typical of plastic shakedown behaviour. It is interesting to note that in these cases the steady state response of the system is reached within 3 load cycles.

Now that the ability of the energy parameter to discern the regimes of elastic and plastic shakedown has been demonstrated, it is important to study the boundaries of applicability of plasticity theorems to frictional problems. More specifically, it is important to consider the implications of

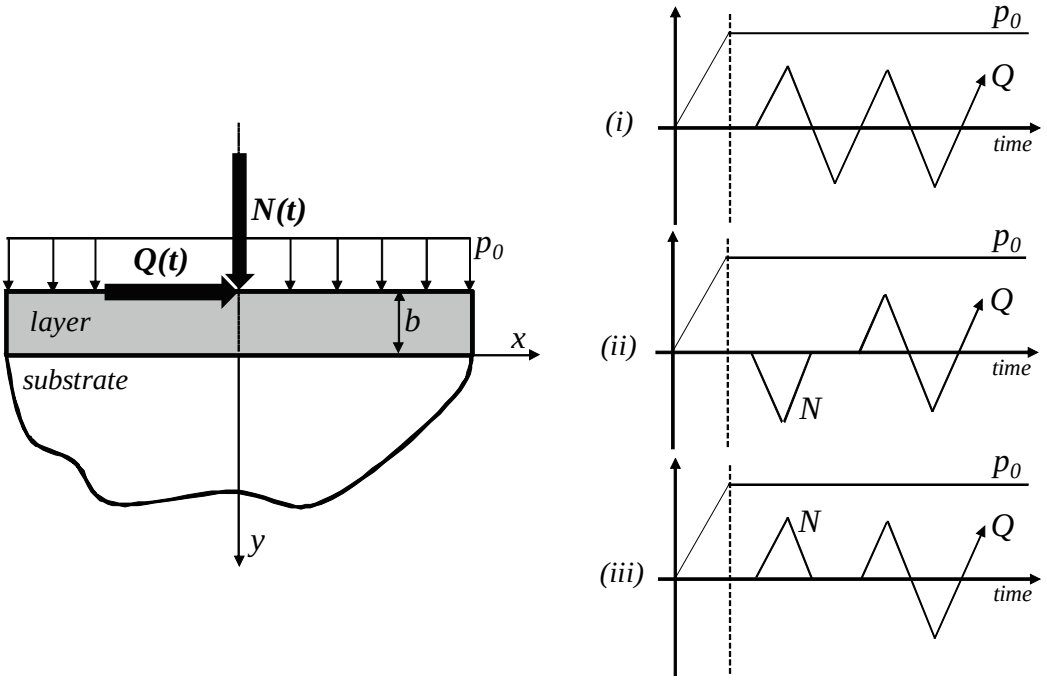


Figure 6.2. Schematic of the elastic contact problem and potential loading histories considered here.

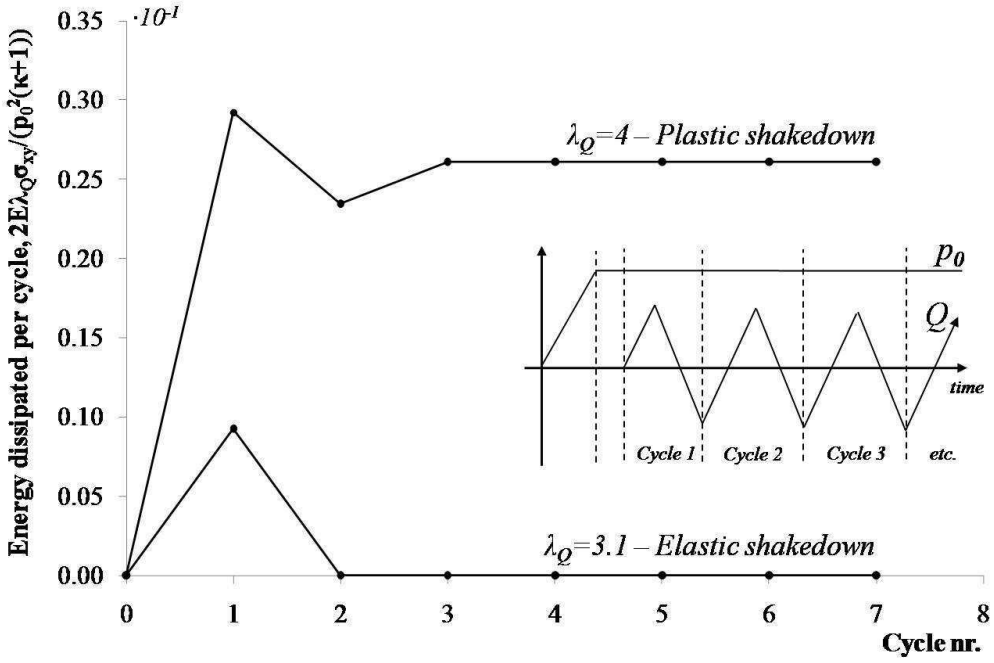


Figure 6.3. Energy dissipated per cycle for f=0.5 and $\lambda_Q = 3.1$ - elastic shakedown - and f=0.5 and $\lambda_Q = 4$ - plastic shakedown.

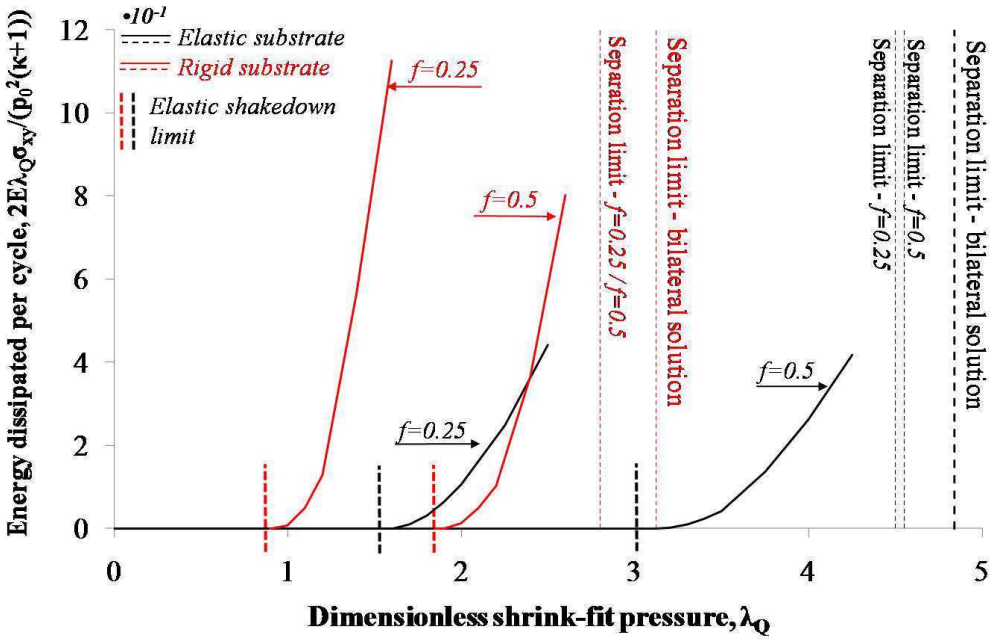


Figure 6.4. Energy dissipated per cycle (steady state) as a function of the dimensionless shrink-fit pressure, λ_Q, for an elastic layer resting on an elastically similar substrate and on a rigid substrate as a function of the dimensionless shrink-fit pressure, λ_Q, for f=0.25 and f=0.5.

using Melan's theorem "out of context". Consider the cases in which f=0.25 and f=0.5 for both rigid and elastic substrates. By introducing a rigid substrate a dissimilarity between the layer and the substrate is obtained. Figure 6.4 shows the frictional elastic shakedown limit and the plastic shakedown behaviour in terms of energy dissipated per cycle, computed using a marching-in-time solution following the formulation developed in Chapter 5, for the cases under investigation.

Figure 6.5 shows a comparison between the elastic shakedown limit computed using the code outlined in the previous chapter, and Melan's theorem predictions for an elastic layer on a rigid and on an elastically similar substrate. A very good agreement between the two results is achieved and this seems to suggest that the coupling induced by the material mismatch and by the finiteness of the layer seems to be negligible for this specific loading configuration.

The attention is now turned to the presence of different initial loading conditions. As mentioned above, if Melan applies, then the system shakes down regardless of the presence of pre-existing

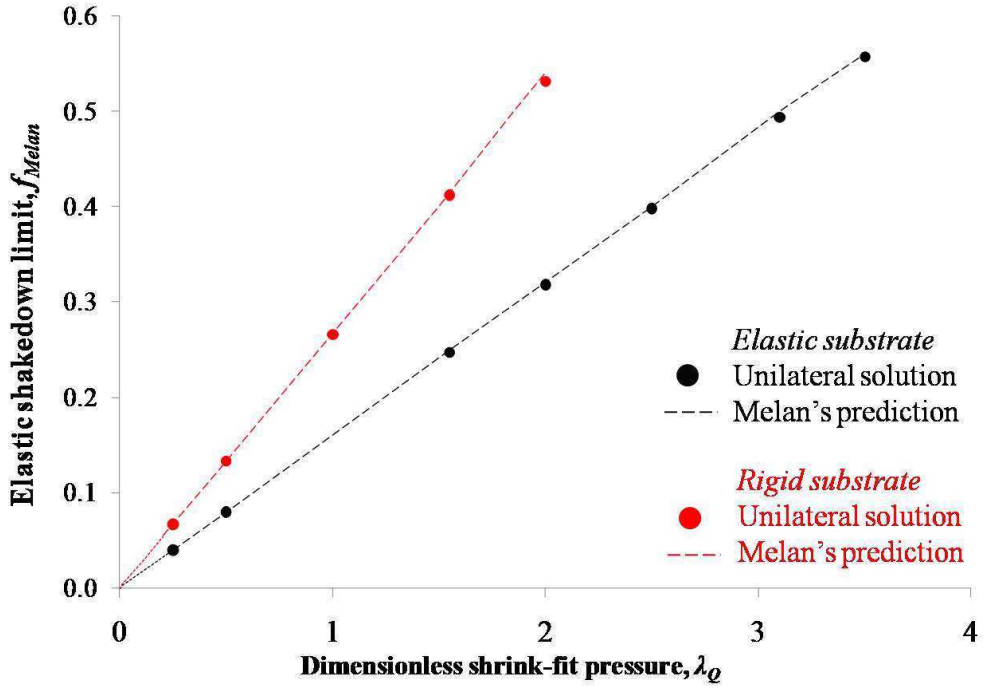


Figure 6.5. Comparison between the elastic shakedown limit as a function of the dimensionless shrink-fit pressure, λ_Q, predicted with Melan's theorem and the unilateral solution for an elastic layer resting on an elastically similar substrate and on a rigid substrate as a function of the dimensionless shrink-fit pressure, λ_Q.

residual stresses caused by different initial loading conditions. Recall the discussion in the second chapter (see Figure 2.9) concerning locked-in tractions induced by relative displacement between layer and substrate: here an example case is chosen to display the energy dissipation trend in the presence of different initial conditions. Figure 6.6 shows the energy dissipated between an elastic layer and an elastically similar substrate when different initial conditions are imposed ($N/Q = 3$ with N compressive - Figure 6.2(ii)) compared with the case where the tangential force was simply cycled ($N = 0$ - Figure 6.2(i)). For both cases λ_Q was set to 2.5 and the interfacial friction coefficient, f, to 0.25. The value of N/Q was chosen so that residual stresses are always generated when the normal load is first monotonically increased.

After a few cycles the two responses cannot be distinguished. Hence, our analysis was extended to different values of the dimensionless contact pressure λ_Q and the material coupling was included in a similar fashion to what was done for the case discussed above in the absence of pre-load. The

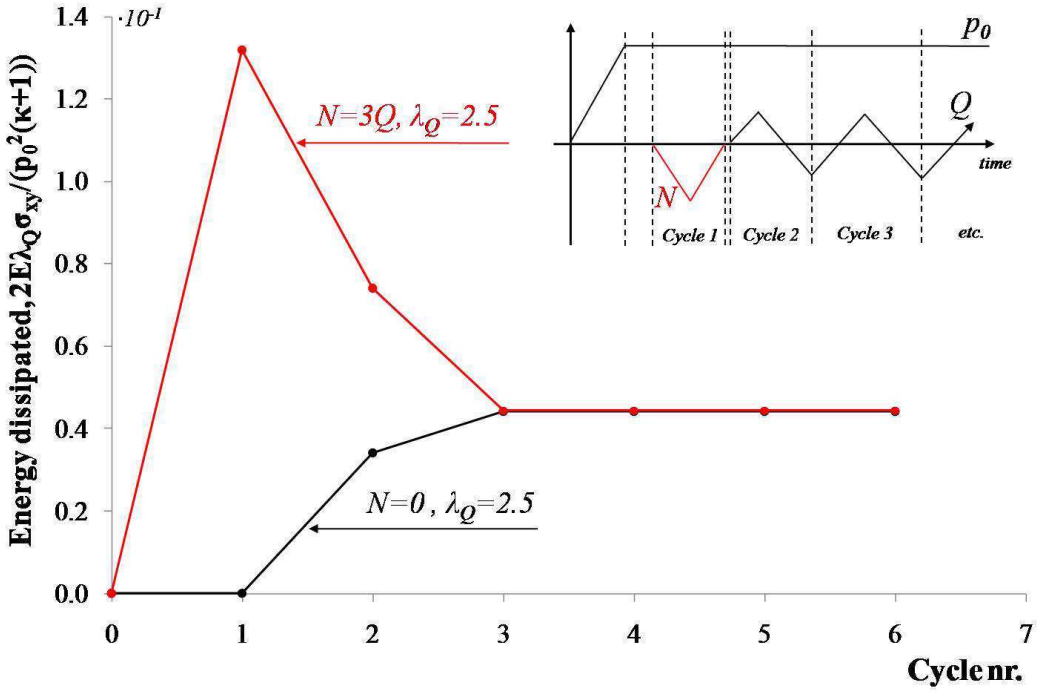


Figure 6.6. Comparison between the energy dissipated per cycle for a layer resting on an elastically similar substrate when different initial conditions are imposed.

initial condition $N/Q = 3$ was maintained for all cases analysed. Figure 6.7 shows how different initial conditions do not affect the steady state response of the system. Similarly, the same behaviour can be observed for a different set of initial conditions. In fact, for the case of $N/Q = 0.75$ with N tensile (i.e. "pinching" the layer, see Figure 6.2(iii)), Figure 6.8 shows how the steady state behaviour of the system is unaffected by the presence of initial residual stresses at the interface between layer and substrate. The value of N/Q was here chosen so that residual stresses are locked in for all cases and separation never occurs.

Up to this point the results suggest that the coupling due to material properties may be considered negligible for the geometry and the loading conditions investigated here. In other words, the system may be termed practically uncoupled from an engineering point of view.

So far only point forces as loading boundary conditions have been considered, and, therefore, the area of application of the load is infinitesimally small when compared to the geometry of the assem-

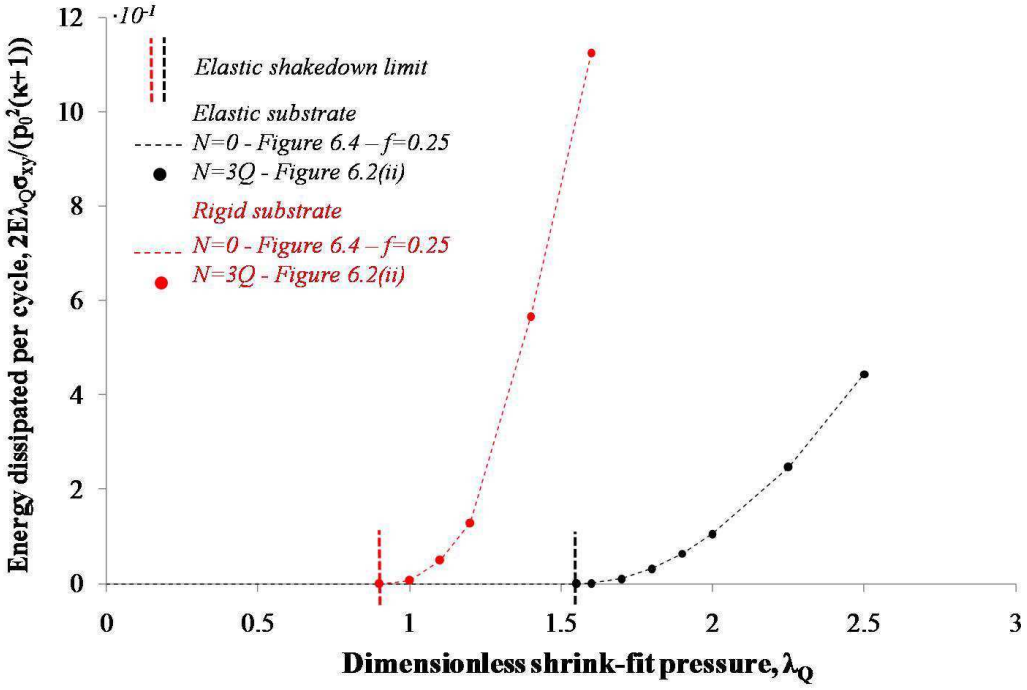


Figure 6.7. Comparison between the energy dissipated per cycle (steady state) as a function of the dimensionless shrink-fit pressure, λ_Q, when different initial conditions are imposed, for a layer resting on an elastically similar and rigid substrate - f=0.25 and $N < 0$.

bly. In the next section, the contact problem described in Chapter 2, where the coupling between loading boundary conditions and geometry of the assembly is present, is considered. This problem will be used as a vehicle to study the influence of geometric coupling on the system response in terms of shakedown.

6.3.2 Rolling problem

The schematic of the contact problem investigated here is shown in Figure 1.6(b). The rigid roller is now subject to an alternating normal force whilst the layer is maintained in position by a constant pressure uniformly applied to the layer surface.

The minimum friction coefficient to ensure shakedown is again implied by the application of Melan's theorem. Its value, f_{Melan}, is plotted in Figure 6.9 as a function of alternating load range, here represented by the variation of the minimum thickness to contact area ratio, $B_{\min}$ and with $B_{\max} = 1$, for different values of $\lambda = p_0/p_H$ (see inset to Figure 6.9).

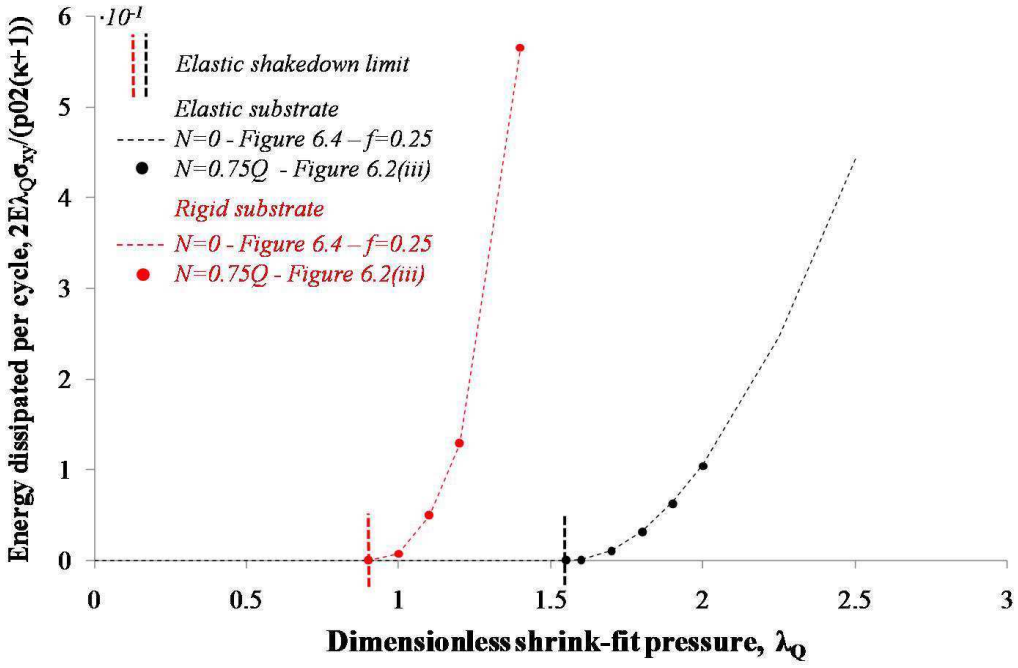


Figure 6.8. Comparison between the energy dissipated per cycle (steady state) as a function of the dimensionless shrink-fit pressure, λ_Q, when different initial conditions are imposed, for a layer resting on an elastically similar and rigid substrate - f=0.25 and $N > 0$.

Figure 6.10 also shows a comparison between Melan's theorem prediction (one of the curves already plotted in Figure 6.9) and the exact results, $f_{shakedown}$, obtained from the evolution of the shear traction response at the interface using a marching-in-time solution, obtained incrementally from the unilateral formulation. The coefficient of friction required for the avoidance of slip *from the outset* is also included in the figure. It is noted that the solution obtained using Melan's theorem underestimates the value of the friction coefficient required for the system to shake down in the presence of strong coupling (low values of $B_{\min}$), but provides a good approximation to the shakedown limit for large values of $B_{\min}$, i.e. in the presence of small coupling. It should be noted that the limit solution obtained for $B_{\min} \longrightarrow \infty$ corresponds to the case of a point load applied to the layer surface and, therefore, restores the conditions explored in previous sections. However, this consideration is valid only for the given initial loading condition investigated here (i.e. system unstressed and undeformed before the application of the normal indentation).

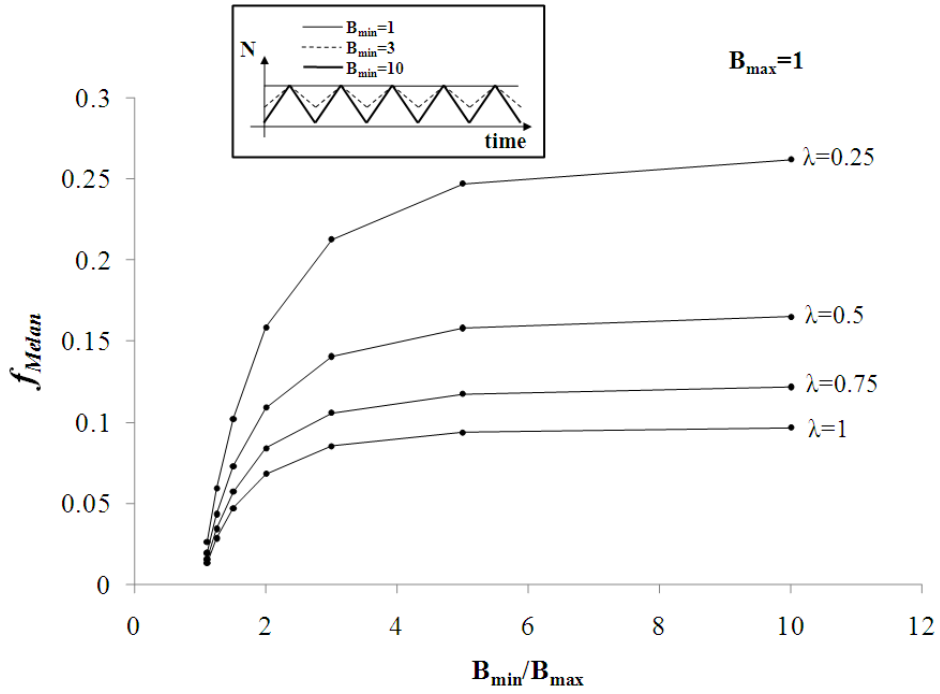


Figure 6.9. Minimum friction coefficient required to ensure shakedown under oscillating normal load and for different values of λ.

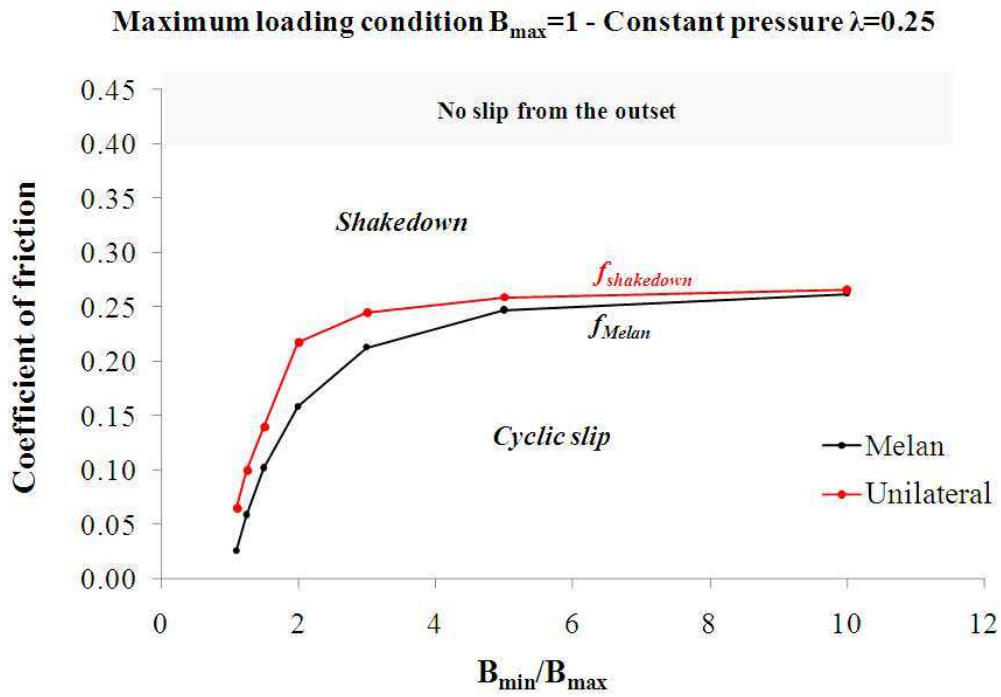


Figure 6.10. Comparison between the shakedown limit obtained by applying Melan's theorem to the bilateral solution and the limit computed using the "marching in time" unilateral solution.

A further investigation was deemed necessary to explore the behaviour of this system and, specifically, to understand better the source of the discrepancy between the exact results and the predictions of Melan's theorem. As explained in Chapter 2, in order to obtain a solution to the rolling problem, the shear and the normal traction distributions are discretised using overlapping triangles which, in turn, generate a piecewise linear approximation of the traction distributions. Hence, the concentrated load force of Figure 6.2 was replaced with a triangle of direct traction. The frictional elastic problem shown in Figure 6.11 has been consequently investigated. Three different loading histories have been investigated: Figure 6.11 (i): the pressure p_n is pulsating from zero to a maximum value while the triangular distribution undergoes a homothetic transformation; Figure 6.11 (ii): the pressure peak, p_n, is cycled between two positive limits and the triangle semi-width is left unchanged; Figure 6.11 (iii): the pressure peak, p_n, is mantained constant and the triangle semi-width, a_{tr}, cycled. The reason why these load scenarios have been investigated is because for the general case, whose solution is shown in Figures 6.9 and 6.10, contact area and pressure distribution vary simultaneously when the normal load is cycled. Here, the two effects, i.e. the variation of the contact area and the variation of the pressure peak are checked independently by the means of a triangular distribution, whose dimensions are easily varied and controlled.

Figure 6.12 illustrates the elastic shakedown limit for the case shown in Figure 6.11(i). Two different load ratios have been considered, viz. $\lambda_{tr} = p_n/p_0 = 6$ and $\lambda_{tr} = 8$, and the elastic shakedown limit was plotted for different values of the ratio $B_{tr} = b/a_{tr}$, specifically, 1, 1.5 and 2. This is because these are the values for which a significant difference between Melan's prediction and our exact solution for the case shown in Figure 6.10 was noticed. As can be seen from the figure, the results obtained using Melan's theorem match the marching-in-time unilateral solution.

However, cycling p_n between two positive values (see Figure 6.11(ii)) to investigate the effect of cyclic loading on the frictional shakedown response of the system implies a different response. The frictional behaviour of the system is now similar to the one illustrated in Figure 6.10. In fact, as can

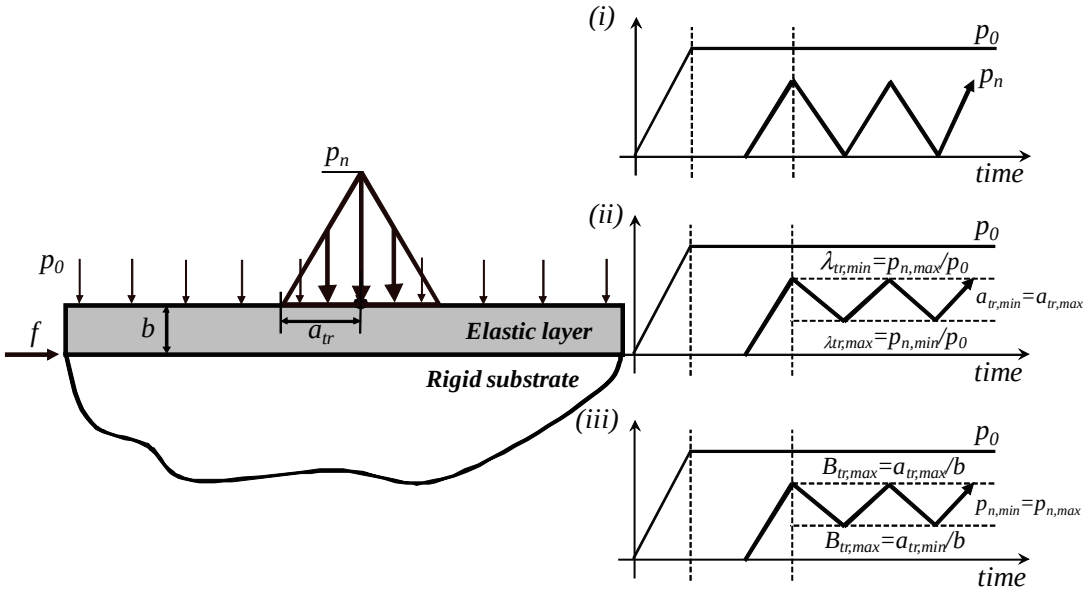


Figure 6.11. Schematic of the layered system subject to a triangular distribution of normal tractions and potential loading histories.

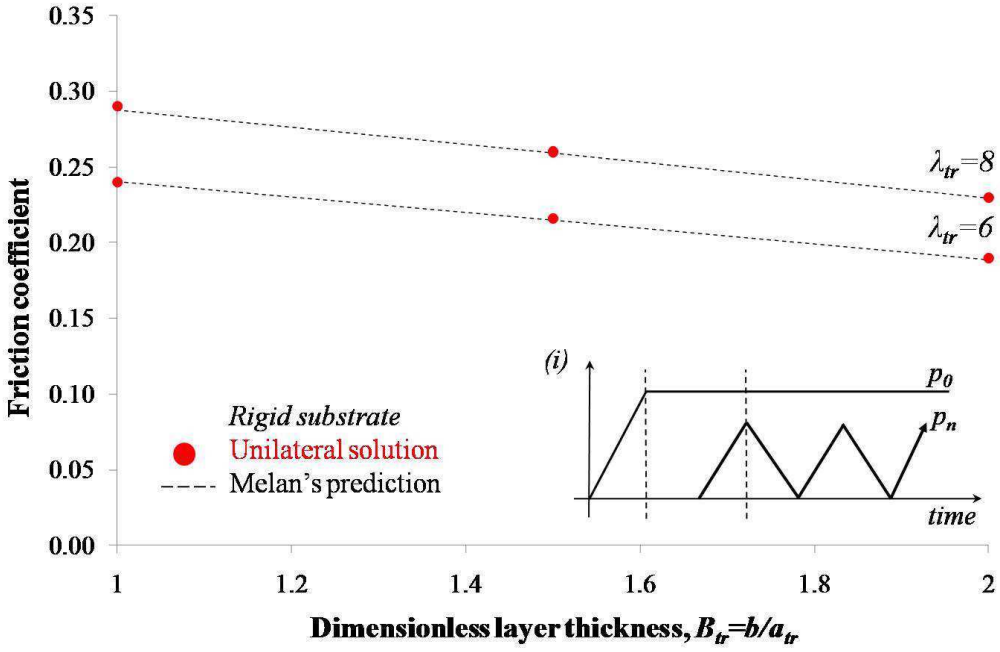


Figure 6.12. Comparison between the elastic shakedown limit as a function of the dimensionless layer thickness, B, predicted by Melan's theorem and the unilateral solution, for λ_Q=6 and 8 - elastic layer resting on a rigid substrate.

be seen from Figure 6.13, there is now a marked difference between our unilateral solution (romboidal symbols) and the predictions obtained using Melan's theorem, which now underestimates the elastic frictional shakedown limit. Furthermore, the full circles shown in Figure 6.13 represent the limit obtained by assuming the system has elastically shaken down when the dimensionless energy dissipated at the interface between layer and substrate was lower than 1e-8. This dimensionless value was chosen arbitrarily as numerical limit below which the energy dissipated can be regarded as negligible. Such arbitrary cut-off produces a much better agreement with the results obtained using Melan's theorem. In this case, the energy of the system goes asymptotically towards the steady state, and it usually takes more than 6 cycles to reach it. This behaviour is very different from that shown in Figure 6.3, where the system shakes down after a maximum of three cycles. This example illustrates how sensitive the solution is to the coupling of the tangential and direct tractions. In fact, regardless of the methodology adopted to determine the shakedown limit computed as an exact limit - romboidal symbols - or as approximated value obtained using a cut-off energy as a lower bound to plastic shakedown for the system - circles, the application of Melan's theorem to find the elastic shakedown limit fails. The margin of error committed while wrongly applying Melan's theorem to find the shakedown threshold seems to vary with the problem under consideration.

The effect of the variation of the triangle semi-width was also explored (see Figure 6.11(iii)). Figure 6.14 illustrates the elastic frictional shakedown limit as a function of the variation of the dimensionless layer thickness to contact area ratio B_{tr}, for $\lambda_{tr} = 6$. As in the previous case, two different limits have been defined and a marked difference between Melan's prediction and the exact numerical solution found.

The results presented in this section show that the variation of the contact area and of the pressure distribution represent an equally important source of coupling. Future work will include an investigating of the possibilty to define a universal parameter capable of quantifying the degree of coupling present in the system and, consequently, to produce an estimate of the error committed by

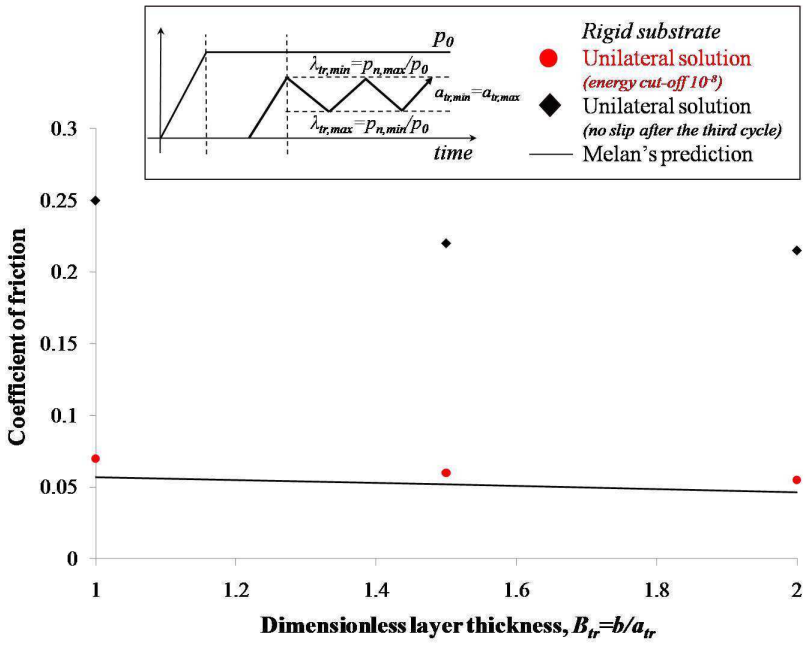


Figure 6.13. Friction coefficient required to ensure elastic shakedown as a function of B, for $\lambda_{tr,\min}$=6 and $\lambda_{tr,\max}$=8.

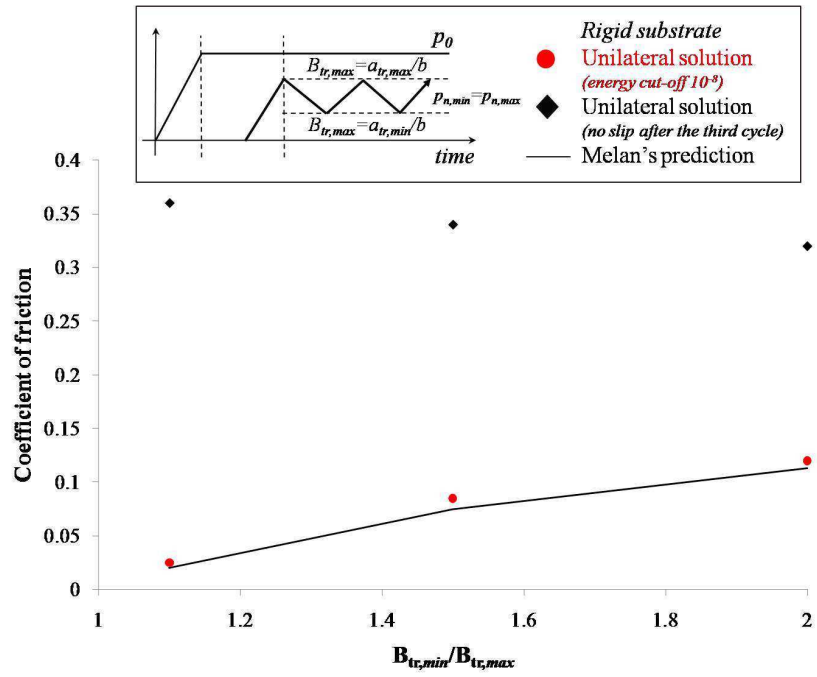


Figure 6.14. Friction coefficient required to ensure elastic shakedown as a function of $B_{tr,min}/B_{tr,max}$ where $B_{tr,max}$=1 and for $\lambda_{tr,\min}$=6.

using Melan's theorem to predict the shakedown limit for layered elastic systems in the presence of friction.

6.4 Summary

The possibility of a layered system shaking down in a frictional sense was treated and Melan's theorem tested as a means of deriving frictional shakedown thresholds. It was confirmed that Melan's theorem cannot be rigorously applied when coupling is present. The application of Melan's theorem to weakly coupled systems seems, however, to produce satisfactory results. Conversely, the shakedown threshold is underestimated in strongly coupled-systems. Furthermore, increased coupling suggests an increased sensitivity of the system behaviour on initial boundary conditions and pre-existed, locked-in, residual stresses.

Chapter 7

Measuring friction in partial slip

7.1 Introduction

This chapter addresses the problem of determining the friction coefficient under partial slip conditions (Reina et al., 2010d). Apart from the case discussed in Chapter 4, all elastic contact problems which have been investigated in this thesis deal with contact interfaces where the frictional law is locally violated and there is no gross sliding between the components in contact. In such context, and within the Coulomb's friction framework, the value of the friction coefficient is a key parameter to be determined as there is very often great uncertainty associated with the friction value as input for semi-analytical and FE models. In Chapter 5 an example problem where the value of the friction coefficient was related to the amount of net relative displacement between mating surfaces in the "partial-slip" condition has been shown. The net displacement was shown to be a strong function of the friction coefficient. In that case, its value was determined using a compression test where gross sliding actually occurs between the mating surfaces. In this chapter a novel method for measuring the interfacial coefficient of friction between two solids, which avoids sliding, is described, and example results are given. The technique makes use of the fact that a carefully controlled sequence of partial slip states between contacting bodies may be used to produce relative motion whose extent is a strong function of the coefficient of friction. This study was also prompted by the fact that a quadratic programming technique similar to that employed in Chapters 5 and 6 to study layered systems is required here to track the evolution of the contact interfaces.

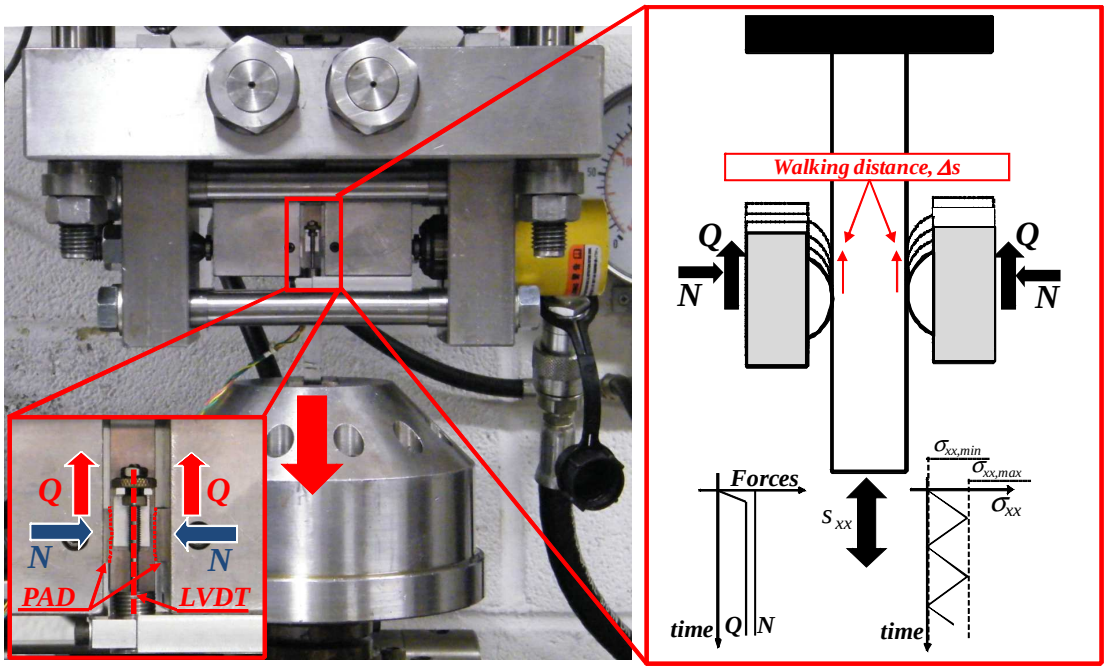


Figure 7.1. Schematic of the test apparatus used to perform the “walking” test.

This work is a combined experimental and numerical investigation carried out using a fretting fatigue test apparatus available at the University of Oxford (Mugadu et al., 2002; and Nowell et al., 2006) and performing a full marching-in-time solution to capture the evolution of the contact area in fretting tests (Kalker, 1971; and Nowell and Dai, 1998a). The apparatus with its key features is shown in Figure 7.1. The reader may refer to (Dini, 2004) for a comprehensive description of the test rig. Although, in principle, a wide range of different loading histories might be exploited, to reduce the number of possibilities which might be investigated the following was chosen (Reina et al., 2010d): first, the indenter is pressed into contact by a normal force, N, so as to produce contact over a strip, and where the contact pressure distribution, $p(x)$, taken as positive when compressive, is given explicitly by the usual Hertz formula (Johnson, 1985). A shear force, Q, insufficient to cause sliding, is then applied and held constant. A bulk tension, σ_{xx}, is now developed, and it is assumed that this varies cyclically between limits $\sigma_{xx,\max}$ and $\sigma_{xx,\min}$, where, for reasons of ensuring stability of the specimen, the latter would be preferred to be positive. It is here argued that this approach induces much less surface damage in the components, and therefore yields a value for the

coefficient of friction which is much more representative of the unmodified materials and surfaces under investigation.

In this chapter, after briefly describing the numerical algorithm used to study the evolution of tractions and displacements at the contact interfaces, the experimental set-up adopted by the author is shown and the inferred value of the coefficient of friction obtained for a specific contact pair are illustrated and discussed.

First, a partial slip analysis needs to be conducted. It should be noted here that the formulation of the contact problem, which is presented in the next section, follows the same mathematical principles used to develop the numerical scheme presented in Chapter 5. Therefore, the formulation will be only briefly introduced within the context of the contact problem to be solved, highlighting the changes in terms of notation and discretisation implemented with respect to the technique presented in Chapter 5.

7.2 Optimisation techniques applied to contact problems

The contact model here described is related to the line-contact problem illustrated in the inset to Figure 7.1. Throughout this model a Coulomb-Amonton's friction law is adopted and, hence, the coefficient of friction is independent of the slip-velocity. Thus, when slip occurs, the shear traction, $q(x,t)$, can be expressed as a fraction, μ, of the normal pressure, which is taken positive when compressive, as follows:

$$q\left(x,t\right) = -\mu p\left(x\right) sign\left(\dot{v}\left(x,t\right)\right) \qquad x \in \text{slip zones} \tag{7.1}$$

where $\dot{v}\left(x,t\right)$, represents the relative surface slip velocity, and μ is the coefficient of friction adopted for a pointwise description of the frictional law. The direction of the shear traction opposes the slip direction, so a minus sign was added before $p\left(x\right)$ in (7.1). Where the friction law is not violated, the slip velocity, $\dot{v}\left(x,t\right)$, is equal to zero and, hence:

$$|q(x,t)| < \mu p(x), \dot{v}(x) = 0 \qquad x \in \text{ stick zones} \tag{7.2}$$

A function which simultaneously includes the boundary conditions for the stick and slip areas needs to be formulated. This can be achieved by multiplying both members of the boundary condition associated with the slip regions by the slip velocity so that:

$$q(x,t)\dot{v}(x,t) + \mu p(x) |\dot{v}(x,t)| = 0 \qquad \text{everywhere,} \tag{7.3}$$

and the following inequalities apply (Kalker, 1990):

$$q(x,t)\dot{v}(x) + \mu p(x) |\dot{v}(x,t)| \geq -|q(x,t)| |\dot{v}(x,t)| + \mu p(x) |\dot{v}(x,t)| \geq 0, \tag{7.4}$$

where the first *equality* holds if and only if slip vanishes or the shear traction has the same direction of slip velocity, and the second *equality* holds if and only if $-|q(x,t)|$ equals $\mu p(x)$ in the slip areas or slip vanishes. The importance of this additional characteristic will become clearer shortly. The object of the technique is to determine the location of slip regions within the contact automatically, and to this end we construct the following integral function:

$$\tilde{F}_C(x,t) = \int_{-a}^{a} [q(x,t)\dot{v}(x,t) + \mu p(x) |\dot{v}(x,t)|] \, dx, \tag{7.5}$$

where $\tilde{F}_C(x,t)$ will be referred to as the functional of the elastic contact problem. This functional has been devised like the functional introduced in Chapter 5 for the distributed dislocation technique. The main difference between the formulations is the definition of the relationship between shear tractions and displacement field (see Chapter 5 and Nowell, 1998a). Also in this case, if the values of slip and shear tractions are the exact solution to the contact problem, then the value of the integral is zero. If not, the value of the functional will be strictly positive. The best approximate solution to the contact problem can be achieved by minimising the value of the integral, and the related minimum principle can be formulated as follows: "minimize the difference between the power

dissipated by the Coulomb friction generated by the slip and the power dissipated by the traction generating the slip" (Kalker, 1971).

The above principle was first proposed by Kalker (1971) and it is completely general. Kalker has shown how it can be applied to solve stationary and moving contact problems by adopting a linear minimization technique (Kalker, 1971). Details of the procedure adopted for the specific contact problem under investigation can be found in Kalker's book (1990), and a piecewise-linear representation of the shearing traction distribution (Bentall and Johnson, 1968; and Johnson, 1985) is used here as already done in Chapter 5 with the distribution of glide dislocations (Qiu et al., 2008). This permits a smooth solution to be found and evolved as a function of time. Clearly, because frictional contact problems are history-dependent it is important to track the solution in the time domain. The excitation is, here, periodic in form and there is an initial transient problem which is not of interest; a steady state is always established within a few cycles of loading. The two dimensionless groups which quantify the performance of the system are the dimensionless shearing force, $Q/\mu N$ (for the time being the coefficient of friction is assumed to be known) and the bulk tension, captured by the ratios $\sigma_{xx,\min}/\mu p_H$ and $\sigma_{xx,\max}/\mu p_H$.

Extensive sets of results have been evaluated and first example results tracked out as a function of time are displayed. First, the boundary between walking and no-walking has to be calculated. In the example case shown in Figure 7.2 the ratio $Q/\mu N$ was set to 0.7. The figure shows the results for $\sigma_{xx,\min}/\mu p_H = 0$ and $\sigma_{xx,\max}/\mu p_H = 1.8$. This shows how the interfacial shearing tractions evolve over a loading cycle by looking at the turning points once the steady state condition is reached. The loading history plot shows how the bulk loading is gradually increased in amplitude, and the transient response permitted to decay. The shearing traction distributions experienced at the turning point in the loading cycle, viz. the maximum bulk tension at point (1) and the minimum at point (2), are also plotted. The hatching below the axis shows the extent of the stick region at point (1) in the loading cycle and the hatching above the axis shows the extent of the stick region

at point (2). It will be noted that there is a region of contact which always remains stuck, and, therefore, it is clear that there is no rigid body motion. Suppose now, that the parameters are adjusted slightly and that, whilst $Q/\mu N$ and $\sigma_{xx,\min}/\mu p_H$ are maintained at the same value, we choose $\sigma_{xx,\max}/\mu p_H = 2.2$; a modest change. The response of the system is displayed in Figure 7.3. The loading history is generally quite similar in form but it will be noted that there is now an overlap of the two slip zones at a point near the origin: slip is injected from one side while just under a half of the contact remains stuck, and when the bulk tension is relaxed slip penetrates from the other contact edge and includes a small portion of the previous slip region (now locked). It follows that a small slip displacement has been 'locked in' when the initial slip zone became locked and this subsequently emerges at the opposite contact edge. It is therefore equivalent to the passage of a dislocation of Burgers vector equal to the total slip displacement within the common slip region, and is the 'ruche' that Comninou and Dundurs (1978) referred to in their prescient paper on moving a rug without sliding it. The limiting condition between walking and no-walking can be now refined by iterating the solution to the contact problem between $\sigma_{xx,\max}/\mu p_H = 1.8$ and $\sigma_{xx,\max}/\mu p_H = 2.2$. For this particular value of the shear force and the minimum bulk tension set to zero, the value of $\sigma_{xx,\max}/\mu p_H$ for which the system is on the verge of walking is 2.125.

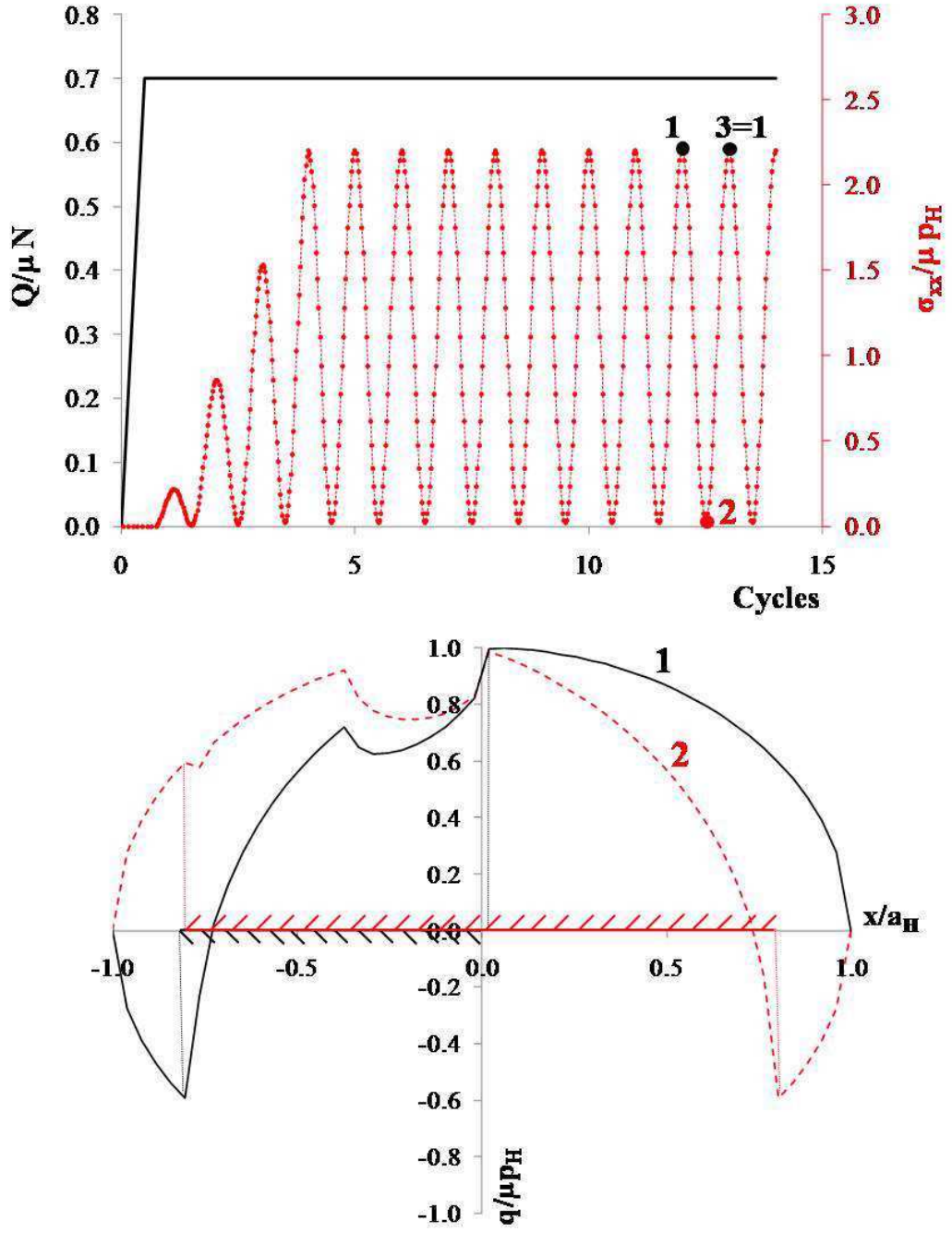


Figure 7.2. Loading history and shear traction distributions after loading (point 1) and unloading (point 2) in the steady-state cycle for $Q/\mu N = 0.7$, $\sigma_{xx,\min}/\mu p_H = 0$ and $\sigma_{xx,\max}/\mu p_H = 1.8$.

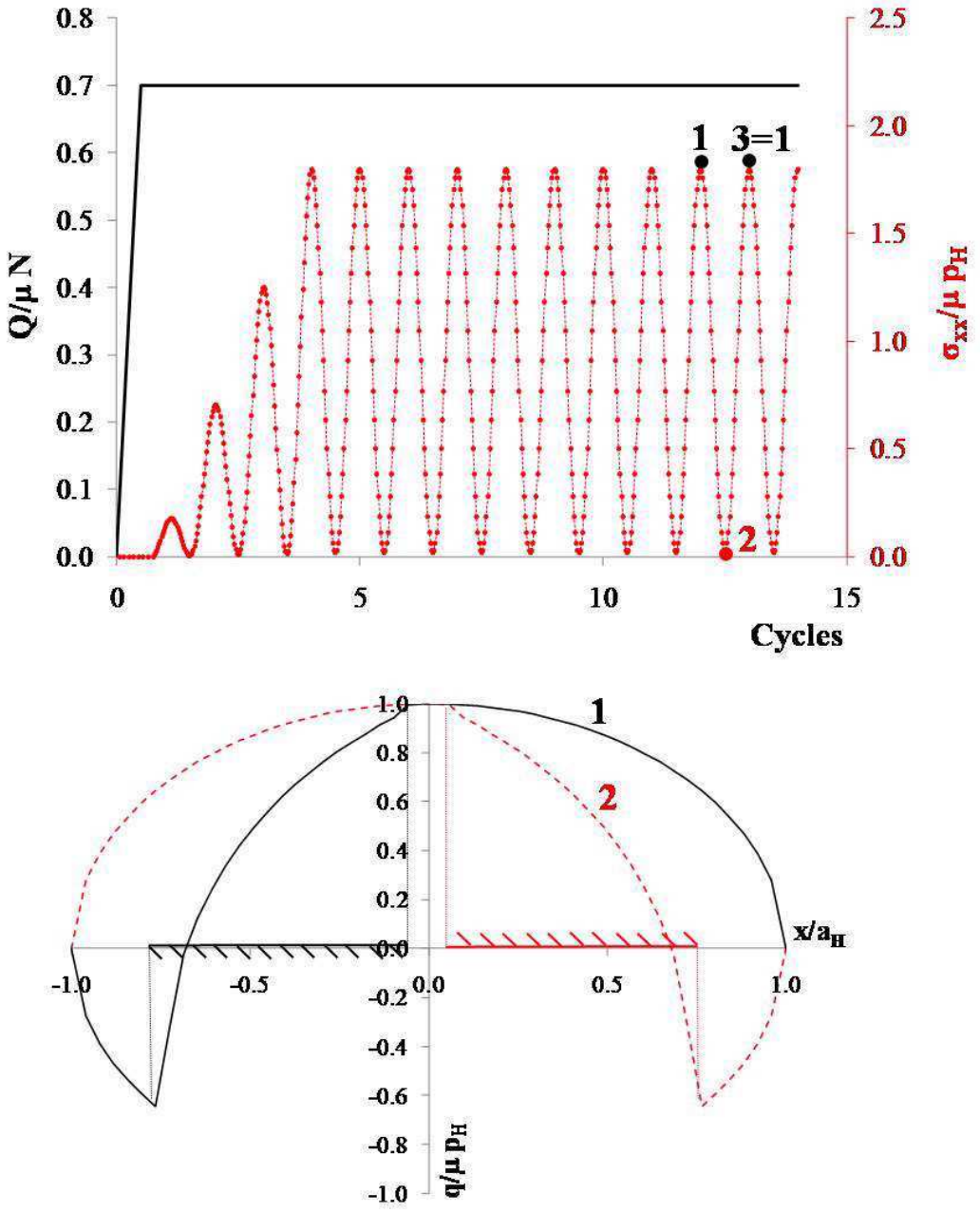


Figure 7.3. Loading history and shear traction distributions after loading (point 1) and unloading (point 2) in the steady-state cycle for $Q/\mu P = 0.7$, $\sigma_{xx,\min}/\mu p_0 = 0$ and $\sigma_{xx,\max}/\mu p_0 = 2.2$.

If different ratios for $Q/\mu N$ are chosen whilst $\sigma_{xx,\min}/\mu p_H$ is maintained fixed, the onset of walking can be calculated as a function of $\sigma_{xx,\max}/\mu p_H$. Figure 7.4 summarises the results of many such calculations, and shows clearly the boundary between walking and no-walking. In fact, the result can immediately be generalised slightly by noting that the boundary depends not separately on the turning-point (or extreme) values of the bulk tension, but simply on its range, $\Delta\sigma_{xx}$, (and therefore $\sigma_{xx,\max}$ here). The example transition point $Q/\mu N = 0.7$, $\sigma_{xx,\max}/\mu p_H = 2.125$ is highlighted. For this value of the dimensionless shear force, Figure 7.5 shows the normalised distance walked per cycle, $E\Delta s/(4\mu a_H p_H(1-\nu^2))$, for values of $\sigma_{xx,\max}/\mu p_H = \Delta\sigma_{xx}/\mu p_H = 2.5, 2.75, 3.0$. The relative increase in step length with bulk tension range is clear. The plot in Figure 7.5 can therefore be used to infer the coefficient of friction once the walking distance per cycle is measured by tuning the value of μ until the computed walking distance matches the measured value.

The calculations summarised above are valid as long as plasticity does not occur. At the same time, the step length is seen to depend on the contact half-width and so, in order to make the distance moved as easily measurable as practicable, it is desirable to have the largest possible contact and, hence, the normal contact load must be moderately high. The elastic limit for the system defines the highest sustainable load whilst maintaining a fully elastic contact field, and this depends on the interfacial friction coefficient and on the loading conditions. These are defined by the load ratio $Q/\mu N$, the coefficient of friction, μ, and by the maximum bulk ratio $\sigma_{\max}/\mu p_H$. It turns out that the elastic limit, p_H/k, where k is the yield stress of the material in pure shear, depends slightly on μ and $\sigma_{xx,\max}$, but only weakly on $Q/\mu N$. Figure 7.6 therefore shows the elastic limit for the case characterised by $Q/\mu N = 0.7$ and $\sigma_{xx,\max}/\mu p_H = 2.125$, 2.2 and 2.4, which is found to be a practically useful range. It is important that plasticity, particularly at the surface, is avoided for the solution to remain fully valid.

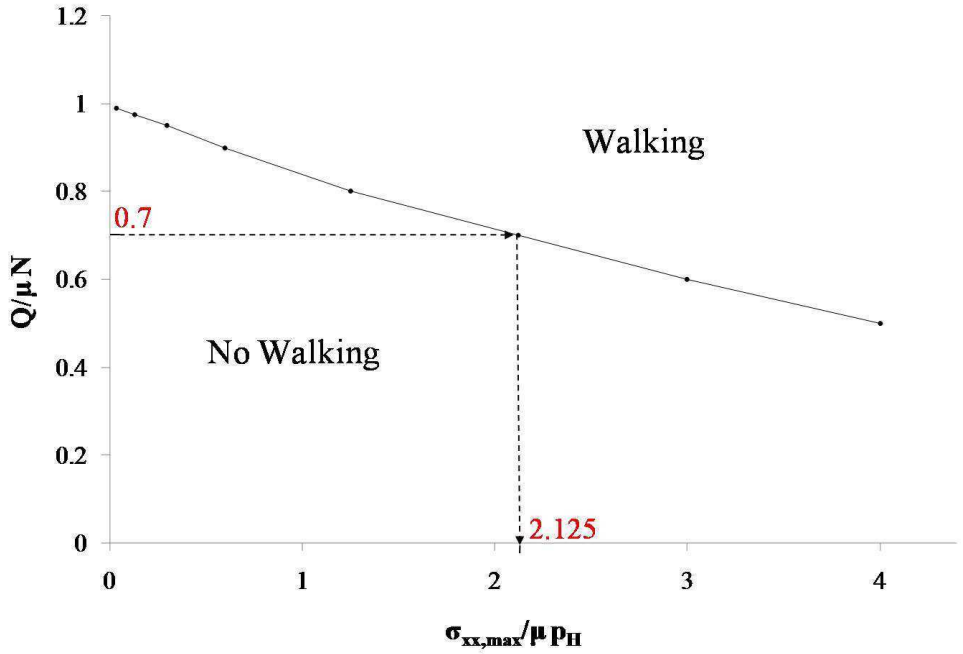


Figure 7.4. Map showing the transition between "walking" and "no walking" as a function of the loading parameters.

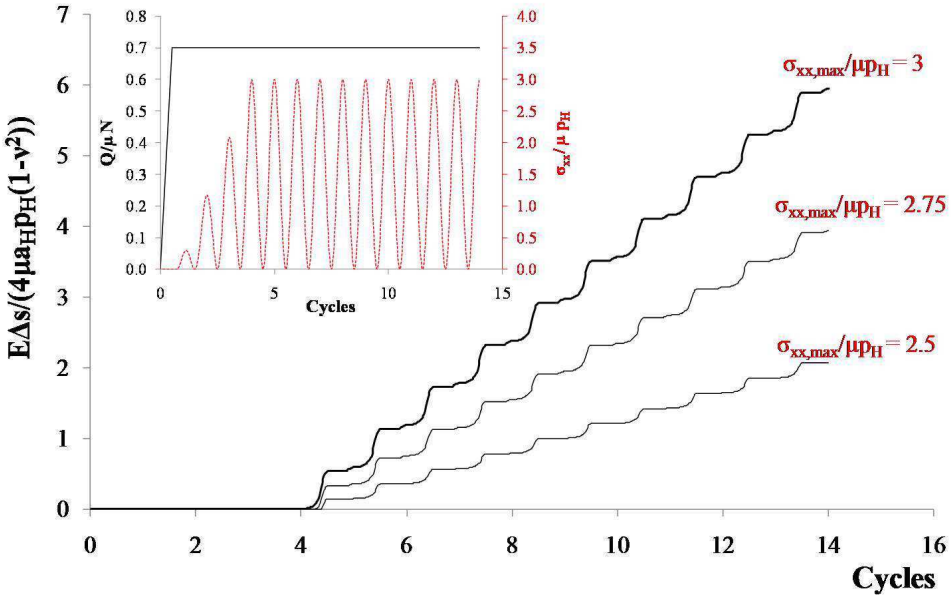


Figure 7.5. Normalised distance walked per cycle, $E\Delta s/(4\mu a_H p_H(1-\nu^2))$, for $Q/\mu N = 0.7$ and $\sigma_{xx,\max}/\mu p_H = 2.5, 2.75, 3.0$.

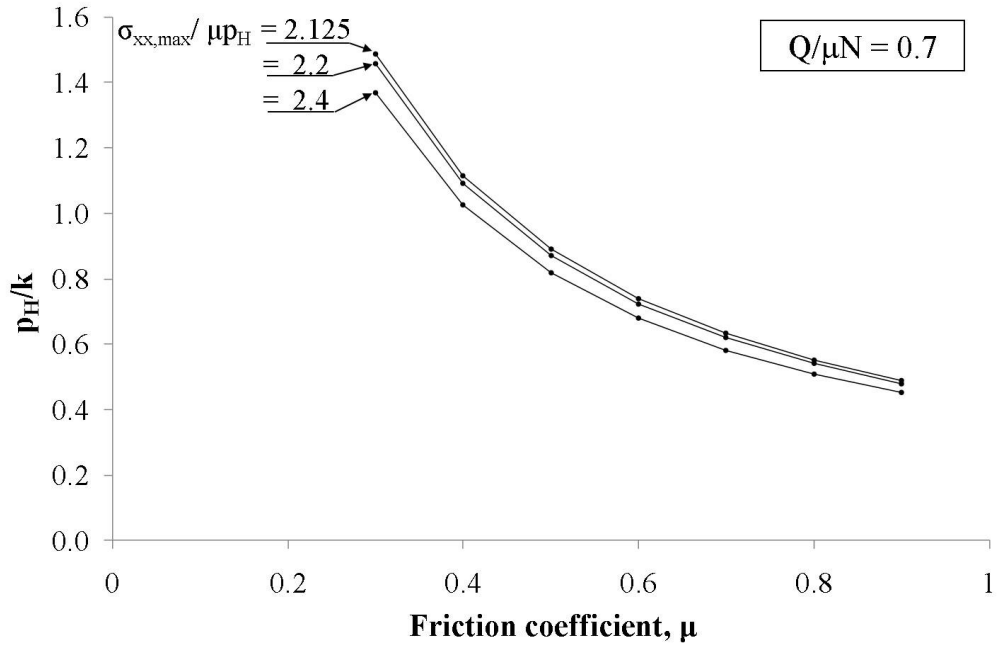


Figure 7.6. Elastic limit vs. friction coefficient for $\sigma_{xx,\max}/\mu p_H = 2.125, 2.2, 2.4$.

7.3 Experiment

An inherent property of the experiment is that the real unknown quantity is, of course, the coefficient of friction, μ, whilst the two parameters which can be controlled are the constant shearing force and the bulk tension range. The bulk tension range is practically limited on the lower side by zero (to avoid all possibility of buckling) and on the upper side by the elastic limit. The results of the analysis are, of course, displayed in terms of dimensionless quantities incorporating the coefficient of friction, but, when the tests are carried out, there is a certain amount of 'feeling our way around' needed in order to get the load parameters in the right region. Also, probing the walking/no-walking boundary proved not to be the best way to determine the coefficient of friction. A much more sensitive measure turned out to be determining the walking length, and this will be apparent from the following description of the experiment itself.

Some preliminary tests have been carried out on mild steel. The tests were carried out in collaboration with Mr. Robert Paynter and Mr. Zhaohan Wang (2009). The central 'dogbone' (see schematic

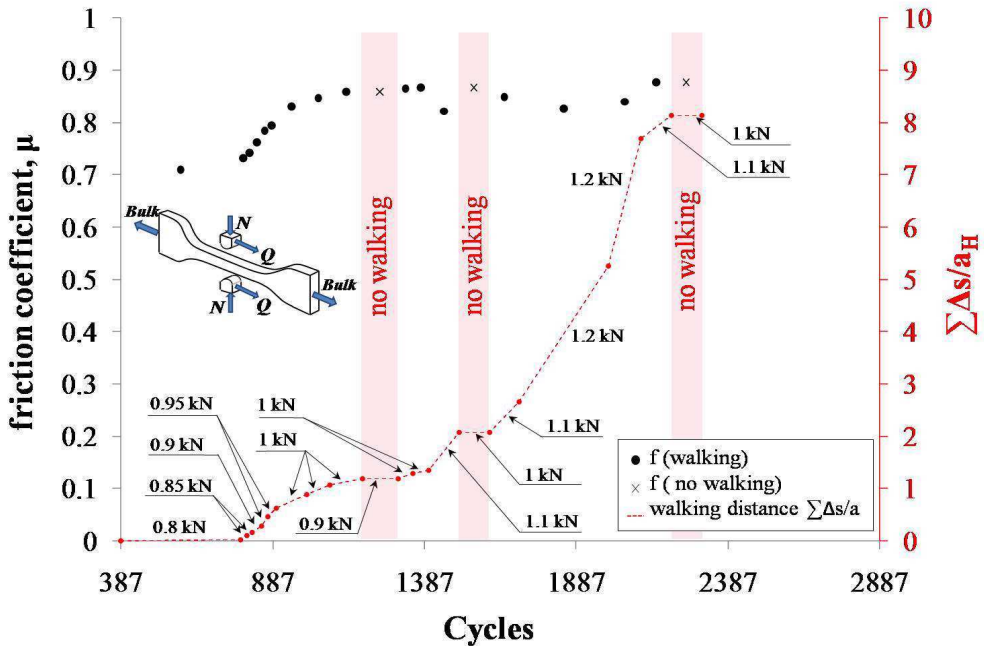


Figure 7.7. Experimental results for a mild steel dogbone specimen ($10mm \times 10mm$ cross-section) in contact with a mild steel cylinder of the same width and radius $100mm$, and pressed by a normal force $N_F = 1.57kN$. The graph shows the accumulated walking distance, $\sum \Delta s/a_H$, and the evolution of the friction coefficient during the test as calculated using the quadratic programming routine.

in Figure 7.7) has a section of $10mm \times 10mm$ and cylinders of the same width and radius $100mm$ are pressed in with a normal force $N_F(= N \cdot 10mm) = 1.57kN$. The corresponding contact semi-width is $a_H = 0.419mm$. The surfaces of both the dogbone and the pads were ground, and the surface roughness is characterised by $R_a = 313nm$ across the grinding direction and $R_a = 54nm$ along the grinding direction, which also corresponds to the walking direction. The results to be described should be read in conjunction with Figure 7.7, where the upper points are the coefficient of friction, to be read with the left hand scale, and the broken line is the accumulated distance walked, to be read off the right hand scale. The loads (given in kN) annotated on the broken line are the tangential force, $Q_F(= Q \cdot 10mm)$. The walking distance per cycle, Δs, was measured using a standard LVDT mounted on a pad assembly of the kind shown in (Mugadu et al., 2002) and with the tip bearing on a 'step' fixed to the tensile test specimen. The technique is capable of measuring the creep distance per loading cycle to the required accuracy with a resolution of about 20 nanometres.

The tangential force was set to a constant value (initially low) and the bulk force in the dogbone was ramped up to $40.4kN$ and set oscillating between the values $0.4kN$ and $40.4kN$ at the frequency of $1Hz$. The test was continued but, approximately every fifty cycles, the tangential load was increased until walking was detected: thus the first 387 cycles were used up with the pads stationary. At this point the shearing force had been increased to $0.8kN$, and some movement of the pads was detected. Subsequently, small increase in the value of the shear force were applied until, by cycle 897, a shear force of $1kN$ was reached and, from the walking distance measured, a coefficient of friction is inferred, at this point, of about 0.83. Over the next 10 cycles the distance walked per cycle fell slightly, as the coefficient of friction increased. As an experiment, at this point the shearing force was reduced to $0.9kN$, whereupon walking stopped. At cycle 1325 the shearing force was restored to the value of $1.0kN$ and walking resumed, but the pace length reduced further, indicating another small increase in the coefficient of friction, to about 0.865. At cycle 1500 the shearing force was increased to $1.1kN$ permitting the pad to take 'a pace', and reducing it back to $1.0kN$ caused walking to cease. Further increases in the shearing force to $1.1kN$ and subsequently $1.2kN$ were imposed and the walking length increases significantly, whilst the coefficient of friction fell very slightly (from a maximum of 0.867 to about 0.85). This was believed to be because key parts of the contact were now moving onto less heavily modified material. It should be noted here that the values of coefficient of friction obtained using the newly developed technique compare reasonably well with those resulting from fully sliding tests carried out imposing a sliding distance of $1mm$ per cycle, and which produced values of coefficient of friction ranging between 0.7 and 0.83 (note that it is very hard to justify quoting coefficients of friction to more than one significant figure in a conventional sliding test, because of the variability experienced during the test).

As has been stated, the walking 'rate' is a very strong function of the coefficient of friction, and so this test is a precise tool for measuring its value. In the present experiment the maximum walking distance per cycle, and therefore the maximum slip distance exhibited, was $0.85\mu m$. It follows that,

in order for the contact to move by a rigid body displacement equal to one contact patch width a total of 490 cycles must be made. Also, the contact pressure present during the motion is known, and this gives a quantitative idea of the amount of surface damage inflicted.

In due course it is hoped to evolve the experimental procedure to enable the influence of contact pressure and number of cycles of load on the coefficient of friction to be found explicitly and systematically. This seems feasible because the problem is entirely controlled by elastic stress, strains and displacement, and, hence, these are known to great accuracy without the need for external transducers.

7.4 Summary

The procedure described in this chapter seems a viable method of measuring, with precision, the coefficient of friction between solids. Modest changes in the load range cause sufficient change in the walking distance for the coefficient of friction, at least on aggregate, to be quoted to two significant figures with confidence. The test does not cause the amount of surface damage usually associated with sliding (Vingsbo and Söderberg, 1998; and Fouvry and Kapsa, 2001). Also, the damage which has been caused is well documented because the precise contact pressure distribution and slip displacement are fully known during the test. Indeed, it is possible that this could be exploited by putting very carefully controlled amounts of surface modification into the specimen before a test is conducted - for example by deliberately putting the specimen in the equivalent of a ‘cyclic plasticity’ (walking back and forth) regime of response. Further work should permit the instantaneous variation of the coefficient of friction across the contact patch to be deconvolved, and this will form part of a future investigation.

Chapter 8

Investigation on 3D tyre/wheel assembly

8.1 Introduction

In the introduction to this thesis, the salient features of the industrial case that prompted our investigation have been described briefly. Then the structure of the theoretical investigation carried out to explore the practical problem of interfacial creep for rubber tyres fitted on steel wheels, starting from a simplified description of layered frictional joints, has been illustrated. In this chapter the 3D prototypical assembly is studied in detail to remove some of the first order approximations made in studying the simplified 2D problem in Chapters 2-6. The work covers different aspects of the problem based on the findings that emerged during our investigation. In fact, not only it discusses the problem of the onset of slip in this type of mechanical assemblies, but it also focuses on the investigations carried out to shed light on various phenomena: a number of issues were tackled, from the lubrication of the interface between the mating surfaces to the stress field generated in the wheel due to different loading conditions and tyre structures and, eventually, to the consequences associated with tyres misfit. The discussion is here supported by numerical results generated using the FE commercial code ABAQUS (Abaqus, 2007), whose results have been corroborated by experimental results provided by our industrial partners (Michelin, GKN, JCB and Corus). Finally, considerations about potential future work to be carried out in collaboration with the project partners are discussed.



(a) *(b)*

Figure 8.1. (a) Michelin XMCL: radial tyre object of our investigation (*image courtesy of Michelin - www.michelin.com*); (b) JCB 4CX: Backhoe loader dedicated to the project (*image courtesy of JCB - www.jcb.com*).

8.2 Onset of slip-Preliminary considerations

The onset of slip for rubber tyres fitted on steel wheels is the first problem that was addressed with respect to the 3D assembly. The semi-analytical model, exhaustively discussed in previous chapters, gave us a thorough understanding of the physics ruling interfacial creep in shrink fitted systems. However, as explained in the introduction to this thesis, the real engineering case is far more complex than the simplified scenario which has been treated so far using semi-analytical and numerical approaches. Hence, a purely numerical approach based on FE was deemed necessary. Figure 8.1a illustrates the tyre that was adopted in our investigation. It is a common Michelin XMCL Radial tyre which was mounted on a JCB 4CX backhoe loader (Figure 8.1b) that was one of the resources dedicated by JCB to our project.

Even if a comprehensive discussion of the structure of the tyre is outside the scope of our investigation, a brief description is only provided here. The tyre is made of vulcanised rubber, which is obtained by adding sulphur to natural rubber. This process significantly improves the mechanical properties of rubber (Treloar, 1958). Other substances are also added to rubber compound to

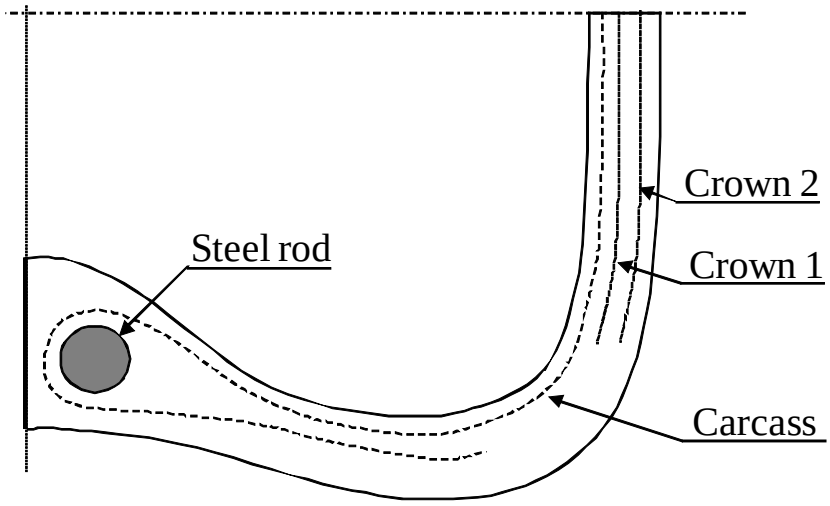


Figure 8.2. Schematic of the tyre cross-section and of the tyre reinforcements.

achieve the desired mechanical properties. The material characterisation for the tyre under investigation was performed at Michelin's laboratories. Their findings were implemented in our material model. Specifically, the viscoelasticity of our compound has been modelled using the Mooney-Rivlin model, which is a generalization of the neo-Hookian model that is obtained from strain energy functions (coefficients C_{01}=1, C_{01}=0, D_1=0.1) (Abaqus, 2007). Furthermore, the elastomeric behaviour of the rubber compound has been considered by describing the time domain response of the rubber relaxation modulus using a Prony series expansion (coefficients coefficients g_{Prony}=0.3, k_{Prony}=0, τ_{Prony}=0.1/ relaxation modulus, $g_{RM}(time) = 1 - g_{Prony}(1 - exp(-time/\tau 1))$) (Abaqus, 2007). The latter response models the dissipative effects associated with the elastomeric behaviour of the rubber compound. A complete description of the rubber material model is outside the scope of our work and the reader may refer to (Treloar, 1958) for further details.

In general, the desired mechanical characteristics of the tyre are obtained by reinforcing the tyre structure using textile fabrics and metal crowns. Figure 8.2 shows a schematic of the main elements used as reinforcements and embedded in an agricultural radial tyre. A detailed description of the material properties and geometric features characterising the reinforcements of the named Michelin tyre can be found in Table 8.1. The reader may refer to Abaqus (2007) for more details related to

tyre reinforcements, and their characteristics and implementation.

crown 1 and crown 2 are fabrics made of steel (E=220 GPa – ν=0.3) where crown 1: area per bar 1.48 mm^2 – spacing 2.8 mm – orientation angle 70° crown 2: area per bar 1.48 mm^2 – spacing 2.8 mm – orientation angle 110°
carcass is a polymeric (PET E=16.1 GPa – ν=0.3) textile fabric made of two layers of different orientation layer 1: area per bar 0.65 mm^2 – spacing 1.16 mm – orientation angle 8° layer 2: area per bar 0.65 mm^2 – spacing 1.16 mm – orientation angle 8°
steel rod is a steel cable made of steel wires wrapped around a central wire. It is modelled as an isotropic cable whose Young's modulus is 90 GPa and Poisson's ratio is 0.3.

Table 8.1: Technical characteristics of the main tyre reinforcement elements (see Figure 8.2).

As mentioned in the introduction to this chapter, the FE commercial software chosen for our investigation is ABAQUS. The reason for this is that ABAQUS has already been extensively used by our sponsors for other projects and it has a specific section dedicated to tyre modelling (Abaqus, 2007).

To address the problem of the onset of slip the following strategy was implemented:

1) The first step was to explore the accuracy of ABAQUS in capturing the interfacial pressure between tyre and rim. A 3D FE model of a tyre mounted on a rigid rim was consequently devised. The deformability of the wheel was, therefore, initially neglected. This is a reasonable assumption given the difference in stiffness between the tyre and the steel wheel. Furthermore, material history effects are neglected at this stage. This is a realistic assumption as there is no interest in analysing the tyre transient behaviour typical of the tyre response to harmonic loadings commonly associated with the dynamics of the vehicle at this stage (Abaqus, 2007). All numerical results have been compared with experimental data provided by Michelin.

2) After the FE model had been developed, the capability of the model to assess the onset of slip was investigated. Again, Amonton-Coulomb's friction law was implemented in the FE. This assumption is acceptable given the fact that the onset of slip is investigated. Since no net displacement occurs between the mating surfaces, the effect of the rubber deformability on the tribological performance of the coupling does not need to be taken into account with more sophisticated friction models

(Pacejka, 2002). The onset of slip was determined for two loading conditions: (i) static loading in absence of rolling and (ii) steady state rolling. This latter condition, important to assess the performance of the assembly during in-service loading, was explored using the rigid rim configuration because ABAQUS does not allow to efficiently model the relative motion between the ground and the tyre when the rim deformability is introduced and tyre and rim are not tied but free to move with respect to each other (Abaqus, 2007).

3) After the onset of slip had been determined, the effect of wheel deformability on the interfacial pressure distribution was explored. This was done by devising a 3D FE model of a tyre mounted on a deformable rim. This FE model has been proven very useful when the stress field induced by various loading conditions had been computed to assess the wheel fatigue performance (although this is outside the scope of the research presented in this thesis).

4) A new rim profile has been also introduced by GKN as a planned outcome of the research collaboration. Consequently, a second FE model of a tyre mounted on a rigid rim was devised and a comparison between the existing and the new rim profile was performed in terms of pressure distribution at the interface between tyre and wheel. Furthermore, similarly to what already done with the original rim profile, a new FE model was devised to include the deformability of the wheel in our investigation.

In the following section the FE models developed by the author will be presented and a detailed discussion of the numerical results provided.

8.3 FE models and numerical results

The model of a tyre mounted on a rigid rim was the first to be devised. In order to generate the FE model, an axysimmetric model of the assembly was created in ABAQUS CAE. Once the generation of the axi-symmetric model had been completed, the 3D model was generated by fully revolving the tyre section. This was done using the ABAQUS command SYMMETRIC MODEL GENERATION

(Abaqus, 2007). Figure 8.3 shows a series screenshots of the tyre model where all elements used as reinforcement have been highlighted individually.

8.3.1 Loading conditions

The parameters that can be varied in our model are the inflation pressure and the loading conditions to which the tyre is subjected. In general, there are three main different loading configurations that can be superposed to obtain the desired loading condition: (i) pure vertical loading; (ii) application of a camber angle in combination with vertical loading; (iii) application of slip angle in combination with vertical loading. The three configurations can be differentiated based on the tyre position with respect to the normal direction to the ground, as schematically illustrated in Figure 8.4, where x is the direction of motion coming out of the page (see the tyre reference system in Figure 8.4).

Each simplified configuration can be reproduced either individually or in different combinations using the full scale in-house test rig available at GKN-FAD in Italy and at the Michelin R&D site in France.

8.3.2 Mesh optimisation, convergence issues and model set-up

Before proceeding to show the results obtained using the 3D FE model, further details related to the convergence of the FE model are needed. Solving a contact problem where one of the bodies is not purely elastic and, most importantly, reinforced by element of different stiffness, creates a number of convergence issues. The critical element that rules the convergence and, equally important, the computational cost of our model is the mesh of the tyre. Figure 8.5 shows the mesh of the tyre bead, which was adopted after a mesh-size parametric investigation was carried out. This is the most critical part of the tyre since it is the part in contact with the wheel where our attention is focussed. The mesh illustrated in Figure 8.5 guarantees the convergence of the model together with an acceptable resolution of the interfacial contact pressure between tyre and wheel.

Another important aspect related to the convergence of the model is the tyre fitting process. The

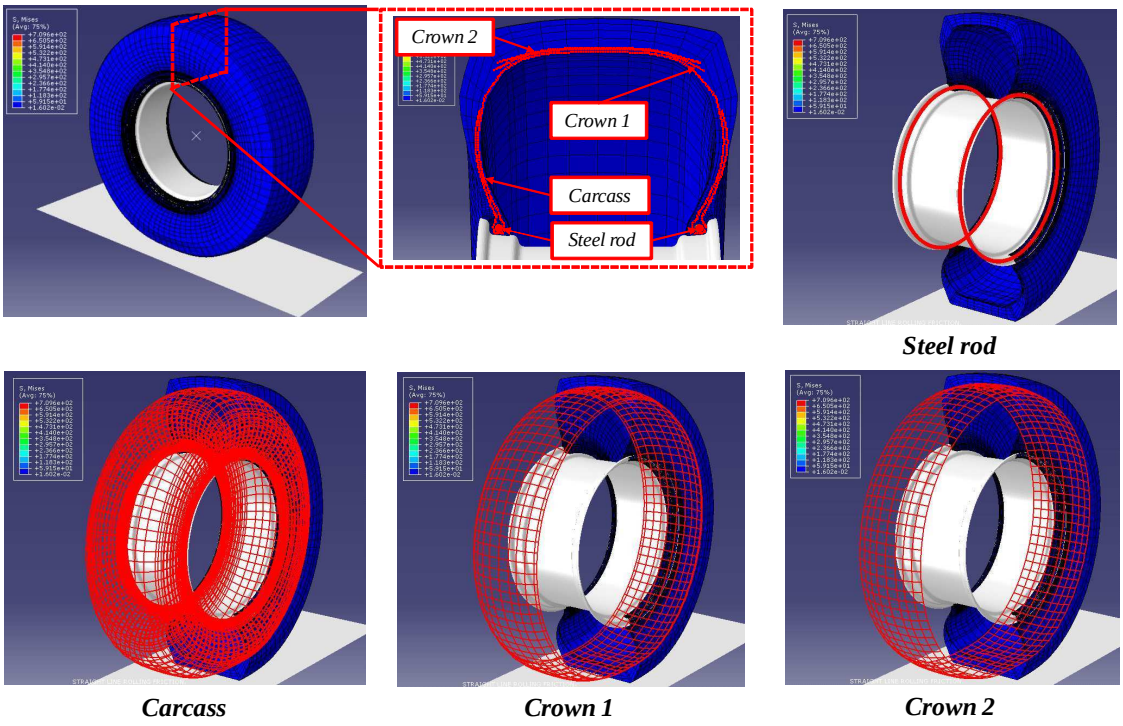


Figure 8.3. FE model of a tyre mounted on a rigid rim; detail of all tyre reinforcements.

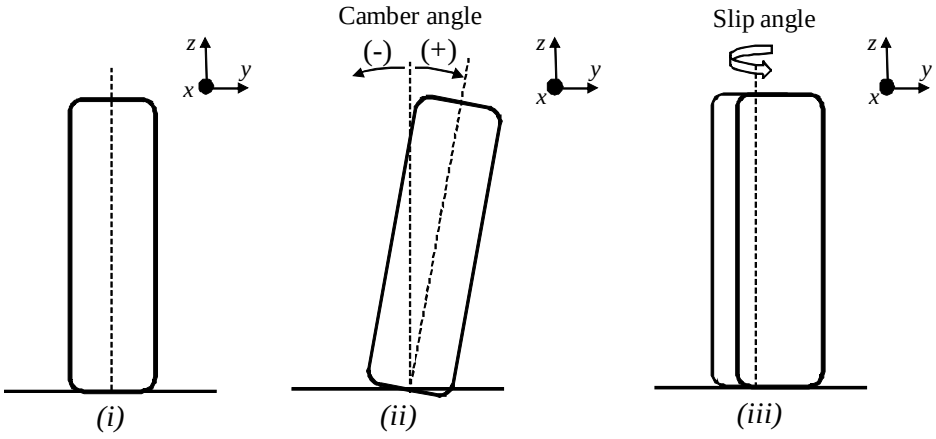


Figure 8.4. Main tyre loading configurations: (i) pure vertical loading; (ii) application of a camber angle; (iii) application of a slip angle.

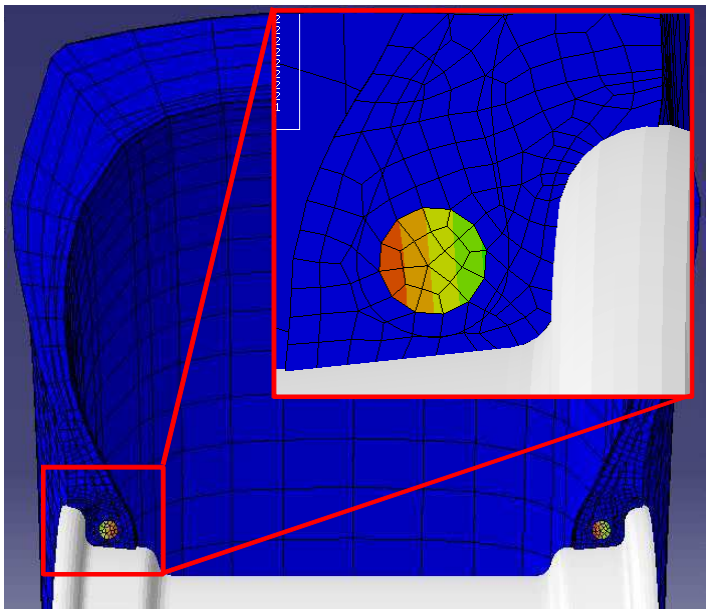


Figure 8.5. Detail of the tyre bead mesh.

fitting process has to be realistically reproduced in order to mount the tyre on the wheel and, consequently, generate the interference pressure needed to maintain the tyre in place. In fact, this coupling is a shrink fitted system where the components are kept in place thanks to the combined effect of contact pressure and friction. The numerical solution that was chosen to make the model converge was to split the wheel hub into two parts as shown in Figure 8.6. This does not reflect the real fitting process that implies moving the tyre beads inwards and, subsequently, inflating the tyre up to a maximum of 2.5 bar (Michelin, 2004) until the beads are perfectly seated against the rim sidewalls. However, this method guaranteed convergence and was the easiest to implement. A similar procedure is described in the Abaqus on-line documentation (Abaqus, 2007). For the purpose of our analysis, this different fitting process does not affect the final outcome of our analysis. In fact, the position of the tyre with respect to the rim sidewalls is unaffected by the different fitting process as this is performed in frictionless condition in order to speed-up the convergence and enabling the fitting process to be completed. The role of the friction coefficient in the fitting process will be discussed at a later stage in this chapter as it is at the origin of some specific in-service failures of the tyre-wheel assembly.

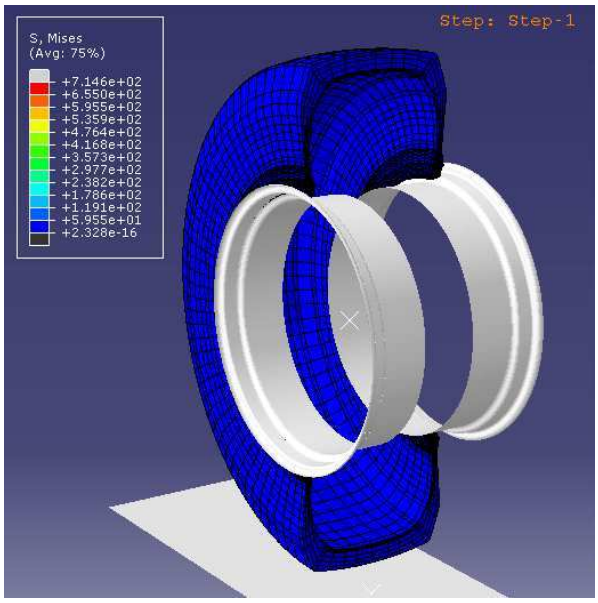


Figure 8.6. Schematic of the tyre fitting process.

After the tyre has been fitted on the wheel, the friction coefficient can be reinstated to the desired value. The value of the friction coefficient between tyre and wheel has been experimentally investigated and results will be shown later in this chapter. Since our first task is to monitor the onset of slip in terms of minimum friction coefficient required to prevent the tyre from slipping locally, the friction coefficient was initially set to 10 to literally "glue" the two surfaces. This is equivalent to enforce bilateral boundary conditions to the contact problem to be solved, analogously to what was done in Chapter 2 to find the bilateral solution to the simplified layered configuration.

8.3.3 Interfacial pressure: model vs experiment

As explained in the previous sub-section, the first aspect investigated with our model is the capability of Abaqus to capture the interfacial pressure between tyre and rim. Figure 8.7 shows the pressure obtained for an inflation pressure of 2.5 bar plotted against the curvilinear coordinate aligned with the wheel rim profile. On the same graph, the experimental results collected by Michelin are plotted (*Michelin private communication*). The experimental pressure was measured using Tekscans (http://www.tekscan.com), a pressure sensitive foil mounted on the rim inner surface to measure the

interfacial contact pressure between the tyre and the rim.

As shown in Figure 8.7, the FE numerical results are in line with the experimental data provided by Michelin. Both the pressure peak and the pressure trend are well captured. The reason for which the pressure goes to zero in the FE model is due to the lack of mesh refinement of the tyre bead. This has been demonstrated by performing mesh-refinement using a 2D model as also shown in Figure 8.7. Performing the same refinement for the 3D model would, however, result in increased computational costs and cause further issues related to the convergence of the 3D analysis. Moreover, an interesting experimental investigation carried out by Michelin (*Michelin private communication, 2009*) showed that the position of the tyre may affect the interfacial pressure distribution largely. The main pressure peak, located at the centre of the bead seat, can reduce to 60 bar while the second peak, corresponding to the rim edge, is less affected by the randomness in the variation of the configuration (*Michelin private communication, 2009*). This can be caused by variation in the rim profile due to the very large tolerances of the mass production process or by an incorrect lubrication of the tyre and wheel surfaces (*Michelin private communication, 2009*). Finally, even the mounting process of the pressure sensors might affect the rim profile locally and, consequently, the pressure distribution. Based on all these considerations, the numerical results were deemed as satisfactory. However, the reader should refer to them as related to the idealised case of a tyre perfectly seated against the wheel profile in ideal mounting conditions.

In the absence of experimental results for the interfacial pressure distribution of an inflated tyre subject to loading conditions but the internal air pressure, the model has been assumed to accurately represent the loaded assembly also when in-service loading conditions are applied. The experimental validation of these scenarios will constitute part of the future work to be carried out in collaboration with Michelin.

8.3.4 Determination of the onset of slip

Once the FE model was consolidated, the onset of slip was determined. As explained in Chapter 2,

this may be done by checking for potential violations of the frictional law, everywhere within the contact, in the bilateral solution. This is obtained by assuring the absence of interfacial slip between tyre and wheel, enforced numerically by setting the friction coefficient to 10. First, the case of a tyre subjected to a vertical load was considered (Figure 8.4(i)). The range of loads chosen was between 3 and 8.5 tons. Figure 8.8 shows the minimum friction coefficient needed to guarantee full adhesion between tyre and wheel for different values of the vertical load. Two lines are plotted on the graph, which constitute upper and lower bounds to the solution of the problem and account for the uncertainty linked to the noise in the numerical results due to lack of mesh refinement. By checking potential violations of the frictional law, it was noted that the bottom part of the wheel takes most of the load whereas the remaining part of the assembly presents a state of stress very similar to the one detected after the inflation process. This can be shown by plotting the pressure distribution before and after loading the tyre. Figures 8.9 and 8.10 show how the pressure distribution varies with the respect to the circumferential position around the wheel.

8.3.5 Effect of speed on the onset of slip

The effect of rolling speed on the onset of slip was then explored. The problem of a tyre moving along the x-direction (see Fig. 8.4) at a rotational speed of 5 rad/s and subject to vertical loads between 3 and 7 tons was investigated. The speed was chosen as representing the average speed of the vehicle when subjected to loads larger than 2 tons (unloaded condition normally referred to as driving condition). The effect of speed was taken into account by modelling the tyre in an Eulerian reference system using the STEADY STATE TRANSPORT command (Abaqus, 2007). The explicit time dependence associated with the purely Lagrangian approach is removed from the problem and a more time-efficient analysis can be performed. The reference frame does not spin with the rolling body, so the mesh remains stationary. This kinematic description of the problem is such that the rigid body rotation can be described in an Eulerian reference system and the material deformation in a Lagrangian manner. Furthermore, this implies that a refined mesh is only required where high

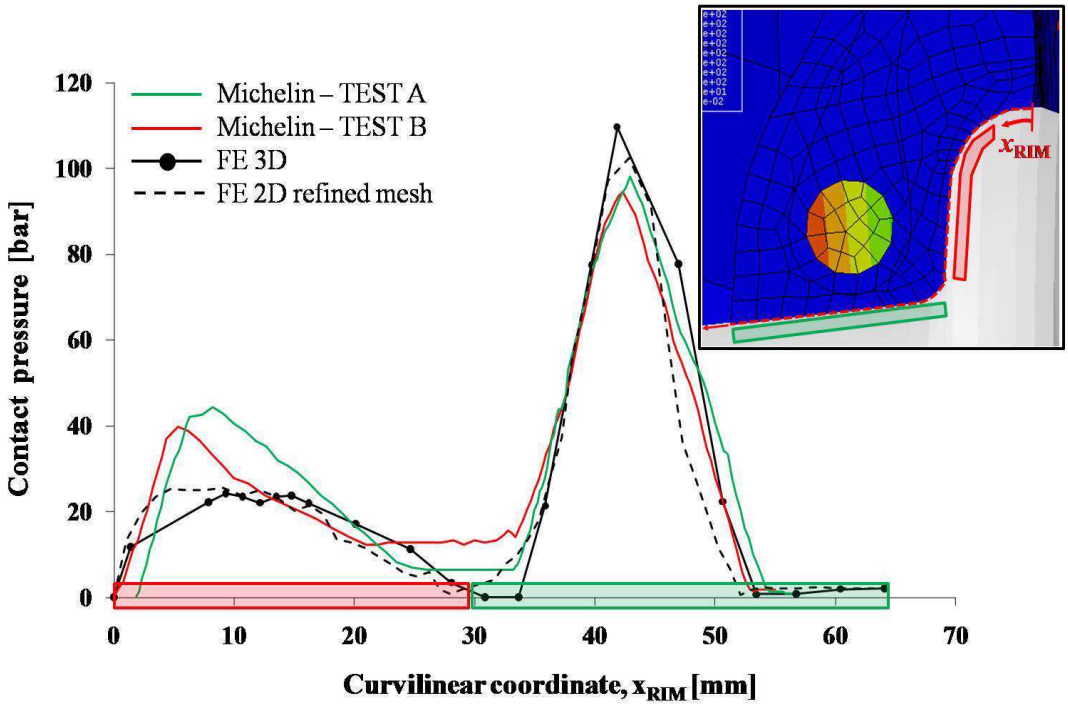


Figure 8.7. FE 3D model of a tyre mounted on a rigid rim – Tyre bead interfacial pressure.

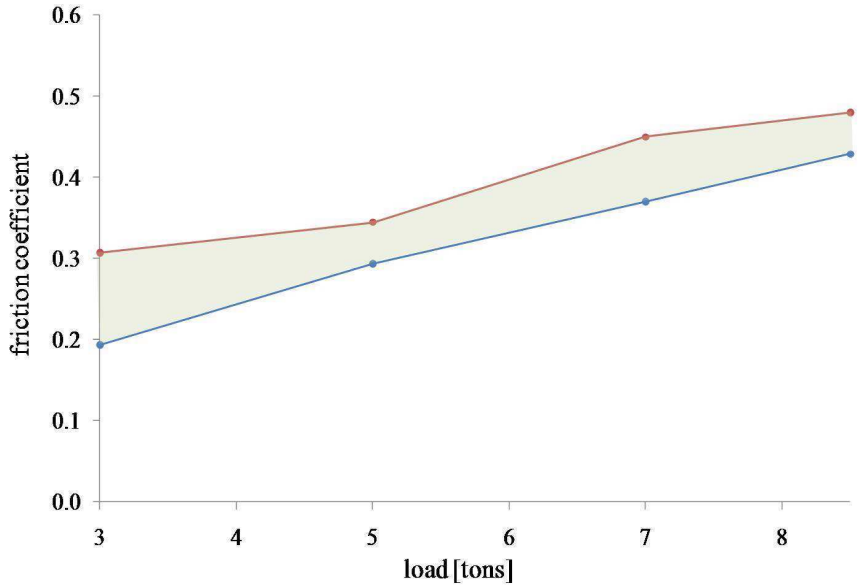


Figure 8.8. Minimum friction coefficient required to avoid slippage between tyre and rim - Normal load only applied.

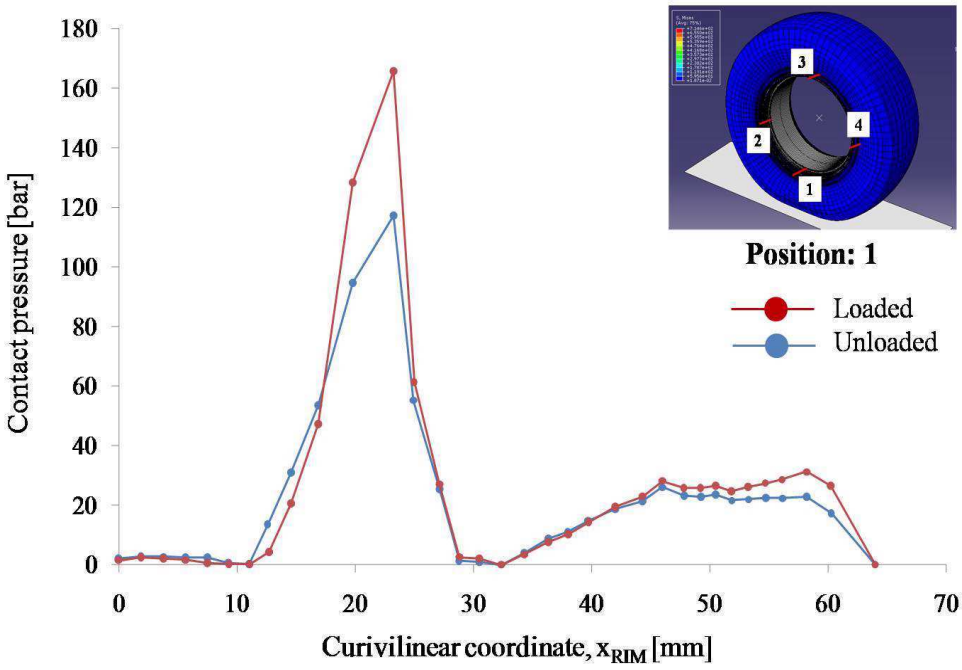


Figure 8.9. FE 3D model of a tyre mounted on a rigid rim – Tyre bead interfacial pressure (normal load only applied - position 1, bottom part of the rim) - vertical load of 5 tons.

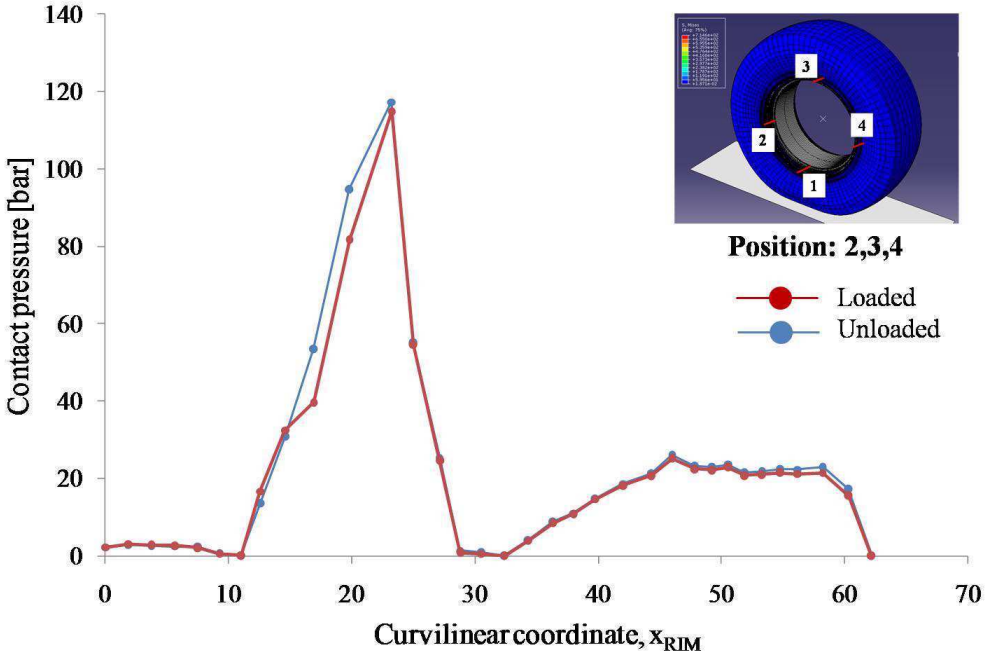


Figure 8.10. FE 3D model of a tyre mounted on a rigid rim – Tyre bead interfacial pressure (normal load only applied - position 2,3 and 4) - vertical load of 5 tons.

stress gradients are expected.

Modelling the assembly using a Lagrangian reference system was ruled out because, despite the accuracy of the results, the computational expense associated with the numerical simulations using a transient analysis in the Lagrangian reference system is already prohibitive for a simple 2D model if the steady-state regime in the presence of creep is to be reached (see Chapter 2). It should be noted here that the presence of interfacial creep has never been explored using this mixed Lagrangian-Eulerian technique (Abaqus, 2007). Hence, with the aim to extend our analyses to such a complex 3D geometry, and, therefore, overcome the limitation of semi-analytical and numerical techniques adopted to solve simplified 2D configurations, the suitability of the FE technique was questioned. To investigate this aspect, first the example problem investigated in Chapter 2 with this Lagrangian-Eulerian technique was modelled and the results were compared with the semi-analytical solutions obtained in Chapter 2, already validated against a FE model devised in a Lagrangian reference system. In the results the Lagrangian-Eulerian solution is referred to as SST which is the acronym of the Abaqus command. Figure 8.11 shows the tangential tractions calculated using the SST together with the bilateral solution (see Chapter 2) in the absence of slip at the layer-substrate interface. It can be concluded that FE results are in line with our semi-analytical model as long as creep is not present.

Essential information can then be obtained from a no-slip analysis in terms of the value of the minimum friction coefficient associated with the incipient slip condition. Based on the satisfactory agreement found between the SST Abaqus analysis and the bilateral solution, the minimum friction coefficient needed to guarantee full adhesion between layer and substrate was calculated for the specific loading conditions already illustrated in Chapter 2. Figure 8.12 shows that results obtained with the SST technique are again in agreement with our semi-analytical results. This means that the SST methodology can be satisfactorily adopted to extract information regarding the possibility of having slippage in tyred systems. Another positive aspect related to the application of the SST

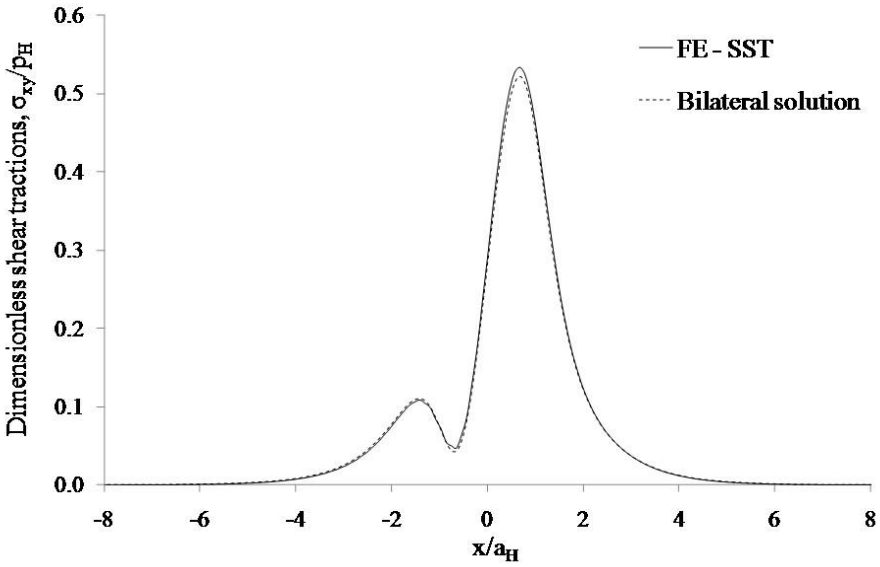


Figure 8.11. Tangential tractions for B=1, ν=0.3, μ=0.7, λ=1 and f=0.2 - full sliding condition – absence of slip at the layer-substrate interface.

technique regards the significant computational time reduction. This advantage, together with the accuracy in the stress field computation, represents the reason for which this technique can be adopted to model the tyre-wheel assembly during rolling. Hence, conditions for the onset of slip were determined for the tyre-wheel assembly when speed is included in the simulation. This part of the work was carried out in collaboration with Mr. Shufan Yang (2009). Figure 8.13 displays the minimum friction coefficient needed to prevent the tyre from slipping plotted together with the results obtained for the static case. By comparing the numerical results, the little discrepancy between the two scenarios[2] implies that rotational speed can be neglected when the analysis is concerned with determing the onset of slip.

Despite the promising results discussed above, this methodology presents two main limitations. The peculiar kinematic description introduced by the mixed Eulerian-Lagrangian representation can be only adopted to model one deformable body (i.e. one of the contacting surfaces needs to be rigid), which means that if the two bodies need to be considered as deformable, one of them has to be

[2] Note that the discrepancy is less than the numerical uncertainty and, therefore, is not significant.

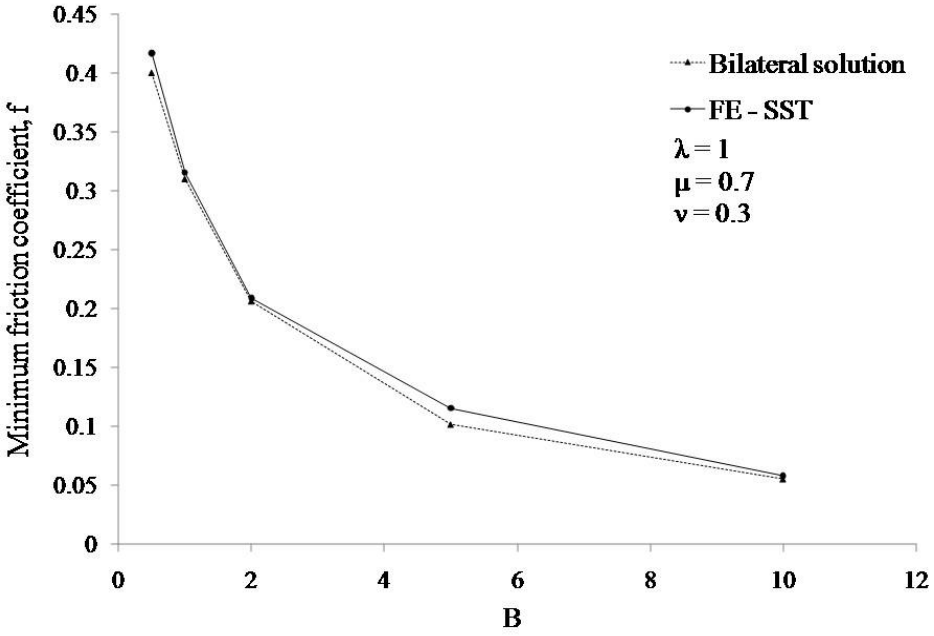


Figure 8.12. Minimum friction coefficient f to guarantee adhesion as a function of the normalised layer thickness B for various friction coefficient μ and ν=0.3 – full sliding condition.

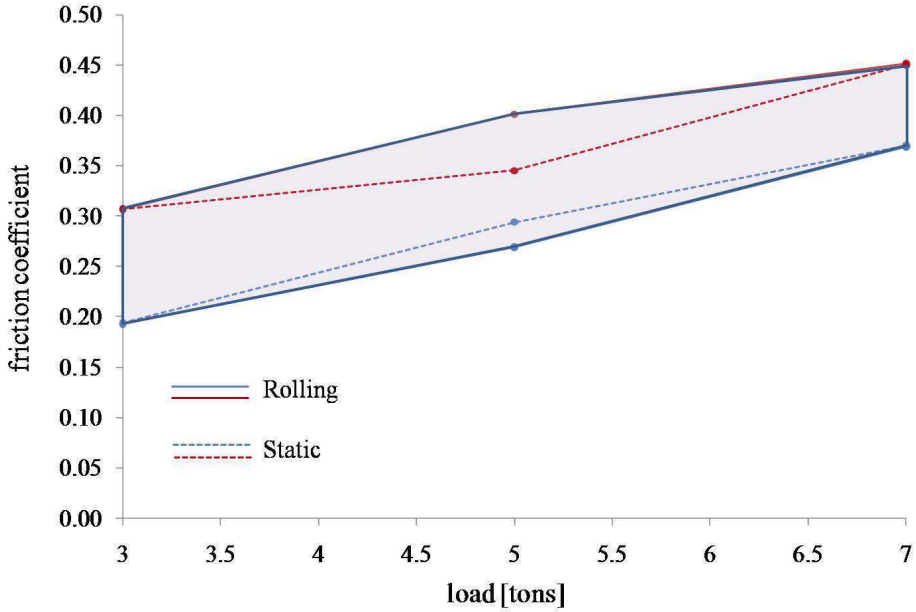


Figure 8.13. Comparison between the minimum friction coefficient needed to prevent the tyre from slipping in presence and absence of rotation.

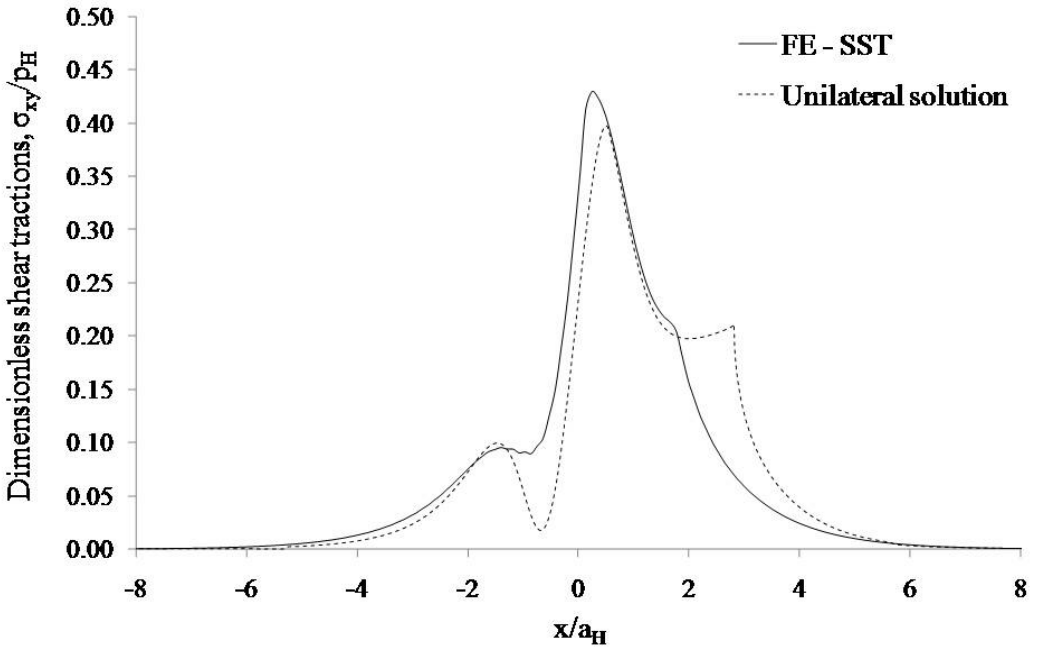


Figure 8.14. Tangential tractions for B=1, ν=0.3, μ=0.7, λ=1 and f=0.2 - full sliding condition - presence of slip at the layer-substrate interface.

described using a Lagrangian formulation (Abaqus, 2007). The second limitation concerns the fact that the SST analysis does not produce accurate results when slip is allowed between the tyre and the rim. Our studies show that incremental creep cannot be correctly identified and monitored using this technique. Figure 8.14 depicts the difference between the semi-analytical unilateral solution calculated for the problem described in Chapter 2 in the presence of interfacial creep and the solution obtained from the SST finite element model when slip is permitted between the mating surfaces. This made us conclude that the SST cannot be used to model the presence of moving loads which give rise to creep. Therefore, only non-slipping conditions can be studied with this technique.

8.4 Effect of wheel deformability on pressure

The deformability of the rim was then introduced. Basically, this considers a different geometrical configuration of the assembly caused by the introduction of the deformability of the wheel and

its influence on the pressure distribution. Figure 8.15 shows the comparison between the contact pressure for a tyre mounted on a rigid and on a deformable rim. The case is related to a tyre inflated to an internal pressure of 2.5 bar in the absence of further loads. The figure shows that the deformability of the rim introduces a modest variation of the pressure profile well within the numerical noise. This is very unlikely to cause considerable variations to the onset of slip map obtained from the rigid model. However, the presence in the model of the deformable components makes it suitable to investigate the wheel stress field. This will be discussed later in this chapter.

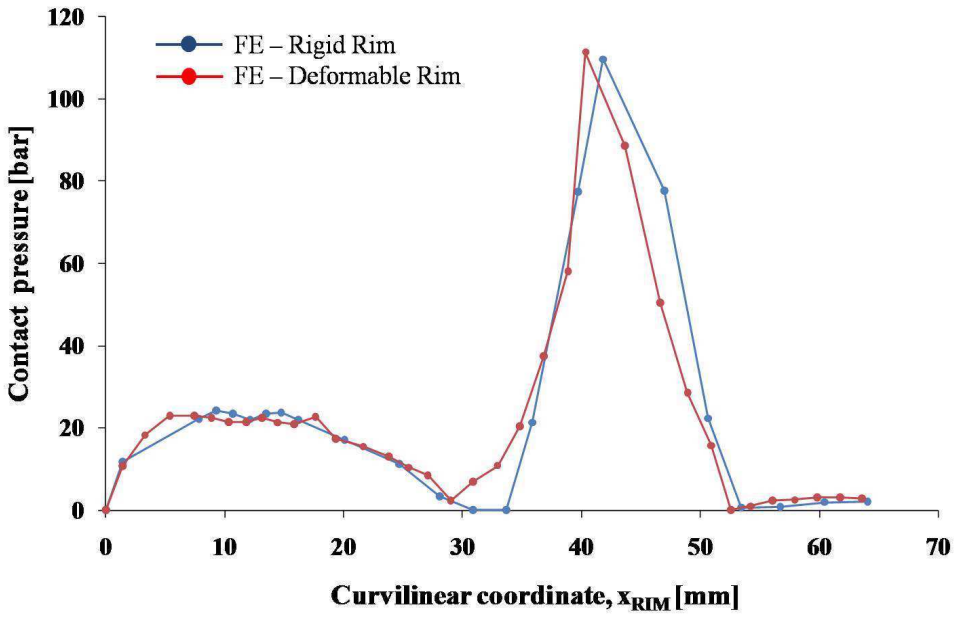


Figure 8.15. Contact pressure distribution between tyre and rim for a rigid (blue line) and a deformable rim (red line).

8.5 Alternative rim profile

A new rim profile has been introduced by GKN as a development of the product currently available on the market. Figure 8.16 shows the comparison between the old and the new profile modelled using Abaqus. The modifications were performed with the aim of reducing the weight of the rim and, consequently, the production costs were reduced (*GKN private communication, 2009*). The real geometries cannot be disclosed.

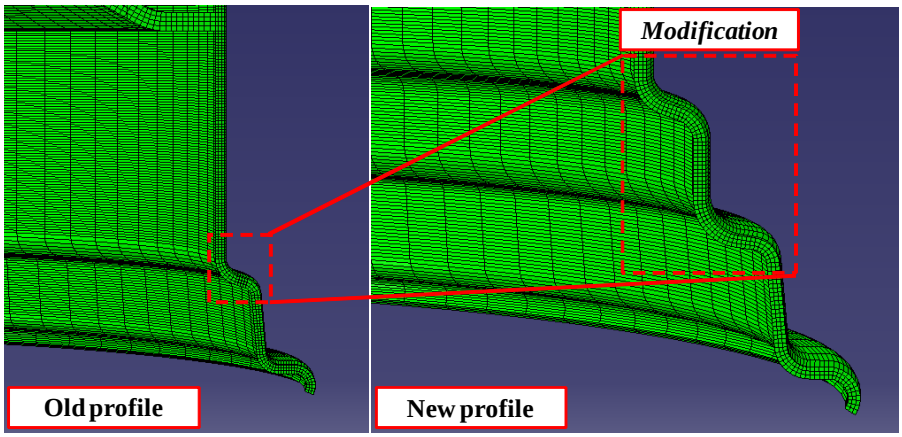


Figure 8.16. Comparison between the old and the new wheel profile.

The variation of the profile did not interest the part of the rim which is in contact with the tyre. For this reason no significant changes of the pressure distribution are expected and, consequently, of the onset of slip. Hence, the onset of slip has not been determined for the new rim profile. Only minor variations are expected between the original and the new FE description of the assembly because the tyre bead mesh was improved to eliminate the discontinuity corresponding to separation along the bead seat. However, it is interesting to plot the numerical results against the FE results generated with for the original geometry and the experimental data provided by Michelin for the new rim profile (*Michelin private communication, 2009*). Such comparison is shown in Figure 8.17. The pressure profile generated with the new FE model seems to have solved the problem with the separation but there is now a marked difference between the main pressure peak obtained from the model and the one experimentally measured by Michelin. Michelin has already anticipated that the pressure measurements have been affected by set-up issues and further investigation will be carried out to understand whether this affected the experimental results. Moreover, as previously explained, many factors may affect the real pressure distribution between tyre and wheel and, consequently, the reader should not be surprised by the apparently marked difference between the experimental and the numerical results.

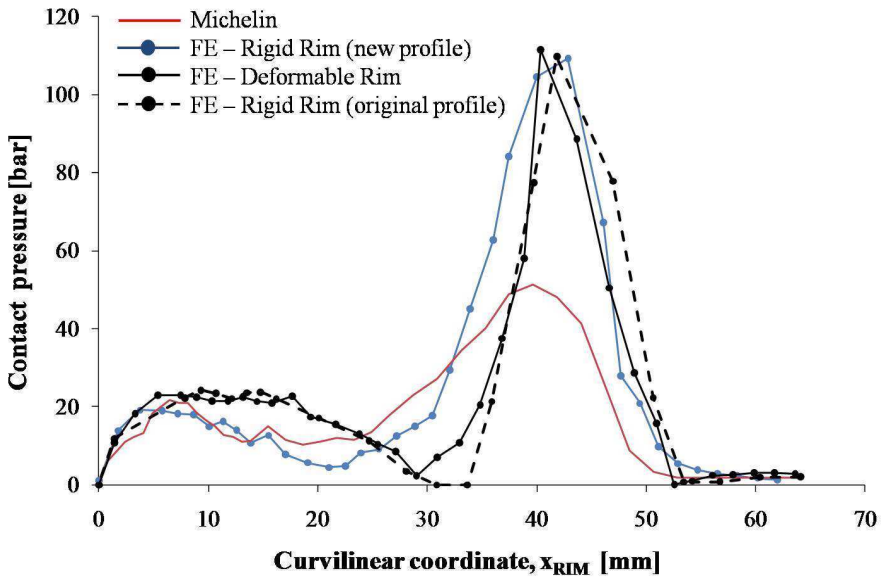


Figure 8.17. Comparison between the numerical and experimental contact pressure distribution between tyre and wheel.

8.6 Tyre-Rim friction coefficient

As mentioned in the previous sections, the Amonton-Coulomb's law was chosen to model the frictional behaviour at the interface between tyre and rim. This means that the friction coefficient has been modelled as independent from the contact pressure and the relative speed between the mating surfaces. It is well known that rubber presents a pressure/speed dependent behaviour which is even more marked when harmonic loads are present (Treloar, 1958; and Persson and Tosatti, 2000). In our specific case there is no relative speed between the mating surfaces and the range of contact pressure varies between 20 and 100 bar depending on the location of the contact points at the tyre-rim interface (see Figure 8.17). Since the focus is on the onset of slip, potential lateral displacements of the tyre bead with respect to the wheel are not considered. Consequently, the local pressure variation that rubber may experience at any point depends only on the location of the point within the contact. In absence of rotation, the contact pressure is space and time invariant. Therefore, apart from the case where significant rotation is present, which is in general limited to applied normal loads below 3 tons, the pressure distribution does not vary with time as the tyre can

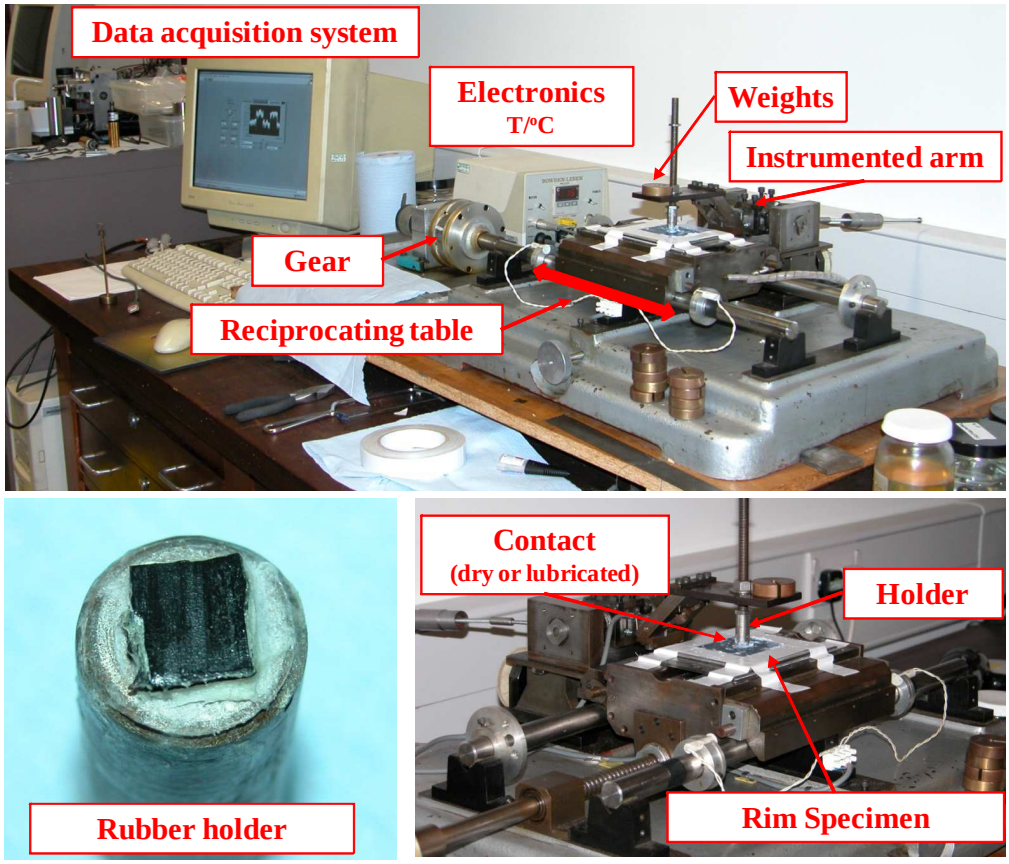


Figure 8.18. Bowden-Leben test apparatus and detail of the rubber holder (rubber pad 3x3 mm).

be considered practically stationary for a significant part of its duty-life. This was considered when developing an experimental protocol to estimate the friction coefficient between the rubber compounds of which the tyre is made and the wheel under different loading and lubricating conditions. The value so obtained have been then compared to the values shown in Figure 8.13 to determine whether conditions for the tyre to slip with respect to the rim are met.

The measurements were done using a Bowden-Leben reciprocating test rig available at Imperial College London (see Figure 8.18). The apparatus is based on the experimental set up described by Bowden and Leben (1939) and it has been widely used since then to investigate several tribological applications (Blau, 1995; Stachowiak and Batchelor, 2004; and Edge, 2008). The test rig is powered by a servo-controlled DC motor. Rotary motion was converted to reciprocating motion via a gearbox and a linear screw-drive assembly. A slider (reciprocating table in Figure 8.18) is connected to the

linear-screw assembly which hold the sliding sample. The samples, represented here by a sheet of rim material, are then loaded normally and reciprocated under the rubber pads. All the specimens were provided by GKN and Michelin. A LABVIEW program (LabView, 2003) was coded and used to control the test and set the sliding speed to the value for which local instabilities were not present in the signal (Persson, 2001). In fact, a marked stick and slip behaviour is present at low speeds and this in turn makes the friction measurements unreliable. The signal coming from the strain gauge placed on the instrumented arm was recorded by the program and transformed into frictional force output after amplification. A MATLAB routine (MATLAB, 2009) was written to post-process the experimental data results acquired during the tests. Finally, at the beginning of each test and every time a modification was made to the rig set-up, the signal was calibrated using known tangential forces applied in the reciprocating direction.

The wheel rim specimens used for the friction tests are shown in Figure 8.19. Three different specimens, corresponding to three different surface finishes, were tested following GKN requirements. Wheels are, in fact, commonly coated in order to protect steel against corrosion and for aesthetic reasons. In particular, here, specimen A is electrically coated, specimen B is simply painted and specimen C is uncoated.

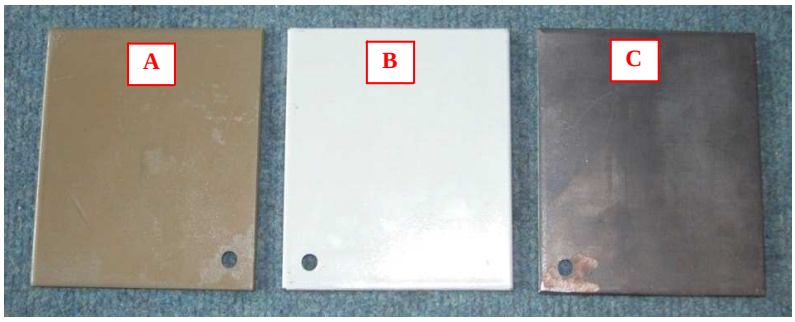


Figure 8.19. Rim specimens: (A) electrically coated, (B) painted and (C) uncoated.

The rubber pads were obtained from a section of a tyre provided by Michelin. The size of the rubber pad was dictated by the maximum pressure that can be measured using the experimental apparatus. In our case the specimens were 2.5x2.5mm and, given an estimate of the interfacial

friction coefficient between 1 and 2 (Treloar, 1958), the maximum contact pressure was limited to 2.7 bar.

First the tests were carried out in dry condition and, then, lubricant was applied to the sample surface. This is because lubricant is commonly used to ease the tyre fitting process. GKN and Michelin suggested to test three common lubricants which are adopted to mount tyres (see Figure 8.20).

A further objective of the investigation carried out by the author was to estimate the drying time of the lubricants since this was originally thought to be one of the major causes of tyre-rim slipping problem. The pressure which can be achieved with our rig is not representative of the pressure at the tyre-rim interface. However, results will be used as a qualitative indication of the tribological behaviour of the coupling in the presence and in the absence of a lubricant film.



Figure 8.20. Lubricants (*http://www.rema-tiptop.co.uk*) suggested by Michelin for the tyre-fitting process .

Figure 8.21 shows the results obtained in dry condition. The sliding speed was set to 0.03 cm/s (slowest speed that avoid signal oscillations due to stick-slip phenomena) and the tests were performed at room temperature. All the values are well above 0.5 (see Figure 8.13)), therefore it seems that there is no reason for a tyre to slip in dry condition when mounted on the wheel correctly. The rubber pad and the rim specimens were thoroughly cleaned using iso-propanol to remove all contaminants that might have been deposited to the mating surface as a consequence of the manufacturing process. As can be seen from the figure, sample B showed the highest friction coefficient and the uncoated specimen the lowest. This could be attributed to the difference in compliance between the

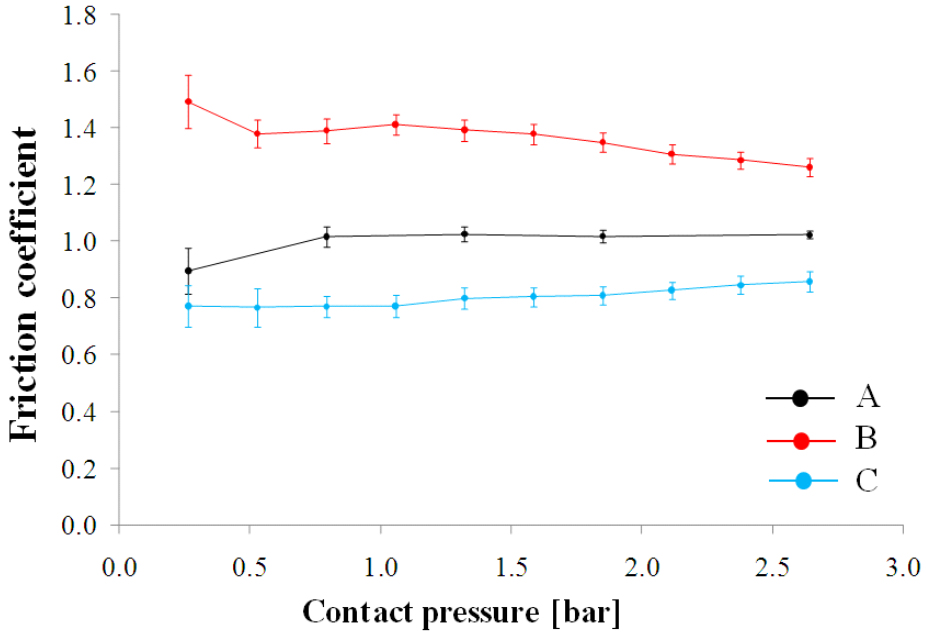


Figure 8.21. Variation of the coefficient of friction between tyre and rim specimens as a function contact pressure for different rim surface specifications and for a sliding speed of 0.03 cm/s. The error bars identify two standard deviations from the mean.

tyre rubber and the steel surfaces. In order to corroborate this hypothesis, a 3D picture of the surface profile of the three specimens was taken using a Veeco optical profilometer (www.veeco.com), available at Imperial College London. As can be seen from Figure 8.22, the painted specimen is smoother and this could be responsible for increased adhesion between rubber and rim samples which is, in turn, responsible for the increased value of the coefficient of friction.

To complete the characterisation of the mechanical and tribological properties of the coupling, the hardness of the uncoated specimen was measured and found to be in line with the standard properties of low carbon steel (145HV20). The value is reported in Figure 8.22 together with the roughness parameters which characterise the surfaces.

Tests in wet conditions were also carried out in order to investigate the effect of each lubricant on the friction coefficient of the coupling. This is an important factor as lubrication is strongly recommended to mount the tyre on the wheel correctly (Michelin, 2004). The drying time of the

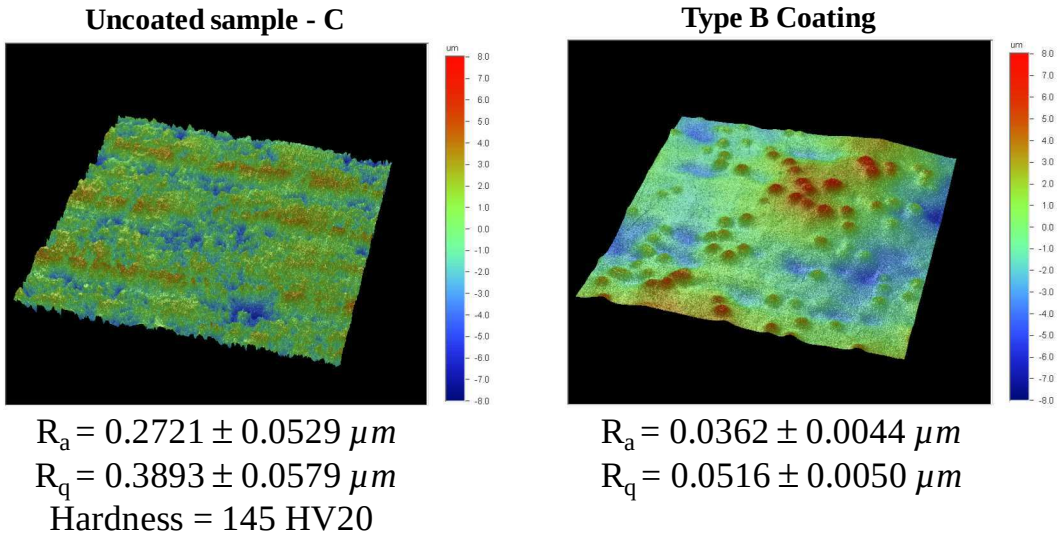


Figure 8.22. Surface topography for the uncoated rim specimen and the rim specimen coated with white paint (area 10x10 mm).

lubricant was also investigated, as this might constitute one of the most important factors governing the tyre spinning problem. In order to investigate this aspect, the friction test was carried out immediately after the application of the lubricant (0hr), then after 24hrs, 48hrs and, eventually, 96 hrs. Between each test, the equipment was adequately protected from external contamination and kept in a controlled environment. Figures 8.23, 8.24 and 8.25 show, respectively, the effect of lubricants A, B and C on the friction coefficient of the coupling. The results suggest that conditions for the tyre to slip are met whether the tyre is used immediatly after it has been mounted on the wheel (see Figure 8.13 for comparison). This suggests that an adequate time may be required for the lubricant to dry out.

Figure 8.26 shows the variation of the friction coefficient with time. The lubricant does not seem to have dried out after 96 hrs and did not show a consistent trend of increasing friction over time. Discussion with Michelin and the lubricant supplier led us to believe that the reason behind this kind of unexpected behaviour may be due to the fact that the applied pressure is not enough to generate a lubricant film thickness which is representative of the in-service conditions. Lubricant ageing effects associated which a much thicker film thickness than the one related to the real application

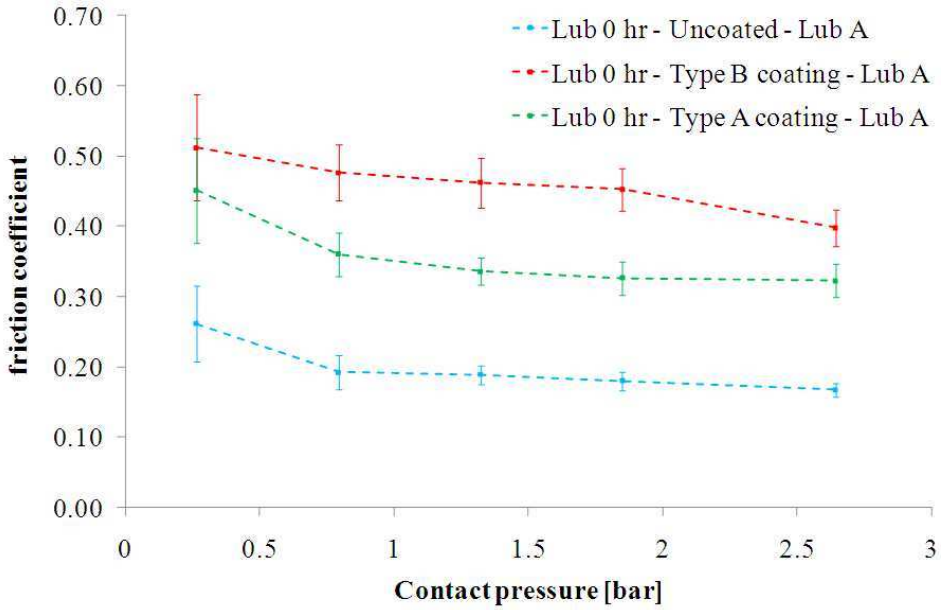


Figure 8.23. Measure of the coefficient of friction between tyre and rim specimens as a function of contact pressure for different rim surface specifications in presence of lubrication (lubricant type A); values obtained immediately after lubricant application.

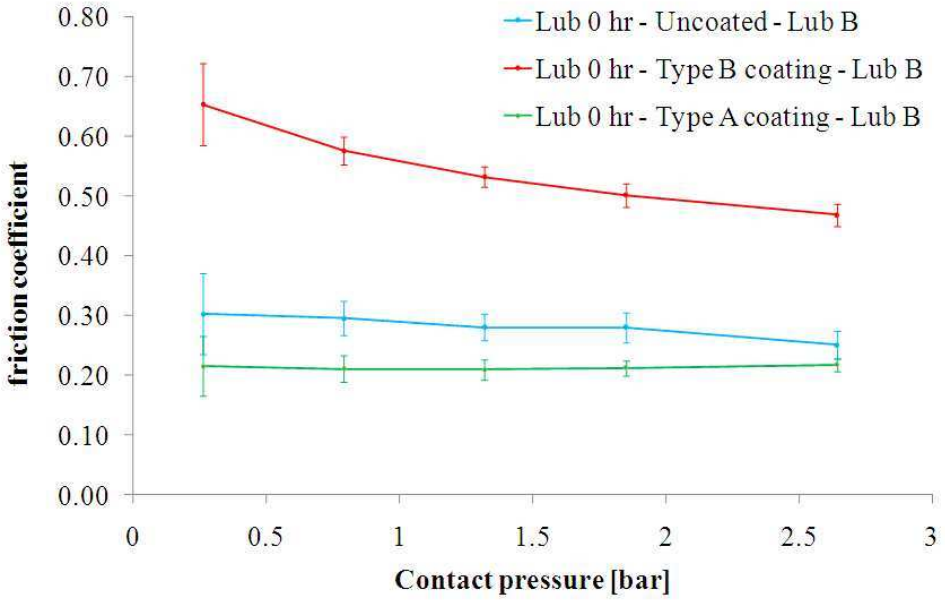


Figure 8.24. Measure of the coefficient of friction between tyre and rim specimens as a function of contact pressure for different rim surface specifications in presence of lubrication (lubricant type B); values obtained immediately after lubricant application.

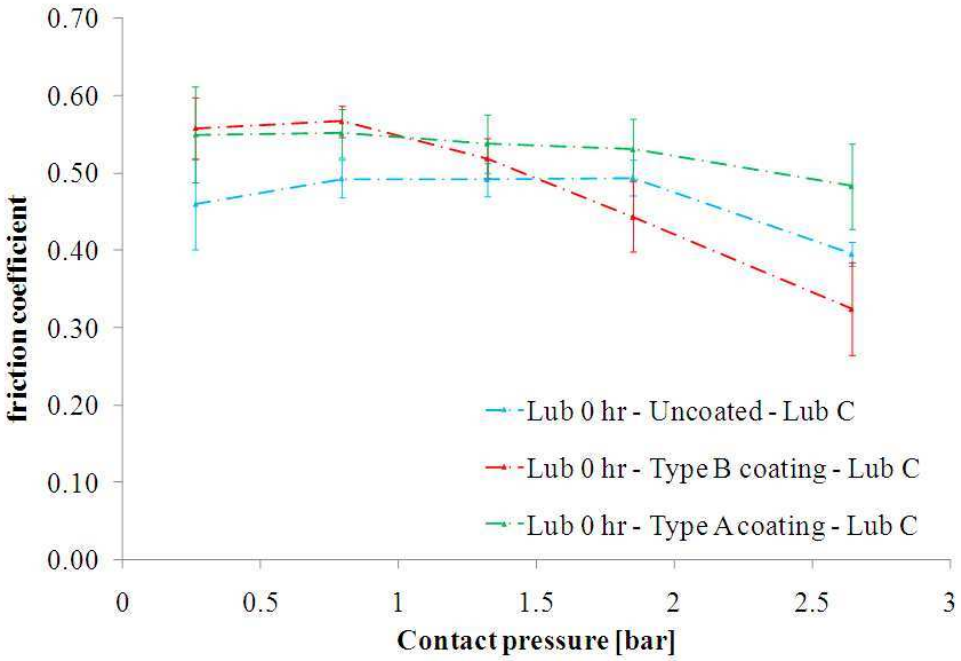


Figure 8.25. Measure of the coefficient of friction between tyre and rim specimens as a function of contact pressure for different rim surface specifications in presence of lubrication (lubricant type C); values obtained immediately after lubricant application.

may, therefore, be responsible for the results obtained using the Bowden-Leben test apparatus.

A similar behaviour was shown by the other two lubricants. In order to improve the fidelity of our measurements and to better replicate the mounting characteristics of the assembly, the development of a new rig was deemed necessary. The new test apparatus has been designed to enable us to increase the applied pressure at the contact interface and to estimate the optimum drying time which is needed to guarantee perfect adhesion between tyre and wheel (see Figure 8.13). This aspect will be covered in the next section together with the study of the effect of knurling on the tribological performance of the tyre-wheel coupling.

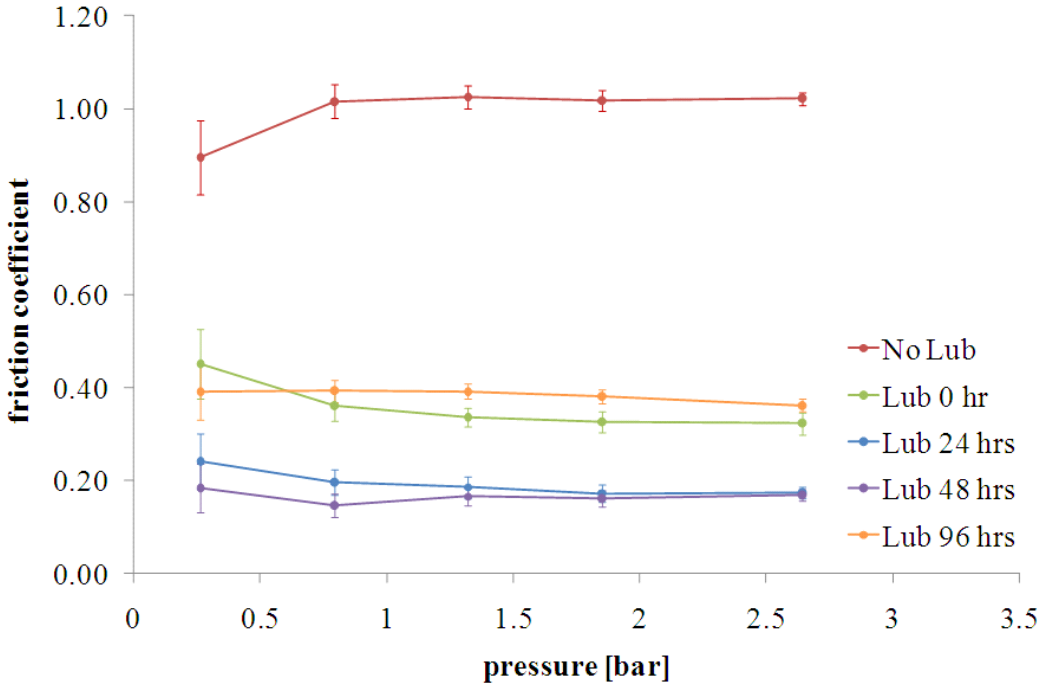


Figure 8.26. Variation of the coefficient of friction between tyre and rim as a function of contact pressure and time passed after the lubricant application for different rim surface specifications - Rim specimen A - Lubricant type A.

8.7 Effect of knurling on tyre-rim interface slip

Knurling is a surface profile corresponding to an "artificial roughness" which is added to wheel rim profile in order to improve the tyre bead grip in the area where the peak pressure occurs and most of the load is transmitted (see Figure 8.27).

Based on an internal investigation carried out by Michelin and GKN, knurling was introduced about 40 years ago to prevent large tyres (above 24 inches in diameter) from slipping. Since then, tyre and wheel hub have changed significantly and a thorough investigation has never been carried to explore the effect of knurling from a quantitative point of view. Meanwhile, different knurling profiles have been introduced and standardised (www.etrto.org). Hence, the need to explore the effect of lubricants by generating more realistic conditions for testing the tyre-rim interfaces in the



Figure 8.27. Example of knurled wheel (*image courtesy of GKN - http://www.gkn.com*).

presence of lubricant films (see previous section) and to quantify the effect of knurling prompted the development of a new experimental apparatus. The conceptual design of the apparatus is shown in Figure 8.28, 8.29 and 8.30 together with its salient features. The idea is the result of the collaborative efforts of the project partners. The drawings have been made in collaboration with Mr. Sun Yu (2010), MSc student working on the knurling characterisation under Dr. Dini's and my supervision.

The main specification for the new rig design is to try to mimic the prototypical application in terms of pressure peak and local distribution at the tyre-rim interface. The vertical load will be applied using a lever system and a dead weight (Fig. 8.29) and the tyre will be kept in place, once seated on the rim equivalent profile, by using a moving pad, which slides along a dovetail joint and is connected to a dead weight via a pulley system (Fig. 8.29). This mimics the effect of the internal pressure induced by the inflation on the tyre walls. Figure 8.30 shows the test pad whose surface can be machined to reproduce the knurled profile to be tested. The pad will be connected (Fig. 8.28) to an actuator via a test sample holder. The relative displacement between the knurled sample and the tyre will be induced by torque applied via the actuator on the driving shaft connected to the sample holder (see Figure 8.28), and force and displacement will be recorded by the means of a data acquisition system. The test apparatus should enable (a) the comparison of the effect of the

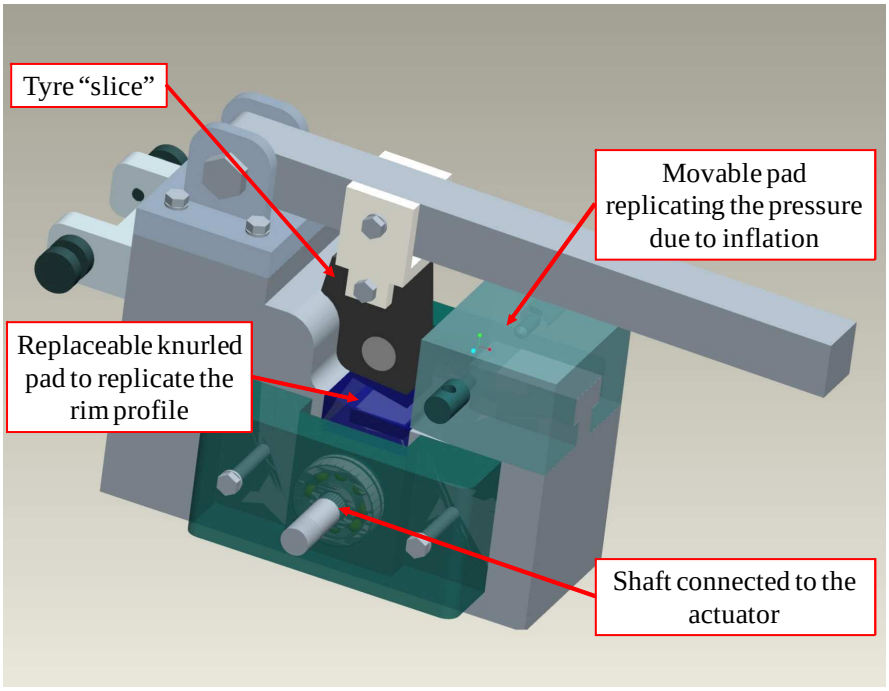


Figure 8.28. Rig concept design to investigate the effect of knurling on the tyre-rim interface (tyre "slice" width=20 mm).

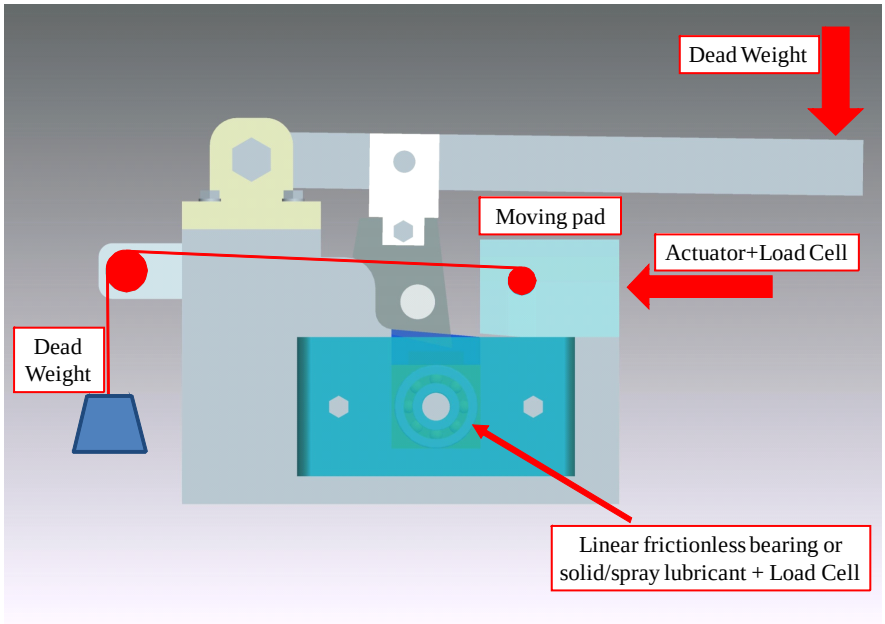


Figure 8.29. Lateral view of the rig concept design to investigate the effect of knurling on the tyre-rim interface.

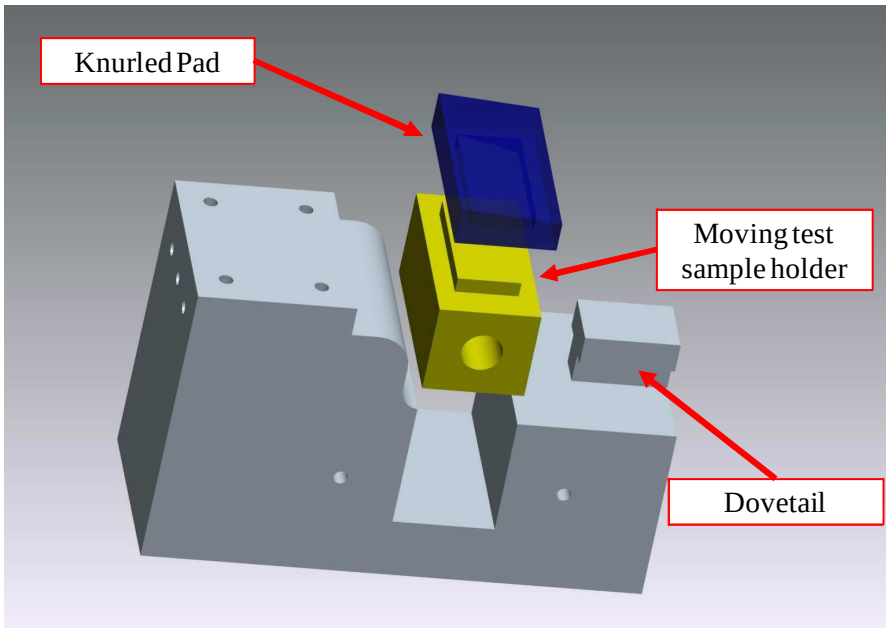


Figure 8.30. Explosion of a sub-assembly of the rig concept design to investigate the effect of knurling on the tyre-rim interface.

knurling on the response of the system by testing various knurled and an unknurled profiles, (b) discerning the behaviour of different knurling profiles, (c) optimising the knurling profile and (d) testing the effect of lubricants in more realistic configurations. The completion of the rig design, its manufacturing and the performance of the tests for a better characterisation of the tyre-rim interface will constitute the object of future work.

8.8 Tyre misfit and effect of improper lubrication

A visit to the Michelin facilities in Stoke on Trent highlighted the following problems: (a) if the lubricant is not applied following Michelin's best practice suggestions, the tyre may not be seated properly during the fitting process and this cannot be easily identified by the tyre fitters; (b) if the tyre is not adequately fitted, the tyre bead tends to rock with respect to the rim and the pressure distribution between tyre and rim is significantly modified by the new contact geometry; (c) the tyre bead could twist under the effect of high loads and the designed interference between tyre and rim

may be lost during operation; (d) the tyre bead wears out as the tyre bead rocks over the knurling. This has led to an investigation of the problems associated with the tyre-rim fitting process. This links directly to the the reasons for which the tyre is observed to spin around the wheel rim. In fact, tyre misfit may lead to a reduction of interference pressure between tyre and rim due to the "rocking" effect which takes place at the tyre bead. This is an unnatural rotational movement (see Figure 8.31) that induces permanent deformation in the steel rod which constitutes the core of the tyre bead (see Figure 8.2 and 8.3). This causes a reduction of interference pressure between tyre and rim and may be responsible for interfacial creep and, eventually, lead to the disengagment of the tyre-wheel assembly. The numerical model of the tyre-rim system has been modified to consider the issue related to such process. So far, this problem has been addressed by modelling the tyre as fitted on the rim in ideal circumstances, with the rim being modelled as rigid. Moreover, in the FE models presented in the previous sections, the fitting process has been simulated in absence of friction between the tyre and the rim, with the friction being restored once the fitting process had been completed successfully. Hence, these models do not address the problems associated with the tyre fitting process. Therefore, a further FE model was developed to thoroughly investigate the phenomena which occur during the mounting of the tyre-rim assembly. The new axy-simmetric FE model simulates the fitting process by adding a frictional interface between tyre and rim. This complicates the model and several numerical problems have to be addressed. Figure 8.32 shows the difference between a tyre properly fitted (Fig. 8.32(i)) and a tyre bead which is not perfectly seated due to fitting problems in the presence of high friction coefficient at the tyre-rim interface (Fig. 8.32(ii) friction coefficient=0.2 and 8.32(iii) friction coefficient=0.6). The numerical model confirms that an incorrectly seated tyre bead (Figure 8.32(c)) tends to rock with respect to the rim (see Figure 8.31), and this explains how the tyre bead are damaged and, eventually, severely worn out. This additional investigation places the emphasis on the fact that controlling the tribological performance of the coupling is not only linked to the problem of limiting the interfacial slip between tyre and wheel, but is also related to many other issues associated with the mounting process and

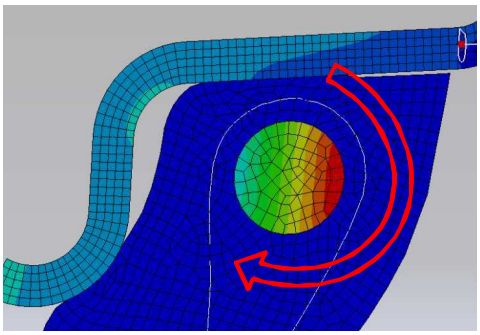
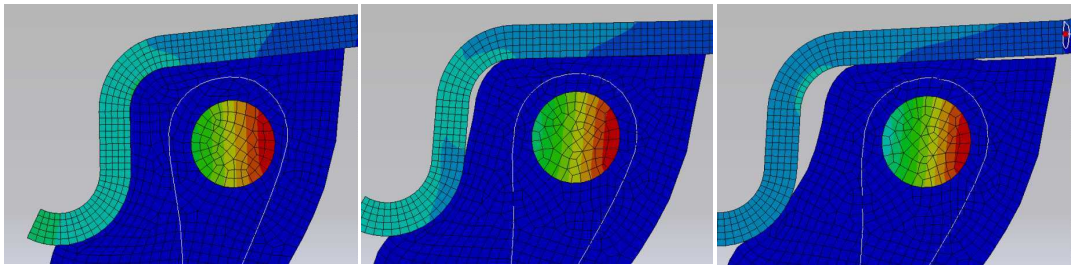


Figure 8.31. Tyre bead rocking effect when the tyre is not correctly seated.



(i) *(ii)* *(iii)*

Figure 8.32. Tyre bead final position when seated as a function of the friction coefficient between tyre and rim (i) friction=0, (ii) friction=0.2 and (iii) friction=0.6

the operating conditions.

8.9 WFT and Rim stress field

A description of the in-service vehicle load history was required to complete the investigation on the tyre-rim assembly. The load history is needed as an input to the FE models, to provide essential information for achieving improved design against fatigue for the wheel, and to extract the load characteristics to be reproduced in the in-house test rigs to perform design validation using GKN and Michelin existing facilities. To do so, the wheel disc-hub attachment of the JCB loader 4CX was equipped with a wheel force transducer (WFT) purchased from KISTLER (www.kistler.com). Figure 8.33 shows the load force transducer mounted on the front wheel hub. The device enables the collection of forces and moments along the three directions depicted in Figure 8.33.

A total of six signals were recorded, corresponding to the three-forces and the three moments along

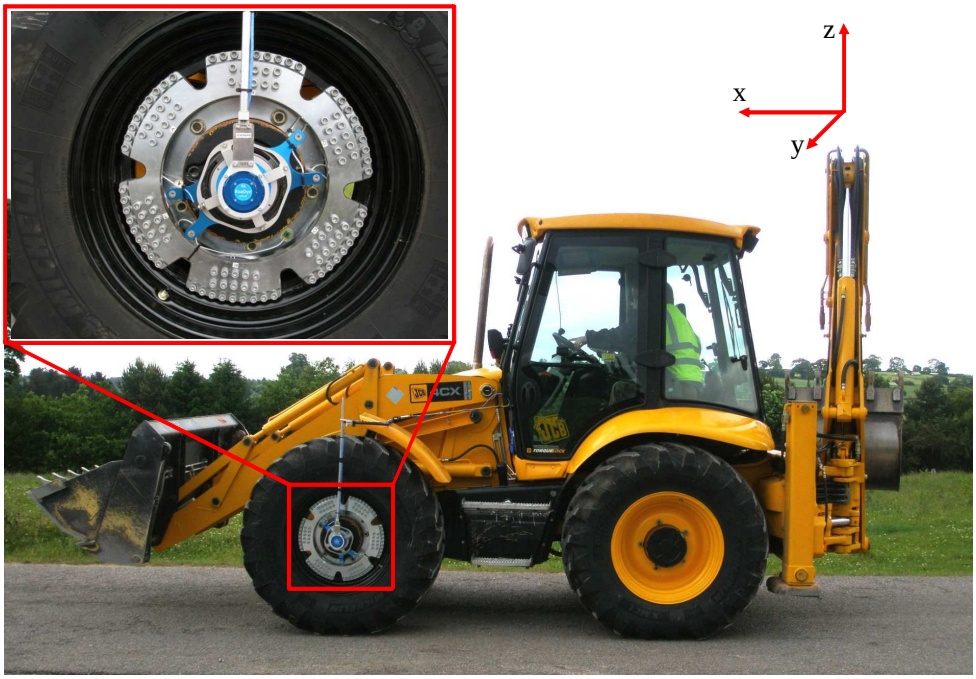


Figure 8.33. JCB 4CX Backhoe loader equipped with the wheel force transducer (WFT - *http://www.kistler.com*) mounted on the front wheel (*image courtesy of JCB - http://www.jcb.com*).

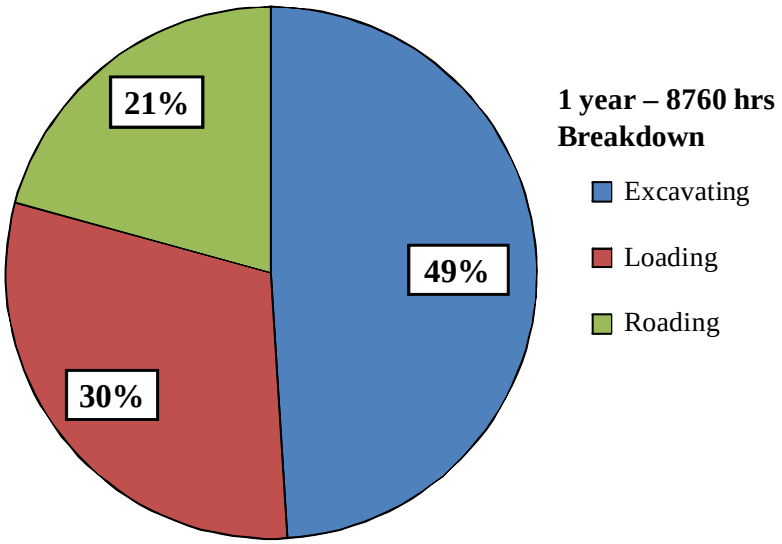


Figure 8.34. Breakdown of the vehicle duty cycle.

the axes, with respect to the steering angle and the rolling speed. The measurements were carried out at both the front and the rear wheel. Because of the architecture of the vehicle, the front wheel was found to be subject to the highest loadings and, consequently, the discussion and the results that follow here are related to the front axle.

After a first series of preliminary calibration tests, a series of activities have been performed at the JCB premises in order to collect data based on the vehicle duty profile. The typical profile was defined by JCB based on the vehicle duty-cycle. Figure 8.34 shows the three main types of operation for the type of vehicle under investigation (JCB 4CX). Specifically, excavating and loading, which count for 79% of the life of the vehicle, are normally classified as static operations. This means that the vehicle is stationary and the rolling speed is zero. The remaining 21% is classified as roading and this implies presence of significant rolling speed. Each operation can be divided into subactivities as shown in Table 8.2. A comprehensive description of each activity is outside the scope of this thesis and more details can be found in the internal project reports submitted to TSB (*confidential data*). The data has been classified based on the information that JCB provided (Figure 8.34 and Table 8.2) and a typical loading history profile generated. Figure 8.35 and 8.36 show examples load history for the vehicle under investigation in static and dynamic condition, respectively, for one of the forces recorded by the WFT. The stories include all operations that a vehicle may experience and it was originated by data recorded and re-organised over a period of 150 hrs. The following procedure was devised to generate the load history: first, each single activity was classified based on its occurrence probability provided by JCB. Then, each force and moment component was separated from the relative signal and, subsequently, filtered to remove the electrical noise incorporated in the signal during the field test. An important aspect which was noticed during the data analysis is that there was drift on the lateral force signal. The drift was compensated as its effect is due to the increase in temperature generated by the operation performed and, as such, is linear. The WFT was then re-calibrated to compensate for temperature drifts automatically. Once all signals were classified

Duty profile	**Activity breakdown**	**%**	**Split %**
Excavating	Site stripping	*62.8*	100
Loading	Rehandling	*37.2*	60
	Rehandling severe		16
	Basement dig		20
	Pry post - Normal, severe and very severe		4
Roading	Brookleys	*100*	23
	Quarry floor laden SRS on		23.5
	Quarry floor laden SRS off		23.5
	High speed oval track clock		11.5
	High speed oval track anti-clock		11.5
	Slalom		3
	Reversal - gear1, gear 2 and gear 3		4

Table 8.2: Vehicle activity breakdown.

and the noise removed, each signal was processed in order to single out potential periodicities using auto-correlation. This is because each activity can be characterized by a basic load history which is representative of the corresponding activity/operation. The information associated with the basic time period of each force and moment was linked to all the corresponding signal components. Then, all basic load histories were combined together based on each occurrence probability to produce the equivalent vehicle duty cycle. This information constitutes the main outcome of the data analysis as it summarises all the loads applied to the assembly and their periodicity over a representative time, which, in turn, can be associated with the periodicity of the loading history. Such loading profiles have been captured and condensed in duty-cycles maps now available to the project partners.

As mentioned at the beginning of this section, the loading history data are to be used as an input for the analyses performed to asses the fatigue performance of the wheels. However, the GKN in-house test rig only capable of reproducing simplified loading conditions such as the ones shown in Figure 8.4. Consequently, the loading histories as shown in Figures 8.35 and 8.36 are too complex to be implemented on that apparatus. Future work will include a further investigation of the possibility to further simplify and reduce the loading history maps according to the requirements of the in-house testing.

Finally, although this is outside the scope of the work presented in this thesis, the FE model developed by the author will be also used to predict the stress field induced by in-service loading conditions while replicating the load path through the tyre. The preliminary results obtained using the FE model of a tyre mounted on a deformable wheel (Figure 8.37) to extract the stress field at the rim-tyre interface align with the data obtained with the strain gauged wheel (*GKN private communication, 2009*). This will constitute a very powerful design tool and the calibration of the FE model results against strain gauged wheel data acquired at GKN FAD to explore the different response of the wheel due to various tyre architectures and loading conditions will constitute part of the future work to be carried out in collaboration with the project partners.

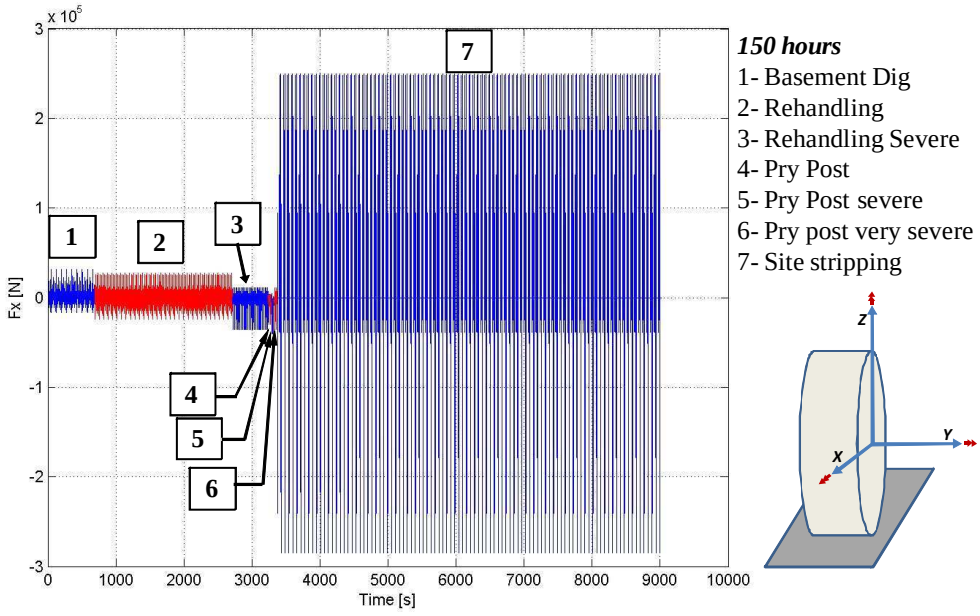


Figure 8.35. Example of vehicle load history - static condition (excavating and loading) - front wheel.

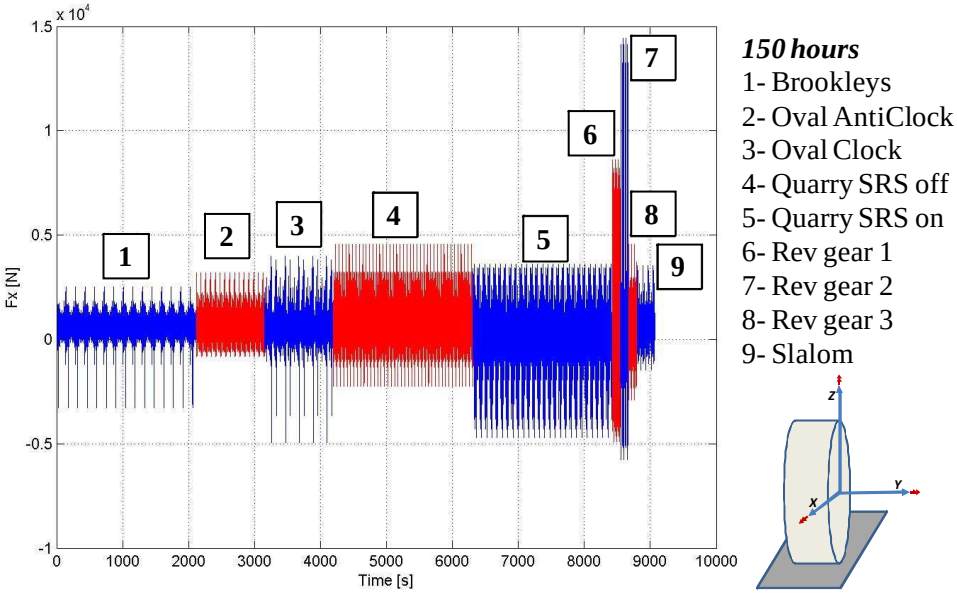


Figure 8.36. Example of vehicle load history - rolling condition (roading) - front wheel.

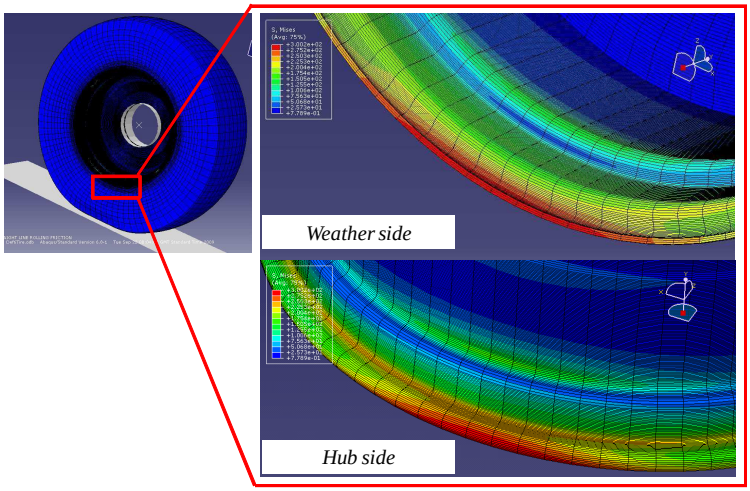


Figure 8.37. Example of Von Mises counter plot of the wheel stress field - pure vertical load of 5 tons.

8.10 Summary

A description of the work carried out on the prototypical 3D assembly was presented. A 3D FE model of a tyre mounted on a rigid and on a deformable rim has been presented and proved capable of capturing the tyre-wheel pressure spatial distribution correctly. The model enabled the determination of the onset of slip in terms of minimum friction coefficient needed to guarantee adhesion between tyre and wheel for the prototypical application.

The tribological characteristics of the tyre-wheel interface were also the subject of our investigation. A Bowden-Leben apparatus was employed to measure the friction coefficient between tyre and wheel in dry and wet conditions. Considerations on the limitations of the apparatus to obtain reliable values of the friction coefficient in presence of lubrication prompted to the design of a new test rig. The design of the apparatus, to be also adopted for the optimisation of the knurled profiles used to avoid tyre-wheel slip for large wheels, has also been presented and discussed.

Finally, the loading history of the assembly was determined based on field measurements carried out on the JCB 4CX based on duty-cycle information. The application of the 3D models developed by the author for the assessment of the wheel fatigue performance has also been proposed and will constitute the object of future investigations.

Chapter 9

Conclusions and future work

The work presented in this thesis was prompted by an investigation of creep and, ultimately, gross sliding, of rubber tyres fitted around steel wheels. In the introduction to the thesis, it was explained how this engineering problem can be idealised and simplified in first approximation as a layered contact problem. Consequently, the class of elastic contact problems commonly referred to as layered contacts has been investigated in depth aiming to contribute to the physical understanding of the phenomenon of interfacial creep in frictional layered systems. Several authors have already analysed this class of mechanical assembly and a comprehensive review was presented in Chapter 1. Only a few authors have, however, proposed effective semi-analytical solutions to model interfacial creep (Hills et al., 1996). Hence, after indenting the most suitable techniques to model relative displacement between mating surfaces, an investigation of the problem was sistematically performed. A through numerical (using FE models) and experimental corroboration of the analyses performed by the author has been also carried out. The main theoretical and experimental achievements of this thesis are summarised in the next section.

9.1 Theoretical and experimental investigation

(i) The first step was to frame our approach on the basis of existing techniques which have never been combined before to model the frictional interfacial behaviour of layered systems. The distributed dislocation technique was chosen to model relative displacement between mating surfaces

since it had been proven to be very accurate in measuring interfacial creep. The implementation of the technique was not modified at this stage and it was applied according to classical schemes. A simplified contact problem was then presented to mimic the basic behaviour of the shrink fitted system under investigation. A series of example cases were treated and the phenomenon of interfacial creep in layered systems fully explained. Moreover, a preliminary investigation of the importance of time history on the solution to the problem was carried out.

(ii) In Chapter 3 a simplified layered form of a very common engineering contact problem, the Carter driving wheel problem, was analysed. This additional investigation was performed in order to give practical advice to engineers for cases where potential interfacial slip could lead to system failures. The main conclusion of this analysis is that where a repleaceble tyre has to be used, its thickness should be as great as possible in relation to the contact size in order to avoid the possibility of fretting. Also, the larger the shrink-fit contact pressure achievable the better, but the other side to this coin is that the strength of the contact will be severely reduced as plasticity is more likely to take place.

(iii) The case of a layer sliding over a rigid substrate has been treated in Chapter 4. A novel formulation for an elastic layer, pressed onto a rigid substrate, and slid along by a local external contact, has been described. The principle adopted by the author is to represent the actual contact tractions using a piecewise linear distribution of overlapping triangles. The influence functions corresponding to the triangular tractions have been derived from first principle and a series of example cases have been investigated. The accuracy of the semi-analytical formulation was also tested. In fact, the output of this phase was to provide a fast and accurate semi-analytical tool to compute the stresses between layer and substrate for this unusual, but realistic, loading configuration.

(iv) Chapter 5 presented the application of quadratic programming optimisation techniques to the solution of 2D layered systems in the presence of localised slip within the distributed dislocation framework developed in previous chapters. This numerical approach enables us to track the

marching-in-time solution to layered contact problems efficiently and accurately, overcoming the main limitation to the classical schemes available in the literature. The newly developed scheme was therefore adopted to investigate frictional shakedown in layered systems. This interesting topic was treated in Chapter 6. Moreover, an experimental investigation was carried out to corroborate our numerical findings. This was made possible by the fact that the novel numerical approach allows modelling complex loading scenarios in real assemblies and, consequently, to predict the outcome of tests characterised by different geometries and various loading conditions. The experimental work, carried out using a micropitting testing machine modified for the purpose of probing interface slip and the presence of net displacement between layer and substrate, proved the developed technique to be accurate and reliable.

(v) The phenomenon of frictional shakedown in layered systems has been treated in Chapter 6. The topic is not novel as it has been investigated since the early 50s. However, a systematic approach has never been established to investigate the problem because of its complexity, and the lack of accurate and fast numerical schemes to compute interfacial slip. The applicability of the novel numerical scheme presented in Chapter 5 to this type of frictional contact phenomenon has been shown. An energy parameter has been proposed to classify the frictional behaviour of the systems under investigation. Moreover, the applicability of plasticity principles has been considered and, particularly, the use of Melan's theorem to predict the frictional behaviour of coupled layered contacts has been considered. It has been clearly shown that Melan's theorem may *understimate* the elastic frictional shakedown limit. A systematic investigation of the causes of such limitation have been framed and some preliminary conclusions drawn.

(vi) A novel experimental method to measure the friction coefficient under partial slip conditions has been presented in Chapter 7. This is an interesting topic as the friction coefficient is usually a critical input to our simulations, but its value has always been assumed given *a priori*. In this work a novel methodology to determine the friction coefficient, limiting the damage to the rubbing surfaces

caused by sliding, has been proposed. In fact, the test does not cause the amount of surface damage usually associated with sliding and it seems a viable method of measuring, with great precision, the coefficient of friction between solids.

(vii) The final chapter presents the work which has been carried out to study the engineering prototypical application. The approach combined both numerical and experimental investigations and comprised a 3D FE model of the tyre-wheel assembly, data analysis on the real forces to which the system is subjected, and a comprehensive characterisation of the tribological properties of the tyre-wheel interface. As main investigators of the problem, our role has also been to collate and interpret all the information collected by the project partners and to provide guidelines for improved design of wheels and tyre-wheel interfaces for off-highway vehicles.

The theoretical and experimental findings presented in this thesis and summarised above have wide engineering impact. The work carried out by the author helps shedding light on the frictional behaviour of tyre/wheel assemblies and, more in general, on shrink-fitted systems whose performance are potentially affected by the relative motion between the mating surfaces. The newly developed semi-analytical and numerical methodologies have been successfully applied to the solution of complex tyred systems. The numerical scheme based on the application of quadratic programming and distributed dislocations to resolve localised microslip and frictional creep at the contact interface between shrink-fitted components as been proven to be fast, accurate and reliable. By tracking in time the interfacial stress field and the relative displacements between the tyre and the wheel, this technique enables to produce behavioural maps of the interfaces under investigation. Of particular engineering relevance are the evaluation of thresholds for the avoidance of microslip in two-dimensional assemblies. The accurate prediction of creep and creep rates which the components undergo in case such limits are exceeded when different loading scenarios are considered is also noteworthy. The experimental evidence provided by the author demonstrates the validity of the proposed approach and shows how a much better understanding of the frictional behaviour

of shrink-fitted systems has been achieved. The fundamental work carried out of two-dimensional systems has also enabled to extend the threshold concept to complex three-dimensional tyre/wheel assemblies and to issue guidelines for the improved design of their interfaces.

Of even more general interest and applicability is the technique developed to measure the friction coefficient between bodies which do not undergo full sliding but are characterised by local (or partial) slip. This methodology can be effectively applied to real problems to infer the value of the friction coefficient in shrink-fitted systems when localised slip or creep take place. This is a key input parameter in our model. Finally, the occurrence of frictional shakedown has been also investigated to understand its relevance to the engineering systems under investigation. This peculiar frictional behaviour always occurs when surfaces are in oscillatory contact and the preliminary investigation carried out in this thesis shows that a better understanding of this phenomenon is needed. Its exploitation may result in a competitive advantage when new products are designed.

9.2 Future work

In this section, a summary of the suggestions for further developments of the semi-analytical and numerical techniques proposed by the author and for further experimental corroboration, is presented. The reader should also refer to the individual chapter summaries for the discussion of some of the proposed investigations.

(i) More experimental work is required to fully corroborate the proposed approach to model interfacial slip in layered systems. In fact, despite the success in corroborating the results obtained using the newly developed numerical methodology discussed in Chapter 5, more tests should be performed to confirm the validity of the approach when applied to different loading conditions and material pairs.

(ii) The quadratic programming technique, together with the distributed dislocation technique, has enabled us to explore the frictional shakedown problem for layered systems. However, the numer-

ical investigation has been limited to a series of simplified loading scenarios which are not always representative of practical problems. Moreover, the numerical findings need to be corroborated experimentally. In fact, despite many researchers have investigated the problem using analytical, semi-analytical or purely numerical tools, experimental investigations of elastic and plastic frictional shakedown of layered systems have never been carried out. This is a very challenging aspect which should be explored in the near future.

(iii) On the novel technique to measure friction in partial slip, further work should permit the instantaneous variation of the coefficient of friction across the contact patch to be deconvolved, and this will form part of a future investigation. Modest changes in the load range cause sufficient change in the walking distance for the coefficient of friction, at least on aggregate, to be quoted to two significant figures with confidence. Also, the damage which has been caused is well documented because the precise contact pressure distribution and slip displacement are fully known during the test. Indeed, it is possible that this could be exploited by putting very carefully controlled amounts of surface modification into the specimen before a test is conducted - for example by deliberately putting the specimen in the equivalent of a 'cyclic plasticity' (walking back and forth) regime of response.

(iv) Various suggestions for the work to be performed to improve the characterisation of the prototypical assembly have also been reported in Chapter 8. They include:(a) calibration of the FE model results against strain gauged wheel data to investigate the different response of the wheel due to various tyre architectures and loading conditions; (b) completition of the proposed testing apparatus for a better characterisation of the tyre-rim interface; (c) simplification and reduction of the load history maps according to the requirements of the in-house testing; and (d) application of 3D FE models for the assessment of the wheel fatigue performance.

Reference

Abaqus User's Manual (2007), version 7.7.1, Karlsson and Sorensen, SIMULIA.

Ahn, Y.J., Bertocchi, E., and Barber, J.R. (2008a), "Shakedown of coupled two-dimensional discrete frictional systems", *Journal of the Mechanics and Physics of Solids*, 56, p. 3433.

Ahn, Y.J. and Barber, J.R. (2008b), "Response of frictional receding contact problems to cyclic loading", *International Journal of Mechanical Sciences*, 50, p.1519.

Anscombe, H. and Johnson, K.L. (1974), "Slip of a thin solid tyre press-fitted on a wheel", International Journal of Mechanical Sciences, 16, p. 329.

Antoni, N., Nguyen, Q. S., Ligier, J. L., Saffré, P., Pastor, J. (2007), "On the cumulative microslip phenomenon", *European Journal of Mechanics - A/Solids*, 26, 626.

Antoni, N. and Nguyen, Q.S. (2008), "Shakedown theorems in Contact Mechanics", *Comptes Rendus Mécanique*, 336, 341.

Araújo, J. A., and Nowell, D. (1999), "Analysis of pad size effects in fretting fatigue using short crack arrest methodologies", *International Journal of Fatigue*, 21(9), pp. 947-956.

Aslantas K. and Tasgetiren, S. (2002), "Debonding between coating and substrate due to rolling-sliding contact", *Materials & Design*, 23, 571.

Barber, J.R. (2002), *Elasticity*, 2nd ed., Kluwer Academic Publisher.

Barber, J.R., Klarbring, A. and Ciavarella, M. (2008), "Shakedown in frictional contact problems for the continuum", *Comptes Rendus Mécanique*, 336, 34.

Bentall, R.H. and Johnson, K.L. (1968), "An elastic strip in plane rolling contact", *International Journal of Mechanical Sciences*, 10, 637.

Blau, P.J. (1995), Friction Science and Technology, CRC Press.

Bowden F. P. and Leben L. (1939), "The Nature of Sliding and the Analysis of Friction", *Proceedings of the Royal Society of London, Series A, Mathematical and Physical Sciences*, 169, pp. 371-391.

Carter, F.W. (1926), "On the action of a locomotive driving wheel", *Proceedings of the Royal Society of London*, Series A, 112, p. 151.

Cattaneo, C. (1938), "Sul contatto di due corpi elastici: distribuzione locale degli sforzi", *Rendiconti dell'Accademia Nazionale dei Lincei*, 27(6), pp. 342–348.

Chand, R., Haug, E.J. and Rim, K. (1976), "Analysis of unbonded contact problems by means of quadratic programming", *Journal of Optimization Theory and Applications*, 20, 171.

Chang, F.K., Comninou, M., Barber, J. R. (1983), "Slip between a layer and a substrate caused by a normal force moving steadily over the surface", *International Journal of Mechanical Science*s, 25, 803.

Chen, Y.H., Polonsky, I.A., Chung, Y.W. and Keer, L.M. (2002), "Tribological properties and rolling-contact-fatigue lives of TiN/SiNx multilayer coatings", *Surface and Coatings Technology*, 154, 152.

Chen, W.T. (1971), "Computation of stresses and displacements in a layered elastic medium", *International Journal of Engineering Science*, 9, 775.

Chen, W.T., Engel, P.A. (1972), "Impact and contact stress analysis in multilayer media", *International Journal of Solids and Structures*, 8, 1257.

Churchman, C. M., and Hills, D.A. (2006), "General results for complete contacts subject to oscillatory shear", *Journal of the Mechanics and Physics of Solids*, 54, p. 1186.

Ciavarella, M. and Demelio, G. (1999), "On non-symmetrical plane contacts", *International Journal of Mechanical Sciences*, 41(12), p. 1533-1550.

Cole, S.J. and Sayles, R.S. (1992), "A Numerical Model for the Contact of Layered Elastic Bodies With Real Rough Surfaces", *Journal of Tribology*, 114, 334.

Comninou, M. and Dundurs, J. (1978), "Can two solids slide without slipping?", *International Journal of Solids and Structures*, 14(4), pp. 251-260.

Comninou, M., Schmueser, D. and Dundurs, J. (1980), "Frictional slip between a layer and a substrate caused by a normal load", *International Journal of Engineering Science*, 18, 131.

Comninou, M., and J.R. Barber (1983a), "Frictional slip between a layer and a substrate due to a periodic tangential surface force", *International Journal of Solids and Structure*s, 19, p. 533.

Comninou, M., Barber, J.R. and Dundurs, J. (1983b), "Interface slip caused by a surface load moving at constant speed", *International Journal of Mechanical Sciences*, 25, 41.

Comninou, M. and Dundurs, J. (1983c), "Partial closure of cracks at the interface between a layer and a half space", *Engineering Fracture Mechanics*, 18, 315.

Comninou, M. (1978), "The interface crack in a shear field", Journal of applied mechanics, 45(2), p. 287-90.

Dini, D. (2004), "Studies in fretting fatigue with particular application to almost complete contacts", Ph.D. Thesis, Department of Engineering Science, University of Oxford.

Dini, D., and Nowell, D. (2003), "Prediction of the slip zone friction coefficient in flat and rounded contact", *Wear*, 254(3-4), pp. 364-369.

Dundurs, J. and Mura, T. (1964), "Interaction between edge dislocation and circular inclusion", *Journal of Mechanics and Physics of Solids*, 12(3), p. 177-189.

Dundurs, J. and Sendeckyj, G.P. (1965), "Edge dislocation inside circular inclusion", *Journal of Mechanics and Physics of Solids*, 13(3), p. 141-147.

Dundurs, J. (1967), "Effect of elastic constants on stress in a composite under plane deformation", *Journal Composite Material*, 1, pp. 310–322.

Dundurs, J. and Comninou, M. (1979), "Some consequances of the inequality conditions in contact

and crack problems", *J. Elasticity*, 9, p. 71.

Drucker, D.C. (1954), "Coulomb friction, plasticity, and limit loads ", *ASME J. Appl. Mech.*, 21, 71-74

Eberhardt, A.W., Lewis, J.L. and Keer, L.M. (1991), "Normal Contact of Elastic Spheres With Two Elastic Layers as a Model of Joint Articulation", *Journal of Biomechanical Engineering*, 113, 410.

Edge, J. (2008), 4th Year Project Thesis, Mechanical Engineering Department, Imperial College London.

Erdogan, F.F. (1971), "On the numerical solution of singular integral equations", *Quarterly of applied mathematics*, 29, p. 525-534.

Fouvry, S., Kapsa, Ph., Vincent, L. (1998), "Developments of fretting sliding criteria to quantify the local friction coefficient evolution under partial slip condition", *Tribology Series*, 34, pp. 161-172.

Fouvry, S., and Kapsa, Ph. (2001), "An energy description of hard coating wear mechanisms", *Surface and Coatings Technology*, 138(2-3), pp. 141-148.

Fredriksson, B. and Rydholm, G. (1981), "Shakedown in frictional systems - some considerations", In: Rydholm, G. (ed.), On Inequalities and Shakedown in Contact Problems, Diss. No. 61, Linkoping Studies in Science and Technology, F1-F21.

GKN (2009), *Private communication*.

Gladwell (1980), *Contact problems in Classical Theory of Elasticity*, Sijtoff and Noordhoff, Maryland, USA.

Gobbi, M., Aiolfi, M., Pennati, M., Previati, G., Levi, F., Ribaldone, M. and Mastinu, G. (2005), Measurement of the forces and moments acting on farm tractor pneumatic tyres, *Vehicle System Dynamics*, 43, p. 412-33.

Heisenberg, W. (1927), "Über den anschaulichen Inhalt der quantentheoretischen Kinematik und Mechanik", Zeitschrift für Physik 43: 172–198.

Hills, D.A., Kelly, P.A., Dai, D.N. and Korsunsky, A.M. (1996), Solution of crack problems: the distributed dislocation technique, Kluwer Academic Publisher.

Hills, D.A., Nowell, D. and Sackfield, A. (1993), Mechanics of elastic contacts, Butterworth Heinemann.

Ihara, T., Shaw, M.C. and Bhushan, B. (1986a), A finite element analysis of contact stress and strain in an elastic film on a rigid substrate -Part I: zero friction, *Transactions of ASME, Journal of Tribology*, 108, 4, pp. 527–533.

Ihara, T., Shaw, M.C. and Bhushan, B. (1986b), A finite element analysis of contact stress and strain in an elastic film on a rigid substrate -Part II: with friction, *Transactions of ASME, Journal of Tribology*, 108, 4, pp. 534–539.

Jaffar, M.J. (1988), "A numerical solution for axisymmetric contact problems involving rigid in-

denters on elastic layers", *Journal of the Mechanics and Physics of Solids*, 36, p. 401.

Jaffar, M.J. (1989), "Asymptotic behaviour of thin elastic layers bonded and unbonded to a rigid foundation", *International Journal of Mechanical Sciences*, 31, p. 229.

Jaffar, M.J. (1991), "Elastic strips in sliding contact", *The Journal of Strain Analysis for Engineering Design*, 26, p. 193.

Johnson, K. L. (1985), Contact Mechanics, Cambridge University Press, Cambridge.

Kadiric A., Sayles, R.S. and Ioannides, E. (2008), "Thermo-Mechanical Model for Moving Layered Rough Surface Contacts", *Journal of Tribology*, 130, 011016.

Kalker, J.J. (1971), "A minimum principle for the law of dry friction with application to elastic cylinders in rolling contact. Part 1: fundamentals, application to steady state rolling", *Transaction ASME, Journal of Applied Mechanics*, 38, 875.

Kalker, J.J. (1990), *Three-dimensional elastic bodies in rolling contact*, Springer.

Kelly, P.A., Hills,D.A. and O'Connor, J.J. (1999), "Elastic contact on a double-layered substrate", Proceedings of the Institution of Mechanical Engineers; Part C; *Journal of Mechanical Engineering Science*, 213, 331.

Keer, L.M. and Guo, Q. (1990), "Stress analysis for symmetrically loaded bonded layers", *International journal of fracture*, 43, 69.

King, R.B. and O'Sullivan, T.C. (1987), "Sliding contact stresses in a two-dimensional layered elastic half-space", *International Journal of Solids and Structures*, 23, 581.

Klarbring, A. (1986), "A mathematical programming approach to three-dimensional contact problems with friction", *Computer Methods in Applied Mechanics and Engineering*, 58, 175.

Klarbring, A. and Björkman, G. (1988), "A mathematical programming approach to contact problems with friction and varying contact surface", *Computers & Structures*, 30, 1185.

Klarbring, A., Ciavarella, M. and Barber, J.R. (2007), "Shakedown in elastic contact problems with Coulomb friction", *International Journal of Solids and Structure*s, 44, p. 8355.

Komvopoulos, K. (1988), "Finite element analysis of a layered elastic solid in normal contact with a rigid surface", *Trans. ASME, J. Tribology*, 110(3), 477.

Kral, E.R. Komvopoulos, K. and Bogy, D.B. (1995a), "Finite Element Analysis of Repeated Indentation of an Elastic-Plastic Layered Medium by a Rigid Sphere, Part II: Subsurface Results", *Journal of Applied Mechanics*, 62, 29.

Kral, E.R., Komvopoulos, K. and Bogy, D.B. (1995b), "Finite Element Analysis of Repeated Indentation of an Elastic-Plastic Layered Medium by a Rigid Sphere, Part I: Surface Results", *Journal of Applied Mechanics*, 62, 20.

Kral, E.R. and Komvopoulos, K. (1996a), "Three-Dimensional Finite Element Analysis of Subsurface Stresses and Shakedown Due to Repeated Sliding on a Layered Medium", *Journal of Applied Mechanics*, 63, 967.

Kral, E.R. and Komvopoulos, K. (1996b), "Three-Dimensional Finite Element Analysis of Surface Deformation and Stresses in an Elastic-Plastic Layered Medium Subjected to Indentation and Sliding Contact Loading", *Journal of Applied Mechanics*, 63, 365.

Kral, E.R. and Komvopoulos, K. (1997), "Three-Dimensional Finite Element Analysis of Subsurface Stress and Strain Fields Due to Sliding Contact on an Elastic-Plastic Layered Medium", *Journal of Tribology*, 119, 332.

Krenk, S.S. (1975), "On the use of interpolation polynomial for solutions of singular integral equations", *Quarterly of applied mathematics*, 32(4), p. 479-84.

Lainé, E., Olver, A.V and Beveridge, T.A. (2008), "Effect of lubricants on micropitting and wear", *Tribology International*, 41, 1049.

Lee, C. (2006), "Rim Slip and Bead Fitment of Tires: Analysis and Design", *Tire Science and Technology*, 34(1), p. 38-63.

Lovell, M. (1998), "Analysis of contact between transversely isotropic coated surfaces: development of stress and displacement relationships using FEM", *Wear*, 214, 165.

Lovell, M.R., Khonsari, M.M. and Marangoni, R.D. (1996), "A finite element analysis of the frictional forces between a cylindrical bearing element and MoS2 coated and uncoated surfaces", *Wear*, 194, 60.

LabView User Manual (2003), National Instruments.

Ma, L.F. and Korsunsky, A.M. (2004), "Fundamental formulation for frictional contact problems of coated systems", International Journal of Solids and Structures, 41, 2837.

Maier, G. (1968a), "A quadratic programming approach for certain classes of non linear structural problems", *Meccanica*, 3, 121.

Maier, G. (1968b), "Quadratic programming and theory of elastic-perfectly plastic structures", *Meccanica*, 3, 265.

Maier, G. (1969a), "A method for approximate solutions of stationary creep problems", *Meccanica*, 4, 36.

Maier, G. (1969b), "Shakedown theory in perfect elastoplasticity with associated and nonassociated flow-laws: A finite element, linear programming approach", *Meccanica*, 4, 250.

MATLAB Documentation (2009), v.R2009a, The MathWorks.

Matos, P.F.P. and Nowell, D. (2007), "On the accurate assessment of crack opening and closing stresses in plasticity-induced fatigue crack closure problems", *Engineering Fracture Mechanics*, 74, 1579.

Meijers, P. (1968), "The contact problem of a rigid cylinder on an elastic layer", *Applied scientific research*, 18, 353.

Melan, E. (1936), "Teorie statisch unbestimmter Systeme aus ideal-plastichem", Baustoff. *Sitzungsber.d.Akad.d.Wiss.*, Wien 2A, 145, 195.

Michelin (2004), "Maintenance guide for Earthmover Tyres".

Michelin (2009), *Private communication*.

Mugadu, A., Hills, D. A., and Nowell, D. (2002), "Modifications to a fretting-fatigue testing apparatus based upon an analysis of contact stresses at complete and nearly complete contacts", *Wear*, 252(5-6), pp. 475-483.

Mugadu, A., Sackfield, A. and Hills, D.A. (2004), "Analysis of a Rocking and Walking Punch—Part I: Initial Transient and Steady State", *Journal of Applied Mechanics*, 71, 225.

Munisamy, R., Hills, D.A. and Nowell, D. (1991), "Brief note on the tractive rolling of dissimilar elastic cylinders", *International Journal of Mechanical Sciences*, 33, 225.

Muskhelishvili (1946), Singular Integral Equations, P. Noordhoff Ltd.

Nikas, G.K. and Sayles, R.S. (2008), "Finite-element analysis of layered rolling contacts", Proceedings of the Institution of Mechanical Engineers; Part J; *Journal of Engineering Tribology*, 222, 865.

Nikas, G.K. and Sayles, R.S. (2009), "Surface coatings and finite-element analysis of layered fretting contacts", Proceedings of the Institution of Mechanical Engineers; Part J; *Journal of Engineering Tribology*, 223, 159.

Nowell, D. and Hills, D.A. (1988a), "Tractive rolling of dissimilar elastic cylinders", *International Journal of Mechanical Sciences*, 30, 427.

Nowell, D., and Hills, D.A. (1988b), "Tractive rolling of tyred cylinders", *International Journal of Mechanical Sciences*, 30, p. 945.

Nowell, D., Hills, D.A. and Sackfield, A. (1988c), "Contact of dissimilar elastic cylinders under normal and tangential loading", *Journal of the Mechanics and Physics of Solids*, 36, 59.

Nowell, D. and Dai, D.N. (1998a), "Analysis of Surface Tractions in Complex Fretting Fatigue Cycles Using Quadratic Programming", *ASME - Journal of Tribology*, 120, 744.

Nowell, D. (2004), "Analysis of a Rocking and Walking Punch—Part II: General Numerical Solution Using Quadratic Programming", *Journal of Applied Mechanics*, 71, 234.

Nowell, D., Dini, D. and Hills D.A. (2006), "Recent developments in the understanding of fretting fatigue", *Engineering Fracture Mechanics*, 73, 207.

Oliveira, S.A.G. and Bower, A.F. (1996), "An analysis of fracture and delamination in thin coatings subjected to contact loading", *Wear*, 198, 15.

O'Sullivan, T.C. and King, R.B. (1988), "Sliding Contact stress field due to a spherical indenter on a layered elastic halfspace", *Journal of Tribology*, 110, 235.

Pacejka, H.B. (2002), Tyre and Vehicle Dynamics, 2002, Butterworth Heinemann.

Pasanen, A., Lehtovaara, A., Rabb, R. and Riihimäki (2010), P., "Friction behavior of quenched and tempered steel in partial and gross slip conditions in fretting point contact", *Wear*, In Press, Corrected Proof.

Persson, B.N.J. and Tosatti, E. (2000), "Qualitative theory of rubber friction and wear", *Journal of Chemical Physics*, 112(4), p. 2021-9.

Persson, B.N.J. (2001), "Elastic instabilities at a sliding interface", *Physical Review B (Condensed Matter)*, 63(10), p. 104101-1.

Persson, B.N.J. and Volokitin, A.T. (2006a), "Rubber friction on smooth surfaces", *European Physical Journal E*, 21(1), p. 69-80.

Persson, B.N.J. (2006b), "Contact mechanics for randomly rough surfaces", *Surface Science Reports*, 61(4), p. 201-27.

Po, B. (2009), 4th Year Project Thesis, Mechanical Engineering Dpt., Imperial College London.

Polonsky, I.A. and Keer, L.M. (2000), "A Fast and Accurate Method for Numerical Analysis of Elastic Layered Contacts", *Journal of Tribology*, 122, 30.

Polonsky, I.A. and Keer, L.M. (2001), "Stress Analysis of Layered Elastic Solids With Cracks Using the Fast Fourier Transform and Conjugate Gradient Techniques", *Journal of Applied Mechanics*, 68, 708.

Porter, M. I., and Hills, D.A. (2002a), "A flat punch pressed against an elastic interlayer under conditions of slip and separation", *International Journal of Mechanical Sciences*, 44, 465.

Porter, M. I., and Hills, D.A. (2002b), "Note on the complete contact between a flat rigid punch and an elastic layer attached to a dissimilar substrate", *International Journal of Mechanical Sciences*, 44, 509.

Qiu, H., Dini, D., Hills, D.A. (2008), "Torsional contact of an elastic flat-ended cylinder", *Journal of the Mechanics and Physics of Solids*, 56, 3352.

Reina, S., Dini, D. and Hills, D.A. (2009), "On the accurate prediction of interfacial micro-slip in frictional joints using distributed dislocations and quadratic programming techniques", *Procedia Engineering*, 1, 181.

Reina, S., D. Dini, and D.A. Hills (2010a), “Incipient slip conditions in rolling contact of tyred wheels”, Proceedings of the Institution of Mechanical Engineers, Part C: Journal of Mechanical Engineering Science, doi:10.1243/09544062JMES2075.

Reina, S., D. Dini, and Hills, D.A. (2010b), “Interfacial Slip and Creep in rolling contact incorporating a Cylinder with an Elastic Layer”, European Journal of Mechanics A/Solids,

doi:10.1016/j.euromechsol.2010.02.009.

Reina S., Hills D.A. and Dini D. (2010c), “Contact of a rigid cylinder indenting an elastic layer sliding over a rigid substrate”, European Journal of Mechanics A/Solids,

doi:10.1016/j.euromechsol.2010.02.006.

Reina S., Hills D.A. and Dini D., (2010d), “Determining the coefficient of friction without sliding”, Wear (2010), Wear (2010), doi:10.1016/j.wear.2010.04.017.

Schmueser, D.D. and Comninou, M. (1979), "The interface crack in a combined tension-compression

and shear field", *Journal of applied mechanics*, 46(2): p. 345-8.

Sneddon, I.N. (1951), *Fourier Transforms*, McGraw-Hill, New York.

Stachowiak, G. and Batchelor, A.W. (2004), *Experimental Methods in Tribology*, Elsevier.

Stearns, J., Srivatsan, T.S., Prakash, A. and Lam, P.C. (2004), "Modeling the mechanical response of an aluminum alloy automotive rim", *Materials Science and Engineering A*, 366(2), p. 262-268.

Su, R.K.L., Zhu, Y. and Leung, A.Y.T. (2002), "Parametric quadratic programming method for elastic contact fracture analysis", *International journal of fracture*, 117, 143.

Sun, Y. (2010), MSc Project Thesis, Mechanical Engineering Department, Imperial College London, *to be submitted in September 2010*.

Tian, H. and Saka, N. (1991a), "Finite element analysis of an elastic-plastic two-layer half-space: sliding contact", *Wear*, 148, 261.

Tian, H. and Saka, N. (1991b), "Finite element analysis of an elastic-plastic two-layer half-space: normal contact", *Wear*, 148, 47.

Timoshenko, S. and Goodier, J.N. (1970), *Theory of Elasticity*, McGraw-Hill, New York.

Treloar, L.R.G. (1958), *The physics of rubber elasticity* 2^{nd} ed., Oxford University Press.

Truman, C.E. and Booker, J.D. (2007), "Analysis of a shrink-fit failure on a gear hub/shaft assembly", *Engineering Failure Analysis*, 14, 557.

Vingsbo, O., and Söderberg S. (1988), "On fretting maps", *Wear*, 126(2), pp. 131-147.

Vorvolakos, K. and Chaudhury, M.K. (2003), "The effects of molecular weight and temperature on the kinetic friction of silicone rubbers", *Langmuir*, 19(17), p. 6778-6787.

Yang, S. (2009), 4th Year Project Thesis, Mechanical Engineering Department, Imperial College London.

Ye, N. and Komvopoulos, K. (2003a), "Effect of Residual Stress in Surface Layer on Contact Deformation of Elastic-Plastic Layered Media", *Journal of Tribology*, 125, 692.

Ye, N. and Komvopoulos, K. (2003b), "Indentation Analysis of Elastic-Plastic Homogeneous and Layered Media: Criteria for Determining the Real Material Hardness", *Journal of Tribology*, 125, 685.

Wang, Z. (2009), 4th Year Project Thesis, Department of Engineering Science, University of Oxford.

Wille, R., Bohm, F. and Duda, A. (2005), "Calculation of the rolling contact between a tyre and deformable ground", *Vehicle System Dynamics*, 43, p. 483-92.

http://www.jcb.com

http://www.tekscan.com

http://www.veeco.com

http://www.kistler.com

http://www.michelin.com

http://www.etrto.org

http://www.instron.co.uk

http://www.dowcorning.com

http://www.pcs-instruments.com/mpr

http://www.rema-tiptop.co.uk

Appendix A

The influence functions for a triangular distribution of traction, of half-width a_{tr}, height (p_i, q_i), and located at x_i, on the surface normal displacement, v, at a point x along the interface between the indenting disc and the elastic layer are given by:

$$F^p(x, x_i) = \int_0^\infty \left[\frac{\omega b - \frac{1}{2}(3-4\nu)\sinh(2\omega b)}{(\omega b)^2 + (1-2\nu)^2 + (3-4\nu)\cosh^2(\omega b)} \right] \frac{2}{a_{tr}\omega^2} \sin^2\left(\omega \frac{a_{tr}}{2}\right) \cos\left(\omega\left(x - x_i\right)\right) \frac{d\omega}{\omega} \tag{A.1}$$

$$F^q(x, x_i) = \int_0^\infty \left[\frac{(\omega b)^2 + (1-2\nu)(3-4\nu)\left(1 - \cosh^2(\omega b)\right)}{(\omega b)^2 + (1-2\nu)^2 + (3-4\nu)\cosh^2(\omega b)} \right] \frac{2}{a_{tr}\omega^2} \sin^2\left(\omega \frac{a_{tr}}{2}\right) \sin\left(\omega\left(x - x_i\right)\right) \frac{d\omega}{\omega}. \tag{A.2}$$

The kernels to be used in conjunction with equations (2.3) and (2.4) are:

$$N_{12} = 4\left[(1+\beta^2)\tau^2 + \beta\right] e^{\tau} - 2\beta(1+\alpha)e^{-\tau} \tag{A.3}$$

$$N_{22} = 2\left\{2\left(1+\beta\right)\left[\left(1+\beta\right)\tau - \left(1-\beta\right)\right]\tau + 1 + \beta^2\right\} e^{\tau} - 2(\alpha + \beta^2)e^{-\tau} \tag{A.4}$$

$$D_{12} = D_{22} = \left(1-\beta^2\right) e^{2\tau} + \left(\alpha^2 - \beta^2\right) e^{-2\tau} - 4(1+\beta)(\alpha-\beta)\tau^2 - 2(\alpha - \beta^2). \tag{A.5}$$

Appendix B

The influence functions for normal and tangential displacements for a layer sliding over a rigid substrate are given by:

$$\begin{aligned} I_{up} &= e^{|\phi|b}\left[A_p\phi^2 + B_p(2\,|\phi|\,(\nu_1{-}1) - \phi^2 b)\right] + \\ &\quad + e^{-|\phi|b}\left[C_p\phi^2 + D_p(2\,|\phi|\,(-\nu_1+1) - \phi^2 b)\right] \end{aligned} \tag{B.1}$$

$$\begin{aligned} I_{uq} &= e^{|\phi|b}\left[A_q\phi^2 + B_q(2\,|\phi|\,(\nu_1{-}1) - \phi^2 b)\right] + \\ &\quad + e^{-|\phi|b}\left[C_q\phi^2 + D_q(2\,|\phi|\,(-\nu_1+1) - \phi^2 b)\right] \end{aligned} \tag{B.2}$$

$$\begin{aligned} I_{vp} &= e^{|\phi|b}\left[A_p\phi^2\,|\phi| + B_p\phi(1 - 2\nu_1 - |\phi|\,b)\right] + \\ &\quad + e^{-|\phi|b}\left[-C_p\phi^2\,|\phi| + D_p\phi(1 - 2\nu_1 + |\phi|\,b)\right] \end{aligned} \tag{B.3}$$

$$\begin{aligned} I_{vq} &= e^{|\phi|b}\left[A_q\phi^2\,|\phi| + B_q\phi^2(1 - 2\nu_1 - |\phi|\,b)\right] + \\ &\quad + e^{-|\phi|b}\left[-C_q\phi^2\,|\phi| + D_q\phi^2(1 - 2\nu_1 + |\phi|\,b)\right] \end{aligned} \tag{B.4}$$

where the eight additional constants, $A_p, B_p, C_p, D_p, A_q, B_q, C_q, D_q$, are found by imposing the boundary conditions. For the normal traction components:

$$\begin{bmatrix} A_p \\ B_p \\ C_p \\ D_p \end{bmatrix} = \frac{1}{\Delta P} \begin{bmatrix} I_{Ap} \\ I_{Bp} \\ I_{Cp} \\ I_{Dp} \end{bmatrix} \tilde{p}(\phi) \tag{B.5}$$

with

$$\begin{aligned}\Delta P &= \phi^2 i\left(-1+e^{2b|\phi|}\right)^2 f\phi^3\left(-1+2\nu_1\right)\rho_{sub} - \left(-1+e^{4b|\phi|}\right)\phi^2\left|\phi\right|\left(-1+2\nu_1\right)+ \\ &\quad -4be^{2b|\phi|}\phi^4(-1+2\nu_1)+\left(-1+e^{4b|\phi|}\right)\phi^2\left|\phi\right|+4be^{2b|\phi|}\phi^4\left(1-ibf\phi\rho_{sub}\right)\end{aligned} \tag{B.6}$$

$$\begin{aligned}I_{Ap} &= -(e^{b|\phi|}(-1+e^{2b|\phi|}+b\left|\phi\right|\left(1+e^{2b|\phi|}\right))* \\ &\quad *(if\phi^3\rho_{sub}\left(-1+2\nu_1\right)+\phi^2\left|\phi\right|\left(1-2\nu_1\right)+\phi^2\left|\phi\right|))\end{aligned} \tag{B.7}$$

$$\begin{aligned}I_{Bp} &= -e^{b|\phi|}\left|\phi\right|(i\left(1+e^{2b|\phi|}\right)f\phi^3\left(-1+2\nu_1\right)\rho_{sub}+ \\ &\quad -\left(-1+e^{2b|\phi|}\right)\phi^2\left|\phi\right|\left(-1+2\nu_1\right)+ \\ &\quad -2if\rho_{sub}\phi^3+\phi^2\left|\phi\right|\left(-1+e^{2b|\phi|}+2ibf\phi\rho_{sub}\right))\end{aligned} \tag{B.8}$$

$$\begin{aligned}I_{Cp} &= -(e^{b|\phi|}(-1+e^{2b|\phi|}+b\left|\phi\right|\left(1+e^{2b|\phi|}\right))* \\ &\quad *(if\phi^3\rho_{sub}\left(1-2\nu_1\right)+\phi^2\left|\phi\right|\left(1-2\nu_1\right)+\phi^2\left|\phi\right|))\end{aligned} \tag{B.9}$$

$$\begin{aligned}I_{Dp} &= -i(e^{b|\phi|}\left|\phi\right|(-\left(1+e^{2b|\phi|}\right)f\phi^3\left(-1+2\nu_1\right)\rho_{sub}+ \\ &\quad -i\phi^2\left|\phi\right|\left(-1+e^{2b|\phi|}\right)\left(-1+2\nu_1\right)+2\phi^3 f\rho_{sub}e^{2b|\phi|} \\ &\quad +\phi^2\left|\phi\right|\left(-i+e^{2b|\phi|}(i+2bf\phi\rho_{sub})\right)))\end{aligned} \tag{B.10}$$

and for the tangential tractions:

$$\begin{bmatrix} A_q \\ B_q \\ C_q \\ D_q \end{bmatrix} = \frac{1}{\Delta Q}\begin{bmatrix} I_{Aq} \\ I_{Bq} \\ I_{Cq} \\ I_{Dq} \end{bmatrix}\tilde{q}(\phi) \tag{B.11}$$

with

$$\Delta Q = \phi \left(\begin{array}{c} \left(-1+e^{2b|\phi|}\right)^2 f\phi^3 \left(-1+2\nu_1\right)\rho_{sub} + i\left(-1+e^{4b|\phi|}\right)\phi^2\left|\phi\right|\left(-1+2\nu_1\right) + \\ +4ibe^{2b|\phi|\phi}\left(-1+2\nu_1\right) - i\phi^2\left|\phi\right|\left(-1+e^{4b|\phi|}\right) - 4be^{2b|\phi|}\left(i+bf\phi\rho_{sub}\right)\phi^4 \end{array} \right) \tag{B.12}$$

$$I_{Aq} = -be^{b|\phi|}\left(-1+e^{2b|\phi|}\right)\left(if\phi^3\left(-1+2\nu_1\right)\rho_{sub} + \phi^2\left|\phi\right|\left(1-2\nu_1\right) + \phi^2\left|\phi\right|\right) \tag{B.13}$$

$$\begin{aligned} I_{Bq} \;=\; & -e^{b|\phi|}(i\left(-1+e^{2b|\phi|}\right)f\phi^3\left(-1+2\nu_1\right)\rho_{sub} + \\ & -\left(1+e^{2b|\phi|}\right)\phi^2\left|\phi\right|\left(-1+2\nu_1\right) + \phi^2\left|\phi\right|\left(1+e^{2b|\phi|}-2ibf\phi\rho_{sub}\right)) \end{aligned} \tag{B.14}$$

$$I_{Cq} = -be^{b|\phi|}\left(-1+e^{2b|\phi|}\right)\left(if\phi^3\left(1-2\nu_1\right)\rho_{sub} + \phi^2\left|\phi\right|\left(1-2\nu_1\right) + \phi^2\left|\phi\right|\right) \tag{B.15}$$

$$\begin{aligned} I_{Dq} \;=\; & -e^{b|\phi|}(-i\left(-1+e^{2b|\phi|}\right)f\phi^3\left(-1+2\nu_1\right)\rho_{sub} + \\ & +\left(1+e^{2b|\phi|}\right)\phi^2\left|\phi\right|\left(-1+2\nu_1\right) + \phi^2\left|\phi\right|\left(-1+e^{2b|\phi|}(-1+2ibf\phi\rho_{sub})\right)). \end{aligned} \tag{B.16}$$

Also

$$I\tilde{V}1 = \int_{-\infty}^{+\infty} I\tilde{V}P\frac{\sin^2\left(Z\psi\right)}{Z\psi^2}e^{-i2\psi Z(i_m-i_n)}\frac{d\psi}{\psi^2} \tag{B.17}$$

$$I\tilde{V}2 = \int_{-\infty}^{+\infty} I\tilde{V}Q\frac{\sin^2\left(Z\psi\right)}{Z\psi^2}e^{-i2\psi Z(i_m-i_n)}\frac{d\psi}{\psi^2} \tag{B.18}$$

$$I\tilde{U}1 = \int_{-\infty}^{+\infty} I\tilde{U}P\frac{\sin^2\left(Z\psi\right)}{Z\psi^2}ie^{-i2\psi Z(i_m-i_n)}\frac{d\psi}{\psi} \tag{B.19}$$

$$I\tilde{U}2 = \int_{-\infty}^{+\infty} I\tilde{U}Q \frac{\sin^2(Z\psi)}{Z\psi^2} i e^{-i2\psi Z(i_m - i_n)} \frac{d\psi}{\psi} \tag{B.20}$$

$$\begin{aligned} I\tilde{V}P &= \frac{e^{|\psi|}}{4}\left[|\psi|\,\psi^2 \frac{\tilde{I}_{Ap}}{\tilde{I}_{\Delta \mathrm{P}}} + |\psi| \frac{\tilde{I}_{Bp}}{\tilde{I}_{\Delta \mathrm{P}}}\left(2\left(1-2\nu_1\right) - |\psi|\right)\right] + \\ &+\frac{1}{4}\left[-|\psi|\,\psi^2 \frac{\tilde{I}_{Cp}}{\tilde{I}_{\Delta \mathrm{P}}} + |\psi| \frac{\tilde{I}_{Dp}}{\tilde{I}_{\Delta \mathrm{P}}}\left(2\left(1-2\nu_1\right) + |\psi|\right)\right] \end{aligned} \tag{B.21}$$

$$\begin{aligned} I\tilde{V}Q &= \frac{e^{|\psi|}}{4}\left[|\psi|\,\psi^3 \frac{\tilde{I}_{Aq}}{\tilde{I}_{\Delta \mathrm{Q}}} + \psi^3 \frac{\tilde{I}_{Bq}}{\tilde{I}_{\Delta \mathrm{Q}}}\left(2\left(1-2\nu_1\right) - |\psi|\right)\right] + \\ &+\frac{1}{4}\left[-|\psi|\,\psi^3 \frac{\tilde{I}_{Cq}}{\tilde{I}_{\Delta \mathrm{Q}}} + \psi^3 \frac{\tilde{I}_{Dq}}{\tilde{I}_{\Delta \mathrm{Q}}}\left(2\left(1-2\nu_1\right) + |\psi|\right)\right] \end{aligned} \tag{B.22}$$

$$\begin{aligned} I\tilde{U}P &= e^{|\psi|}\left[\frac{\psi^2}{4}\frac{\tilde{I}_{Ap}}{\tilde{I}_{\Delta \mathrm{P}}} + \frac{|\psi|}{\psi^2}\frac{\tilde{I}_{Bp}}{\tilde{I}_{\Delta \mathrm{P}}}\left(|\psi|\left(\nu_1 - 1\right) - \frac{\psi^2}{4}\right)\right] + \\ &+\left[\frac{\psi^2}{4}\frac{\tilde{I}_{Cp}}{\tilde{I}_{\Delta \mathrm{P}}} + \frac{|\psi|}{\psi^2}\frac{\tilde{I}_{Dp}}{\tilde{I}_{\Delta \mathrm{P}}}\left(|\psi|\left(1-\nu_1\right) - \frac{\psi^2}{4}\right)\right] \end{aligned} \tag{B.23}$$

$$\begin{aligned} I\tilde{U}Q &= e^{|\psi|}\left[\frac{\psi^3}{4}\frac{\tilde{I}_{Aq}}{\tilde{I}_{\Delta \mathrm{Q}}} + \psi\frac{\tilde{I}_{Bq}}{\tilde{I}_{\Delta \mathrm{Q}}}\left(|\psi|\left(\nu_1 - 1\right) - \frac{\psi^2}{4}\right)\right] + \\ &+\left[\frac{\psi^3}{4}\frac{\tilde{I}_{Cq}}{\tilde{I}_{\Delta \mathrm{Q}}} + \beta\frac{\tilde{I}_{Dq}}{\tilde{I}_{\Delta \mathrm{Q}}}\left(|\psi|\left(1-\nu_1\right) - \frac{\psi^2}{4}\right)\right] \end{aligned} \tag{B.24}$$

$$\begin{aligned} \tilde{I}_{\Delta \mathrm{P}} &= \frac{\psi^3}{4} i\rho_{sub} f\left(-1+2\nu_1\right)\left(-1+e^{|\psi|}\right)^2 + \\ &-\frac{\psi^2|\psi|}{2}\left(-1+e^{2|\psi|}\right)\left(-1+\nu_1\right) + \frac{\psi^4}{2}e^{|\psi|}\left(2\left(1-\nu_1\right) - if\rho_{sub}\frac{\psi}{2}\right) \end{aligned} \tag{B.25}$$

$$\tilde{I}_{Ap} = -\left(-1+e^{|\psi|} + \frac{|\psi|}{2}\left(1+e^{|\psi|}\right)\right)\left(\rho_{sub} i f\psi\left(-1+2\nu_1\right) + 2|\psi|\left(1-\nu_1\right)\right) \tag{B.26}$$

$$\tilde{I}_{Bp} = -\left(\begin{array}{l} \frac{\psi^3}{2} i f\rho_{sub}\left(-3+2\nu_1 - e^{|\beta|}\left(1-2\nu_1\right)\right) + \\ +\psi^2|\psi|\left(\left(1-\nu_1\right)\left(e^{|\psi|}-1\right) + \frac{i}{2}f\rho_{sub}\psi\right) \end{array}\right) \tag{B.27}$$

$$\tilde{I}_{Cp} = -\left(-1+e^{|\psi|} + \frac{|\psi|}{2}\left(1+e^{|\psi|}\right)\right)\left(\rho_{sub} i f\psi\left(1-2\nu_1\right) + 2|\psi|\left(1-\nu_1\right)\right) \tag{B.28}$$

$$\begin{aligned}\tilde{I}_{Dp} &= \frac{\psi^3}{2} i f \rho_{sub} \left(-1+2\nu_1 - e^{|\psi|}\left(3-2\nu_1\right)\right) + \\ &+ \frac{\psi^2 |\psi|}{2}\left(2\left(1-\nu_1\right)\left(e^{|\psi|}-1\right) - i f \rho_{sub}\psi e^{|\psi|}\right)\end{aligned} \tag{B.29}$$

$$\begin{aligned}\tilde{I}_{\Delta \mathrm{Q}} &= \frac{\psi^3}{2}\rho_{sub} f\left(-1+2\nu_1\right)\left(-1+e^{|\psi|}\right)^2 + \\ &+ \psi^2 |\psi| \, i \left(1-e^{2|\psi|}\right)\left(1-\nu_1\right) + \psi^4\left(e^{|\psi|}\left(2i\left(\nu_1-1\right) - f\rho_{sub}\frac{\psi}{2}\right)\right)\end{aligned} \tag{B.30}$$

$$\tilde{I}_{Aq} = \left(1-e^{|\psi|}\right)\left(i f \rho_{sub}\psi\left(-1+2\nu_1\right) + 2|\psi|\left(1-\nu_1\right)\right) \tag{B.31}$$

$$\tilde{I}_{Bq} = -\left(i f \rho_{sub}\psi\left(-1+e^{|\psi|}\right)\left(-1+2\nu_1\right) + |\psi|\left(2\left(1-\nu_1\right)\left(1+e^{|\psi|}\right) - i f\rho_{sub}\psi\right)\right) \tag{B.32}$$

$$\tilde{I}_{Cq} = \left(1-e^{|\psi|}\right)\left(i f \rho_{sub}\psi\left(1-2\nu_1\right) + 2|\psi|\left(1-\nu_1\right)\right) \tag{B.33}$$

$$\begin{aligned}\tilde{I}_{Dq} &= i f \rho_{sub}\psi\left(-1+e^{|\psi|}\right)\left(-1+2\nu_1\right) + \\ &- |\psi|\left(2\left(\nu_1-1\right)\left(1+e^{|\psi|}\right) + i f \rho_{sub}\psi e^{|\psi|}\right)\end{aligned} \tag{B.34}$$

Appendix C

When the materials are similar, with similar meaning having the same Poisson's ratio and the same Young's modulus, the expressions for the influence functions and the constant A_{SM} to be substituted into (5.2) are

$$G_{yy}(x,\xi) = 16\left(-\frac{3b^3}{\left[4b^2+(x-\xi)^2\right]^2}+\frac{16b^5}{\left[4b^2+(x-\xi)^2\right]^2}\right) \tag{C.1}$$

$$G_{xy}(x,\xi) = 2\left(\begin{array}{c}\frac{1}{x-\xi}-\frac{x-\xi}{4b^2+(x-\xi)^2}+\\ +\frac{12b^2(x-\xi)}{\left[4b^2+(x-\xi)^2\right]^2}-\frac{64b^4(x-\xi)}{\left[4b^2+(x-\xi)^2\right]^3}\end{array}\right) \tag{C.2}$$

$$A_{SM} = \frac{2E}{\pi(\kappa+1)} \tag{C.3}$$

where

$$\kappa = 3-4\nu \tag{C.4}$$

When the materials are dissimilar, if the layer is indicated with 1 and substrate with 2, the influence functions and the material constant A_{DM} can be expressed as follows

$$G_{xy}(x,\xi) = \frac{1}{x-\xi} - \frac{1-\alpha}{2b}\int_0^\infty \frac{N_{12}}{D_{12}} e^{-\tau} \sin\left(\frac{x-\xi}{BA}\tau\right) d\tau \tag{C.5}$$

$$G_{yy}(x,\xi) = -\pi\beta\delta(x-\xi) + \frac{1-\alpha}{2b}\int_0^\infty \frac{N_{22}}{D_{22}} e^{-\tau} \sin\left(\frac{x-\xi}{BA}\tau\right) d\tau \tag{C.6}$$

$$A_{DM} = \frac{2E_2(1-\alpha)}{(\kappa_2+1)\left(1-\beta^2\right)} \tag{C.7}$$

where

$$N_{12} = 4\left[\left(1+\beta^2\right)\tau^2 + \beta\right] e^{\tau} - 2\beta(1+\alpha) e^{-\tau} \tag{C.8}$$

$$N_{22} = 2\left\{2(1+\beta)\left[(1+\beta)\tau - (1-\beta)\right]\tau + 1 + \beta^2\right\} e^{\tau} - 2\left(\alpha+\beta^2\right) e^{-\tau} \tag{C.9}$$

$$D_{12} = D_{22} = \left(1-\beta^2\right) e^{2\tau} + \left(\alpha^2-\beta^2\right) e^{-2\tau} - 4(1+\beta)(\alpha-\beta)\tau^2 - 2\left(\alpha-\beta^2\right) \tag{C.10}$$

$$\kappa_2 = 3 - 4\nu_2 \tag{C.11}$$

α and β are the Dundur's parameters (Dundurs, 1967), which can be expressed as follows

$$\alpha = \frac{E_2(\kappa_1+1) - E_1(\kappa_2+1)}{E_2(\kappa_1+1) + E_1(\kappa_2+1)} \tag{C.12}$$

$$\beta = \frac{E_2\left(\kappa_1 - 1\right) - E_1\left(\kappa_2 + 1\right)}{E_2\left(\kappa_1 + 1\right) + E_1\left(\kappa_2 + 1\right)}. \tag{C.13}$$